UNIVERSITY OF OKLAHOMA

GRADUATE COLLEGE

THERMAL CONDUCTIVITY MEASUREMENTS OF IV-VI SEMICONDUCTOR NANOSTRUCTURES

A DISSERTATION

SUBMITTED TO THE GRADUATE FACULTY

in partial fulfillment of the requirements for the

Degree of

DOCTOR OF PHILOSOPHY

By

JAMES DOMINIC JEFFERS
Norman, Oklahoma
2013

THERMAL CONDUCTIVITY MEASUREMENTS OF IV-VI SEMICONDUCTOR NANOSTRUCTURES

A DISSERTATION APPROVED FOR THE
SCHOOL OF ELECTRICAL AND COMPUTER ENGINEERING

BY

Dr. Patrick J. McCann, Chair

Dr. James J. Sluss, Jr.

Dr. Zhisheng Shi

Dr. Hjalti Sigmarsson

Dr. Deborah Trytten

ACKNOWLEDGEMENTS

I would like to thank Dr. Patrick McCann for his guidance, support, and opportunities he provided to me throughout the last 13 years of career at or with the University of Oklahoma and various private enterprises. I am unbelievably fortunate to have been allowed to participate in academically rigorous research with such grand social implications as biomedical and renewable energy. I also want to thank Dr. James Sluss for being the first professor to involve me in publications and attending my first conference. In addition I want to thank Dr. Deborah Trytten for being the most influential computer programming professor I have had. Every chapter in this dissertation involves some form of programming. I would like to thank Dr. Zhisheng Shi for his influence on optical measurements and devices. I would also like to thank Dr. Hjalti Sigmarsson for agreeing to be on my committee.

In addition to the faculty I would like to thank Dr. Khosrow Namjou, Dr. Zhihua Cai, and Mr. Leonard Olona for the tireless effort in thin film MBE growth and characterization. I would also like to thank Dr. Mark Nanny and Dr. Ze'ev Reches for financial support as a research assistant and Dr. Pakise Pulat for allowing me to be an instructor for sections of the Freshman Engineering Experience class.

I would also like to thank my father, David, and acknowledge the memory of my mother Mary who passed away from Alzheimer's during my Ph.D. studies. Their inspiration and support made it possible for me to pursue my dreams.

TABLE OF CONTENTS

TABLE OF FIGURES

LIST OF TABLES

ABSTRACT

This dissertation describes photoluminescence (PL) measurement and finite element thermal modeling to quantify optically induced surface heating of lead chalcogenide (IV-VI) semiconductor thin films and extract thermal conductivity for different superlattice (SL) materials. The results provide the first experimental evidence on the role of PbSe and $Pb_{0.85}Sn_{0.15}Se$ SL layer thicknesses in modifying thermal transport properties in the temperature range from 300 K to 90 K. Low temperature data at 90 K indicated a reduction in lattice thermal conductivity by a factor of 9, from 4.0 $Wm^{-1}K^{-1}$ to 0.45 $Wm^{-1}K^{-1}$, for 1.2 nm thick SL layers as compared to bulk PbSe. This dissertation also contains characterization data for the electrical conductivity, σ, and Seebeck coefficient, S, for lightly doped SL materials. The performance of these materials was estimated using the thermoelectric (TE) figure of merit $ZT \equiv S^2\sigma T/k$. The data indicate SL materials with an optimal dopant concentration of 3 x 10^{18} cm^{-3} at 300 K can be fabricated with σ = 1000 S/cm, S = -190 μV/K and a cross-plane thermal conductivity k = 1.0 $Wm^{-1}K^{-1}$ which would result in a $ZT \geq 1.0$. The same SL will have a ZT = 0.20 at 100 K, much better than bulk PbSe, which has a ZT = 0.05 at 100 K. These results show that IV-VI SL materials can enable development of next generation TE devices for cooling applications. The first in-depth analysis of phonon wave theory for the IV-VI semiconductor system is also presented to estimate the potential for further reduction of cross-plane thermal conductivity from interface reflections. The standard transfer matrix method for optical distributed Bragg reflectors (DBRs) adapted to acoustic waves was implemented to calculate the thickness of SL layers and the number of mirror pairs required for reflectance of different phonon energies.

Chapter 1

Introduction

1.1 Motivation

The objective of this research is to advance the understanding of thermal and electronic processes in nanostructured materials. Periodic materials such as multiple quantum wells (MQWs) and superlattices (SLs) can be engineered to utilize both quantum size and coherent wave effects to alter cross-plane thermal and electrical properties [1-6]. Novel engineered nano-materials, such as those characterized in this research, have been shown to greatly reduce cross-plane thermal conductivity. The molecular beam epitaxy (MBE) growth of MQWs on SLs represents the first attempt to integrate advanced thermoelectric materials on industry standard silicon wafers.

New IV-VI semiconductor nanostructured material can improve the performance of optical and thermoelectric (TE) devices. Improved TE material could both lower the theoretical and practical limits of solid-state refrigeration devices while reducing the physical size. These same materials can also be used to generate electric power from waste heat. Improving power generation efficiency could lead to the development of cost effective renewable energy with both social and environmental impact. In addition the epitaxial fabrication of multi-layer IV-VI semiconductor optical devices provides a clear pathway to the realization of compact sensors using mid-infrared (IR) lasers and detectors for trace gas detection in biomedical [7], environmental [8], and agricultural [9] applications.

1.2 Quantum Electronics

1.2.1 Macro (Ray) Optics

Modern physics employs a wave-particle duality to describe photon energy and motion when the size of objects approaches the wavelength of the photon [10]. Two fundamental laws of classical physics are employed throughout this research: the first is the Beer-Lambert law, Eq. 1.1, that states the intensity of a photon beam traveling in a medium at a given wavelength λ, is proportional to the incident intensity and decays

$$I(\lambda) = I_0 e^{-\alpha(\lambda)cL} \tag{1.1}$$

exponentially proportional to the distance traveled. The variable function, $\alpha(\lambda)$, is the absorption coefficient and varies with both material and wavelength of the photon. The variable c is the concentration of a given absorber in a multi-component mixture and is equal to or less than 1. The distance traveled in the medium is often symbolized by L, for path length or d for distance when the mixture is homogenous and $c = 1$. The second ray optic principle used is Snell's Law and the Fresnel Equations, Eq. 1.2 a) and b), to calculate the transmission and reflection of photons at the boundary of two

$$a)\ \frac{\sin(\theta_i)}{\sin(\theta_t)} = \frac{n_2(\lambda)}{n_1(\lambda)}, \quad b)\ R_s = \left[\frac{\sin(\theta_t - \theta_i)}{\sin(\theta_t - \theta_i)}\right]^2 \tag{1.2}$$

different media. The angle of the transmitted beam, θ_t, is related to the incident beam angle, θ_i, and the wavelength dependent index of refraction, $n(\lambda)$, for each material. The reflection coefficient for un-polarized light (R_s) can be calculated from these three values to determine the percentage of optical power reflected at the material surface.

These classical descriptions for a plane wave photon beam fail to explain the experimentally observed focusing effects of a convex lens. Light velocity in the lens is

reduced compared to air that combined with the lens geometry delays and redirects approaching photons to the same focal point on exit. However, the focal point has a finite size with a non-constant optical intensity that has been measured to be spatially distributed along a given axis by the Gaussian function. The total integral of the Gaussian function is equal to unity, Eq. 1.3, and is defined by the width (spread), σ, and

$$I = \int \frac{1}{\sigma\sqrt{2\pi}} e^{\left(\frac{-(x-\mu)^2}{2\sigma^2}\right)} = 1 \qquad \textbf{(1.3)}$$

an axis offset, μ. Figure 1-1 a) shows two Gaussian functions with different values of σ. Figure 1-1 b) shows the normalized intensity and total integral as a function of distance from the central maximum relative to σ. The minimum width of the focal "spot" size varies with both the wavelength of light being focused and lens properties providing experimental evidence of wave diffraction limited optics.

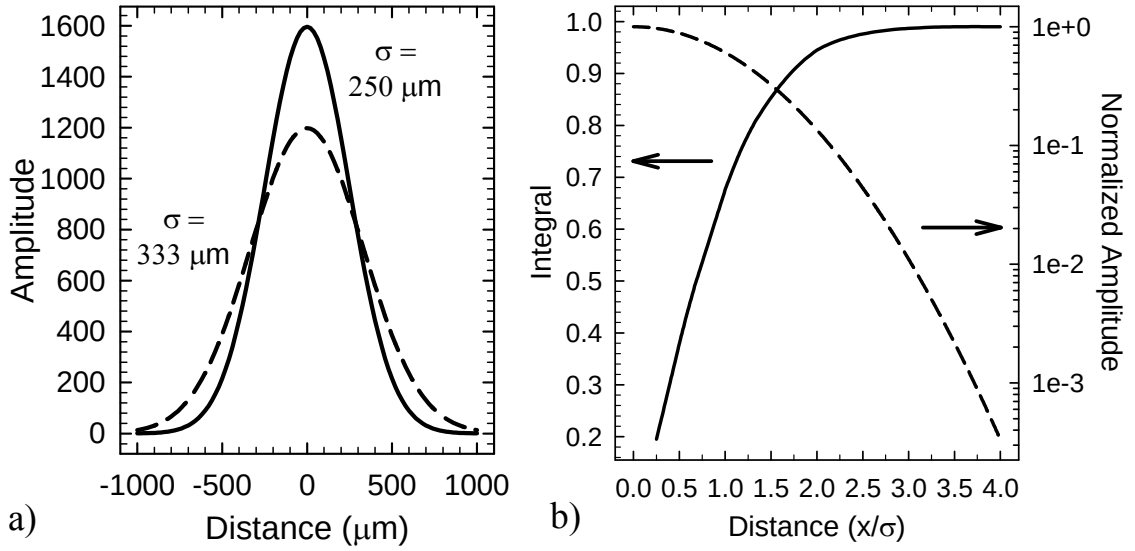

Figure 1-1: a) Two Gaussian curves with σ = 250 μm and σ = 333 μm and b) the function amplitude and integral as a function of distance from the maximum value.

1.2.2 Blackbody Radiation

Diffraction limited optics lead to acceptance of photons having a relationship between energy and wavelength. This alone did not explain the disagreement of macro physics theory with the measured blackbody spectral emission from objects at different temperatures, Figure 1-2. Gas molecule absorption in the optical path between the blackbody and measurement device are visible in the experimental data. The decrease in optical intensity at higher energies was explained by Plank's theory in 1900 that energy existed in finite quanta with an experimentally determined constant h = 6.63 x 10^{-34} Joule • sec. This theory results in an ideal blackbody spectral emittance, $S(E=h\upsilon)$, that varies with the photon energy, E, that is related to the wave frequency, υ, through Plank's constant, Eq. 1.4. The first term in the equation, $\rho(E)$, defines a concept called the density of states that describes the number of solutions for a wave equation within a fixed energy interval around a given energy. The second term known as the expectation value of energy $\langle h\nu(T)\rangle$ is the product of the energy and the probability of occupation

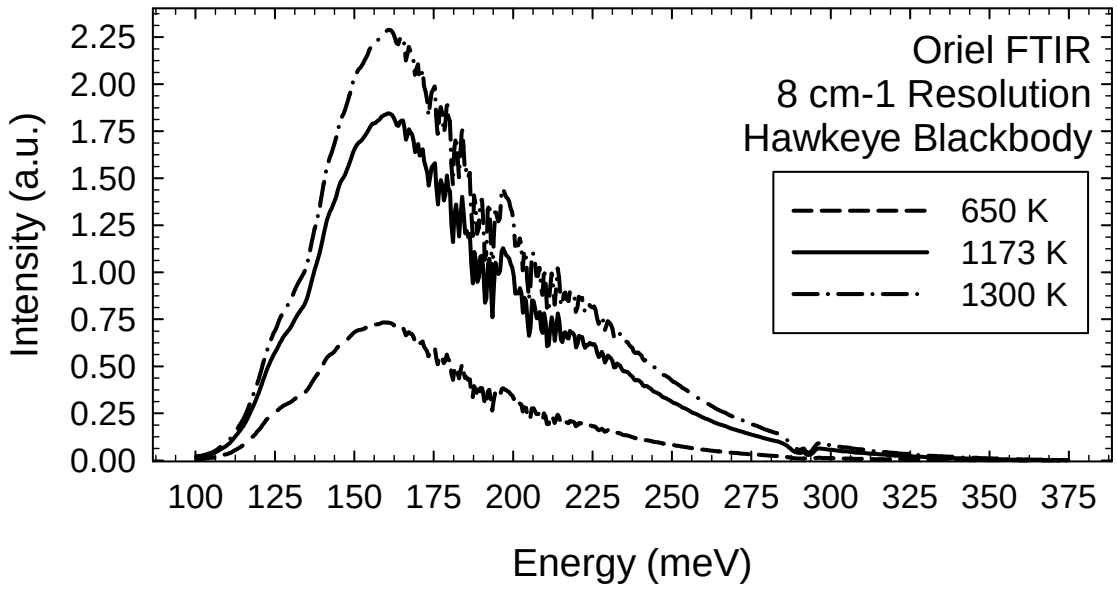

Figure 1-2: Blackbody emission from an object at three different temperatures measured by Fourier Transform spectroscopy.

at a given temperature, T. The solution to this equation is based on a three dimensional volume and electron energy level occupation governed by the Pauli Exclusion Principle and described by the Fermi-Dirac distribution relating thermal energy through

$$S(h\nu) = \rho(h\nu)\langle h\nu(T)\rangle = \frac{8\pi\nu^2}{c^3}\frac{h\nu}{e^{h\nu/k_BT} - 1} \quad \textbf{(1.4)}$$

Boltzmann's constant, k_B = 1.3806 10^{-23} J/K. The solution for the total optical power emitted by a blackbody was described by Stefan and Boltzmann, Eq. 1.5. For real materials an additional energy dependent parameter called the emissivity, $e(h\nu)$,

$$P = e(h\upsilon)\frac{2\pi^5 k_B^4}{15c^2h^3}T^4 \quad \textbf{(1.5)}$$

describes the probability a photon will be emitted from the material surface. Quantum theory was expanded upon by Einstein with the photoelectric effect and others to describe the wave-energy-momentum relationship for photon emission and absorption.

1.2.3 Photon-Electron Interaction

First Compton with x-rays [11] then later Raman with optical photons [12], observed inelastic scattering of monochromatic beams, see Figure 1-3. The scattering process in a solid object begins at Time 0 with absorption of photons having the same energy, $E = h\upsilon$. Each photon transfers all of its energy to a single exciton (electron-hole pair) that exists for a finite time at this excited energy level before radiative recombination and creation of another photon. During this period of time the energy of some of the excitons changes due to interaction with a third quasi-particle, referred to as a phonon with energy $E = \hbar\omega$, where the angular frequency, $\omega = 2\pi\upsilon$, and $\hbar = h/(2\pi)$. The phonon is a wave-like periodic deformation of the localized atomic lattice

equilibrium with a real mass and momentum that results in an energy that can be approximated by Hook's Law [14]. Phonons can be created that lowers the energy of excitons or phonons can be absorbed that increases exciton energy. Elastic scattering of photons at the same incident energy by a material is the most likely process to occur and is referred to as Rayleigh scattering.

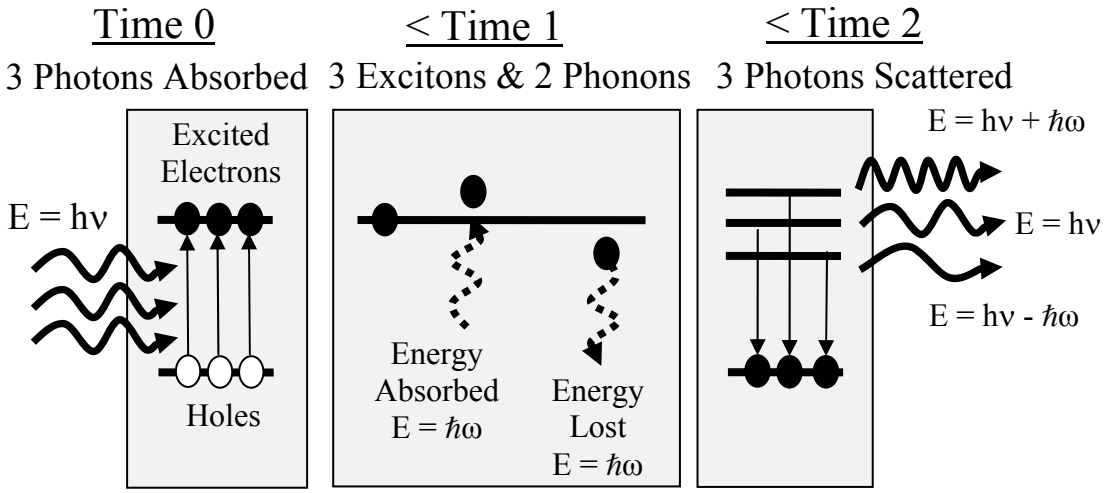

Figure 1-3: Diagram explaining Raman spectroscopy: radiation with energy E = hυ incident on an object at Time 0, phonons change the energy of electrons at Time 1, and the electrons recombine and emit photons with different energies at Time 2.

The Raman spectrum of each material is unique and has a regular temperature dependence that has enabled development of microscopes that can be used to identify both composition and temperature of samples [13]. The photons scattered by a material sample are measured over a wide range of energies however, the spectra has several distinct emission peaks with symmetric spacing around the monochromatic input as shown in Figure 1-4. The relative amplitude and Raman shift of these peaks is an inherent material property based on the allowed energy and population density of phonons. The scattering events that lower exciton energy, through the creation of phonons or additional excitons with lower energy, are referred to as the Stokes processes. The Anti-Stokes processes, where exciton energy increases, are less likely as

shown in the relative amplitudes of the two spectral peaks. Scattering occurs on a timescale called the lifetime of a particle, τ, that is a probabilistic measure of the average time a given percentage of a large number of excited particles. The total number of excited particles decays exponentially with time, $n(t) = n(0)exp(-\tau t)$.

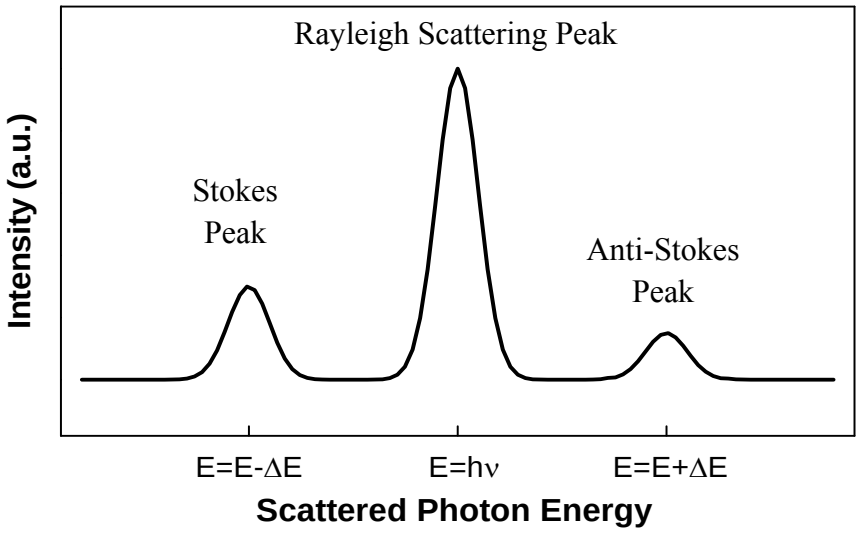

Figure 1-4: Theoretical Raman spectra of monochromatic photons with $E = h\upsilon$.

1.2.4 Crystals and Phonons

The unique wave motion/energy of phonons in a material is based on atomic spacing and interaction. Materials known as salts form cubic crystals structure similar to sodium chloride (NaCl) with two-intertwined face-centered cubic (FCC) sub-lattices with lattice parameter, a_0, and atomic spacing at half the distance [15], Figure 1-5. These structures represent the lowest allowable free energy for a given set of atoms based primarily on electro-static effects. Atomic crystal dynamics is approximated with a ball-spring model with displacement described by a wave equation that has a harmonic solution with a given relationship between angular frequency and velocity, v. The periodic displacement of perpendicular atomic planes along a given propagation

direction is called a longitudinal acoustic (LA) phonon. Differential solutions to the wave equations show the phonon velocity is related to the stiffness (C) and the density (ρ) of a material, Eq. 1.6, with the stiffness parameters for NaCl crystals

$$v_{LA}(111) = \sqrt{\frac{c_{11} + 2c_{12} + 4c_{44}}{3\rho}} \quad \textbf{(1.6)}$$

[16]. In addition to the longitudinal wave a transverse acoustic (TA) phonon exists with a velocity that can be calculated using Eq. 1.7. The symmetry of the cubic crystal leads to four-fold L-point <111> and six-fold x-point <100> degeneracy with identical

$$v_{TA}(111) = \sqrt{\frac{c_{11} - c_{12} + c_{44}}{3\rho}} \quad \textbf{(1.7)}$$

wave-energy solutions [17]. The elastic coefficients have been investigated thoroughly and are summarized for some materials of interest in Table 1-1. In addition to acoustic waves other types of periodic atomic motion include higher energy optical phonons (both LO and TO) and nanostructure specific phonons such as "twisting" modes in carbon nanotubes [18]. The energy of several types of phonons for different materials

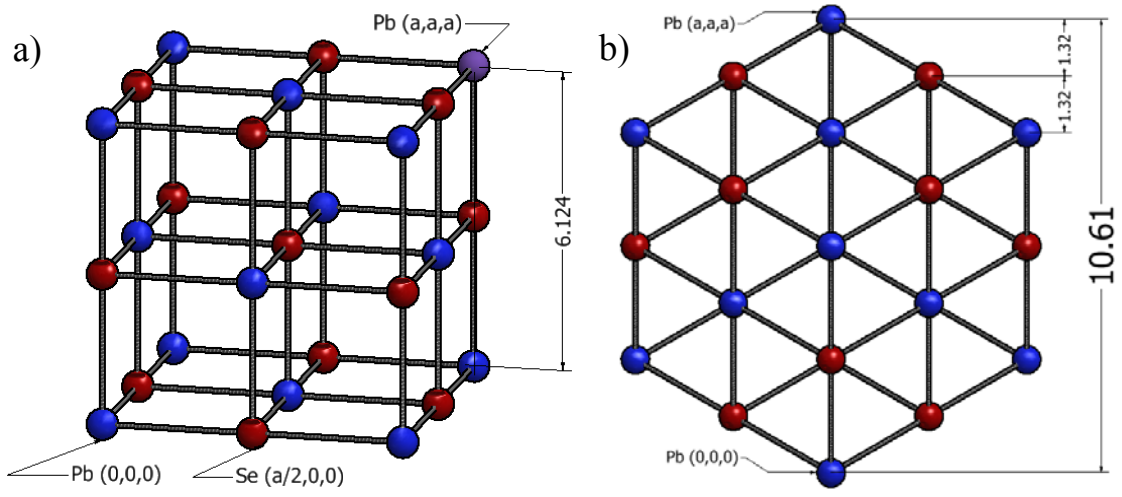

Figure 1-5: PbSe rock-salt crystal structure with dimensions in Angstroms: a) isometric view and b) a cross-section view of the <111> orientation.

Table 1-1: Sound velocity calculations for IV-VI semiconductors from reported material crystal properties.

	Reported Parameters				Crystal	Velocity (km/sec)		
Material	**c_{11} GPa**	**c_{12} GPa**	**c_{44} GPa**	**ρ g/cm^3**		**Plane**	**V_L**	**V_T**
PbSe	124	19.3	16.0	8.274	Cubic	100	3.87	1.39
						111	3.02	2.21
PbTe	108	7.50	13.2	8.242	Cubic	100	3.62	1.27
						111	2.67	2.14
SnSe	103	*28	18	6.179	Rhomb	100	4.08	1.71
SrSe	120	13	54	4.540	Tetra.	100	5.14	3.45

Table 1-2: Reported phonon energies for various semiconductor compounds.

Semiconductor	**Phonon Type and Energy (meV)**					
	TA	**LA**	**TO**		**LO**	
Symmetry	**<111>**	**<111>**	**<111>**	**<110>**	**<111>**	**<110>**
Silicon (Si)	13.8	47.0	61.4	63.0	52.0	63.0
Lead Selenide (PbSe)	7.3	12.9	16.1	5.6	17.9	16.3
$Pb_{0.93}Sr_{0.07}Se$ (Strontium)	7.1	12.6	15.9	5.5	17.9	16.1
$Pb_{0.85}Sn_{0.15}Se$ (Tin)	7.7	14.0	16.6	5.8	18.4	16.4
Lead Telluride (PbTe)	7.5	11.6	12.5	4.6	14.8	13.3

used in this research is listed in Table 1-2. These phonon properties were measured using Raman spectroscopy and several well developed mechanical techniques [19]. The phonon obeys quantum mechanical principles such as the density of states and an occupation probability that varies as a function of temperature that is best modeled by the Bose-Einstein distribution. Phonons also exhibit a finite lifetime dictated by the probability of different types of scattering events including interaction with electrons and other phonons.

1.3 Thermopower

The relationships between electrical energy, a voltage potential difference (ΔV) or current (I), and temperature were reported in the 1800s by Seebeck (S), Peltier (Π), and Thompson (β). The thermoelectric properties, Eq. 1.8 a)-d), of novel materials and device structures have seen recent research interest due to applications in power generation and solid-state cooling [20]. The relative conversion efficiency between

$$a)\ S \equiv \frac{\Delta V}{\Delta T}, \quad b)\ \Pi \equiv \frac{I}{Q}, \quad c)\ \beta \equiv \frac{Q}{I\Delta T}, \quad d)\ ZT \equiv \frac{S^2\sigma}{\kappa}T \qquad \textbf{(1.8)}$$

energy forms for a material is described by thermopower figure of merit, ZT, that is proportional to the Seebeck coefficient squared and the electrical conductivity, σ, and inversely proportional to thermal conductivity, k. Figure 1-6, taken from [21], shows a comparison of ZT for different materials at different temperatures. The dashed lines represent bulk materials and both BiSbTe and SiGe have a maximum $ZT \approx 1$ at 50 °C and 950 °C respectively. Bulk PbTe has a lower maximum $ZT \approx 0.6$ than both of these materials but this maximum occurs at a temperature of 400 °C. Therefore both PbTe and PbSe, which have $k \approx 2 - 5$ $Wm^{-1}K^{-1}$, are promising materials for power generation from waste heat recovery [22]. However, the ZT value is not limited by these intrinsic bulk material properties. A second class of nanostructured materials has been developed to lower thermal conductivity through engineering design. Nanostructured material has two categories: one has structural differences that occur on the order of 10 nm or less within a thicker material while the second material type including quantum wires, dots, or atomic layer sheets employs dimensional confinement [18]. Increases in phonon scattering with material boundaries and intentional crystal defects such as imbedded nanoparticles in silicon and SiGe (solid lines in Figure 1-6) has resulted in a

2X improvement in *ZT* due to reduction of thermal conductivity [23]. Low dimensional structures limit the types of phonons that can exist and reduces thermal transport.

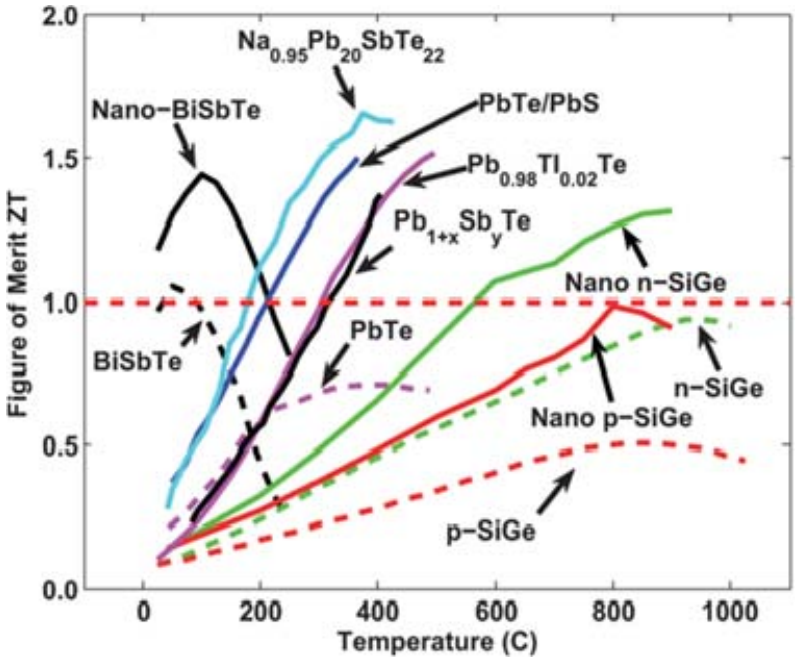

Figure 1-6: Thermopower figure of merit, ZT, reported for various materials [21]: bulk materials are dashed lines and nanostructured materials have solid lines.

1.3.1 Macro-to-Nano Thermodynamics

The first law of thermodynamics, Eq. 1.9 a), explains energy conservation through changes in thermal energy (Q), the internal energy (U), and particle continuity (n) of a system. The second law, Eq. 1.90 b), states that entropy (S) production, or irreversible losses, of ordered to disordered energy will continue until equilibrium is

$$a)\ dQ = dU + \delta A - \mu dn \quad b)\ TdS \geq \delta Q \tag{1.9}$$

reached. The "phenomenological" solution to describe heat transfer from a hot object to a cold object through conduction results in Fourier's law, Eq. 1.10: that any solid object with a temperature differential is a thermal "resistor" and has a linear temperature gradient. However, as objects get smaller thermodynamics must be approached with

quantum mechanical principles. Debye and Einstein both proposed theories with a similar form, Eq. 1.11, to calculate the temperature dependence of the internal energy of

$$\nabla(\kappa \bullet \nabla T) = -Q \tag{1.10}$$

solid based on the heat capacity of a given volume (C_V) using the phonon energy, $\hbar\omega$, the density of states, $D(\hbar\omega)$, and the occupation probability at given energy, $\langle n(\hbar\omega)\rangle$. The lattice thermal conductivity, k_{lat}, or heat transfer from atomic motion can be

$$C_v \equiv \left(\frac{\partial U}{\partial T}\right)_V, \quad U = \int \mathrm{d}\omega D(\hbar\omega)\langle n(\hbar\omega)\rangle\hbar\omega \tag{1.11}$$

calculated from this equation using the relaxation time approximation [24] and results in Eq. 1.12 that is proportional to C_V, the phonon velocity, $v(\hbar\omega)$, and the phonon lifetime, $\tau(\omega)$, summed over all of the different phonon types, j. The latter two terms

$$k_{Lat} = \sum_j \int C_j(\hbar\omega) v_j^2(\hbar\omega)\tau_j(\hbar\omega)\,\mathrm{dx} \approx \int C_v v \Lambda dE \tag{1.12}$$

can be grouped together to define the mean free path, $\Lambda \equiv v \times \tau$, as a statistical measure of the distance a phonon travels before a scattering event. The temperature dependence of thermal conductivity for PbSe is shown in Figure 1-7 adapted from *Shalyt et al* [25]. At higher temperatures, greater than 100 K, the phonon lifetime and therefore the mean free path is dominated by Umklapp scattering and k_{lat} is inversely proportional to temperature. As the material temperature is lowered the mean free path increases until it reaches a maximum equal to the size of the object. At temperatures below the value when the mean free path "size" limit occurs the lattice thermal conductivity becomes proportional only to C_V. Low temperature measurements of heat capacity verified the Debye model that states $C_V \propto (T/\theta_D)^3$ where the intrinsic material parameter, θ_D, is referred to as the Debye temperature.

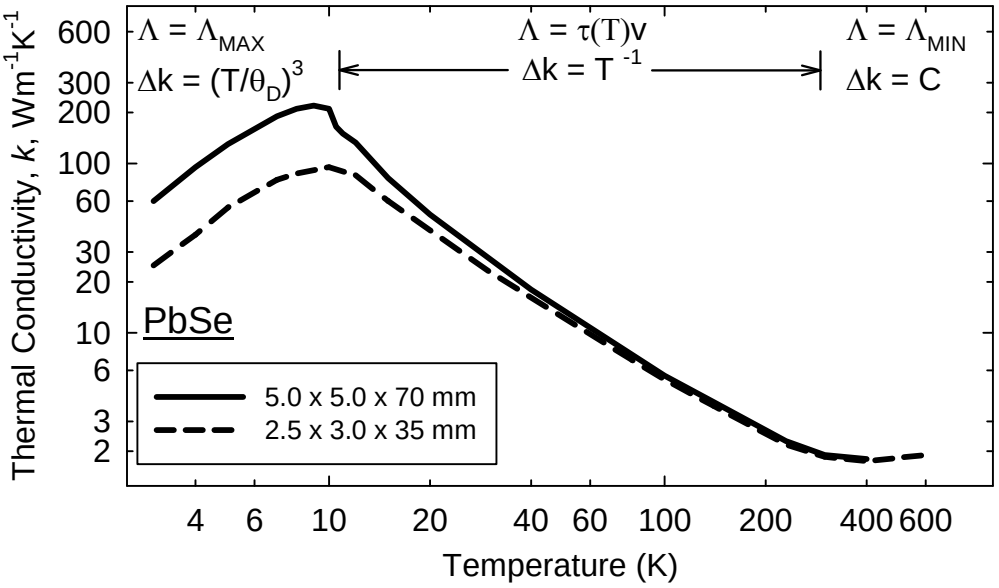

Figure 1-7: Thermal conductivity as a function of temperature for two different size samples of PbSe [25].

1.3.2 Engineering Thermopower

The most simple and straight-forward approach to engineer improved TE material is to increase the electrical conductivity, Figure 1-8, through manipulation of doped semiconductor carrier concentration. However, increased carrier concentrations reduce the Seebeck effect in a material and lowers $ZT \propto S^2$. In addition, experimental

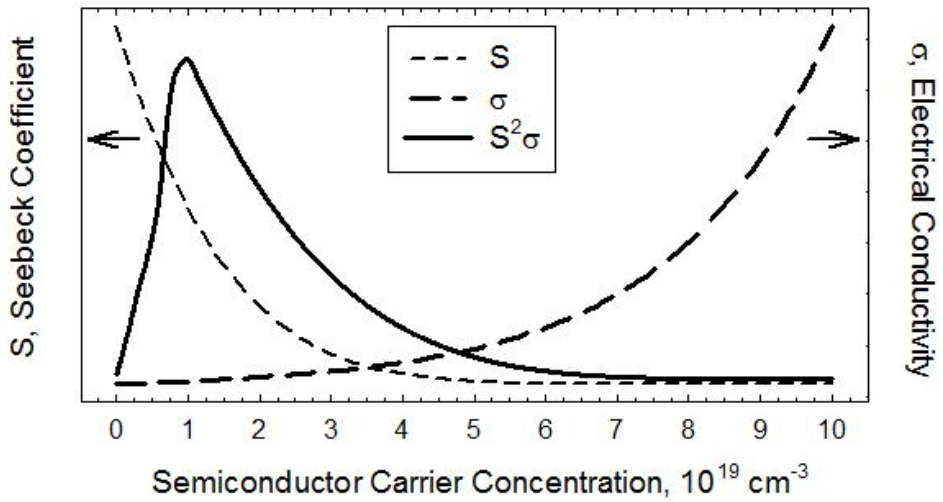

Figure 1-8: TE material properties as a function of carrier concentration adapted [1].

results have shown that electronic carriers are a second heat transport mechanism and increased concentrations raise the total thermal conductivity, $k_{tot} = k_{lat} + k_e$, further reducing *ZT*. The electronic component of thermal conductivity is proportional to the carrier concentration as shown Figure 1-9. The relative contribution of k_e is determined by the total thermal energy each free carrier possesses and the ability to diffuse throughout the material. For metals the maximum value is governed by the Wiedemann-Franz law where $k_e = L_0 T\sigma$ with L_0 referred to as the Lorenz number. Therefore scientific researchers have focused on reducing k_{lat} with nanostructures to engineer an improved TE material. Low dimensional materials such as graphene, or a carbon monolayer, cannot have phonon modes transverse to the sheet and therefore has a reduced thermal conductivity compared to graphite. However, when graphene is rolled into a single wall nanotube rope, Figure 1-10 a), an additional "twisting" phonon mode has been observed [26]. This material structure was shown to have an increased thermal conductivity compared to graphene alone but less than graphite. In addition to graphene, TE properties have been investigated for several material systems including PbSnTe SLs [27] and nanocrystal composites [28], Figure 1-10 b).

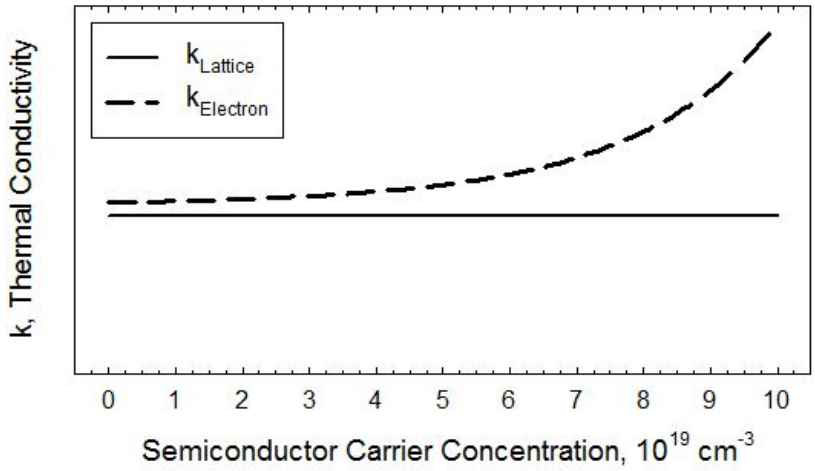

Figure 1-9: Carrier concentration and total thermal conductivity adapted [1].

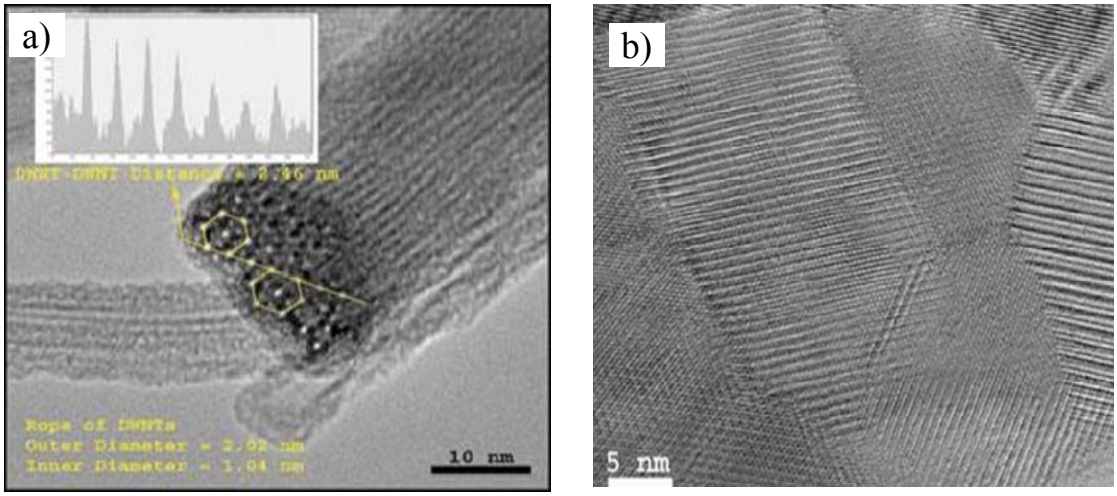

Figure 1-10: High resolution microscope images of a) single wall nanotube rope [26] and b) nanocrystal composite material [28] with reduced thermal conductivity.

1.4 Nanostructures

Periodic nanostructured materials with alternating layers of two or more elementally different compounds create quantized energy levels where a near continuum existed. The small size of a single layer in one direction removes energy-directional (dispersion) symmetry and alters the allowed solutions for the electron wave function. Careful design and precision fabrication of multiple repeated nanometer thick layers also affects carrier lifetimes and enables carrier population inversion at a higher energy level resulting in devices such as the quantum cascade laser (QCL) [29] and the interband cascade laser (ICL) [30]. The periodic nanostructure also enhances optical wave absorption and device efficiency in the both the quantum well infrared photodetector (QWIP) [31] and HgCdTe graded SL detectors [32].

When the wavelength of a particle becomes similar to the periodicity of a nanostructure additional enhancement of heterogeneous interface wave reflection may occur. These coherent effects result in nanostructures such as the distributed Bragg

reflector (DBR) that is used in the optical design of the vertical cavity surface emitting laser (VCSEL) [33]. Periodic nanostructured composite materials have also been demonstrated to have both coherent and diffuse effects on phonon waves. The acoustic microcavity [34] has been used to demonstrate phonon reflection while thin film SLs have been shown to greatly reduce k_{lat} through interface scattering between the different alloy layers [35]. Research attempts to clearly demonstrate any coherent phonon effects altering k_{lat} have thus far been unsuccessful [36]. However, the concept remains the primary motivation for this research due to the possibility of optimizing the ZT value of a material at a given temperature and the magnitude of the improvement that might be possible from directing heat flow.

1.4.1 Quantum Wells and Superlattices

Schrödinger's wave equation for electrons in a finite potential well formed by two materials with different bandgap energies, E_g, and dispersion relationship includes the possibilities of particle tunneling, transmission, and reflection. The energy band diagram for a single $Pb_{0.933}Sr_{0.067}Se/PbSe/Pb_{0.933}Sr_{0.067}Se$ quantum well with a thickness similar to films used in this research is shown in Figure 1-11 a). A standard numeric solution technique included in many text books was used to compute the confined energy levels for layer thicknesses shown at a constant temperature of 300 K. The two energy levels created in both bands of the PbSe material are due to directional symmetry degeneracy lifting in <111> oriented quantum wells [37]. The quantization also reduces Auger scattering [38] by limiting the number of phonons with the exact energy to match the difference between confined levels. When multiple quantum wells are placed next to each other, also called a superlattice when each layer is sufficiently

thin, additional quantum effects occur including mini-band formation shown in Figure 1-11 b) by the dashed line. The efficiency of this design, used in the QCL, is still limited by LO phonon scattering therefore research into the design of electron injection/extraction, active layer, and confinement energies based on the LO phonon energy and picosecond relaxation time is ongoing [39]. A significant focus has been placed on varying the thickness of these layers across the MQW or SL creating a graded structure energy band that optimizes energy level resonance between nearby wells with a voltage bias and increases barrier tunneling probabilities shown in Figure 1-11 c).

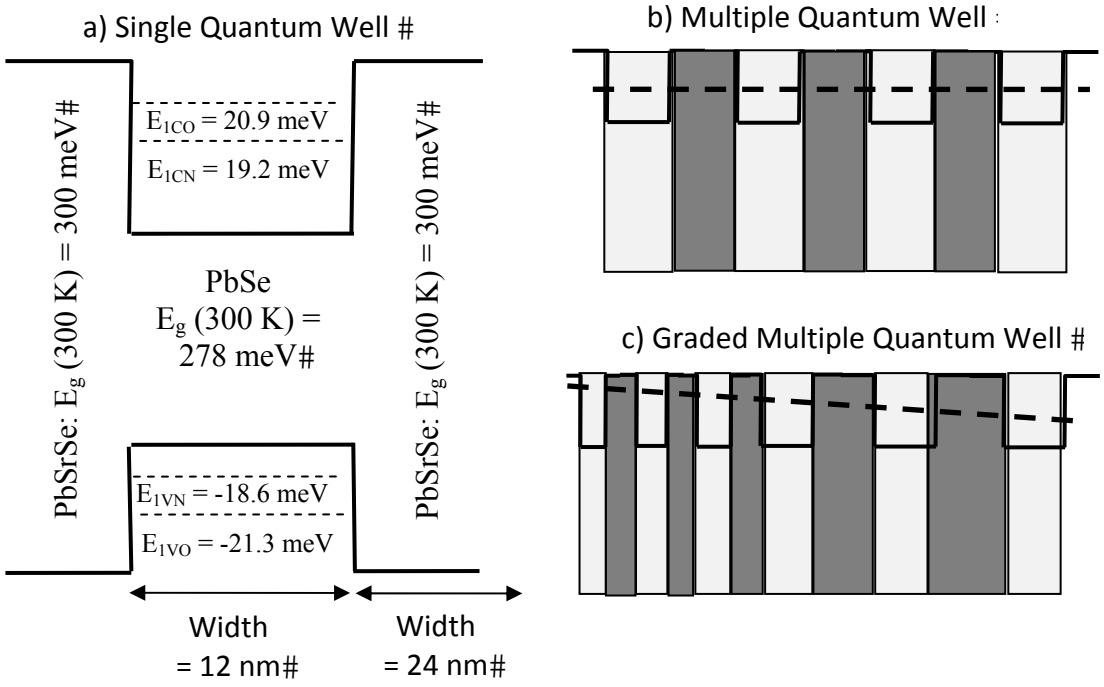

Figure 1-11: Quantum well confinement: a) a single well of PbSe with PbSrSe barriers in the <111> crystal direction that removes energy level degeneracy, b) a regular multiple quantum well design with four similar wells, and c) a graded MQW.

1.4.2 Quantum Reflection and Distributed Bragg Reflectors

Differential solutions to Maxwell's equations indicate electromagnetic waves are reflected at material boundaries due to a change in the index of refraction, dielectric

constant (permittivity), ε, and magnetic permeability, μ. The DBR design parameters applied to optical waves are shown in Figure 1-12. Two materials such as silicon and silicon dioxide have a significantly different optical index of refraction n = 3.4 and n = 1.5 respectively. The maximum reflection for a 1 μm optical wave occurs when thickness of each alternating layer is designed to be λ/4 scaled by the difference the speed of light in each material ($c_{vac} = c_1 n_1$). The absolute reflectivity is determined by the number of mirror pairs and the ratios (n_1/n_2) and either ($\varepsilon_1/\varepsilon_2$) or ($\mu_1/\mu_2$) between the

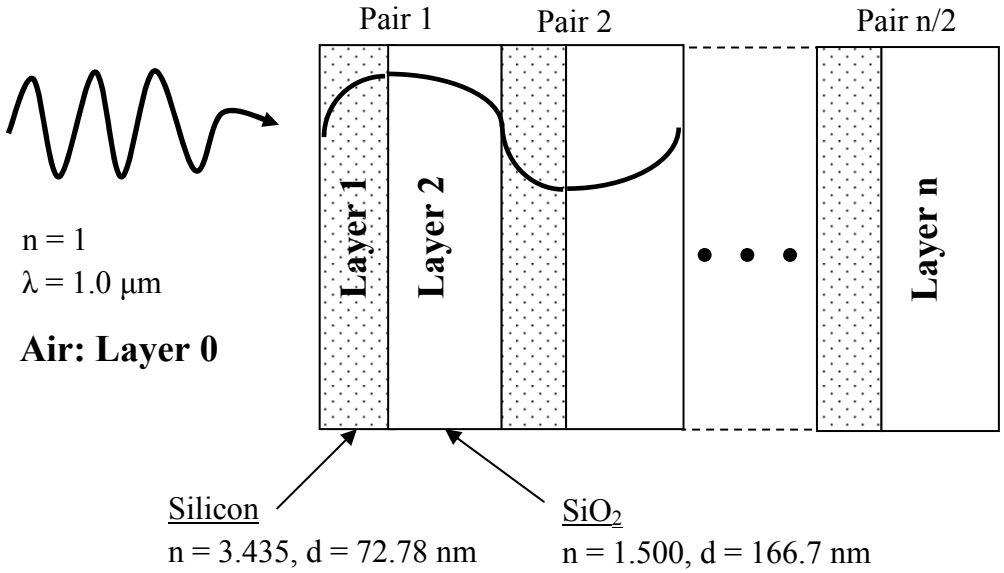

Figure 1-12: Optical distributed Bragg reflector design for maximum reflectance using silicon and silicon dioxide layers.

different material layers depending on the orientation of the transverse EM wave. While DBRs have been used extensively for photon reflection the concept has also been successfully applied to the phonon wave. Acoustic microcavities have been demonstrated by several research groups using AlAs/GaAs [40], SiGe [41], and piezo-electric oxides [42] mirror layers that confined the highest energy LO phonons in a gain medium between two acoustic DBR mirrors designed with the relation λ/2.

1.5 IV-VI Semiconductor Nanostructure Fabrication

IV-VI nanostructured materials have been fabricated using many crystal growth techniques including liquid phase epitaxy (LPE) [43], Bridgman-Stockbarger [44], spark plasma sintering [27], and chemical vapor deposition (CVD) [45] in addition to MBE. The semiconductor materials analyzed in this research were fabricated by several different researchers at the University of Oklahoma between 2009 and 2011 using an Intevac Gen II MBE shown in Figure 1-13. This system had eight different source materials located in load cells with temperature controlled crucibles and electronically controlled mechanical shutters. The substrates used were commercial 3-inch diameter silicon wafers from multiple vendors that were ≈ 350 μm thick and were prepared with a modified Shiraki method [50] prior to being loaded into the vacuum chamber. MBE films exhibit high quality crystal growth and the technique provides accurate control of thickness for fabrication of MQW or SL material layers on the order of 10 Å thick or quantum dot structures several nanometers in size [46]. IV-VI semiconductors typically employ the element lead (Pb) and have historically been referred to as the lead salts or lead chalcogenides. The rock-salt crystal structure and large lattice constant of IV-VI semiconductors compared to the industry standard silicon substrates, Figure 1-14, limits the availability and utility of these films grown on other materials [47]. However, using fluoride buffer layers between the substrate and film growth in the <111> crystal direction has resulted in high quality IV-VI materials capable of repeated temperature cycling [48].

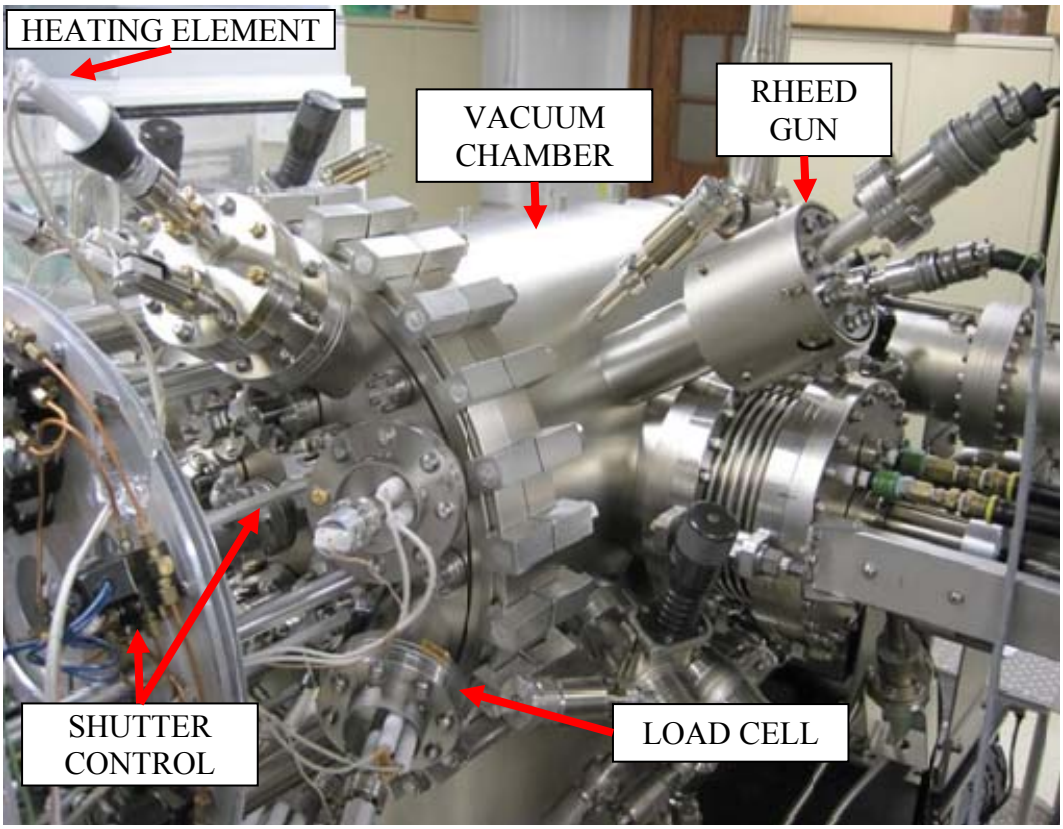

Figure 1-13: Molecular beam epitaxy system at the University of Oklahoma used to fabricate IV-VI semiconductor nanostructures.

1.5.1 Material Properties

Research into IV-VI semiconductors has been primarily stimulated by interest in their application to optics due to a direct band-gap in the mid-IR spectral region that can be varied with ternary compositions as shown for a temperature of 300 K in Figure 1-14. Eq. 1.13 shows how the bandgap energy of PbSe varies with temperature. In particular PbSe has been used extensively in Fabry-Perot cavity lasers for gas phase

$$Eg\,(PbSe,T) = 0.135 + 0.450 \times 10^{-3}\,T \ \text{(eV)} \qquad \textbf{(1.13)}$$

spectroscopy [7-9] and long-wavelength photosensitive detectors [17, 32]. The intrinsic bandgap energy of this material can be lowered through introduction of tin (Sn) or increased with strontium (Sr). The compound $Pb_{1-x}Sr_xSe$ where x denotes the

percentage of strontium has been well investigated by several research groups. Eq. 1.14 is an experimental data fit of the bandgap energy for this ternary compound

$$Eg\,(x,T) = 0.15 + 3.608x - 1.314x^2 + (0.430 - 3.093x + 6.495x^2) \times 10^{-3}\,T \text{ (eV)} \qquad \textbf{(1.14)}$$

measured by *Shen et al* [49]. The element bismuth (Bi) has been used as an n-type dopant to control carrier concentration in these films and was introduced to select films. Appendix B contains a summary of the design parameters including nanostructure thickness, the ternary compounds used, and doping for samples tested in this research.

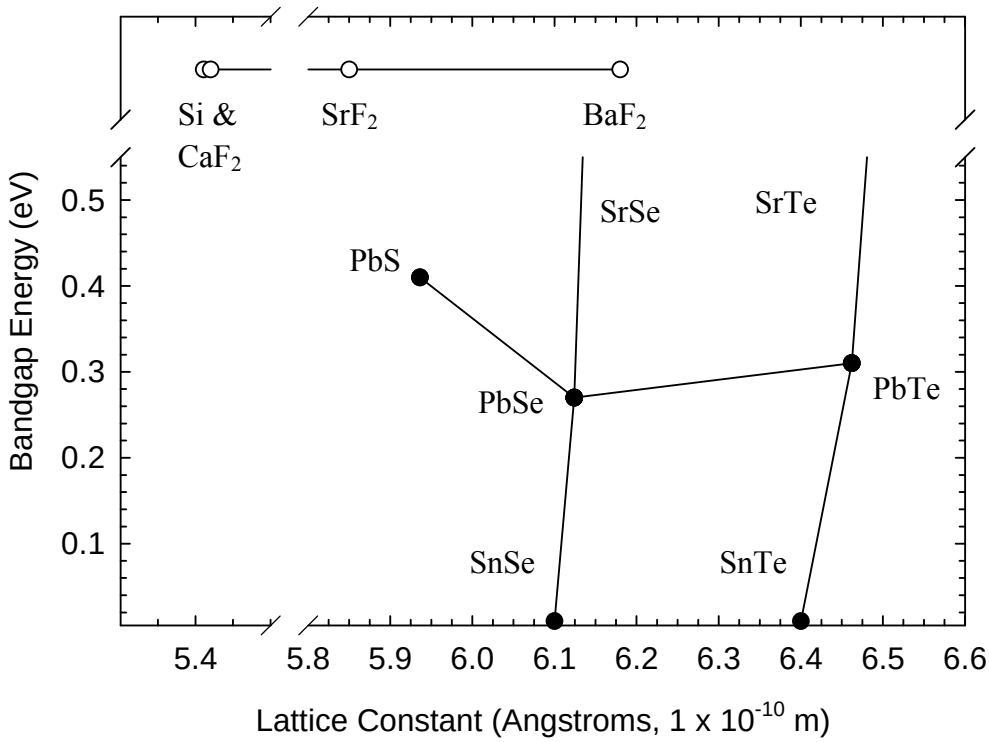

Figure 1-14: Bandgap energy and lattice constants of various ternary IV-VI semiconductor compounds at 300 K.

1.5.2 Automated Molecular Beam Epitaxy (MBE)

The growth of single crystal IV-VI semiconductor thin films by MBE is a multi-step process that requires multiple expert operators including computer programmers. Figure 1-15 is a screen image of the Molly 2000 software user interface from Veeco,

Inc. that controlled the MBE. The script language program shows a timed loop that waits until the substrate temperature is at a target value before additional growth continues. A growth recipe for a typical MQW on SL film consisted of shutter opening times less than one second to fabricate a film layer 1 nm or thinner that could be repeated up to 300 times. The total time to fabricate a film of approximately 3 µm thick could exceed 12 hours depending on complexity. The Molly software ran on a standard personal computer equipped with National Instruments analog data acquisition hardware. Two different programs written for this software and used for fabricating thin films analyzed during this research are contained in Appendix A.

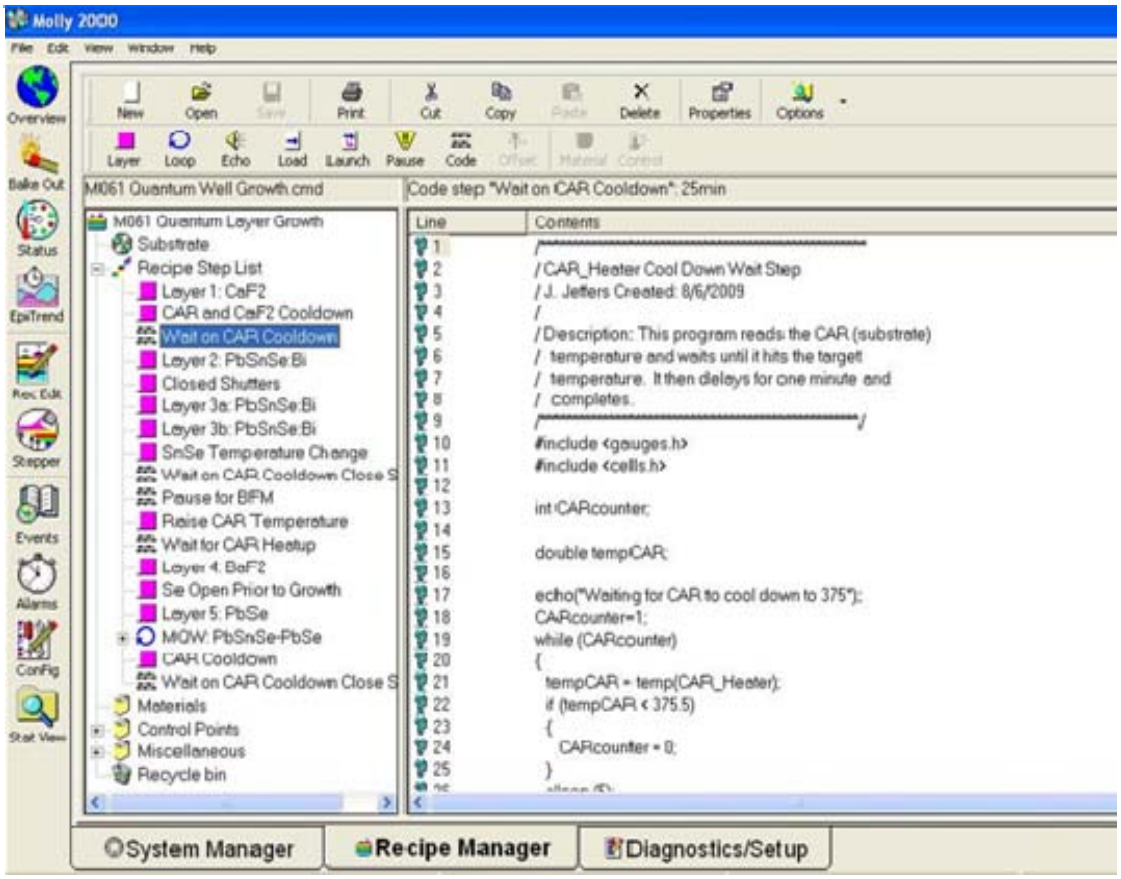

Figure 1-15: Text based program to control shutters and temperatures while monitoring time and pressure.

1.6 Material Characterization

Material characterization for the films analyzed in this research was performed at the University of Oklahoma and by off-site commercial facilities. Figure 1-16 shows a scanning electron microscope (SEM) image and tunneling electron microscope (TEM) image of two different films. The SEM cross-section of MBE film #M074 (left image) shows a material layer with thickness ≈ 6 μm that has been removed from the silicon substrate and attached to a copper mount using gallium indium (GaIn). The high-resolution TEM cross-section (right image) of a nanostructured SL film with a total thickness less than 0.6 μm exhibits two material densities, indicated by the light

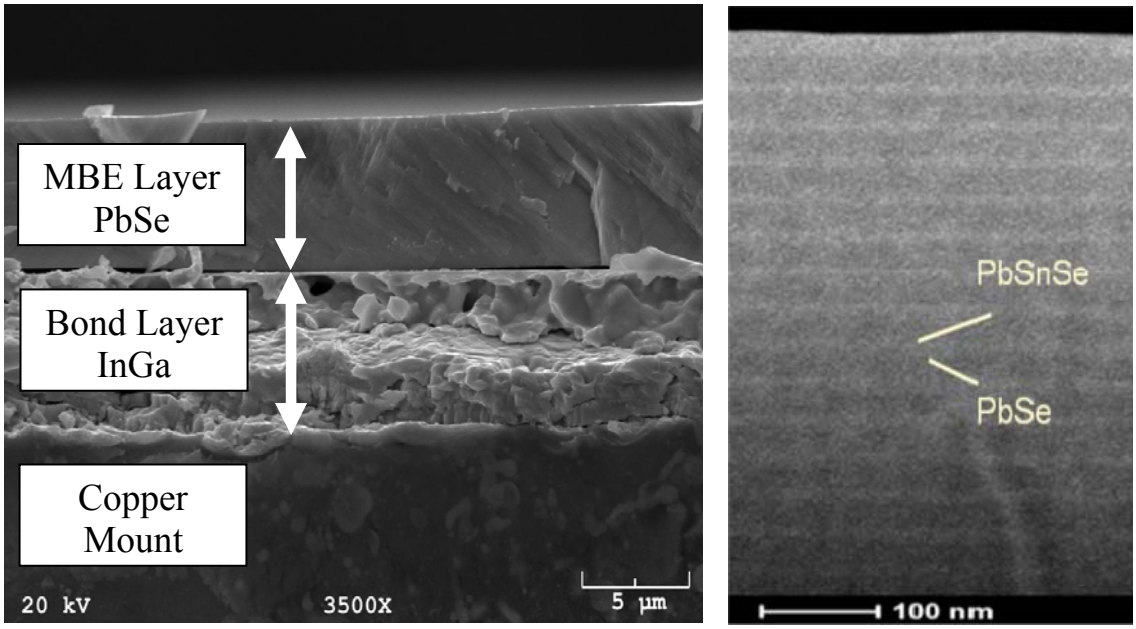

Figure 1-16: SEM (left) and TEM (right) images at different resolutions for various thin film structures grown by MBE and characterized during this research.

and dark colors, that change periodically throughout the thickness of the film for fifteen different pairs. The light grey material is the lower density $Pb_{0.85}Sn_{0.15}Se$ ternary material approximately 25% as thick as the darker PbSe layers that are ≈ 30 nm thick.

Additional film images and other standard material characterization results for selected films are contained in Appendix B.

1.6.1 Crystal Diffraction

Diffraction effects that result in constructive/destructive interference patterns for electron and photon beams provides a valuable tool for investigating the crystal spacing of semiconductor crystals. Eq. 1.15 shows the condition for constructive interference in a material with distance, d, between atomic planes for incident radiation with a wavelength, λ, at a given angle, θ, with respect to the surface. Two techniques,

$$n\lambda = 2d\,\sin(\theta) \qquad \textbf{(1.15)}$$

reflection high energy electron diffraction (RHEED) and X-ray diffraction (XRD), have been readily applied to semiconductor characterization and were used to verify thin films used in this research. The RHEED technique for MBE systems is an *in situ* characterization that helps determine the appropriate time and temperature required to thermally desorb the oxide layers on silicon wafers. The RHEED system used for these films employed an electron gun and phosphor screen mounted on the exterior wall of the vacuum chamber. The RHEED pattern image data, shown in Figure 1-17, provides information on both film quality and structure. The 1x1 oxide pattern on the left image changes to a more "streaky" 7x7 silicon crystal pattern in the right image. Figure 1-18 show the variation of the XRD signal for film #168 with an MQW optical film design with a variable SL layer thickness below. In a PbSe film the distance between the nearest atomic planes in the <222> direction is ≈ 1.75 Å that combined with an x-ray wavelength of 1.54 Å in Equ. 1.15 would result in an intensity maximum at 25.4º.

However the variation in lattice parameter with the introduction of tin in the ≈ 2 μm of SL films and strontium in the ≈ 1 μm of MQW material results in both a change in the angle of maximum intensity and the "satellite" intensity peaks regularly spaced around the central angle. The average peak spacing of 0.14º indicates a distance between two planes of ≈ 43 nm that is the designed thickness of the MQW pairs.

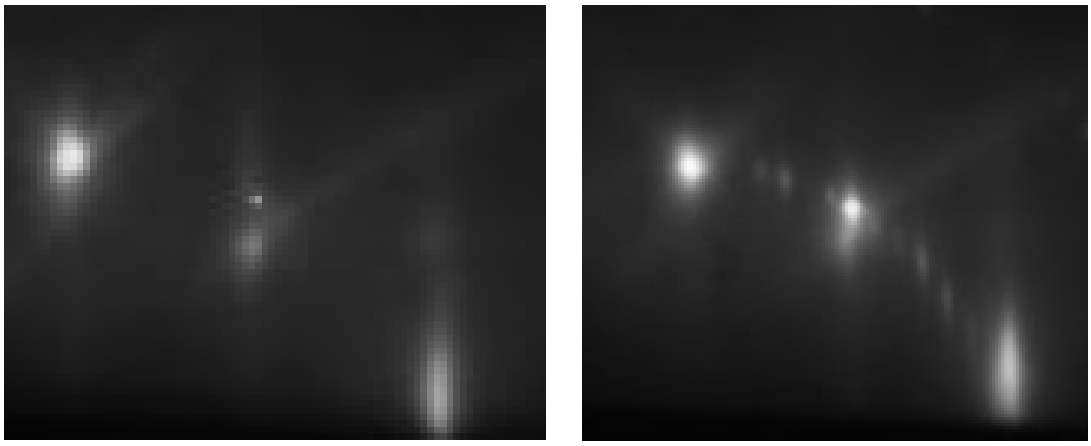

Figure 1-17: RHEED images during substrate surface reconstruction: 1x1 pattern at 800 °C (left) and 7x7 pattern after 30 minutes at 830 °C (right).

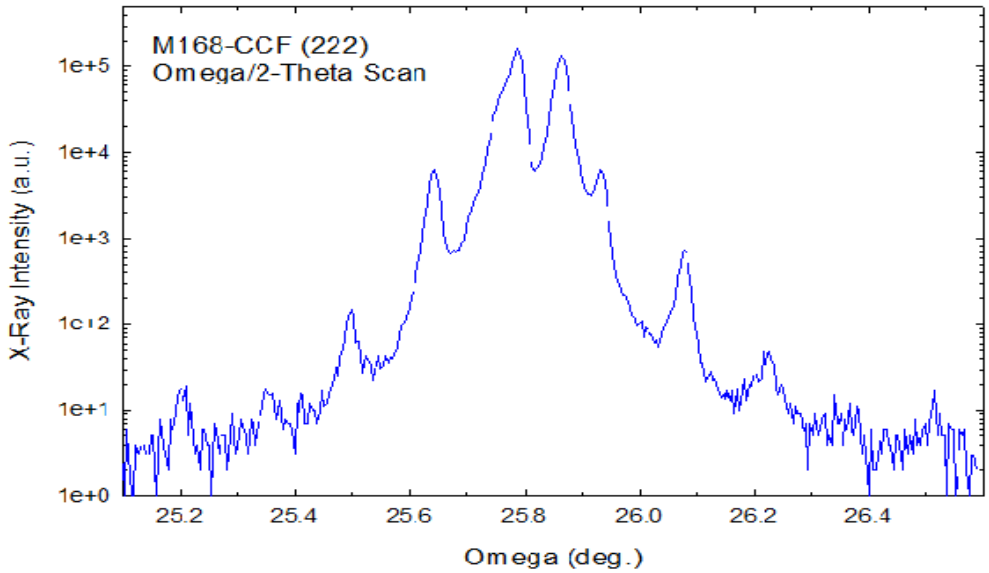

Figure 1-18: XRD pattern for film #M168 with a multiple quantum well structure.

1.6.2 Electronic and Thermal Properties

One of the most common and useful electronic characterization techniques for semiconductors is Hall Effect measurements. The temperature dependent carrier concentrations and mobilities for two thin films characterized for this research are shown in Figure 1-19. This method determines both the carrier type and mobility in a volume of semiconductor by measuring voltages and currents under the influence of transverse magnetic fields. For the films shown the majority carrier concentration is p-type and decreases by a factor of 10X while the mobility increases by a factor of 100X as the temperature is lowered from 300 K to 77 K. These measurements were completed using the van der Pauw four probe technique with electronic leads attached to the film surface with indium. The Seebeck coefficient can be measured with a similar electrical apparatus to record the change in voltage potential due to a resistive heater or similar thermal energy source [51]. The Seebeck coefficient has been investigated for many semiconductors and has been shown to vary with dopant

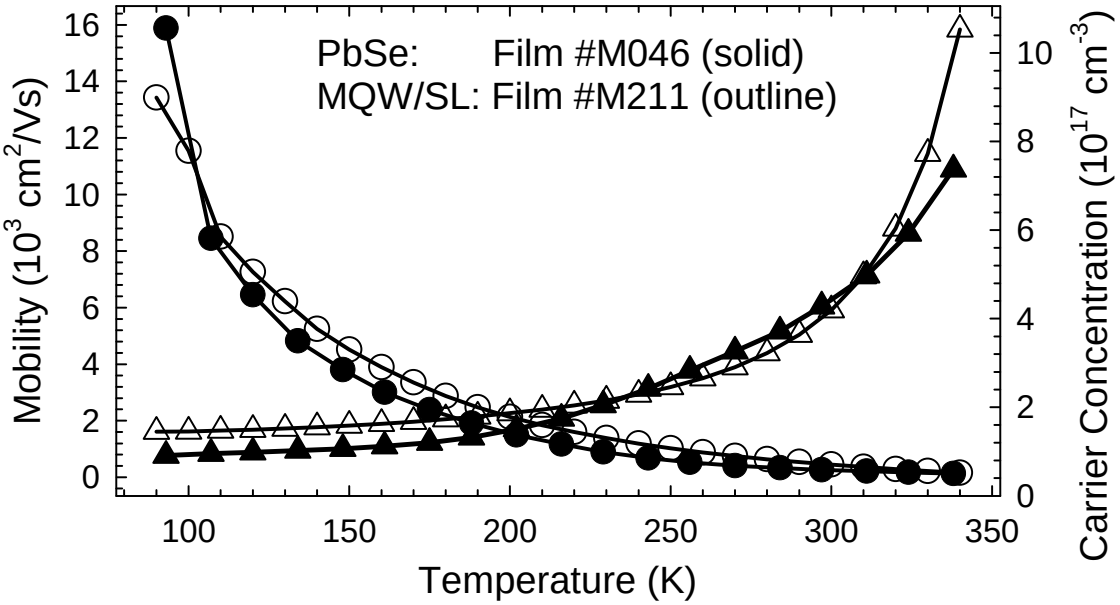

Figure 1-19: Hall Effect measurements of a uniform PbSe film #M046 compared to MQW and SL thin film #M212 over a temperature range.

concentration [52] and magnetic fields. Several MBE-grown film samples were analyzed by Panco GmbH (Mülheim Kärlich, Germany) using potential Seebeck microprobe (PSM) testing and sample #M074 had an average S = -216 μV/K and sample #M088 had S = -181 μV/K for as carrier concentration ≈ 2 x 10^{18} at 300 K [53].

The thermal conductivity of a thin film can be measured through a variety of mechanical, electrical, and optical methods including transient thermo-reflectance (TTR) [54] shown in Figure 1-20. This non-contact method measures a change in the reflected power of one laser (the probe) as the surface of the sample is heated by a second laser. Raman spectrometers have been used to assess the thermal conductivity of novel nanostructures including carbon nanotubes [26] by measuring the temperature dependent shift of the Stokes energy peak. Photoluminescence (PL) is another well-established technique employed to measure the optical, electronic, and thermal properties of thin films. This measurement has been used to assess the thermal resistance of opto-electronic device mounting [55] and to compare thin film heating at 300 K [56] and is employed throughout this research to characterize nanostructured

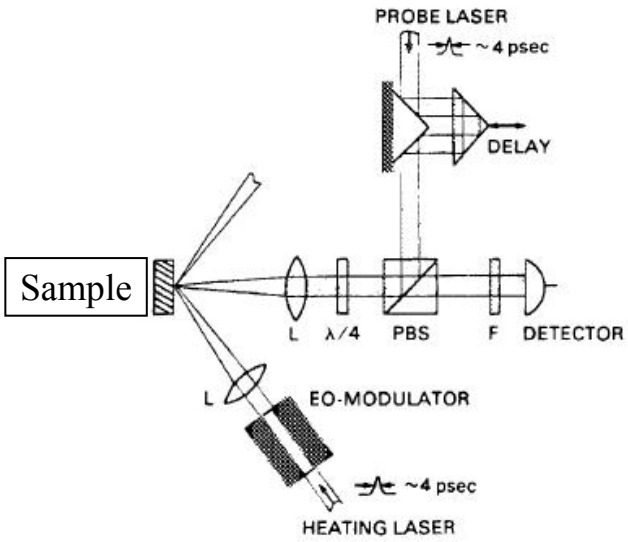

Figure 1-20: Thin film thermal conductivity TTR measurement diagram [53].

materials. The *3ω* method [57] is a mechanical technique that measures the temperature dependent frequency-locked change in resistance for a "sensor" attached to the film surface. Thin films #M103, #M106, #M107, #M109, #M116, #M117, and #M118 were tested at the University of Illinois Urbana-Champagne using the TTR method and had thermal conductivity measurements k = 1.5-2.2 $Wm^{-1}K^{-1}$ at 300 K [53]. Multiple samples of film #M108 were tested with k_{M108g} = 1.2 $Wm^{-1}K^{-1}$ and k_{M108f} = 1.3 $Wm^{-1}K^{-1}$.

1.7 Dissertation Organization

This dissertation outlines the experimental evidence of thermal and electronic transport theory for periodic nanostructures developed for thermoelectric applications. The background and motivation for the manufacture of novel IV-VI semiconductor TE materials was shown in this chapter. The rest of this research is organized as follows: Chapter 2 describes the development of a room-temperature PL system for assessing optical heating in thin films, Chapter 3 details the quantum theory and a novel approach to thermal model assessment for different types of thin films, Chapter 4 evaluates the temperature dependence of thermal conductivity for different nanostructure film designs, Chapter 5 explores the quantum theory and solutions for periodic acoustic properties in these same films, and Chapter 6 provides conclusions and recommendations for future research in this area.

Chapter 1 References

1. D. M. Rowe (Ed.), *Thermoelectrics Handbook: Macro to Nano*, Taylor and Francis, Boca Raton, (2006)

2. R. Venkatasubramanian, E. Siivola, T. Colpitts, and B. O'Quinn, "Thin-film thermoelectric devices with high room-temperature figures of merit", *Nature*, **413**, pp. 597-602 (2001)

3. J. P. Heremans, V. Jovovic, E. S. Toberer, A. Saramat, K. Kurosaki, A. Charoenphakdee, S. Yamanaka, G. J. Snyder, "Enhancement of thermoelectric efficiency in PbTe by distortion of the electronic density of states", *Science*, **321**, pp. 554-558 (2008)

4. V. Damodara Das and N. Soundararajan, "Size and temperature effects on the thermoelectric power and electrical resistivity of bismuth telluride thin films", *Phys. Rev. B,* **37**(9), pp. 4552-4559 (1988)

5. B. Poudel, Q. Hao, Y. Ma, Y. Lan, A. Minnich, B. Yu, X. Yan, D. Wang, A. Muto, D. Vashaee, X. Chen, J. Liu, M. S. Dresselhaus, G. Chen, and Z. Ren, "High-thermoelectric performance of nanostructured bismuth antimony telluride bulk alloys", *Science*, **320**, pp. 634-639 (2008)

6. A. I. Hochbaum, R. Chen, R. D. Delgado, W. Liang, E. C. Garnett, M. Najarian, A. Majumdar, and P. Yang, "Enhanced thermoelectric performance of rough silicon nanowires", *Nature*, **45**, pp. 163-168 (2008)

7. K. Namjou, C. B. Roller, T. E. Reich, J. D. Jeffers, G. L. McMillen, P. J. McCann, and M. A. Camp, "Determination of exhaled nitric oxide distribution in a diverse sample population using tunable diode laser absorption spectroscopy", *Appl. Phys. B*, **85**, pp. 427-435 (2006)

8. J. Jeffers, C. Roller, K. Namjou, M. A. Evans, L. McSpadden, J. Grego, and P. J. McCann, "Real-time diode laser measurements of vapor phase benzene", *Analytical Chem.*, **76**(2), pp. 424-432 (2003)

9. L. Burciaga-Robles, B. P. Holland, D. L. Step, C. R. Kreihbel, G. L. McMillen, C. J. Richards, L. Sims, J. D. Jeffers, K. Namjou, and P. J. McCann, "Evaluation of breath biomarkers and serum haptoglobin concentration for diagnosis of bovine respiratory disease heifers newly arrived at a feedlot", *Am. J. Vet. Res.*, **70**(10), pp. 1291-1298 (2009)

10. M. Born and E. Wolf, *Principles of Optics (7th Edition),* Cambridge University Press, Cambridge, UK (1999)

11. H. Compton, "A general quantum theory of the wave-length of scattered x-rays", *Phys. Rev.*, **24**(2), pp. 168-176, (1924)

12. V. Raman and K. S. Krishnan, "Optical analogue of the Compton effect", *Nature*, **121**(3053), p. 711 (1928)

13. W. E. Smith and G. Dent, *Modern Raman Spectroscopy – A Practical Approach*, John Wiley & Sons, Ltd (2005)

14. U. Rössler, *Solid State Theory: An Introduction 2 Ed.*, Springer, New York NY, USA (2009)

15. E. F. Shubert, *Physical Foundations of Solid-State Devices*, Rensselaer Polytechnic Institute, Troy NY, USA (2007)

16. B. Lüthi, *Physical Acoustics in the Solid State*, Springer-Verlag, Berlin, Germany (2007)

17. R. Dalven, "A review of the semiconductor properties of PbTe, PbSe, PbS, and PbO", *Infrared Phys.*, **9**, pp. 141-184 (1969)

18. A. K. Buin, A. Verma, and M. P. Anantram, "Carrier-phonon interaction in small cross-sectional silicon nanowires", *J. Appl. Phys.*, **104**(5), 053716 (2008)

19. G. A. Northrop and J. P. Wolfe, "Ballistic phonon imaging in solids – a new look at phonon focusing", *Phys. Rev. Lett.*, **43**(19), pp. 1424-1428 (1979)

20. M. S. Dresselhaus, G. Chen, M. Y. Tang, R. Yang, H. Lee, D. Wang, Z. Ren, J.-P. Fleurial, and P. Gogna, "New directions for low-dimensional thermoelectric materials", *Adv. Materials*, **19**, pp. 1043-1053 (2007)

21. A. J. Minnich, M. S. Dresselhaus, Z. F. Ren, and G. Chen, "Bulk nanostructured thermoelectric materials: current research and future prospects", *Energy Env. Sci.*, **2**, pp. 466-479 (2009)

22. H. Wang, Y. Pei, A. D. Lalonde, and G. J. Snyder, "Heavily doped p-type PbSe with high thermoelectric performance: an alternative for PbTe", *Adv. Materials*, **23**, pp. 1366-1370 (2011)

23. N. Mingo, D. Hauser, N. P. Kobayashi, M. Plissonnier, and A. Shakouri, "Nanoparticle-in-alloy approach to efficient thermoelectrics: silicides in SiGe", *Nano Letters*, **9**(2), pp. 711-715 (2009)

24. J. Callaway, "Model for lattice thermal conductivity at low temperatures", *Physical Review*, **113**(4), pp. 1046-1051 (1959)

25. S. S. Shalyt, V. M. Muzhdaba, and A. D. Galetskaya, "Lattice and electronic thermal conductivity of PbTe, PbSe, and PbS", *Sov. Phys. – Solid State*, **10**(5), pp. 1018-1024 (1968)

26. J. Hone, B. Batlogg, Z. Benes, A. T. Johnson and J. E. Fischer, "Quantized phonon spectrum of single wall carbon nanotubes", *Science*, **289**, pp. 1730-1733 (2000)

27. J. Androulakis, C.-H. Lin, H.-J. Kong, C. Uher, C.-I. Wu, T. Hogan. B. A. Cook, T. Caillat, K. N. Paraskevopoulos, and M. G. Kanatzidis, "Spinodal decomposition and nucleation and growth as a means to bulk nanostructured thermoelectrics: enhanced performance in $Pb_{1-x}Sn_xTe$-PbS", *J. Am. Chem. Soc.*, **129**, pp. 9780-9788 (2007)

28. B. Poudel, Q. Hao, Y. Ma, Y. Lan, A. Minnich, B. Yu, X. Yan, D. Wang, A. Muto, D. Vashaee, X. Chen, J. Liu, M. S. Dresselhaus, G. Chen, and Z. Ren, "High-thermoelectric performance of nanostructured bismuth antimony telluride bulk alloys", *Science*, **320**, pp. 634-639 (2008)

29. J. Faist, F. Capasso, D. L. Sivco, C. Sirtori, A. L. Hutchinson, and A. Y. Cho, "Quantum Cascade Laser", *Science*, **264**(5158), pp. 553-556 (1994)

30. J. R. Meyer, I. Vurgaftman, R. Q. Yang, and L. R. Ram-Mohan, "Type-II and type-I interband cascade lasers", *Elec. Lett.*, **32**(1), pp. 45-46 (1996)

31. R. Q. Yang, Z. Tian, J. F. Klem, T. D. Mishima, M. B. Santos, and M. B. Johnson, "Interband cascade photovoltaic devices", *Appl. Phys. Lett.*, **96**, 063504 (2010)

32. A. Rogalski, J. Antoszewski, and L. Faraone, "Third generation infrared photodetector arrays", *J. Appl. Phys.*, **105**, 091101 (2009)

33. Z. Shi, G. Xu, P. J. McCann, X. M. Fang, N. Dai, C. L. Felix, W. W. Bewley, I. Vurgaftman, and J. R. Meyer, "IV-VI compound midinfrared high-reflectivity mirrors and vertical-cavity surface-emitting lasers grown by molecular-beam epitaxy", *Appl. Phys. Lett.*, **76**(25), pp 3688-3690 (2000)

34. S. Adachi, "GaAs, AlAs, and $Al_xGa_{1-x}As$: material parameters for use in research and device applications", *J. Applied Physics*, **58**(3), pp. R1-R29 (1985)

35. D. G. Cahill, K. E. Goodson, and A. Majumdar, "Thermometry and Thermal Transport in Micro/Nanoscale Solid-State Devices and Structures", *ASME J. of Heat Transfer*, **124**(2), pp. 223-241 (2002)

36. D. G. Cahill, "Heat transport in dielectric thin films and at solid-solid interfaces", *Microscale Thermophysical Engineering*, **1**(3), pp. 85-109 (1997)

37. L. A. Elizondo, Y. Li, A. Sow, R. Kamana, H. Z. Wu, S. Mukherjee, F. Zhao, Z. Shi, and P. J. McCann, "Optically pumped mid-infrared light emitter on silicon", *J. Appl. Phys.*, **101**, 104504 (2007)

38. G. E. Cragg and A. L. Efros, "Suppression of Auger processes in confined structures", *Nano Lett.*, **10**, pp. 313-317 (2010)

39. J. Lloyd-Hughes, Y. L. Delley, G. Scalari, M. Fischer, V. Liverini, M. Beck, and J. Faist, "Spectroscopic determination of the doping and mobility of terahertz quantum cascade structures", *J. Appl. Phys.*, **106**, 093104 (2009)

40. A. Fainstein, B. Jusserand, V. Thierry-Mieg, "Raman scattering enhancement by optical confinement in a semiconductor planar microcavity", *Phys. Rev. Lett.*, **75**(20), pp. 3764-3767 (1995)

41. A. Soukiassian, W. Tian, D. A. Tenne, X. X. Xi, D. G. Schlom, N. D. Lanzillotti-Kimura, A. Bruchhausen, A. Fainstein, H. P. Sun, X. Q. Pan, A. Cros, and A. Cantarero, "Acoustic Bragg mirrors and cavities made using piezoelectric oxides", *Appl. Phys. Lett.*, **90**, 042909 (2007)

42. N. D. Lanzillotti-Kimura, A. Fainstein, A. Huynh, B. Perrin, B. Jusserand, A. Miard, A. Lemaitre, "Coherent generation of acoustic phonons in an optical microcavity", *J. of Physics: Conference Series*, **92**, 012016 (2007)

43. P. J. McCann, S. K. Aanegola, and J. E. Furneaux, "Growth and characterization of thallium- and gold-doped $PbSe_{0.78}Te_{0.22}$ layers lattice matched with BaF_2 substrates", *Appl. Phys. Lett.*, **65**(17), pp. 2185-2187 (1994)

44. J. Androulakis, D.-Y. Chung, X. Su, L. Zhang, C. Uher, T. C. Hasapis, E. Hatzikraniotis, K. M. Paraskevopoulos, M. G. Kanatzidis, "High-temperature charge and thermal transport properties of the n-type thermoelectric material PbSe", *Phys. Rev. B*, **84**, 155207 (2011)

45. B. Zhang, J. He, X. Ji, and T. M. Tritt, "Size-selective high-yield growth of lead telluride (PbTe) nanocrystals using a chemical vapor deposition technique", *Appl. Phys. Lett.*, **88**, 043119 (2006)

46. P. J. McCann, K. Namjou, and X. M. Fang, "Above-room-temperature continuous wave mid-infrared photoluminescence from PbSe/PbSrSe quantum wells", *Appl. Phys. Lett.*, **75**(23), pp. 3608-3610 (1999)

47. H. Zogg, P. Muller, A. Fach, J. John, C. Paglino, and A. N. Tiwari, "Epitaxy of narrow gap IV-VI materials on Si(111) and Si(100)-substrates: Growth, properties and thermal mismatch strain accommodation," *Proc. SPIE*, **2554**, pp. 35-42 (1996)

48. H. Zogg, S. Blunier, A. Fach, C. Maissen, P. Muller, S. Teodoropol, V. Meyer, G. Kostorz, A. Dommann, and T. Richmond, "Thermal-mismatch-strain relaxation in epitaxial CaF2, BaF2/CaF2, and PbSe/BaF2/CaF2 layers on Si(111) after many temperature cycles", *Phys. Rev. B*, **50**(15), pp. 10801-10810 (1994)

49. W. Z. Shen, H. F. Fang, L. F. Jiang, K. Wang, G. Yu, H. Z. Wu, and P. J. McCann, "Band gaps, effective masses and refractive indices of PbSrSe thin films: Key properties for mid-infrared optoelectronic device applications", *J. Appl. Phys.*, **91**(1), pp. 192-198, (2002)

50. L. A. Elizondo, *Low-dimensional IV-VI Semiconductor Materials*, Ph. D Dissertation, University of Oklahoma (2008)

51. T. H. Geballe and G. W. Hull, "Seebeck effect in germanium", *Phys. Rev.*, **94**(5), pp. 1134-1140 (1954)

52. T. H. Geballe and G. W. Hull, "Seebeck effect in silicon", *Phys. Rev.*, **98**(4), pp. 940-947 (1955)

53. Private communication with Dr. Allan Gray from Phononic Devices, Inc on 7/25/2010

54. C. A. Paddock and G. L. Eesley, "Transient Thermoreflectance from Thin Metal Films", *J. Appl. Phys.*, **60**(1), pp. 285-290 (1986)

55. F. Zhao, X. Lv, A. Majumdar, and Z. Shi, "Influence of mounting on continuous-wave photoluminescence from midinfrared PbSrSe/PbSe multiple quantum wells", *Appl. Phys. Lett.*, **84**(8), pp. 1251-1253 (2004)

56. J. D. Jeffers, K. Namjou, Z. Cai, P. J. McCann, and L. Olona, "Cross-plane thermal conductivity of a PbSnSe/PbSe superlattice material", *Appl. Phys. Lett.*, **99**, 41903 (2011)

57. A. Jain and K. E. Goodson, "Measurement of the Thermal Conductivity and Heat Capacity of Freestanding Shape Memory Thins Films Using the 3ω Method", *ASME J. of Heat Transfer*, **130**, 102402 (2008)

Chapter 2

Photoluminescence Measurement of Thin Films

2.1 Motivation

Mid-infrared IV-VI semiconductor nanostructures, with E_g < 500 meV at 300 K, are routinely characterized with photoluminescence (PL) using either a continuous wave (cw) or pulsed near-infrared (NIR) laser [1-5]. The commercial availability of high power NIR semiconductor diodes enables compact systems capable of steady-state optical material characterization [6-9]. Figure 2-1 shows the PL emission peak energy change or "blue shift" with increased temperature and absorbed optical power from a PbSrSe/PbSe multiple quantum well (MQW) material. The shift of PL emission with increased optical power is attributed to a change in lattice temperature for the optically active material from thermalization and non-radiative recombination of photogenerated

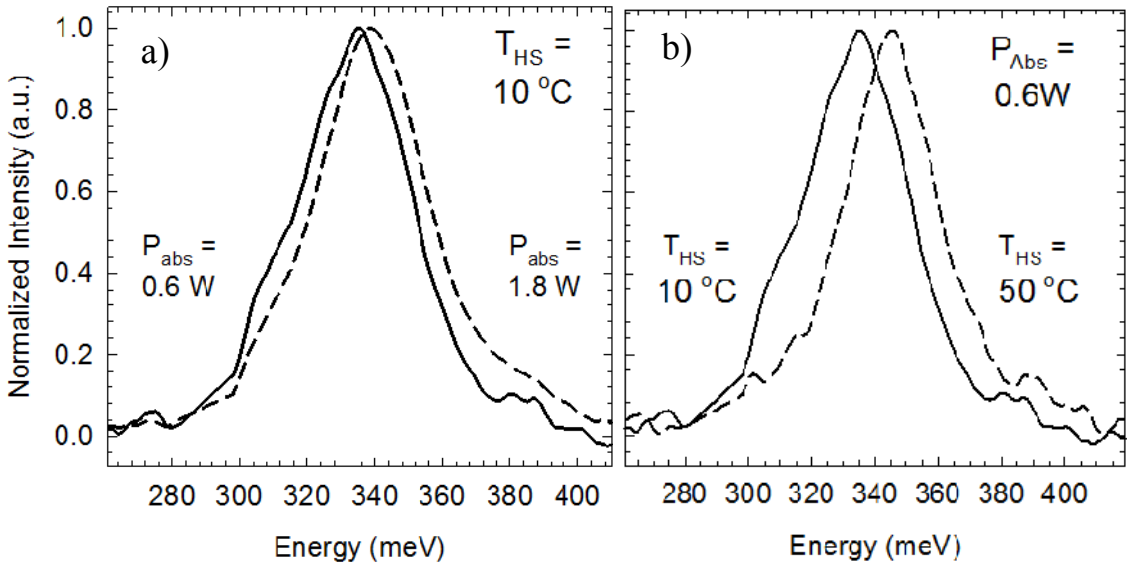

Figure 2-1: PL emission shift for MQW sample #M141-A1: a) with increased optical pump power absorbed (P_{abs}) at a constant heatsink temperature T_{HS} = 10° C and b) with increased heatsink temperature at a constant P_{abs} = 0.6 W.

carriers. This assertion is supported by *McCann et al.* [10] who showed an increased blue shift, and therefore more heating, from the same amount of optical power in a 910 nm laser compared to one operating at 2.5 μm. This data also confirmed thermalization, or the rapid decay of carriers with energy above the band minima, near the surface of the film as the dominant heating mechanism in cw PL. Therefore, the lattice temperature of a IV-VI semiconductor sample being optically heated can be calculated using the techniques described in [1,10] by measuring the shift in PL peak energy due to optical power $\Delta E_{PL}(P)$ and comparing it to the shift due to a change in the heatsink temperature $\Delta E_{PL}(T)$. This non-contact method overcomes limitations of standard mechanical thermometry techniques [11] by using a laser probe with a surface "footprint" diameter on the order of hundreds of microns. This technique differs from Raman spectroscopy [12] and thermoreflectance [13] opto-thermal characterization that detects a signal in the scattered or reflected laser probe beam. This chapter describes an optical material measurement technique and computer controlled PL testing system for IV-VI semiconductor thin film nanostructures. The techniques described here were optimized using an automated rapid data collection system used by six different researchers to perform over 1000 tests on 40 different thin films over a 3 year period. The thin films tested were grown by molecular beam epitaxy (MBE) using techniques described previously elsewhere [5, 7].

2.2 Experimental Procedures

Figure 2-2 shows a diagram for the PL measurement system used in this research with a modular Fourier transform infrared (FTIR) spectrometer (Newport, Inc. Newport, RI model # MIR8000) for broadband optical detection covering the energy

range, 100 meV ≤ E_{PL} ≤ 400 meV. The FTIR spectrometer was equipped with either a photoconductive HgCdTe or photovoltaic HgCdZnTe detector (Fermionics, Simi Valley, CA) with amplifier electronics and cutoff wavelengths of 10 μm and 6 μm respectively. An optical power meter (Newport model # 1916-C) with a thermopile detector (Newport model # 818P-12) was used to measure the reflected and incident near-IR pump laser power. The additional significant elements of the system are: a) semiconductor diode laser (described in the next section), b) focusing optics, c) a sample mount stage with temperature control hardware, d) control software, and e) control electronics. Several optical pumping system designs were employed using a current supply up to 8 Amperes (A) (ILX Lightwave, Bozeman, MT model # LDC-3900). The sample mount stage temperature was stabilized with a thermoelectric (TE)

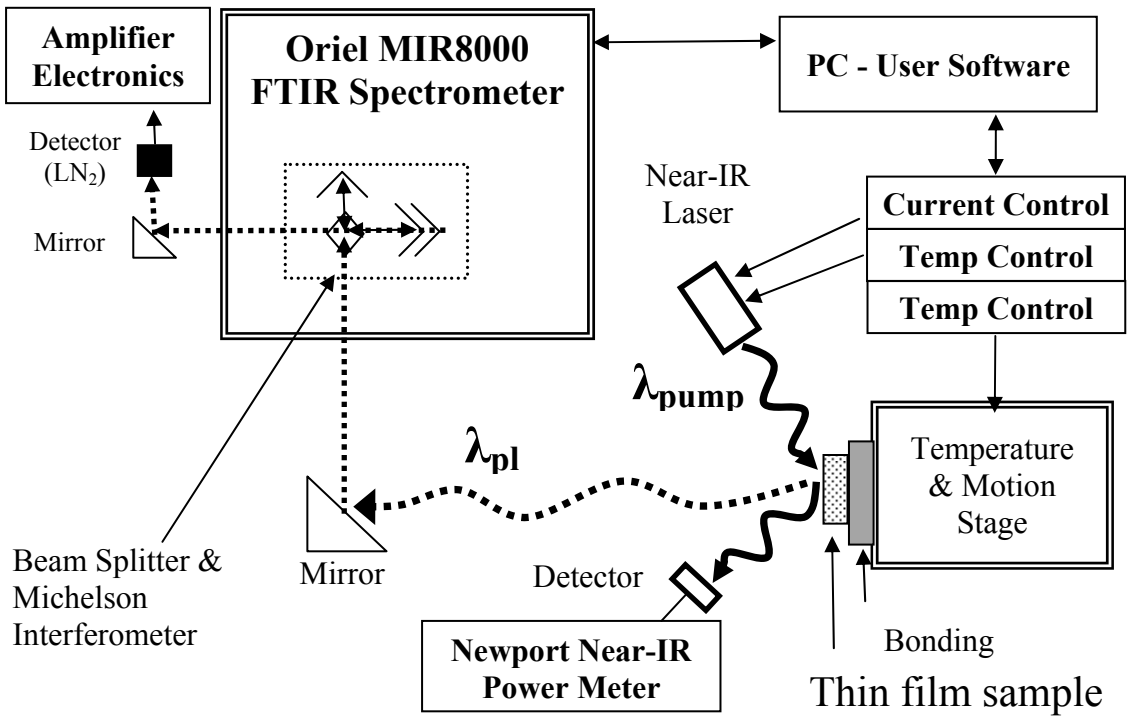

Figure 2-2: PL system block diagram that includes an FTIR, near-IR power meter, and sample mount stage. The solid line represents the NIR pump laser optical path and the dotted line represents the optical path for PL.

cooler (Melcor, Trenton, NJ), 5 kOhm thermistor temperature sensor (ILX Lightwave), and control module (Stanford Research Systems, Palo Alto, CA model # 535).

2.2.1 Optical System Characterization

Two pump lasers were used in the PL systems: a fiber coupled 875 nm InGaAs diode (Ser. #06JUN16, QPhotonics, Ann Arbor, MI model # QSP-915-7) and an 805 nm laser (Ser. # E18418, SNOC Electronics Guangdong, China model # SL808T3000) on a c-mount package with an attached cylindrical lens and no external optics required. Figure 2-3 shows the total optical power measured for each laser over their operating range and the unique spatial power distribution from the cylindrical lens attached to laser #E18418. The fiber coupled laser package from QPhotonics was terminated with a 2.3 mm aperture collimator (Thor Labs, Newton, NJ model # F220SMA-780). The output beam was focused onto the film surface with either a 2-inch or 4-inch diameter convex glass lens with 2-inch focal length. The lasers were mounted with thermal

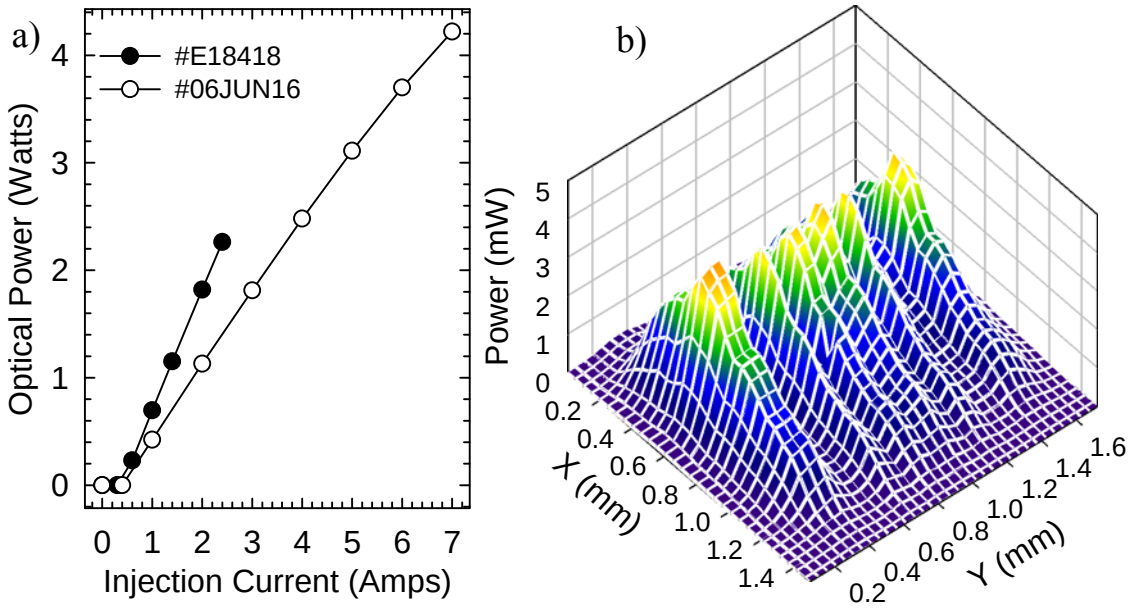

Figure 2-3: PL laser characterization: a) total power for lasers E18418 and 06JUN16 for different injection currents, b) the power distribution for laser E18418.

adhesive to air-cooled copper heatsinks with DC voltage fans to stabilize operation near room temperature, ≈ 20 °C. Laser #E18418 operated over the current range of 0.3 A to 2.6 A with a maximum output power of 2.5 W. The fiber coupled laser #06JUN16 operated over the range 0.4 A to 7.0 A with maximum power of 4 Watts.

The optical beam power distribution, or cross-section, on the film surface was measured using a pin-hole technique. A thin piece of sheet metal, with a small hole drilled in the center (d < 2.5 mm), was affixed to a linear translation stage and placed in the beam path. The power was measured at each point as the apparatus was translated across a single direction in the optical cross section with results for laser #E18418 shown Figure 2-3 b). Laser #E18418 had a nearly Gaussian power distribution along the horizontal (or x) axis that was aligned with the length of the cylindrical lens. Along the vertical axis the power was distributed among six different peaks with even spacing and amplitude. Figure 2-4 shows a diagram of the lens geometry for the fiber collimated laser that had a circularly symmetric Gaussian power distribution with a measured minimum standard deviation, σ ≈ 125 μm. The width of power distribution increased as a function of deviation distance (Δf) from the focal length (f_L) of the lens as

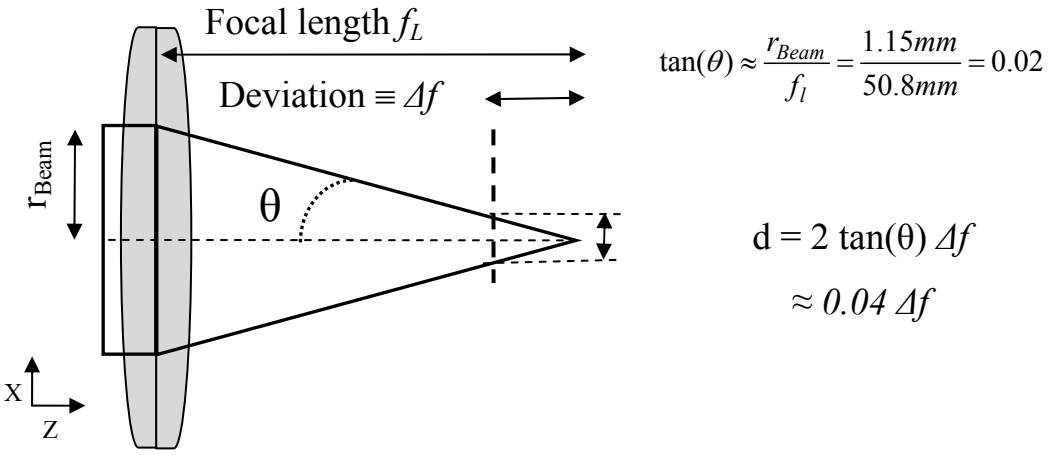

Figure 2-4: Diagram of lens geometry used for focusing the PL pump laser.

shown. A deviation Δf = 2 mm would correspond to an 80 μm increase in the focused beam cross-section diameter for the 2.3 mm fiber laser beam.

2.2.2 Sample Mounting

The techniques employed to mount thin film nanostructures during thermoelectric characterization greatly affect the interface thermal conductivity or thermal contact resistance (TCR) [12]. In order to thermally isolate the nanostructure under test a low thermal resistance bonding material must hold the silicon substrate to a temperature stabilized surface. Chemically reactive bonding techniques such as epoxy or paint typically have low TCR but are generally permanent and may be difficult to apply. Temporary bonding techniques such as solder or thermal adhesive (tape) may provide more flexibility but typically have a higher TCR [14] and the application process may be destructive. Indium solder has a melting point ≈ 156 °C that must be applied to the entire sample over a period of time similar to an annealing step and thermal tape requires pressure to be applied to surface of the thin film.

Alternatively $Ga_{0.75}In_{0.25}$, a eutectic material (EGaIn) or liquid metal, above its liquidus temperature of 15 °C has been investigated in thermal management systems [15]. The elasticity of the material is controlled by surface pressure and layer thickness. EGaIn handling [16] consisted of using a wooden or metal rod to apply an excess amount of material to "wet" the surface of a copper sub-mount, Figure 2-5. A piece of thin film was placed on top of the EGaIn and was "thinned" by horizontal motion of the sample until surface tension increased enough to hold the sample in place. Additional research on thin film bonding with copper sub-mounts and EGaIn was verified with scanning electron microscope (SEM) images showing the final bond layer thickness

was comparable with film thickness, $d_{bond} \leq 5$ μm. This sub-mount was then attached with a layer of EGaIn and two #2-56 screws to a 5 mm thick piece of copper containing a thermistor temperature sensor mounted with epoxy in a blind drill hole less than 0.5 mm below the surface and directly beneath the thin film sample location. This mount was attached to a TE cooler on a multi-axis motion stage for optical alignment.

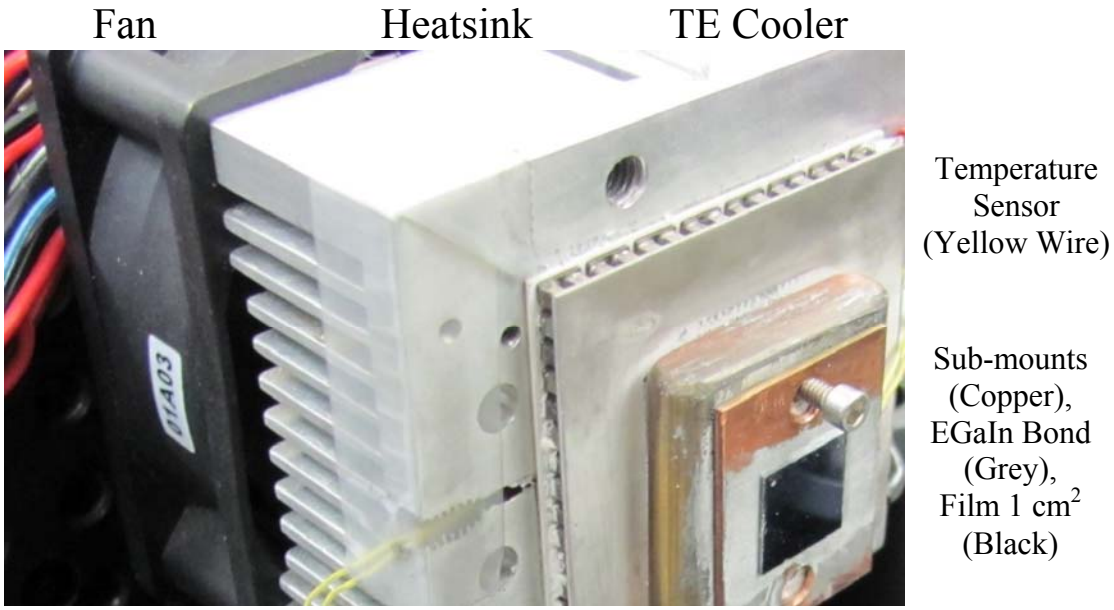

Figure 2-5: Photo of thermal control mount stage for PL testing with a TE cooler.

2.3 Automated Data Collection

Automated testing software was created using the LabVIEW programming language [17] with examples contained in Appendix A. The front panel of the "FTIR Characterize" executable program is shown in Figure 2-6. The software controlled all aspects of testing including several important time delays needed for thermal stability. The software allowed for two data acquisition modes: real-time user and automated testing. Of particular importance was system safety with a maximum 4 W of mid-IR laser power being generated and thin film temperatures as high as 50 ºC. During three

years of operation no equipment or samples received damage due to software failure. This was accomplished using a custom graphical programming technique with two simultaneous loops and event based programming. This technique has shown wide applicability for process automation and rapid prototyping with near real-time data acquisition and processing on standard personal computers [18].

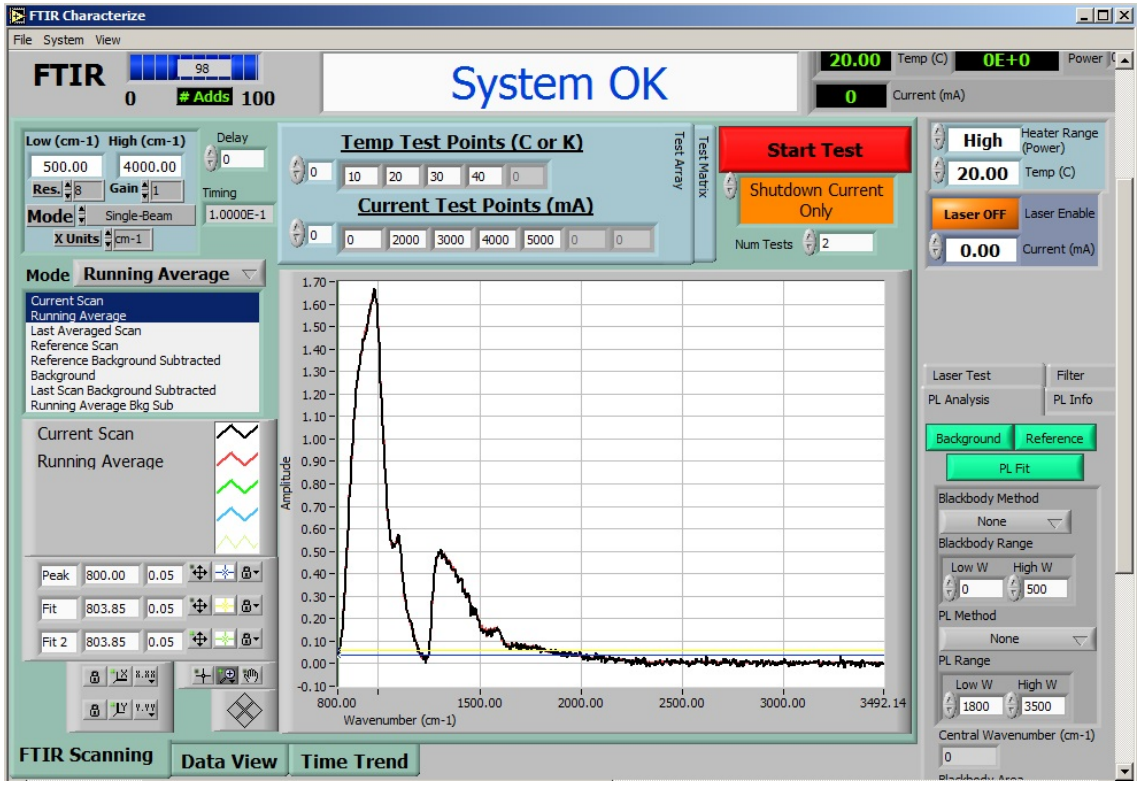

Figure 2-6: FTIR Characterize program user interface and graphical block diagram developed using LabVIEW Ver. 7.0.

Figure 2-7 shows the FTIR spectral data acquired during an automated test. The software required entering a starting value, an ending value, and number of steps between for both heatsink temperature (T_1, T_{max}, and n_{temp}) and optical power (P_1, P_{max}, and n_{opt}). During data acquisition with the laser pump on the reflected power, P_{Ref}, measured on the near-IR detector was recorded in the data file. The open-air TE cooled sample mount was typically operated between 20 ºC and 60 ºC, operation at lower

temperatures led to the formation of condensation on films being tested. Each test began when the temperature of the thin film was stabilized within 0.5 K of the first set point, T_1. At this and subsequent temperatures n_{opt} +1 emission spectra were acquired including a "background" spectrum with the pump laser not enabled. Background subtraction is a technique commonly employed in many forms of optical spectroscopy to remove system dependent anomalies including etalon fringes [19-20].

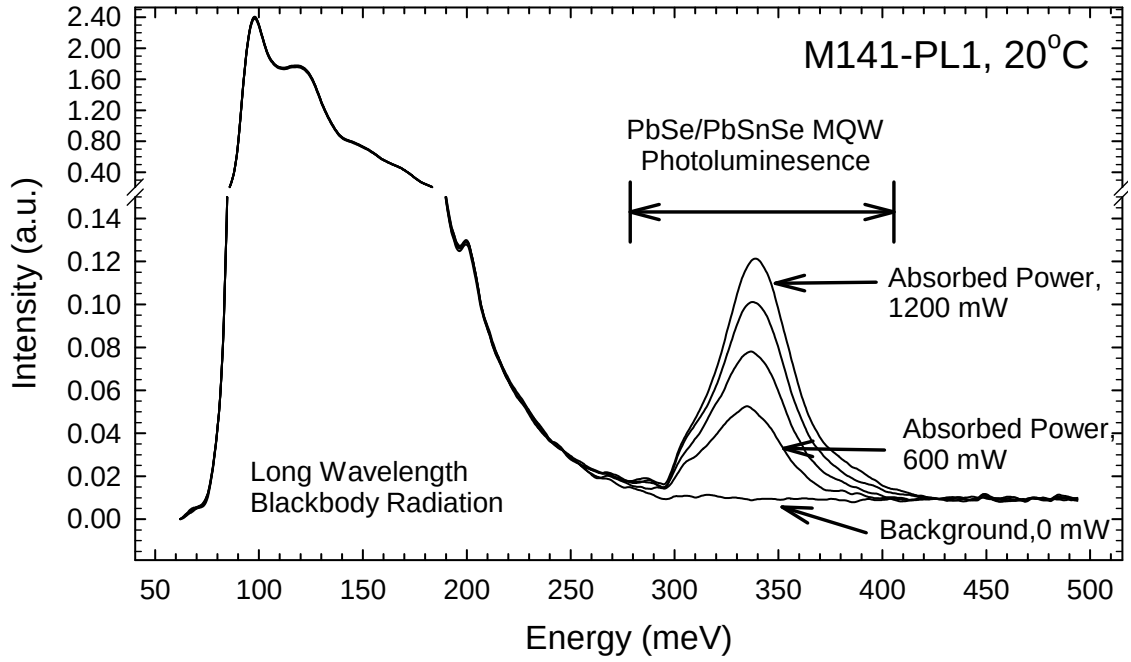

Figure 2-7: PL stimulated emission spectrum from MQW sample, #M141-PL1, at a heatsink temperature of 20 ºC.

2.3.1 PL Emission Analysis

The acquisition software was capable of simple real-time analysis of the PL emission spectral feature "peak" between 200 meV and 450 meV, Figure 2-8. The simplest technique analyzed the background subtracted PL emission spectrum maximum value as a function of absorbed optical pump laser power $\Delta E_{PL}(P)$ using Eq. 2.1, by employing a Linear Least Squares (LLS) fitting technique [21]. The quality of

the fit, or data linearity, is described by the coefficient of determination or the R^2 value. While different values may be deemed acceptable, the data threshold for a valid test was held at $R^2 \geq 0.95$. Due to many complications to be addressed in the next chapter a PL emission spectral fitting routine is typically employed [10, 22] using known quantum theory to minimize system white noise effects by using multiple data points. A standard

$$\Delta E_{PL}(P) \equiv \frac{\Delta E_{PL}}{\Delta P_{Abs}} = \frac{\sum_{P} (E_{Max} P)^2 - E_{Max}^2 P^2}{\sum_{P} (E_{Max} P)^2}, \frac{meV}{Watt} \qquad \textbf{(2.1)}$$

quantum function such as a Gaussian peak fit to the PL emission data shown in Figure 2-8 is not ideal ($R^2 < 0.85$) and clearly does not follow the data curve but the maximum value, $E_{FitMax}(P)$, of these fit curves change linearly with power and has R^2 values greater than use of a single PL data maximum point. Values from the two techniques may vary as much as 50%. During a test, spectral data were acquired at several

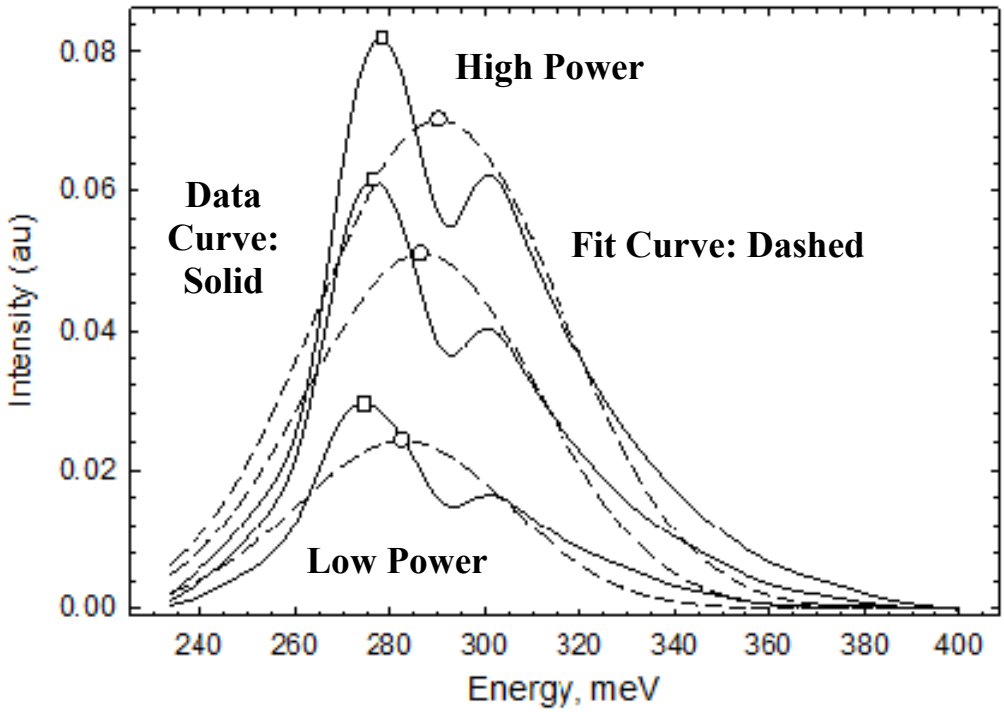

Figure 2-8: PL stimulated emission from sample #M046-A with peak fitting and center frequency shift with different optical power and molecular absorption.

temperatures to enable calculation of a second material parameter, $\Delta E_{PL}(T)$ in Eq. 2.2, that should be nearly equal to the linear relationship of bandgap energy, E_g, to

$$\Delta E_{PL}(T) \equiv \frac{\Delta E_{PL}}{\Delta T_{Set}} = L.L.S.(E_{Max}, T) \approx \Delta E_g(T), \frac{\mu eV}{K} \qquad \textbf{(2.2)}$$

temperature. This relation assumes the only significant contribution to changes in spectral distribution, for example the energy of the maximum value, is due to increased temperature in the optically active material. Eq. 2.3 defines an optical heating effect (*HE*) that translates the measured PL energy shift due to absorbed optical power to an

$$HE \equiv \Delta T(P) = \frac{\Delta E(P)}{\Delta E(T)} \approx \frac{\Delta E(P)}{\Delta E_g(T)}, \frac{K}{Watt} \qquad \textbf{(2.3)}$$

equivalent temperature increase for use in thin film comparisons or in further thermal calculations. This test result describes the temperature increase per unit of absorbed optical power in units K/Watt that when multiplied by the absorbed power, P_{abs}, describes the average volumetric temperature of the luminescent material.

2.3.2 Blackbody Emission Analysis

In addition to the laser stimulated PL emission peak, lower energy blackbody emission between 100 meV and 200 meV, Figure 2-9, was analyzed by the software to provide thin film material and thermal properties while verifying system performance. Thin film Fabry-Perot fringes are routinely analyzed [7] to provide information on material properties such as the refractive index, n, and film thickness, t. Cavity resonance, showing up as local intensity minima, occurs when the wavelength of photons in a thin film are proportional to thickness. The difference in energy between fringes, ΔE, is related to these two parameters through the equation, $t = (\Delta E 2n)^{-1}$. The

two data peaks in Figure 2-9 are approximately 28 meV apart that combined with n_{PbSe} ≈ 5 results in a calculated thickness of 4.5 μm for film #M046 that agreed with the value measured by SEM to be 4.65 μm.

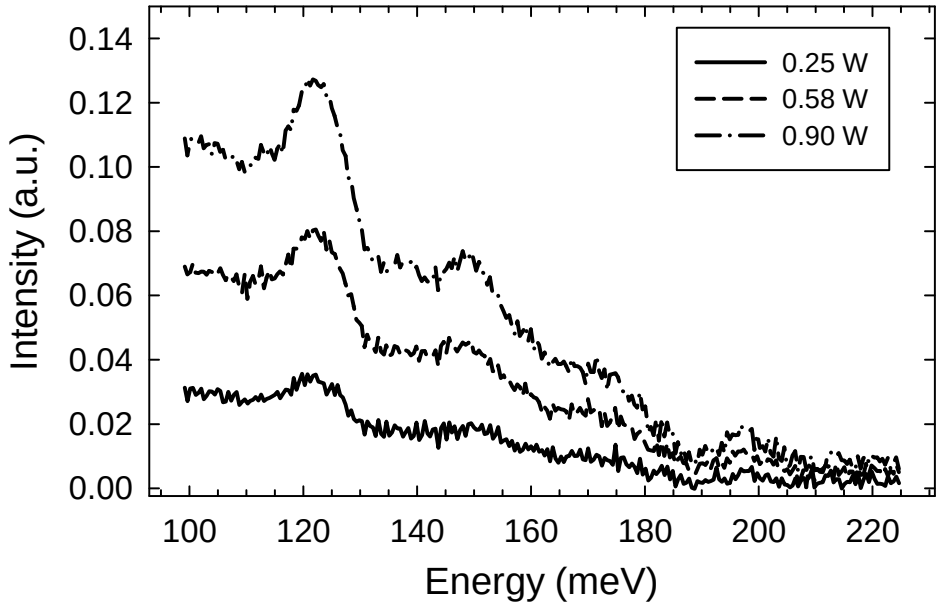

Figure 2-9: Blackbody radiation emission measured from sample #M046-A with total power that increases with increased PL laser power.

The software also assessed the low energy blackbody emission power using pyrometry techniques. The total power in a blackbody spectrum is related to the temperature of all objects within the optical field of view by the Stefan-Boltzmann relation, $P \propto T^4$. The total optical power over this energy range was calculated by numerically integrating the intensity plots. The change in blackbody emission power during optical characterization is shown in Figure 2-10. The variation of power with temperature, $\Delta P_{BB}(T)$, shows a clearly non-linearity over a 30 °K change in temperature during testing while the small changes associated with laser pump power, $\Delta P_{BB}(P)$, are nearly linear. These two values can be used in place of the corresponding PL emission energies of Eq. 2.3 to calculate another optical heating effect, HE_{BB}. However the two heating effects were significantly different, $HE_{PL} > HE_{BB}$, because the blackbody

emission measured comes from a significantly larger volume of material than the stimulated PL emission. The FTIR instrument inlet cross-section was specified to be 2.5 mm, significantly greater than the measured beam cross-section diameter of the fiber-coupled pump laser. Also both silicon and the IV-VI semiconductor films are transparent to long wavelength radiation and material behind the optically active PL region may contribute to the blackbody spectral data.

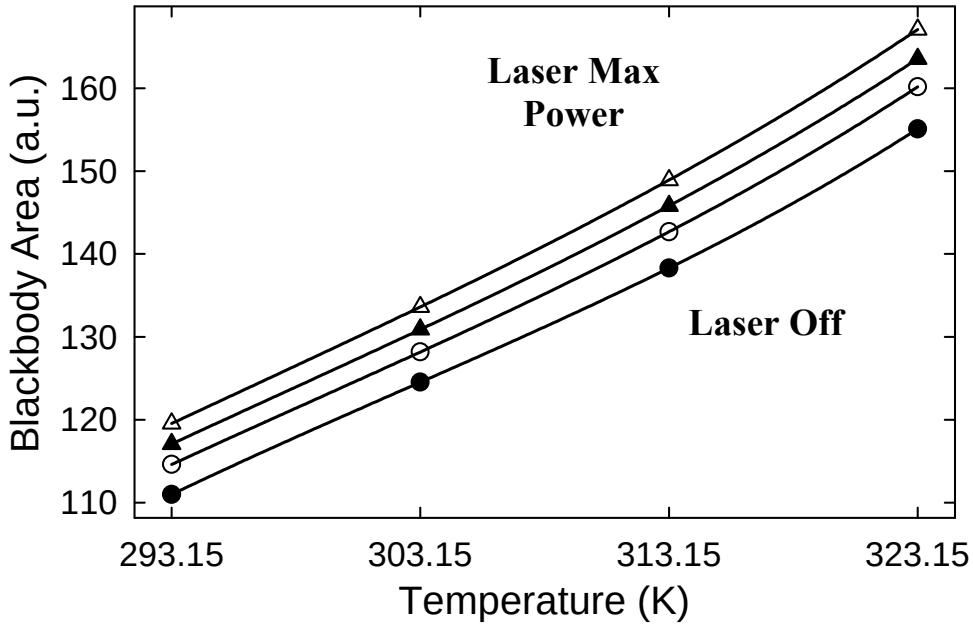

Figure 2-10: Blackbody emission power from sample, #M046-A for various heatsink temperatures with and without optical pumping.

2.4 Testing Repeatability

Open-air FTIR spectroscopy suffers from significant drawbacks including transient optical noise based on environmental conditions and inherent system noise. A standard practice to reduce noise is signal integration or time averaging [23] where the optimum length required can be assessed using an Allan variance plot. For the FTIR systems used 30 – 45 seconds of averaging was required with longer integration times showing negligible signal improvement. The measured baseline root-mean-squared

noise level for a fixed gain (8X) and resolution (8 cm^{-1}) was 0.01 arbitrary units (a.u.). This sets the minimum data feature detection limit, or ability to distinguish a PL emission peak from the noise, at a practical limit of four times this value.

This PL characterization technique required thermal stability of the thin film during testing for both the absolute temperature and optical heating effect. The heatsink temperature was maintained with a proportional, integral, and derivative (PID) controller with auto-tuning. The tuning process adjusted controller gains using a simple calibration routine to force 10 K temperature changes to occur within 4 minutes. Stability at a given temperature was maintained ± 0.1 K. However initial changes in pump laser power from the background acquisition to the first test point caused a temperature increase in the thin film as large as 0.5 K that settled in approximately 45 seconds. The PID controller adjusted to increased heating from subsequent changes in optical power while the laser was operating in 20-25 seconds.

2.4.1 Statistics

The accuracy of this PL technique was improved by averaging multiple measurements over a temperature range and repeating, Figure 2-11. The individual data points with error bars represent the average $\Delta E_{PL}(P)$ value measured at three different temperatures, $n_T = 3$, with a mean standard deviation of 8-10%. The lines on the graphs represent the statistics of repeated tests, $n_{Repeat} = 5$, on the same day. The solid line is the mean of $\Delta E_{PL}(P)$ on each day and the dashed lines show the range of one standard deviation for all measurements, $n_{Total} = n_{Repeat} \times n_T = 15$. The calculated heating effect of 3 or more repeated consecutive tests on the same day reduced the standard deviation

to less than 5 % of the mean value for most test conditions. The improvement in measurement variation on Day B is attributed to a 48-hour wait period after attaching the sub-mount to the temperature control stage with EGaIn. However the results over a longer period of time are highly dependent on several factors including optical instrument noise, oxide formation on exposed surfaces, and possible changes in the EGaIn bonding layers due to temperature cycling and repeated testing.

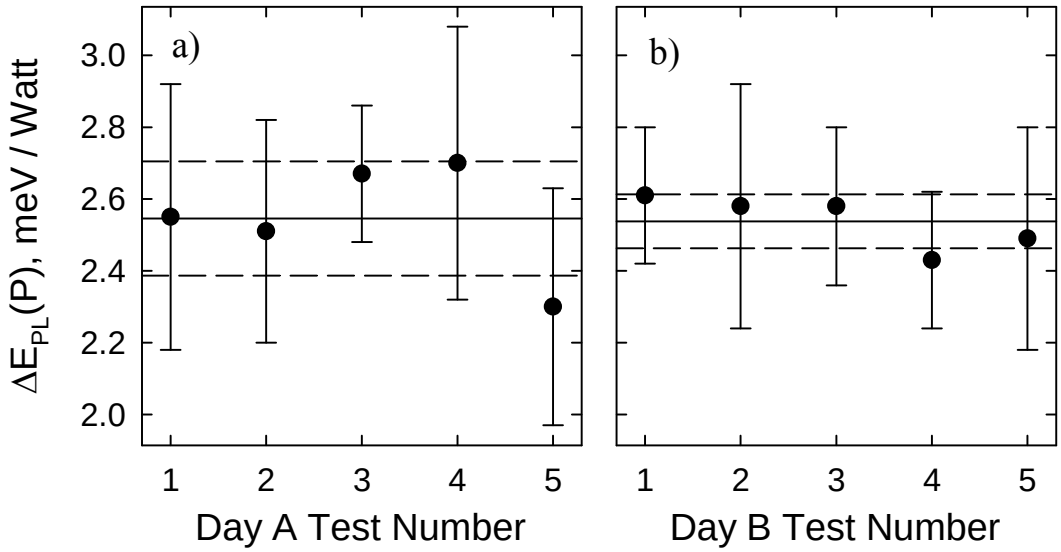

Figure 2-11: Optical heating effect for sample #M141-PL1 during consecutive tests on separate days: a) 5 tests with ΔE_{PL} = 2.58 ± 4% and b) 5 tests with ΔE_{PL} = 2.57 ± 2%.

Figure 2-12 shows the variation in $\Delta E_{PL}(P)$ and $\Delta E_{PL}(T)$ measured over several months for the same sample. The measured shift of PL emission due to a change in heatsink temperature should be a constant related to intrinsic film properties, *Eg*, and therefore independent of optical heating effects. The standard deviation of this measurement over a four month period that included the film sub-mount being removed from the temperature control stage and the optical alignment being altered between some of the measurements is 4%. However, the measured optical power shift had a larger variation, σ = ± 11 %, that is attributed to changes in both the system alignment

and sub-mount TCR. The optical heating calculated from measurement of blackbody emission, $HE_{BB}(P)$ in Figure 2-13, was more susceptible to variation in optical alignment than analysis of the PL signal. The change in blackbody power with heatsink temperature did not vary significantly, $\sigma = \pm 0.8$ %, however the optical effect varied more than 12.7 %. All data reported in the remainder of this dissertation are the average

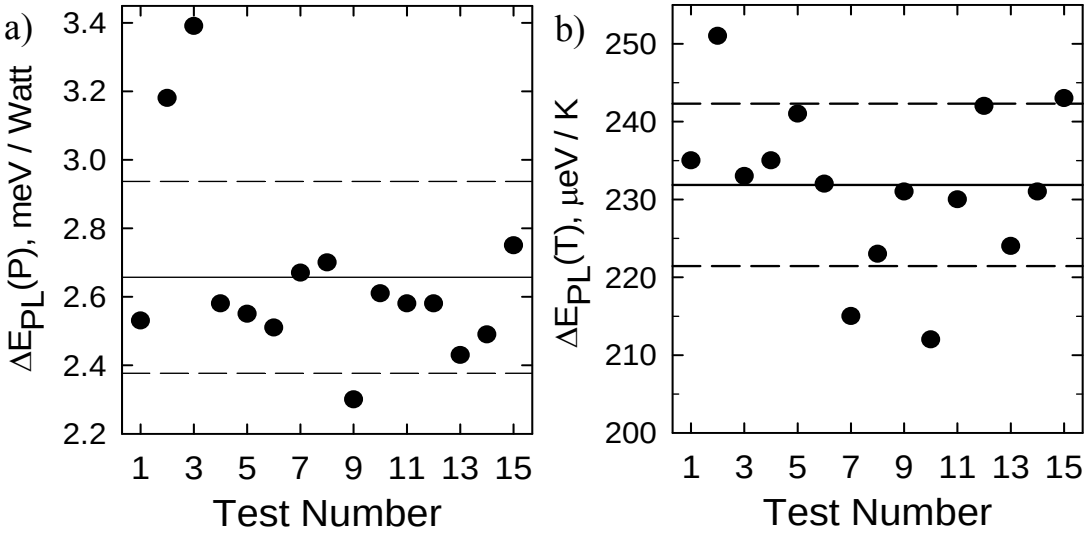

Figure 2-12: Repeatability of PL "shift" for sample #M141-PL1 with temperature and optical power: a) $\Delta E_{PL} = 2.68 \pm 11\%$ meV/W and b) $\Delta E_{PL} = 232 \pm 4\%$ μeV/K.

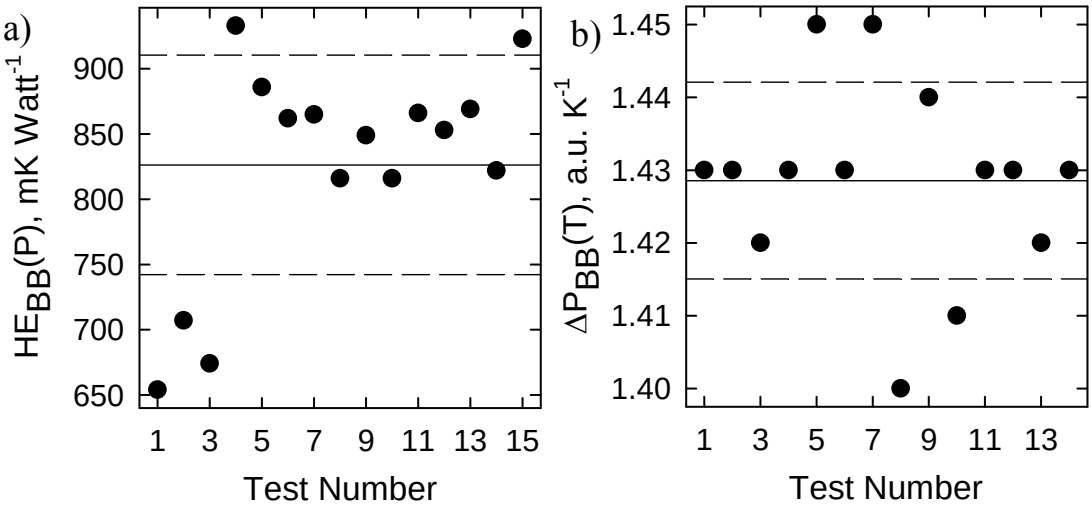

Figure 2-13: Repeatability of blackbody data for sample #M141-PL1: a) the HE = 0.83 ± 10% K/W and b) the change in power for heatsink temperature only 1.43 ± 0.8%.

of nine test points, three different heatsink temperatures repeated three times, with four different optical power settings unless otherwise noted.

2.4.2 Optical System Comparison

To investigate the heating effect defined in Eq. 2.3 as a function of optical beam cross-section on the film surface, $\Delta E_{PL}(\mathbf{P}) = \Delta E_{PL}(P_{xy})$, multiple films were tested with both PL laser pumps (System #1: Laser #E18418 and System #2: Laser #06JUN16) on the same day using similar film bonding methods. Figure 2-14 shows the PL emission spectra from film #M049 stimulated by the two lasers at the same heatsink temperature. Even though the measured power distribution for laser #E18418 exhibited multiple intensity peaks with spacing much greater the diffusion length for carriers in PbSe at room temperature [24] PL emission was a single peak. Despite significant differences for the two lasers the acquired PL spectra were similar in both shape and intensity and

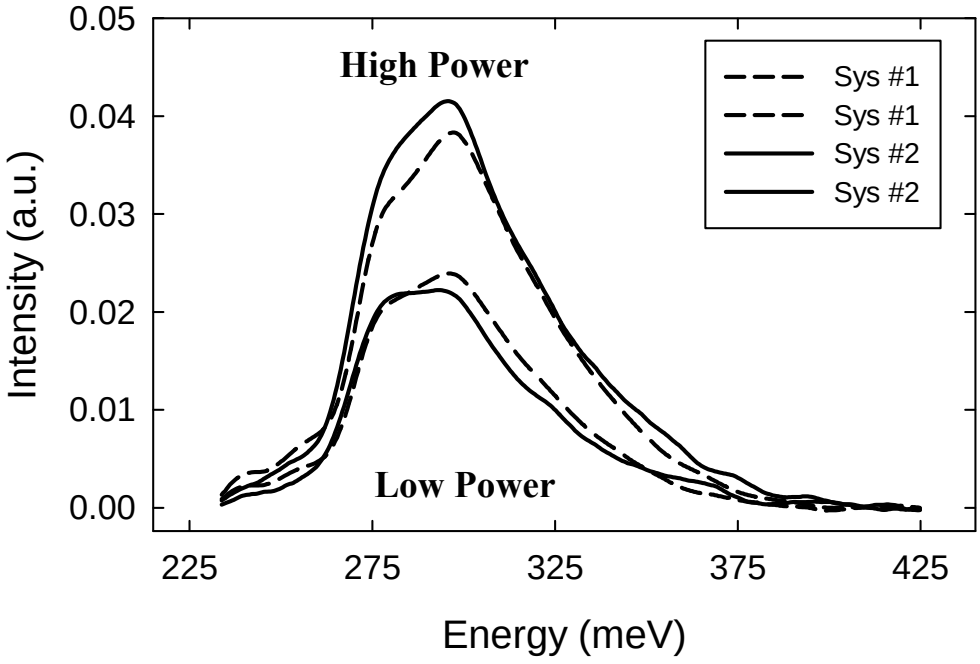

Figure 2-14: Background subtracted and filtered PL spectra for sample #M046-A using two different PL pump lasers and optical systems.

have an $R^2 \geq 0.93$ when the peak was analyzed with an exponentially modified Gaussian curve fit [25]. Figure 2-15 shows the change in the energy of the measured maximum PL intensity for increased optical power. The difference in slope between the two systems is consistent at different sample heatsink temperatures. Since the slope is proportional to the optical heating effect the data indicates the fiber coupled laser, which has a smaller beam diameter on the film surface, heats the sample at a significantly higher rate per unit of total absorbed power.

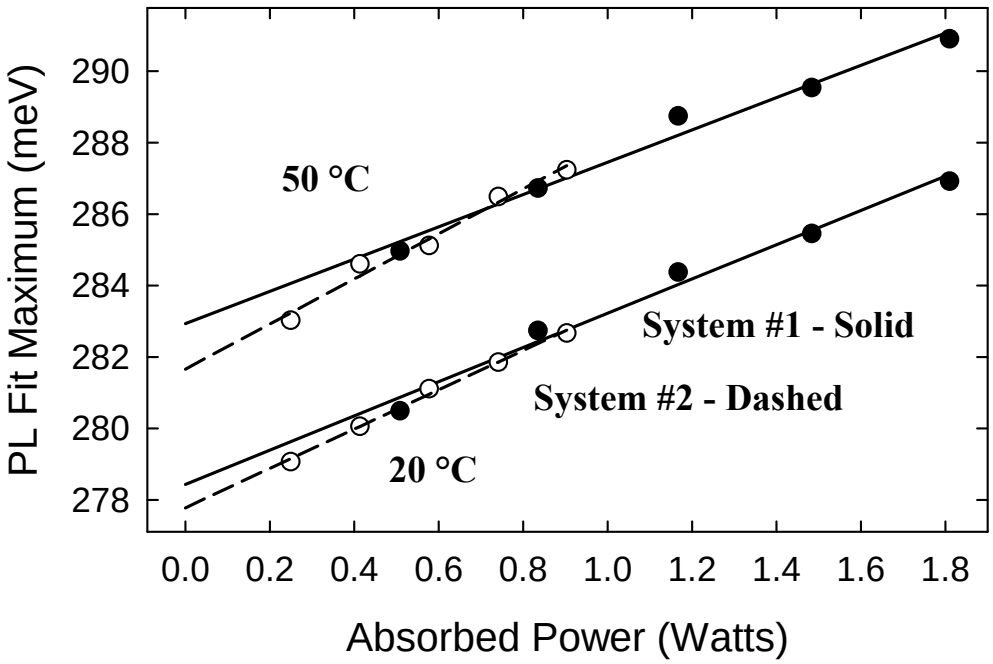

Figure 2-15: Measured optical shift of PL spectra on sample #M046-A with two different laser power distributions at heatsink temperature of 20 °C and 50 °C.

2.4.3 Sample Mounting Technique

The EGaIn sample mounting technique described previously was compared to a variety of materials using multiple film samples and repeated PL testing. Figure 2-16 shows the optical heating effect calculated from both PL emission shift and blackbody power increase for different mounting methods. Between each PL test the film samples

were removed from the testing apparatus and then replaced. Techniques #1 and #2 both used EGaIn to bond the silicon substrate of a sample to an Ag-coated copper sub-mount. The difference between #1 (EGaIn) and #2 (thermal grease) was the bonding material between the sub-mount and the copper thermal stage with temperature sensor. Technique #3 used a sample bond of black wax and a mount bond of EGaIn. These three techniques also used two screws to hold the sub-mount on the thermal stage. Technique #4 did not use a sub-mount and the film was attached directly to the thermal stage with double-sided adhesive. The mounting material with the lowest HE_{PL}, and therefore lowest TCR, was thermal grease. The TCR of the other materials relative to thermal grease were EGaIn (1.1), adhesive (1.6), and black wax (2.0).

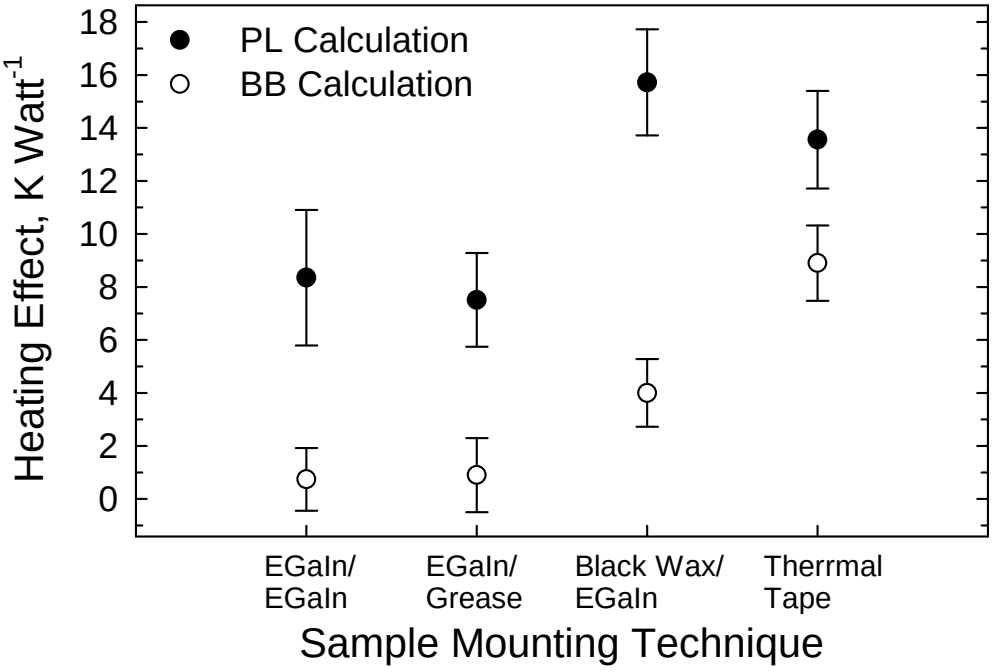

Figure 2-16: Measured heating effect using the PL emission and blackbody spectrum for sample #M141-PL1 with different sample mounting techniques and materials.

The blackbody spectral data also varied depending on the bonding material used as shown in Figure 2-17. The thin film sample bonded to a sub-mount with black wax showed a greatly increased blackbody emission compared to samples mounted with

EGaIn. In addition the PL emission for the black wax test was at greater intensity and higher energy, appearing shifted to the right. However, the difference in HE_{PL} was ~2X while the difference for HE_{BB} was 4X greater for black wax mounting. This can be explained by the EGaIn bonding layer acting as a mirror shielding blackbody emission from behind the substrate and decreasing long wavelength transmission through the thin film. This assertion is supported by comparison of results for the same sample attached to a copper sub-mount with EGaIn and the sub-mount being attached to the thermal stage with either thermal grease compound or EGaIn. The PL heating effect for thermal grease mounting was lower $HE_{PL}(Grease) = 7.7 < 8.2$ K/Watt and the blackbody measurement was higher $HE_{BB} = 0.9 > 0.7$ K/Watt. The effect is demonstrated clearly by the graphs in Figure 2-18. The blackbody intensity for the black wax and thermal

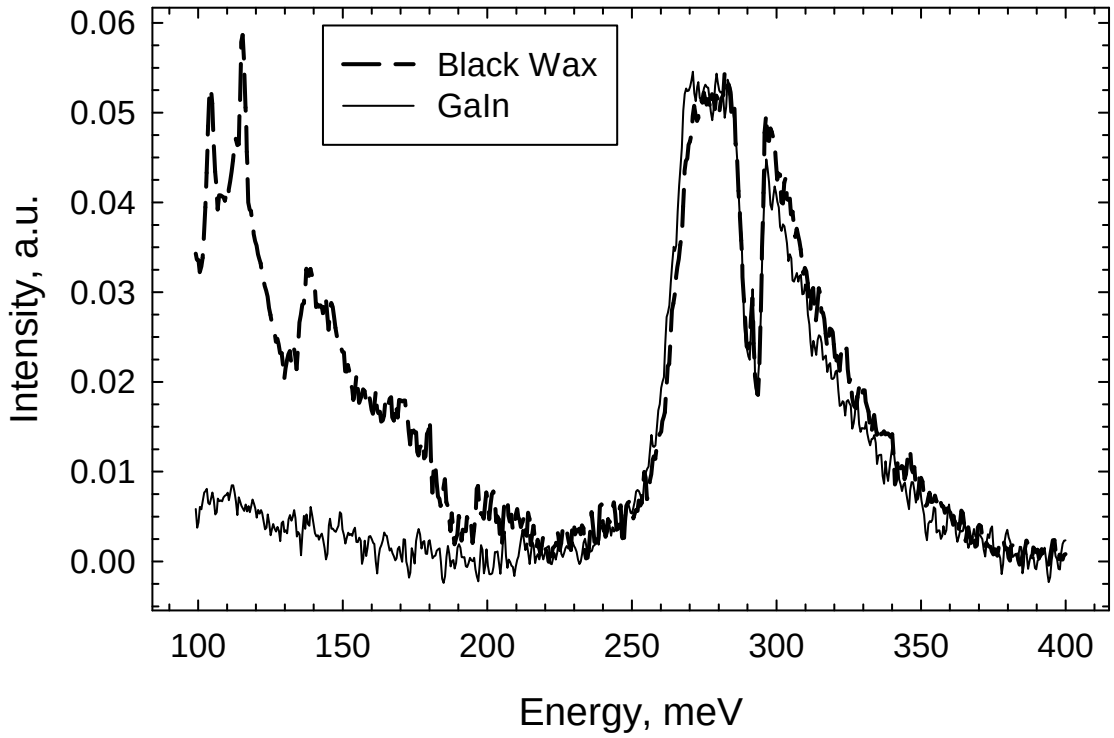

Figure 2-17: Blackbody and PL emission from sample #M048-A mounted with black wax and sample #M048-A1 mounted with eutectic GaIn illustrating the difference in blackbody power for the same PL emission energy.

grease tests begins at a greater level compared the EGaIn/EGaIn film with no optical input and the increase with absorbed optical power, $\Delta P_{BB}(P)$, is greater for both materials. However, the PL measurement is independent of these effects and the LLS analysis of all three mounting techniques resulted in approximately the same calculated energy for no absorbed optical power. The change in PL energy, ΔE_{PL}, for the sample with EGaIn/TG bonding is lower than the sample with EGaIn/EGaIn and indicates thermal grease has a lower TCR. The sample with BW/EGaIn bonding layers had a significantly higher rate of change and more heating.

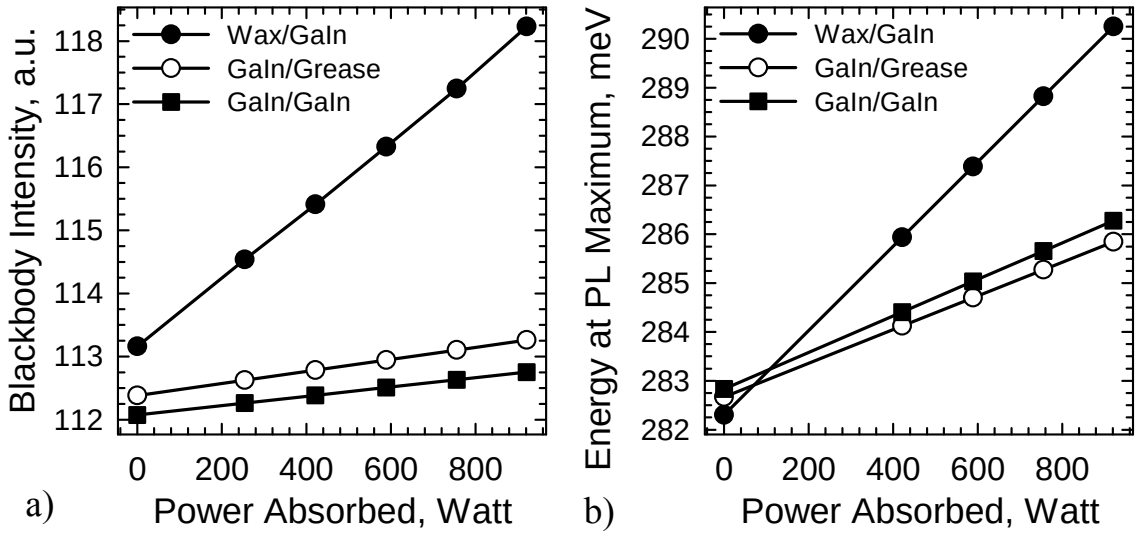

Figure 2-18: Differences in a) the blackbody power and b) the PL shift for increased optical power for thin film #M048 samples mounted with different bonding techniques.

2.5 Comparing Thin Films

The utility of the PL techniques developed is the precise, repeatable data generated enables comparison of different thin film nanostructure designs independent of optical noise and bonding layer TCR. $HE(P)$ can be estimated for all films by assuming $\Delta E_{PL}(T) = \Delta E_g(T) \approx 0.4$ meV/K for PbSe [26] or PbSrSe [27] and changes

linearly at 300 K [28]. However, a more accurate calculation of *HE(P)* for different MBE films with independent material properties requires measurement of $\Delta E_{PL}(T)$ for each sample that is summarized in Table 2-1. The reported measurements of $\Delta E_{PL}(T)$ for PbSrSe/PbSe MQW films vary in different reports: 0.23 meV/K [1], 0.39 meV/K [29], and 0.5 meV/K [30]. Additional experimental data detailed in a later chapter, see Figure 4-8, under similar conditions across a large temperature range has shown that $\Delta E_{PL}(T) \geq 0.42$ meV/K for the MQW films tested. This contradicts the measurements described in this chapter that indicated $\Delta E_{PL}(T) = 0.22\text{-}0.30$ meV/K a value nearly one half that measured on the same samples across a more broad temperature range. This discrepancy can be attributed to a PL signal intensity that falls dramatically at 300 K and therefore the low temperature PL shift data will be used for all calculations. The MQW samples fall into two categories: #M141 is a MQW structure on 1.5 μm PbSe while other films have PbSnSe/PbSe superlattices (SLs) below the optical layers. The SLs consist of more than 300 individual alternating layers of PbSnSe and PbSe.

Table 2-1: Thin film PL peak emission temperature dependence comparison from room temperature down to 90 K.

PbSe Film ID #	**PL Shift: $\Delta E_{PL}(T)$**	**MQW Film ID #**	**PL Shift: $\Delta E_{PL}(T)$**	**PL Shift: $\Delta E_{PL}(T)$**
	300 K ≤ T_{HS} ≤ 330 K		90 K ≤ T_{HS} ≤ 330 K	T_{HS} = 300 K
	μeV/K		μeV/K	μeV/K
M046	0.460	M141	0.433	0.263
M047	0.422	M168	0.430	0.284
M048	0.426	M211	0.405	--
M049	0.452	M212	0.438	--
M199	0.444	M213	0.423	--
		M214	0.407	--

Figure 2-19 shows the shift in PL peak energy for different samples of PbSe with varying thickness listed in Table 2-2. The resulting heating effect values had overlapping error bars but the data does trend linearly with film thickness and has an R^2 = 0.74. Figure 2-20 show the PL data for different MQW samples. The MQW/SL samples with PL emission (#M168 and #M207) show an average 50 % larger blue shift than the MQW/PbSe sample #M141. This is evidence of increased heating in the

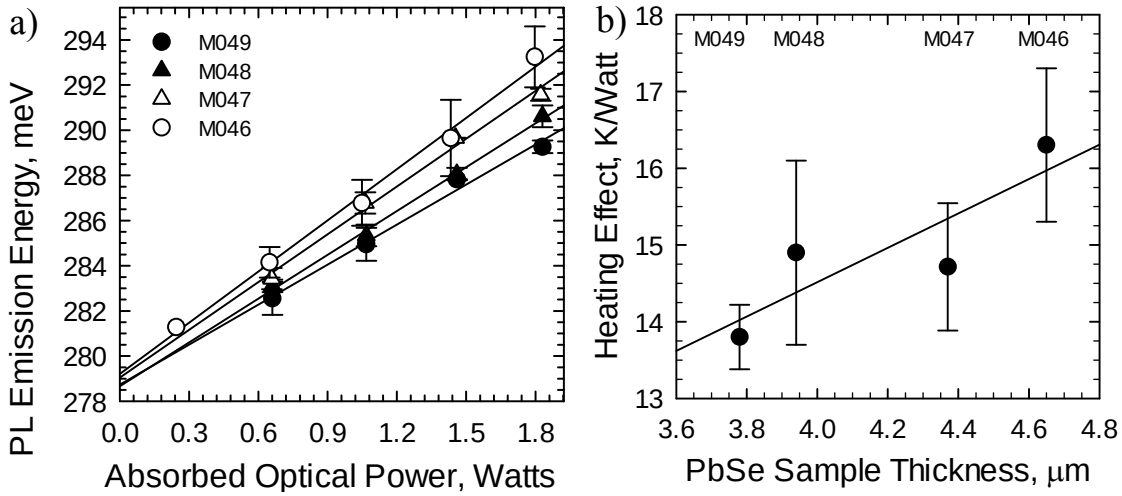

Figure 2-19: PL results for different PbSe samples: a) peak shift for increased absorbed optical power and b) the heating effect for the same data plotted versus film thickness.

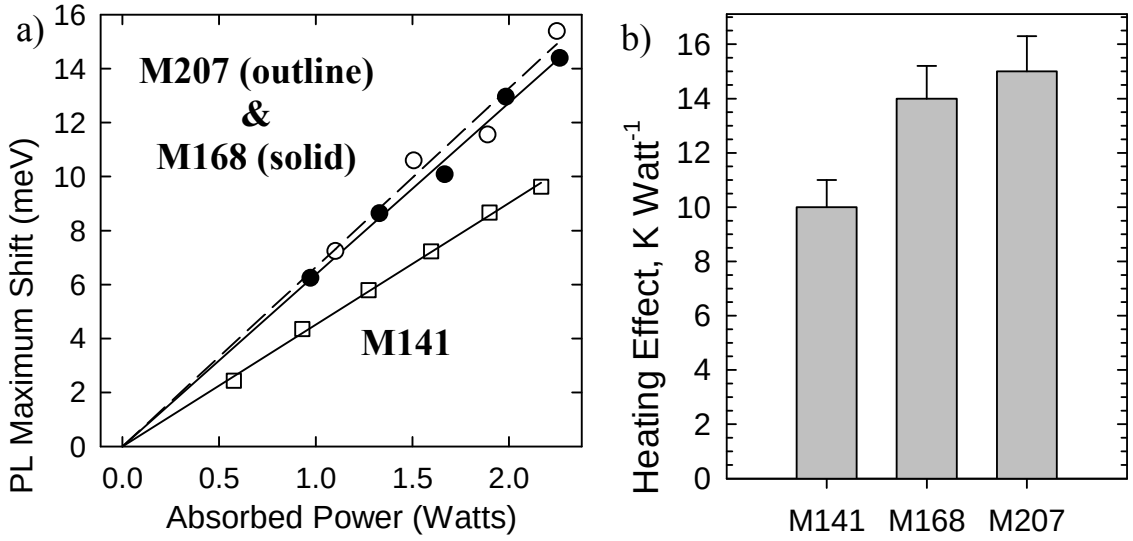

Figure 2-20: PL results for different MQW samples: a) the shift in the PL peak relative to their bandgap energy at 293 K, and b) the heating effect for the same data.

MQW region with PL emission for the samples containing superlattices that is consistent with a lower thermal conductivity for nanostructured materials.

Several thin films tested had little or no photoluminescence at room temperature and could only be compared using blackbody emission. However, this type of film comparison is highly dependent on cavity mode resonances and the reflectivity of surfaces including bonding material as stated previously. The calculation of film thicknesses for samples with periodic structure in their blackbody emission (see Figure 2-9) are summarized in Table 2-2. The SEM images used to assess thickness are contained in Appendix B. The blackbody peak spacing for the three MQW/SL samples are consistent with the entire film thickness. Film #M141, the MQW/PbSe film, showed two peaks ≈ 80 meV apart. This spacing calculates to a film thickness of 1.7 μm that is consistent with the thickness of the PbSe layer.

Table 2-2: Film thickness measurement using analysis of laser stimulated blackbody emission compared to SEM.

Thin Film ID# – Test Sample	Film Type	SEM Measured Thickness (μm)	Blackbody Peak Spacing (meV)	Calculated Thickness (μm)
M046-A	PbSe	4.65	27.5	4.5
M047-A	PbSe	4.37	28.2	4.4
M048-A	PbSe	3.94	30.2	4.1
M049-A	PbSe	3.78	33.6	3.7
M211-R1	MQW	2.85	44.1	2.8
M213-R1	MQW	2.72	38.0	3.3
M214-R1	MQW	3.03	43.8	2.8

The rate that blackbody emission power from a film changed was unique to the optical system and alignment, which was routinely adjusted throughout this research. Figure 2-21 shows a strong correlation, with similar magnitudes, between HE_{PL} and HE_{BB} for the different lasers with different bonding materials on films with both PL

emission and an increase in low energy blackbody emission from optical heating. System #2 (black dots) shows a lower blackbody power increase consistent with use of two layers of EGaIn for bonding and $HE_{BB} = 0.1HE_{PL}$. Table 2-3 shows the PL and blackbody results for six different MQW samples. The raw blackbody data for samples #M211, #M213, and #M214 indicate they heat at a higher rate than the other MQW/SL films with PL emission. However, since these samples were tested several months apart and the optical system alignment was improved the magnitude of this calculation must be adjusted by the change in blackbody power for temperature $\Delta P_{BB}(T)$. This normalization results in a lower temperature calculation for the three samples with no PL measurements and indicates they heat at the same rate as other MQW/SL samples.

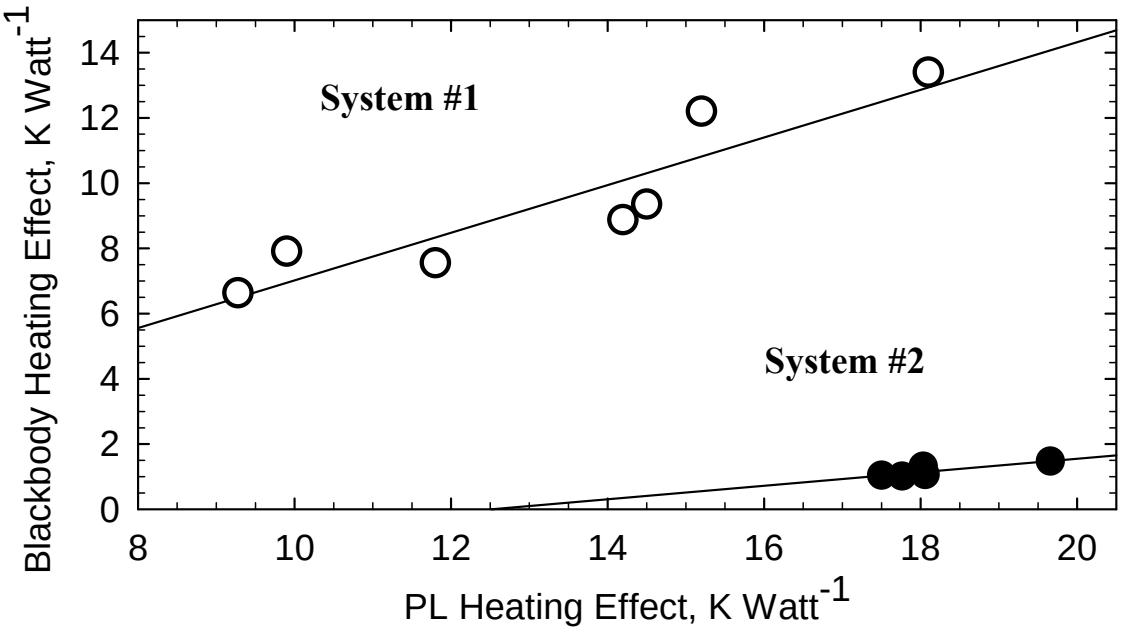

Figure 2-21: Correlation of HE_{BB} and HE_{PL} for multiple films with PL emission and increased on different optical systems.

Table 2-3: Heating effect calculated using blackbody emission on samples with little or no photoluminescence at room temperature.

Film ID #	HE_{PL}	HE_{BB}	$\Delta P_{BB}(293K)$	Equivalent Heating
M141	10.3	0.85	0.88	9.7
M168	14.2	1.77	1.11	15.9
M207	15.0	1.56	1.05	14.9
M211	--	3.47	2.34	14.8
M213	--	3.54	2.15	16.5
M214	--	3.12	2.04	15.3

2.6 Summary and Conclusions

A photoluminescence testing procedure to characterize optically induced heating effects in IV-VI semiconductor thin films was presented and analyzed. Automation through custom software allowed rapid, repeatable tests that emphasized precise control of timing and thermal stabilization using PID controllers. This system was capable of collecting large volumes of data and was used to optimize system design through statistical analysis of thousands of individual tests. The two factors most dramatically affecting system performance were optical alignment and sample bonding material. Two optical system designs were investigated: a laser with an attached cylindrical lens and complex power distribution on the surface of the film resulted in little change in the PL spectrum and heating effect measurement compared to a more highly focused fiber coupled laser pump. However, the optical alignment of both systems was sensitive to variation of the distance between the laser lens and the film. A deviation from the focal length of the fiber-coupled laser of 2 mm was calculated and measured to increase the optical cross-section on the film surface ≈ 80 μm. The thermal and optical properties of

different bonding materials were also investigated. Eutectic Gallium Indium demonstrated a low thermal contact resistance and simple application procedure compared to thermal adhesive and epoxy. However, some time-dependent effects were observed that resulted in increased thermal conductivity of the bonding layer and reduced TCR for the film over a time period greater than 48 hours. In addition EGaIn exhibited a highly reduced blackbody emission signal. This is due to two factors: a lower emissivity compared to other bonding materials and a low transmission factor. This reduced amplitude of low energy radiation during optical characterization increases the signal to noise ratio of the system for the photoluminescence signal.

The performance of this PL system was demonstrated by comparative analysis of thin films fabricated of binary PbSe, with varying thickness, and MQW optical emitters with different sub-layer designs shown in Figure 2-22. Differences in photogenerated carrier confinement between PbSe and MQW films [31] make direct comparison of these film types difficult using the heating effect alone. However, sample #M168 with a thickness of 3 μm heated at a rate of 14.2 K/Watt nearly equal to sample #M047 that was 4.4 μm thick and heated at a rate of 14.7 K/Watt. This result indicates #M168 with a nanostructure superlattice has a lower thermal conductivity. Since the PL emission from single crystal PbSe can occur anywhere in the material based on carrier diffusion and scattering a complex thermal model is needed for comparison to the fixed optically active region in MQW samples. Direct comparison of similar films showed samples #M168 and #M207 with MQW layers fabricated on SLs heated significantly more (50%) compared to MQW layers fabricated on a single layer of PbSe, #M141, under the same test conditions. In addition MQW/SL samples showed

a significantly larger blackbody emission heating effect compared to the MQW/PbSe sample and all other PbSe films. Four PbSe films with thickness difference of ≈ 1 μm exhibited a linear relationship between the calculated heating effect and film thickness. This was verified using measurement of both changes in the photoluminescence spectrum and power changes in the blackbody emission.

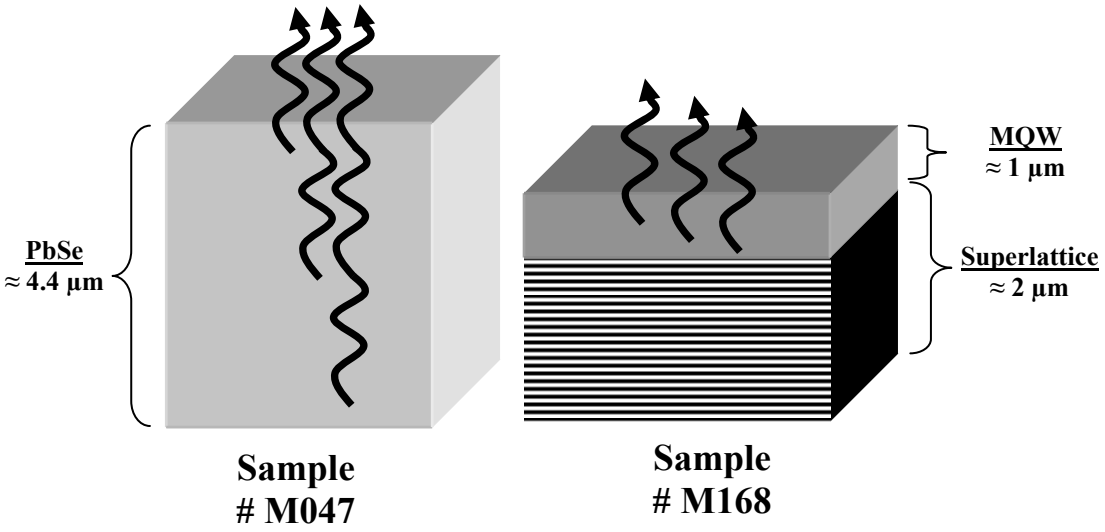

Figure 2-22: Differences in spatial thermometry information provided by PL induced photons in PbSe samples (left) and samples with a 1 μm MQW and 1.5 μm superlattice structures (right).

Chapter 2 References

1. J. D. Jeffers, K. Namjou, Z. Cai, P. J. McCann, and L. Olona, "Cross-plane thermal conductivity of a PbSnSe/PbSe superlattice material", *Appl. Phys. Lett.*, **99**, 41903 (2011)

2. J. O. Dimmock, I. Melngailis, and A. J. Strauss, "Band structure and laser action in $Pb_xSn_{1-x}Te$", *Phys. Rev. Lett.*, **16**(26), pp. 1193-1196 (1966)

3. D. Li, S. Mukherjee, J. Ma, G. Bi, D. Ray, F. Zhao, S. L. Elizondo, G. Yu, and Z. Shi, "Edge-emitting lead salt mid-infrared laser structure on BaF_2 (110) substrate", *J. of Elec. Materials*, **38**(9), pp. 1952-1955 (2009)

4. F. Schwarzl, E. Kaufmann, G. Springholz, K. Koike, T. Hotei, M. Yano, and W. Heiss, "Temperature-dependent midinfrared photoluminescence of epitaxial PbTe/CdTe quantum dots and calculation of the corresponding transition energy", *Phys. Rev. B*, **78**, 165320 (2008)

5. L. A. Elizondo, Y. Li, A. Sow, R. Kamana, H. Z. Wu, S. Mukherjee, F. Zhao, Z. Shi, and P. J. McCann, "Optically pumped mid-infrared light emitter on silicon", *J. Appl. Phys.*, **101**, 104504 (2007)

6. P. J. McCann, K. Namjou, and X. M. Fang, "Above-room temperature continuous-wave mid-infrared photoluminescence from PbSe/PbSrSe quantum wells", *Appl. Phys. Lett.*, **75**(23), pp. 3608-3610 (1999)

7. W. Z. Shen, H. F. Fang, L. F. Jiang, K. Wang, G. Yu, H. Z. Wu, and P. J. McCann, "Band gaps, effective masses and refractive indices of PbSrSe thin films: Key properties for mid-infrared optoelectronic device applications", *J. Appl. Phys.*, **91**(1), pp. 192-198 (2002)

8. H. J. Lian, A. yang, M. L. W. Thewalt, R. Lauk, and M. Cardona, "Effects of sulfur isotopic composition on the bandgap of PbS", *Phys. Rev. B*, **73**, 233202, pp. 1-4 (2006)

9. D. W. McAlister, P. J. McCann, K. Namjou, X. M. Fang, O. Alkhouli, and H. Z. Wu, "Mid-infrared photoluminescence from IV-VI semiconductors grown on silicon", *J. Appl. Phys.*, **89**(6), pp. 3514-3516 (2001)

10. P. J. McCann, P. Kamat, Y. Li. A. Sow, H. Z. Wu, G. Belenky, L. Shterengas, J. G. Kim, and R. Martinelli, "Optical pumping of IV-VI semiconductor multiple quantum well materials using a GaSb-based laser with emission at $\lambda = 2.5$ μm", *J. Appl. Phys.*, **97**, 053103 (2005)

11. A. Jain and K. E. Goodson, "Measurement of the Thermal Conductivity and Heat Capacity of Freestanding Shape Memory Thins Films Using the 3ω Method", *ASME J. Heat Transfer*, **130**, 102402 (2008)

12. Q. Li, C. Liu, X. Wang, and S. Fan, "Measuring the thermal conductivity of individual carbon nanotubes by the Raman shift method", *Nanotechnology*, **20**, 145702 (2009)

13. C. A. Paddock and G. L. Eesley, "Transient Thermoreflectance from Thin Metal Films", *J. Appl. Phys.*, **60**, pp. 285-290, (1986)

14. D. K. Kochhar, *Active Cooling and Thermal Management of Semiconductor Devices and Materials*, Master's Thesis, University of Oklahoma (2011)

15. M. D. Dickey, R. C. Chiechi, R. J. Larsen, E. A. Weiss, D. A. Weitz, and G. M. Whitesides, "Eutectic Gallium-Indium (EGaIn): a liquid metal alloy for the

formation of stable structures in microchannels at room temperature", *Adv. Functional Mater.*, **18**, pp. 1097-1104 (2008)

16. *Gallium Indium Eutectic MSDS*, Alfa Aesar, Inc, www.alfa.com

17. *LabVIEW 7.0 User's Manual*, National Instruments, Austin, TX (2001)

18. J. Jeffers, C. Roller, K. Namjou, M. A. Evans, L. McSpadden, J. Grego, and P. J. McCann, "Real-time diode laser measurements of vapor phase benzene", *Analytical Chem.*, **76**(2), pp. 424-432 (2003)

19. A. Fried, B. P. Wert, B. Henry, and J. R. Drummond, "Airborne tunable diode laser measurements of formaldehyde", *Spectrochimica Acta A*, **55**, pp. 2097-2110 (1999)

20. A. Fried, S. Sewell, B. Henry, B. P. Wert, T. Gilpin, and J. R. Drummond, "Tunable diode laser absorption spectrometer for ground-based measurements of formaldehyde", *J. Geophysical Res.*, **102**(D5), pp. 6253-6266 (1997)

21. A. Fried, B. Henry, and J. R. Drummond, "Tunable diode laser ratio measurements of atmospheric constituents by employing dual fitting analysis and jump scanning," *Appl. Opt.*, **32**(6), pp. 821-827 (1993).

22. R. Rupprecht and H. Pascer, "Interpretation of magnetophotoluminescence spectra of narrow-gap IV-VI semiconductors", *Phys. Rev. B*, **50**(23), pp. 931-942 (1994)

23. P. Kumat, C. Roller, K. Namjou, J. D. Jeffers, A. Faramarzalian, R. Salas, and P. J. McCann, "Measurement of acetaldehyde in exhaled breath using a laser absorption spectrometer", *Appl. Opt.*, **46**, pp. 3969-3975 (2007)

24. B. Giese and M. Mocker, "Carrier heating in lead chalcogenides", *Physica Status Solida B*, **123**(755), pp. 755-782 (1984)

25. F. Geist, W. Herbst, C. Mejia-Garcia, H. Pascher, R. Rupprecht, Y. Ueta, G. Springholz, G. Bauer, and M. Tacke, "Magneto-optical investigations of Eu-based diluted magnetic chalcogenides", *Phys. Rev. B*, **56**(20), pp. 56-67 (1997)

26. K. Lischka, "Bound defect states in IV-VI semiconductors", *Appl. Phys. A*, **29**, pp. 177-189 (1982)

27. A. Majumdar, H. Z. Xu, F. Zhao, J. C. Keay, L. Jayasinghe, S. Khosravani, X. Lu, V. Kelkar, and Z. Shi, "Bandgap energies and refractive indices of $Pb_{1-x}Sr_xSe$", *J. Appl. Phys.*, **95**(3), pp. 939-942 (2004)

28. R. Dalven, "*f*-Sum rule analysis of the band edges in PbS, PbSe, and PbTe", *Phys. Rev. Lett.*, **24**(18), pp. 1015-1017 (1970)

29. H. Z. Wu, N. Dai, M. B. Johnson, P. J. McCann, and Z. S. Shi, "Unambiguous observation of subband transitions from longitudinal valley and oblique valleys in IV-VI multiple quantum wells", *Appl. Phys. Lett.*, **78**(15), pp. 2199-220 (2001)

30. F. Zhao, X. Lv, A. Majumdar, and Z. Shi, "Influence of mounting on continuous-wave photoluminescence from midinfrared PbSrSe/PbSe multiple quantum wells", *Appl. Phys. Lett.*, **84**(8), pp. 1251-1253 (2004)

31. G. Allan and C. Delerue, "Confinement in PbSe quantum wells and nanocrystals", *Phys. Rev. B*, **70**, 245321 (2004)

Chapter 3

Photoluminescence Thermal Analysis

3.1 Motivation

Historical interest in IV-VI semiconductor materials was spurred by applications in mid-infrared opto-electronics [1-4]. PbSe, with direct bandgap energy (E_g) minima along the [111] crystal direction (L-point) as shown in Figure 3-1 a), has been investigated as a room-temperature mid-IR detector. Laboratory measurements of the absorption coefficient, $\alpha(E=h\nu)$, have shown contributions from incident photon resonance with other direct interband transitions, label E_2, and a lower energy transition E_1. However, unlike other material systems, demonstration of room-temperature lasing in IV-VI semiconductors has proven difficult to achieve due to several factors including a relatively low thermal conductivity, $k_{PbSe}(300\text{ K}) \approx 2$ Watts meter^{-1} Kelvin^{-1}. This has

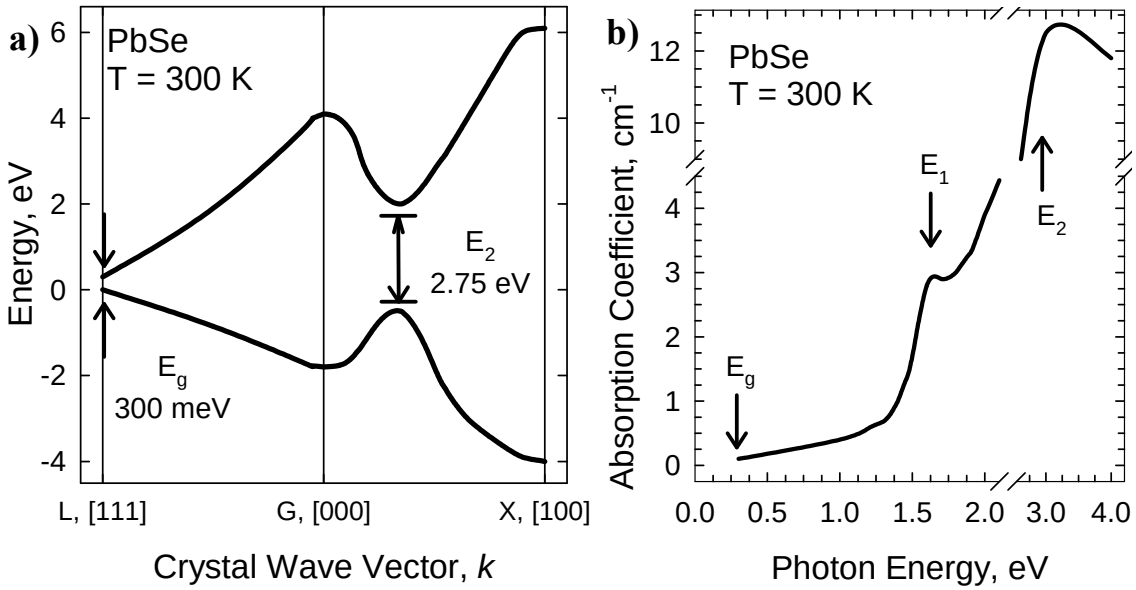

Figure 3-1: PbSe energy dispersion a) and absorption coefficient b) at 300 K adapted from multiple sources notably [1, 3, and 18].

resulted in attempts to decrease the temperature in the optically active material through advanced film bonding techniques [5] and nanostructures including multiple quantum wells (MQWs) and quantum dots (QDs) [6-7] that affect excited electron lifetimes.

This intrinsically low thermal conductivity has lead to more recent experimental and theoretical investigations of IV-VI semiconductor thermoelectric (TE) properties, particularly at high temperature [8-10]. TE material efficiency is defined by the thermoelectric figure of merit, $ZT = T\sigma S^2/k$. Embedded colloidal Pb nanoparticles [11] in PbTe were shown to reduce thermal conductivity (increasing ZT) up to 20% with both the particle density and particle size controlling the magnitude of the effect. Other research has shown that PbTe superlattices (SLs) also reduce thermal conductivity with the magnitude determined by layer thickness [12].

Experiments to investigate these materials are routinely performed with non-contact optical techniques such as photoluminescence (PL). PL characterization has been used to observe MQW band splitting [13], carrier relaxation rates [14], and more recently used to assess thin film thermal conductivity [15]. The first step in extraction of this information is analysis of complex PL emission spectra with curve fitting to determine slight changes in wavelength related to temperature increases, ΔT. The second step is the use of finite element analysis of steady state heat transfer to solve Fourier's law of thermodynamics. This chapter outlines the data analysis techniques used to interpret the PL emission of PbSe thin films and MQW samples. A thermal heat transport model is presented and evaluated using a unique experiment to control optical power density. The data is then used to calculate differences in the cross-plane thermal conductivity of samples with different nanostructure designs.

3.2 Optical Heating in Photoluminescence

Near infrared laser stimulated photoluminescence in PbSe thin films is the absorption of photons at higher energy leading to the subsequent re-emission of photons at a lower energy through a multi-step process governed by the quantum probabilistic theory on a large number of photons. The first step of the process is absorption of laser photons with energy, $E_{h\nu} \geq E_g$. These photons have a probability of being absorbed within a given distance of material below the surface by imparting their energy to an exciton or electron-hole pair (EHP). The Beer-Lambert law states the optical intensity, I, at a distance, d, into a solid is given by the relation $I = I_0 e^{-\alpha d}$ where I_0 is the initial intensity. Figure 3-2 shows the function $1-(I/I_0)$ calculated for different absorption coefficients. *Suzuki et al* [18] measured $\alpha_{PbSe}(1.4\ eV) \approx 10^5$ cm^{-1} at 300 K using spectroscopic ellipsometry that is similar to that reported by several other groups [19-20]. This translates to 37 % of 1.4 eV optical photons, not reflected at the surface

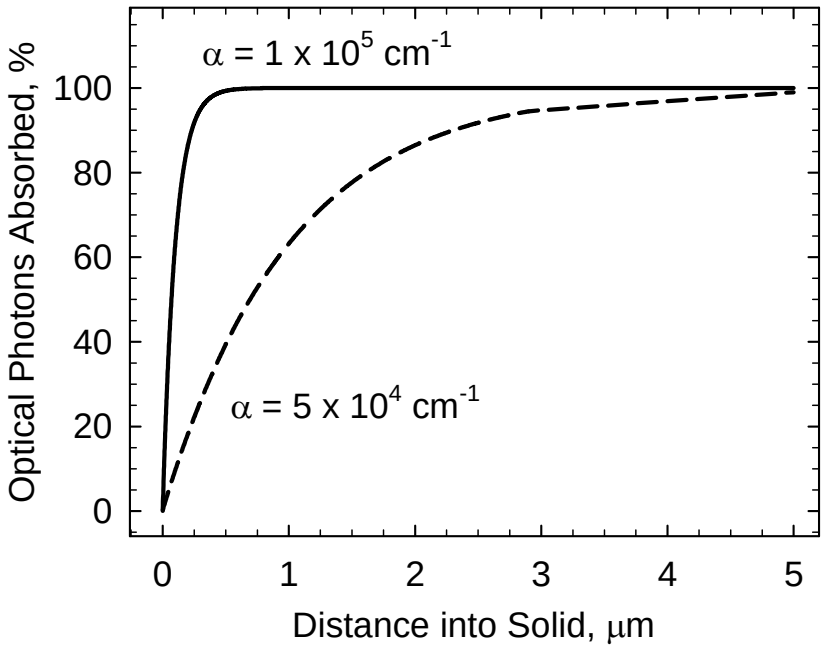

Figure 3-2: Percentage of optical photons absorbed as a function of distance into a PbSe solid crystal for two values of absorption coefficient.

of PbSe, being absorbed within 100 nm of material and an additional 35% being absorbed in the next 200 nm. An absorption coefficient half that value would lead to 50% of the photons penetrating material more than 1 μm below the surface.

The initial optical power density, and therefore optical heating, in PL testing is controlled by the external optics and the magnitude of the photonic flux (or irradiance), $\Phi(x,y)$, incident on the thin film surface as shown in Sec. 2.2.1. The minimum diameter that a circularly distributed coherent beam can be focused to on a perpendicular plane can be calculated using Eq. 3.1 for both an ideal lens and with a real world approximation [16]. For the PL system used in this research, the pump laser beam

$$d_{IdealMin} \geq \frac{2\lambda}{\pi}\frac{f_l}{d_{beam}} \Rightarrow d_{LensMin} \approx \frac{16\lambda f_l}{d_{beam}} \qquad \textbf{(3.1)}$$

emitted photons with a wavelength λ = 875 nm, that exited a fiber collimator with d_{beam} = 2 mm and were focused by a lens with focal length, f_l = 50.8 mm, that resulted in d_{min} ≈ 618 μm. Within the area of the film surface outlined by a circle of this diameter the power distribution can be approximated by a 2D Gaussian function that has a maximum amplitude that is inversely proportional to a directional spread factor, $\sigma_{x,y}$. This function is combined with the derivative of the Beer-Lambert law [17] to form the optical exciton generation rate, Eq. 3.2, in the volume of material beneath the laser illuminated surface. The magnitude is scaled by a variable, P_{abs}, related to the total optical power of the PL pump laser absorbed that can be converted to a photon density through Plank's constant where 1 Watt of 1.41 eV photons corresponds to 4.4 x 10^{18} photons per second. Therefore the theoretical maximum exciton generation rate for PL system used with P_{abs} = 2.5 W and $\sigma_x = \sigma_x$ = 23 μm is g_{ehp} = 8.8 x 10^{30} $cm^{-3}sec^{-1}$. The PL experiments examined with thermal modeling in later sections require the average and maximum

Table 3-1: Maximum and average irradiance for PL testing with different optical focusing diameters on the film surface.

d_{Lens}, µm	Area, 10^{-2} cm^2	Φ_{Avg}, 10^5 W/cm^2	Φ_{Avg}, photons sec^{-1} cm^{-2}	Φ_{Max}, 10^9 W/cm^2	Φ_{Max}, photons sec^{-1} cm^{-2}
2000	3.14	3.18	1.4×10^{24}	6.38	2.8×10^{28}
1500	1.76	5.66	2.5×10^{24}	11.3	5.0×10^{28}
1000	0.785	12.7	5.6×10^{24}	25.5	1.1×10^{29}
750	0.441	22.6	9.9×10^{24}	45.2	2.0×10^{29}
500	0.196	51.0	2.2×10^{25}	102	4.5×10^{29}
400	0.126	79.6	3.5×10^{25}	159	7.0×10^{29}
250	0.049	204	9.0×10^{25}	408	1.8×10^{30}
200	0.031	318	1.4×10^{26}	637	2.8×10^{30}
180	0.025	393	1.7×10^{26}	786	3.5×10^{30}

irradiance to be calculated for 1 W of optical power and various lens focal diameters greater than the minimum, Table 3-1. In addition the steady state carrier change, $\Delta n \equiv g_{ehp}\tau$, must remain below 6 x 10^{26} cm^{-3} or "band-filling effects" have been observed as

$$g_{ehp} \equiv \phi_{xy} \frac{dI}{dz} = P_{abs} \frac{\alpha}{2\pi\sigma_x\sigma_y} e^{-(x/\sigma_x)^2} e^{-(y/\sigma_y)^2} e^{-\alpha z}, cm^{-3}sec^{-1} \quad \textbf{(3.2)}$$

PL emission from the higher energy non-degenerate L- valleys in PbSe/PbSrSe MQW films [7]. Since $\tau << 10^{-4}$ this PL set-up will only generate emission from lowest confined energy levels in the MQW films tested.

Once a pump laser photon is absorbed and an exciton created, the second part of the PL process begins. This quasi-particle has two weakly bound components (*e* for electron and *h* for the "hole" or vacancy created) with different mobility, $\mu_{e,h}$, that will diffuse throughout the crystal lattice. Stimulated particle diffusion occurs over a finite lifetime, $\tau_{e,h}$, before inelastic scattering events lead to recombination. A statistical average of the distance an exciton travels prior to recombination, called the diffusion

length, can be defined using these two material properties, $\Lambda^2 \equiv \tau_e \mu_e (kT/q)$. Figure 3-3 graphically depicts the loss of exciton energy to entropy or heat, commonly referred to as relaxation, involves the creation and annihilation of phonons with energy, $E = \hbar\omega$. The phonons created during scattering events will also diffuse and transport energy further from the film surface. However, this distance $\Lambda_{Ph} \leq 10$ nm [1] is insignificant compared to the distance photons travel or excitons diffuse and can be ignored.

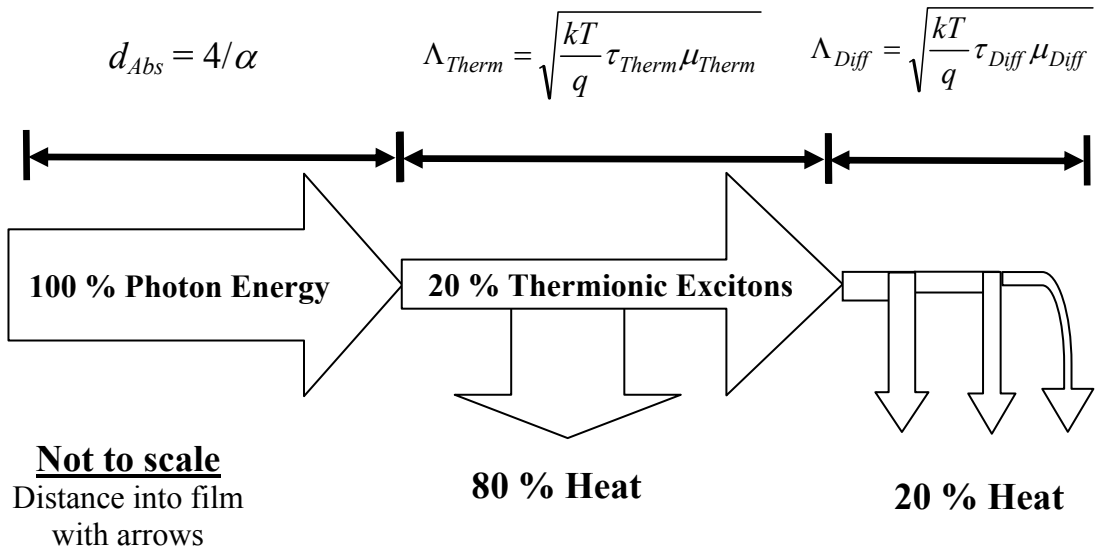

Figure 3-3: Energy transport model beneath the surface of a thin film during PL indicating heat generation.

Excitons with energy greater than the bandgap energy have two distinct time scales for recombination. Thermalization of "hot" carriers, with energy greater than the energy band minima, is a significant limit to the efficiency of photovoltaic power generation [21]. Energy is transferred on the order of $\tau_{Therm} \approx 10^{-15}$ seconds (femtoseconds, fs) through the Auger mechanism, phonon interaction, or generation of a second exciton with each process occurring at an independent rate. Mathiessen's rule is used to calculate the average particle lifetime, Eq. 3.3. Thermalization processes occur in less than 50 femtoseconds in colloidal PbSe [22]. Nanostructures such as PbSe

quantum dots have been demonstrated that increased this lifetime to τ_{Therm} = 250 fs [23]. Using a mobility value of 500 $cm^2V^{-1}sec^{-1}$ for PbSe results in Λ_{Therm} = 1.3 nm << d_{abs}. The thermalization of 1.4 eV excitons in PbSe, *Eg(300 K)* ≈ 300 meV, constitutes approximately 80% of all non-radiative recombination. A second, slower rate of

$$\tau_{Total}^{-1}(\omega) = \frac{1}{\tau_{ph}} + \frac{1}{\tau_{Aug}} + \frac{1}{\tau_{el}} + \cdots + \frac{1}{\tau_{n}}, \quad second^{-1} \tag{3.3}$$

recombination occurs when exciton energy is reduced to the bandgap energy. The creation of a PL photon through radiative recombination occurs during this time period and is the only mechanism that does not convert exciton energy to heat. A band-edge carrier lifetime in PbSe of 0.1 μs at 300 K would correspond to Λ_{Diff} = 2.00 μm. The carrier lifetime in bulk material increases in MQW structures that suppress Auger recombination but add an additional alloy scattering between layers with a band-edge difference [24]. Therefore the 20 % of optical energy absorbed during PL testing that is not converted to heat during thermalization in the first 500 nm of material may become heat up to several microns further below the film surface.

3.3 Spectral Analysis Procedures

Determining the heating effect calculated from the blue-shift in PL spectra can be facilitated by novel analysis techniques. Figure 3-4 shows the visual code segment used to define a mathematical function and perform emission curve fitting using LabVIEW 2010 (National Instruments) programming software [25]. The complexity of luminescence spectra has been investigated for several material systems [26], stimulation techniques [27], and nanostructures [28]. This analysis technique uses *a priori* knowledge of the quantum output function to fit emission spectra and reduce the

effects of optical noise. Non-linear curve fitting was done with an iterative Levenberg-Marquardt algorithm. This function returns the residue, or weighted mean squared error, as a judgment of good fit. The algorithm was terminated after either 10,000 iterations or a residue of 10^{-10} was reached. The most complex analysis techniques using 250 data points completed in two minutes for a single film test.

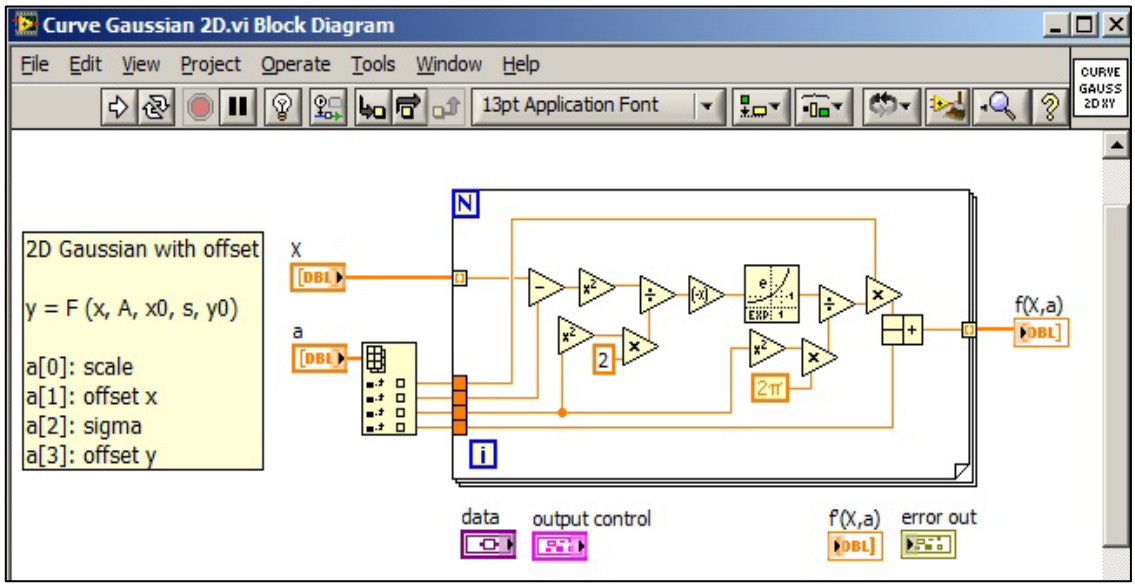

Figure 3-4: Analysis code for curve fitting of PL spectra using the LabVIEW visual programming interface.

3.3.1 Data Processing

The raw spectral data acquired from the FTIR is processed in four steps. The first two steps were performed by the acquisition software: wavelength data channel time-averaging and background subtraction shown in Figure 3-5. The third step was digital post processing of additional background blackbody signal with a filter applied to remove high frequency noise. The filter was implemented as an 8^{th} order infinite impulse response (IIR) using cascaded 4^{th} order tap coefficients. The filter values were calculated using a "smoothing" design to minimize group delay and data shifting. To

further reduce any altering of energy peak shape calculations were completed as a zero-phase filter. This type of filter is implemented in two stages: first the data points are filtered in the acquired order generating an intermediate result that is filtered in reverse order to generate the final output.

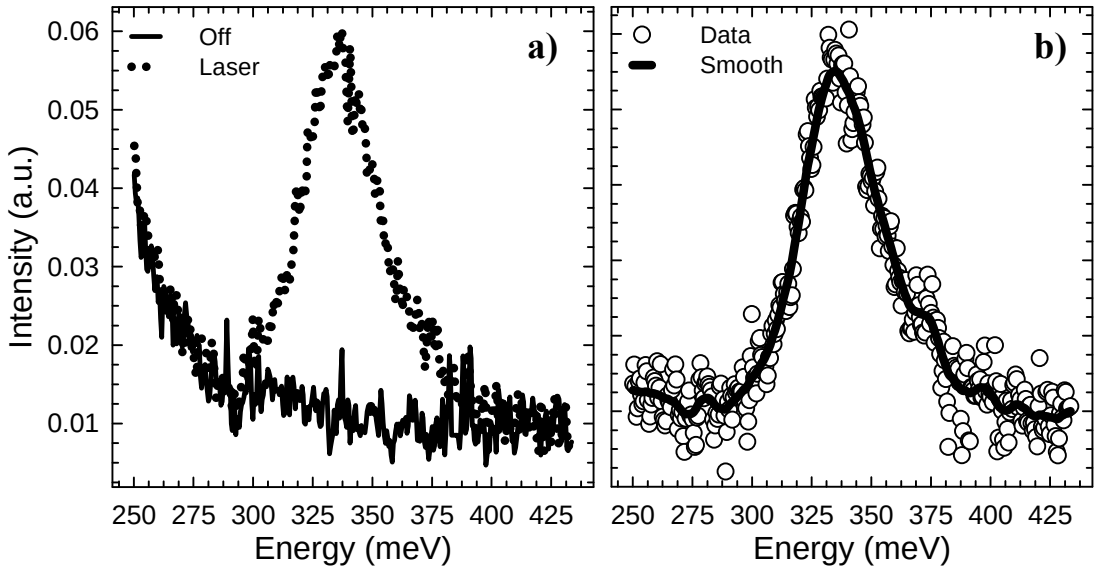

Figure 3-5: a) PL emission spectra from film #M141 at 292 K and b) the data with signal processing to remove blackbody signal and high frequency noise.

The fourth step of data processing, essential in the evaluation of PbSe PL emission near 300 K, was removal of optical artifacts including molecular absorption. The CO_2 absorption band near 280-295 meV is commonly observed in PL data but only noted, Figure 3-6. The data in this spectral region of interest can be reconstructed using the absorption coefficients reported in the HITRAN database [29] and Beer's Law as previously discussed. Individual absorption line intensities on the magnitude of 1×10^{19} cm^{-1} at 293 meV and 6×10^{18} at 290 meV have been measured. Accounting for effects in Doppler line broadening, assuming an ambient CO_2 concentration of 350 parts per million, and with a path length of 20 cm the maximum absorption should be approximately 80 % on the high energy lobe and 67 % on the low energy side with the

minimum absorption of 40% signal intensity at 292.5 meV. After peak reconstruction another smoothing filter was applied to the data.

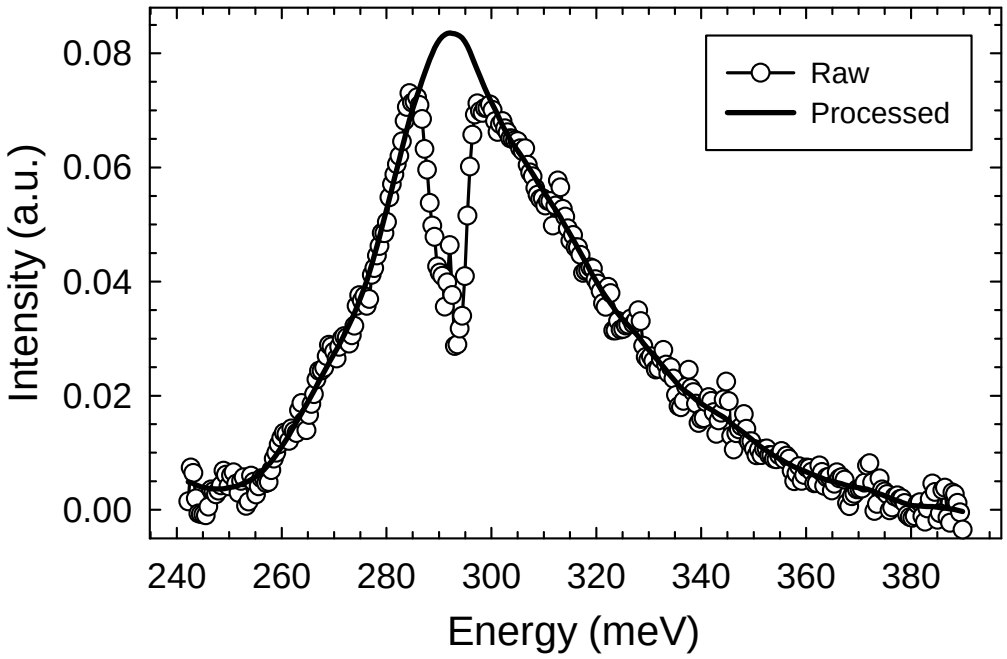

Figure 3-6: Reconstructed PL emission data from sample #M046 at 302 K affected by CO_2 absorption.

3.3.2 PL Peak Emission Shape

PL emission occurs in a volume of material with a three dimensional temperature/exciton distribution and the measured spectra are a superposition (or envelope) of this information. If each portion of the PL volume contributed to the measured PL signal as shown in Figure 3-7, then the spectral intensity would represent a histogram of energy with $Eg \propto T$. The spectrum energy of maximum intensity would represent the statistical mode of material temperature with an asymmetric distribution. Emission intensity at the highest energy (temperature) may be reduced compared to lower energies because of a shorter total carrier lifetime due to increased Auger recombination. However, probability that emission from material deeper within the

film reaches the surface is reduced due to factors such as below bandgap absorption and an exponentially decreasing carrier population. Similarly complicated spectra in mass spectroscopy [30] and the magneto-luminescence of PbSe [27] have been analyzed with the exponentially modified Gaussian (EMG) function, Eq. 3.4. The PL intensity at a given energy, $I(E)$, is a function of a scaling factor I_0, an exponential modification with time constant τ, and a Gaussian function defined by σ. The value E_c represents the

$$I(E) = I_0 \frac{1}{\tau} \exp\left[\frac{1}{2}\left(\frac{\sigma}{\tau}\right)^2 - \frac{E - E_c}{\tau}\right] \int_{-\infty}^{z} \frac{1}{\sqrt{2\pi}} \exp\left(-\frac{u^2}{2}\right) du \qquad \textbf{(3.4)}$$

function centroid and provides for a shift in energy. The integral in Eq. 3.5, does not have a simple solution due to an infinite lower limit with the upper limit $z = (E-E_c)/\sigma - \sigma/\tau$. However, it has been shown to be equal to the error function (*erf*), Eq. 3.6. A finite lower limit of integration means this function can be solved numerically and is included as a table look-up function in numerical calculation programs including LabVIEW. The PL emission fit of a MQW thin film using a Gaussian function and an EMG function is shown in Figure 3-8. The residual error was 1 x 10^{-5} and 1 x 10^{-6} respectively and

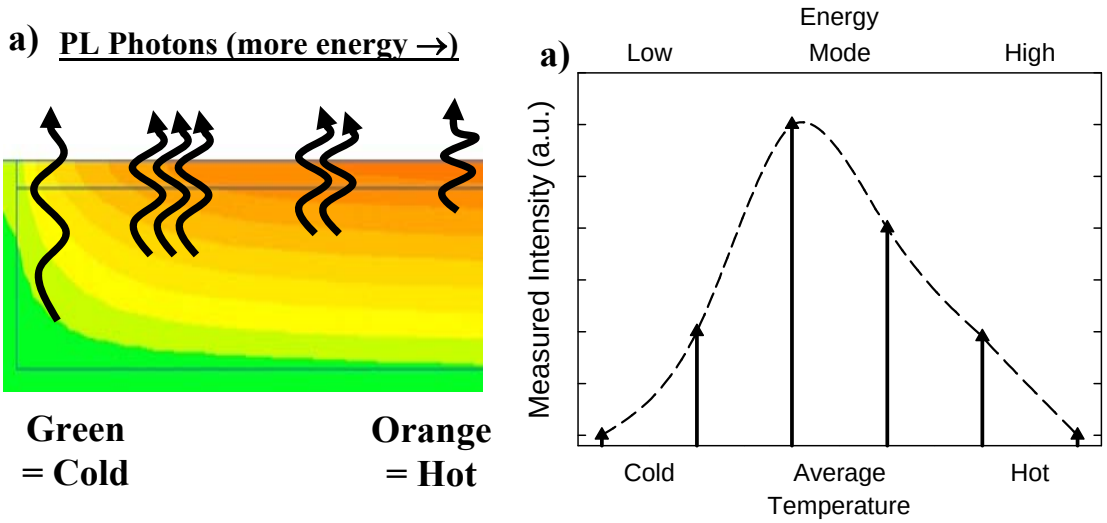

Figure 3-7: Differential volume model of PL emission (left) with associated intensity histogram (right).

increased linearly with emission amplitude indicating neither fit function to be ideal. The use of three independent Gaussian functions as single "peak" fit, taking advantage

$$\int_{-\infty}^{z} \frac{1}{\sqrt{2\pi}} \exp\left(-\frac{u^2}{2}\right) du = \frac{1}{2} + \frac{1}{2} erf\left(\frac{z}{\sqrt{2}}\right) \tag{3.5}$$

of Fourier's Theorem, reduced the residual fit error to 1 x 10^{-7}. This error was independent of emission amplitude and represented the minimum fit error achievable. The magnified peak intensity graph shows the significant advantages of the EMG fit

$$erf(z) = \frac{2}{\sqrt{\pi}} \int_{0}^{z} \exp\left(-u^2\right) du \tag{3.6}$$

(dashed line) in filtering the data feature maximum at 309 meV to a calculated value of 315 meV. The Gaussian fit (dotted line) shows a much lower intensity with a maximum at 318 meV. The EMG fit clearly represents the asymmetric emission data more accurately and the residue of fits to emission data without CO_2 reconstruction was two orders of magnitude lower than a single Gaussian peak.

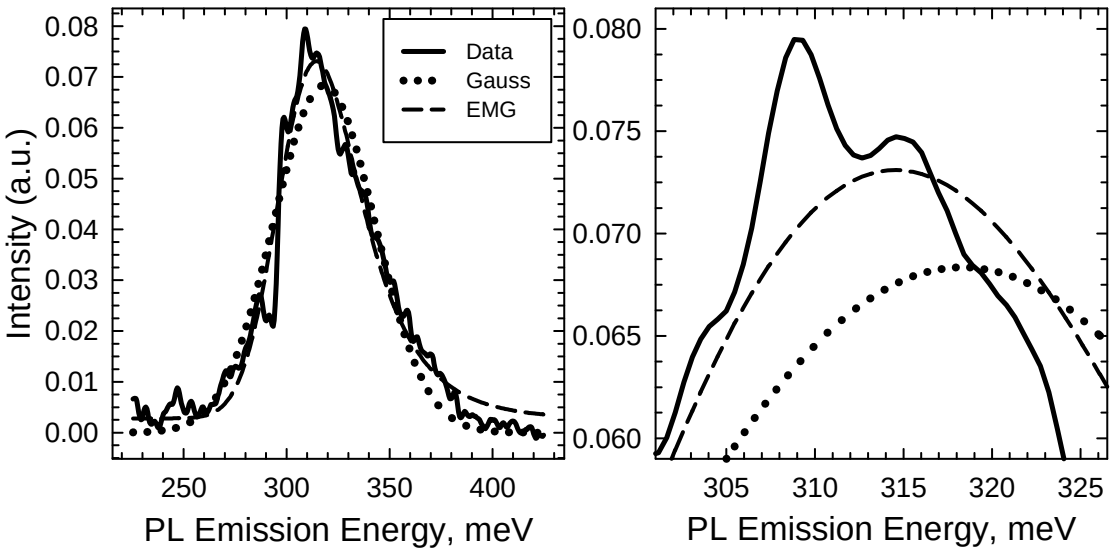

Figure 3-8: Comparison of multiple Gaussian peak fits and exponentially modified Gaussian function on MQW PL emission.

3.4 Thermal Modeling

Thin film thermal conductivity can be calculated from the measured temperature increases associated with PL optical pump density through thermal modeling [15]. For this research calculations were completed with finite element (FE) analysis software (Tera Analysis, Toronto, Canada model Quickfield Ver. 5.0). This program creates a periodically spaced mesh of nodes within an accurately scaled film model, Figure 3-9, to solve the continuous heat conduction problem using a single fixed boundary condition, the heatsink temperature (T_{HS}) of the film being tested, and a given amount of thermal energy, $Q(x,y,z)$, generated within the model. The FE software used this information to calculate the temperature, $T(x,y,z)$, of each node (shown as an intersection of green lines) with the temperature of neighboring nodes connected by the mesh lines serving as additional boundary conditions. The software begins with initial guesses for the temperature of each node and then recursively evaluates the phenomenological solution of Fourier's law for thermodynamics, $\nabla(k \bullet \nabla T) = -Q$, until the fit error of the model temperature reaches an acceptable value similar to the process of one-dimensional PL spectra fitting routines described in the previous section.

The complete FE model shown in Figure 3-9 is 5 mm thick with the IV-VI semiconductor film being divided into several regions as listed: 1) heat is generated near the surface, 2) optically active material shown as a single block in red is beneath this, and 3) the remaining film is referred to as the test layer. Additional model layers include a silicon substrate (k_{Si} = 141 $Wm^{-1}K^{-1}$), a eutectic Gallium Indium (k_{EGaIn} = 40 $Wm^{-1}K^{-1}$) bonding material, and copper (k_{CU} = 393 $Wm^{-1}K^{-1}$) sub-mount between the film surface and an edge of the model at a constant, known temperature equal to the

heatsink setting. The mean temperature of material in the model is calculated within the FE software by averaging the temperature of each node within a specifically outlined volume (i.e. the optically active region). For the PbSe films tested the spatial limits of this region are determined by both the absorption depth and band-edge carrier diffusion. However, the MQW films tested were specifically designed for these experiments to create carrier confinement with an extended PbSrSe barrier layer 140 nm thick below the last PbSe well layer (10 nm). This spatially confines excitons and limits PL emission to a fixed depth below the surface of the film. In order to investigate these properties several *ab initio* calculations were made using multiple thin film models with different heat power distributions and dimensional definitions. Figure 3-10 shows the

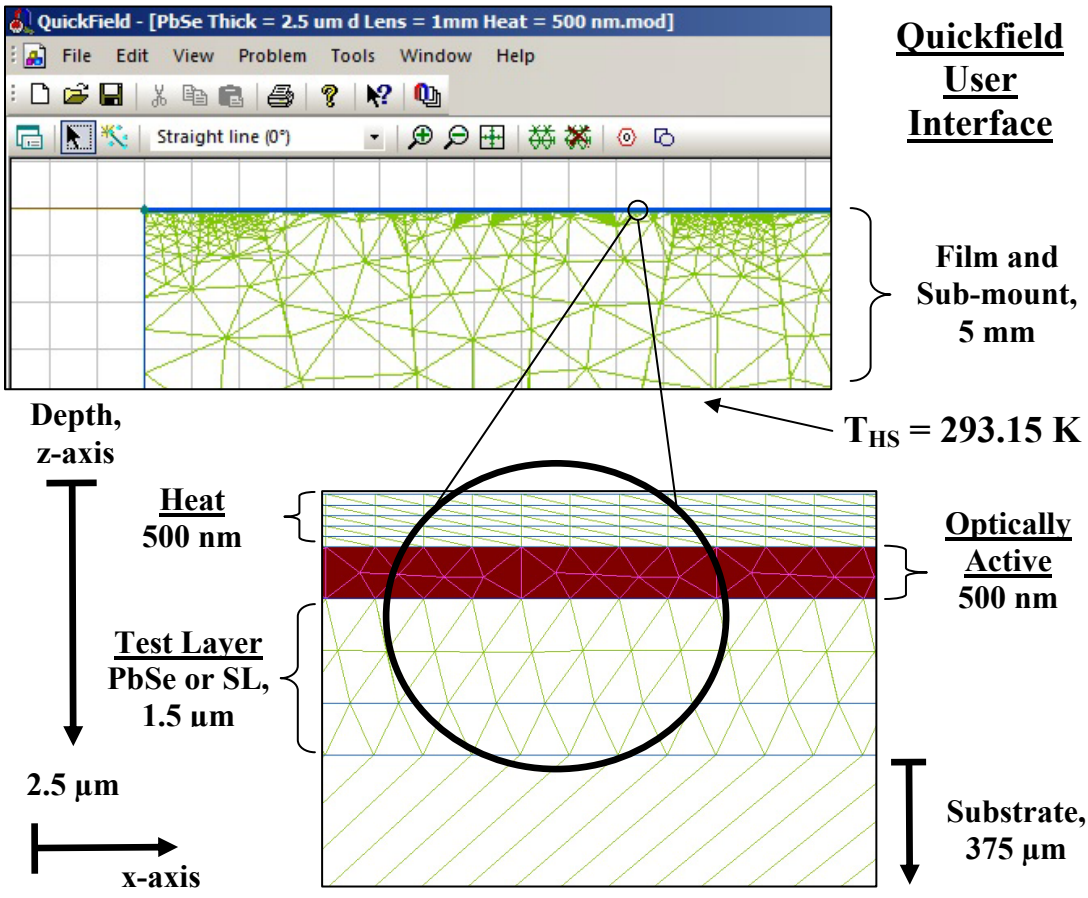

Figure 3-9: Thin film FE software thermal model with node mesh.

FE results as a color map indicating temperature (minimum: blue = 293.15 K and maximum: red = 306 K) with isotherms plotted in black every 0.5 K. The model heat source was 800 µm wide on the film surface and 200 nm below. The average temperature in this same volume of material was 302 K or 8.46 K greater than the heatsink temperature of 293.15 K.

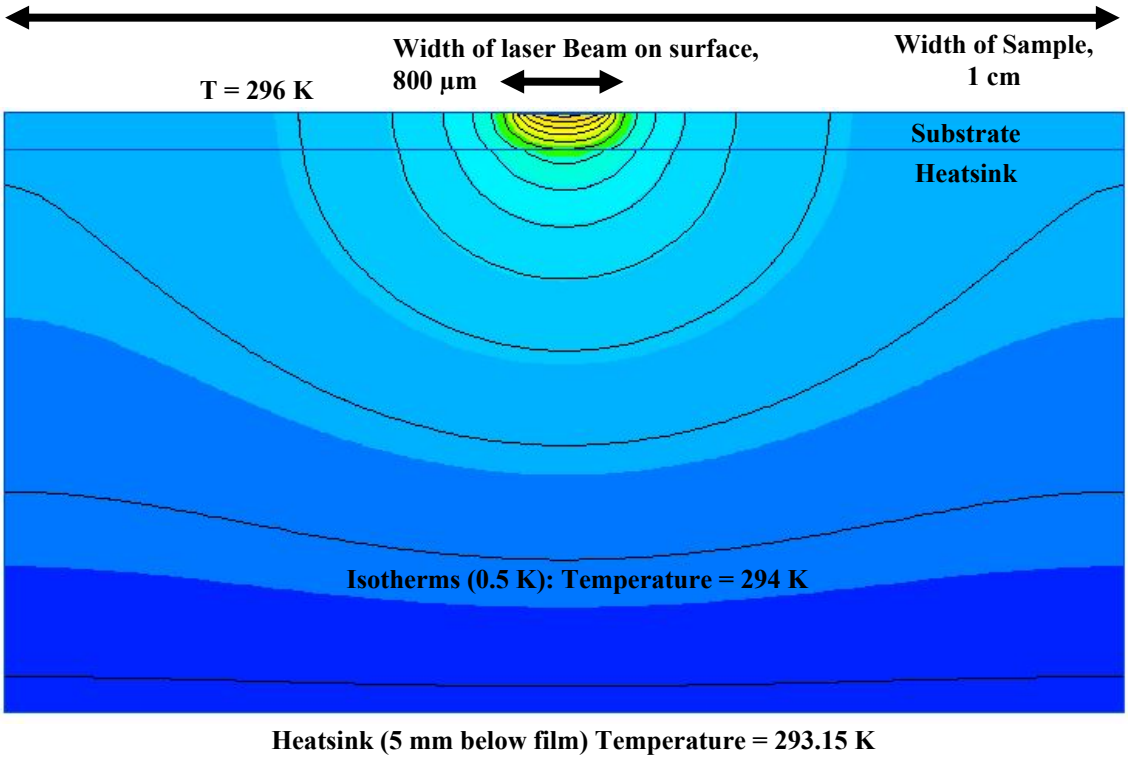

Figure 3-10: FE thermal model results for 1 Watt of heat generated in 1 x 10^9 cm^3 of PbSe material immediately beneath the surface: maximum temperature (red) is 306 K.

3.4.1 Spatial Limits

According to Sec. 3.2 the volume of material that heat is generated within and the material that PL comes from can be approximated using two material properties, d_{abs} = 0.5 µm and Λ_{diff} = 2 µm. In addition the thermal model developed claims the FE model heat source, $Q(x,y,z)$ in units of Watts/m^3, should be the same form as the optical

generation rate, Eq. 3.2. Figure 3-11 shows the difference in thermal modeling results for 1 Watt of absorbed optical power absorbed in the 500 nm immediately below the surface of a 2.5 μm film with heat distributed as a constant average, $Q(x,y,z) = Q_{Avg}$ = constant, and a 2D Gaussian distribution, $Q(x,y,z) = g_{ehp}(x,y,z)$. The data plots shown are the average increase in temperature for the same volume of film material in the thermal model compared to the heat sink temperature, $\Delta T_{Vol} = T_{Avg} - T_{HS}$. For a PL optical beam focused radius greater than 1 mm the difference in optical heating between a variable heat distribution and a constant distribution is less than 10 %. In addition FE calculations completed 40 % faster using a constant Q_{Avg}. The effect of using a three dimensional spatial model for heat generation is only significant at smaller optical beam diameters near the theoretical minimum, d_{Lens} = 500 μm, where the constant average power approximation resulted in 23% less heating.

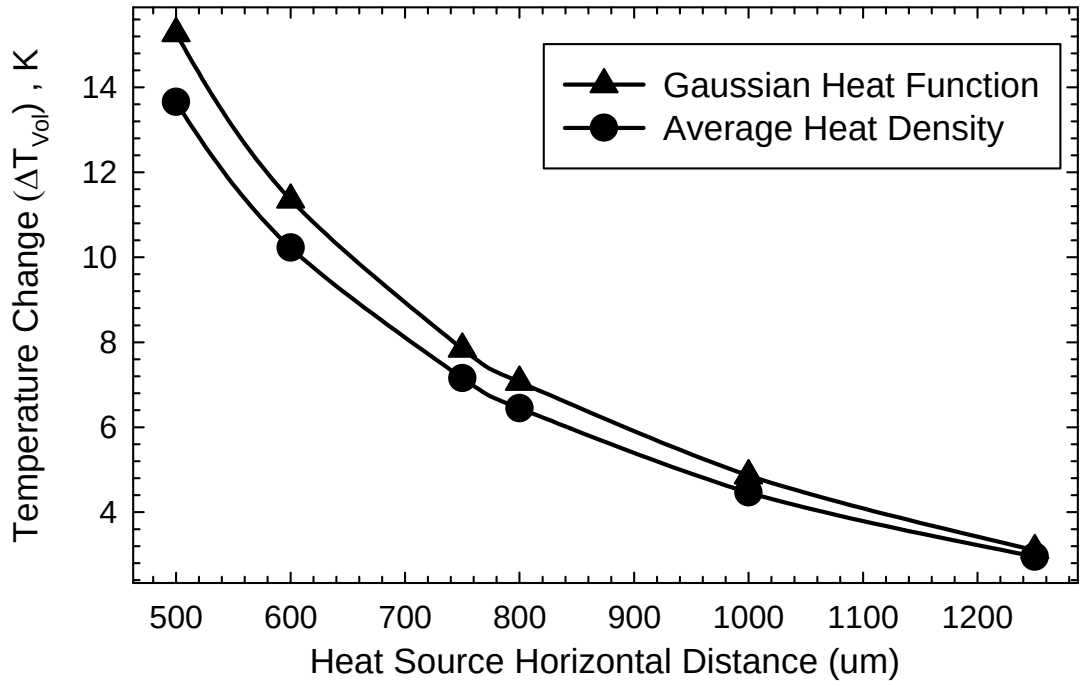

Figure 3-11: Thermal model temperature increase above the heatsink temperature in the volume of material 500 nm below the film surface for different laser spot diameters with a Gaussian heat distribution and an average heat distribution.

The thermal model also assumes that the material properties α and τ will determine the depth below the film surface that heat is generated. Figure 3-12 shows the thermal model results for different values of the absorption coefficient in PbSe resulting in variation of d_{abs}. The ΔT_{Vol} shown was calculated for the MQW region of material in the model independent of the depth of material with heat generation. Changing the depth of the optically heated region from 0.1 μm to 0.5 μm below the surface resulted in less than a 2 % decrease of the expected temperature rise in the MQW material. If $\alpha_{PbSe} = 1 \times 10^4$ and a significant portion of the optical energy passed through the sample and was absorbed by the substrate up to 10 μm below the sample surface ΔT_{Vol} in the MQW region would be 33 % lower. However, the spacing between temperature isotherms (contours) remains the same for the width variable independent of the depth and the absorption coefficient. Therefore, for a laser spot approximately

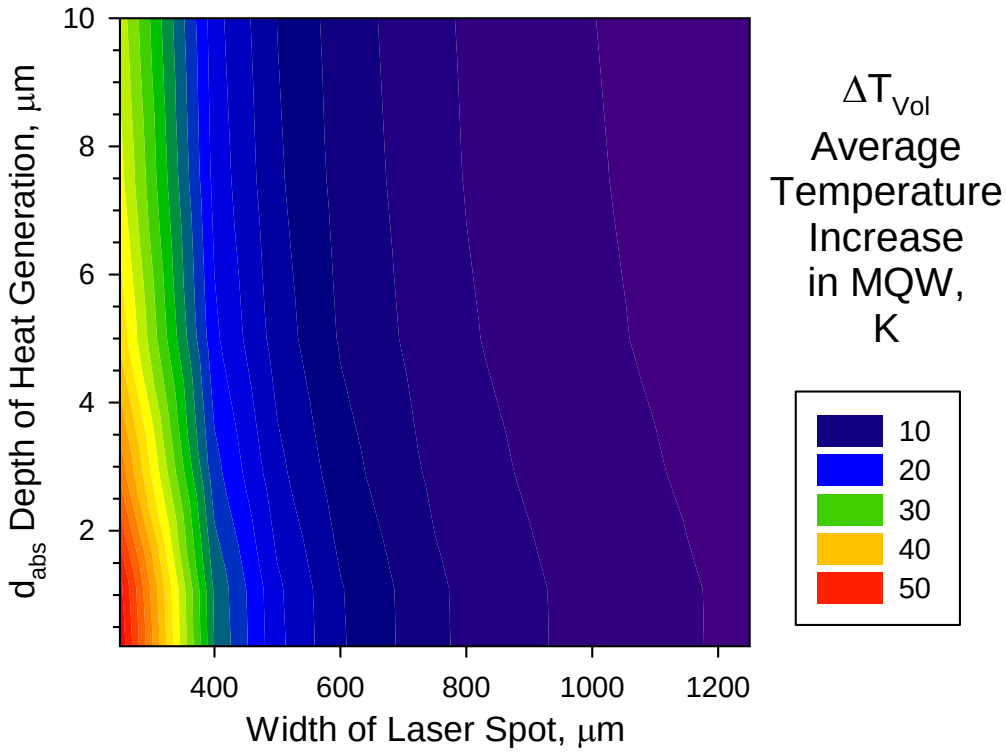

Figure 3-12: Variation of the temperature increase in the MQW region of a thermal model with heat generated in different volumes of material below the film surface.

800 μm wide on the film surface an absorption coefficient of 1 x 10^5 cm^{-1} would only result in 2.5 K more heating in the MQW region of a sample compared to an absorption coefficient of 1 x 10^4 cm^{-1}.

3.4.2 Film Comparison

In order to investigate the expected temperature increases of PL-heated films with different thickness and different thermal conductivity additional models up to 5 μm thick were created. Figure 3-13 shows the average temperature increase in two different volumes of material for FE models with varying thickness. The region of the model between 0.2 μm and 1 μm below the surface is approximately the location of the MQW structure in films #M141 and #M168. The heat source for this analysis used d_{Lens} = 1 mm with a Gaussian distribution and d_{abs} = 500 nm below the surface. The calculated temperature for the region of the film model closest to the surface increases linearly with total model thickness at a rate of 0.83 K/μm. Additional film material

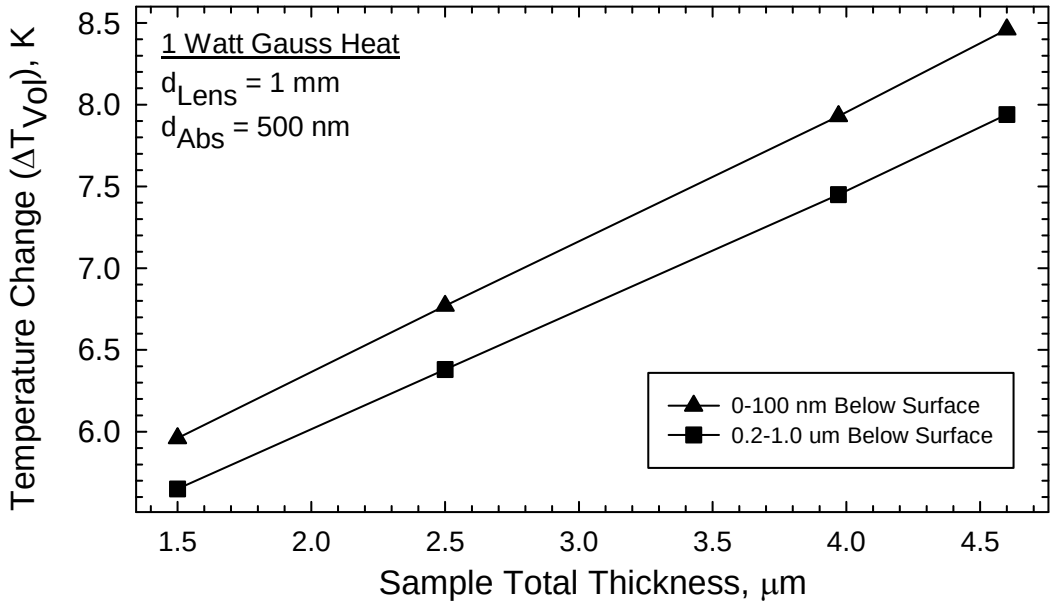

Figure 3-13: Temperature in different regions of FE models with a different total thickness and 1 Watt of heat power generated up to 500 nm below the surface.

further below the surface (MQW layer) shows less significant heating that increases with total model thickness at a rate of ≈ 0.6 K/μm.

The temperature increases in films of different thickness as a function of thermal conductivity in the material layers between the MQW optical layers and the substrate is shown in Figure 3-14. The expected temperature increase for a PbSe thin film with k = 2.2 $Wm^{-1}K^{-1}$ and thickness t = 2.5 μm would be $\Delta T \approx 6$ K. A measured $\Delta T = 8$ K would correspond to a lower thermal conductivity $\kappa = 0.8$ $Wm^{-1}K^{-1}$. If another thicker sample (t = 3.1 μm) had the same measured temperature increase this would only correspond to a reduced thermal conductivity of 1.2 $Wm^{-1}K^{-1}$. A heating effect twice the value expected for the reference value would constitute a reduction of thermal conductivity by nearly 80% to a value of 0.5 $Wm^{-1}K^{-1}$. The area between the lines represents the corresponding relationship between temperature increase, thickness, and thermal conductivity for MQW samples reported on in previous chapters.

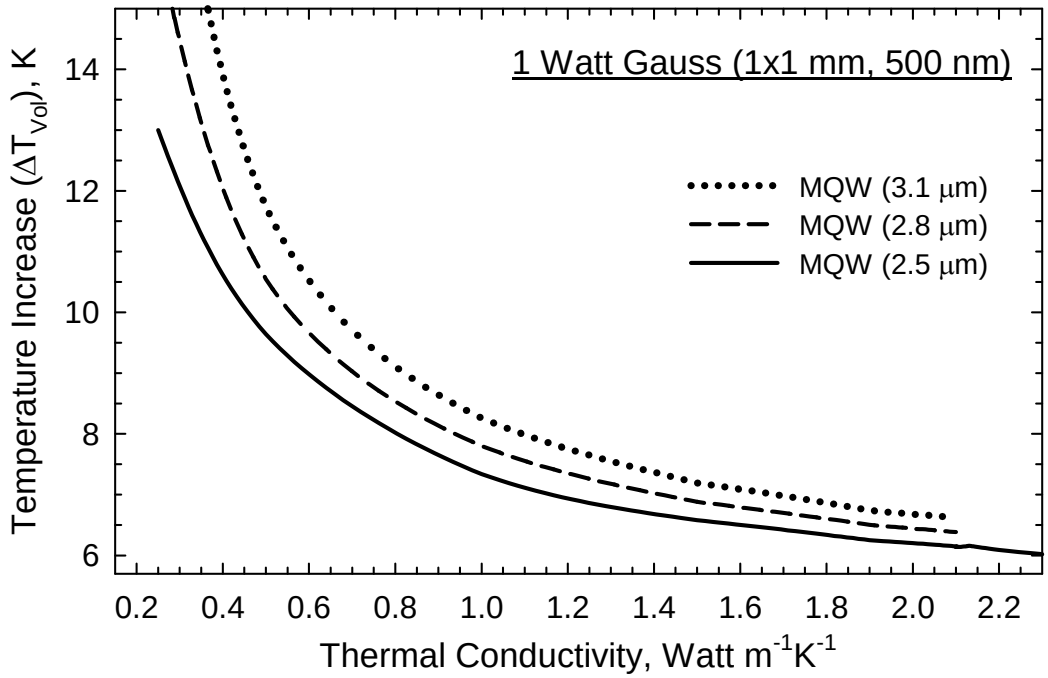

Figure 3-14: Thermal model heat energy distributions in a 200 nm thick disk with varying thermal conductivity.

3.5 Thermal Model Analysis

The accuracy of the PL emission analysis and thermal modeling was tested with a unique experiment using the optical characterization system described in Chapter 2 and elsewhere [15]. An adjustable lens stage was used to "de-focus" the optical beam and decrease the surface irradiance on the film, Figure 3-15. This system consisted of a 1.41 eV diode laser fiber coupled (d_{beam} = 2 mm) and a lens having focal length f_l = 51 mm. The minimum beam diameter was measured to be ≈ 860 μm and increased linearly as the lens was moved from the maximum focus at a rate of $0.03\Delta f_l$. The calculated optical (heat) flux of 1 Watt total optical power through the surface of a PL film is shown in Table 3-2. The system maximum absorbed power decreased 33% from the maximum to the minimum value. Several films were tested a minimum of three times at each optical setting over a three-day period. The first test of each day was excluded from all calculations. The thin films tested, with varying thickness are listed in Table 3-3. The thickness of the cap (or absorbing) layer on the MQW samples was nominally similar ≈ 150 nm. The MQW optical layers consisted of 20 pairs of

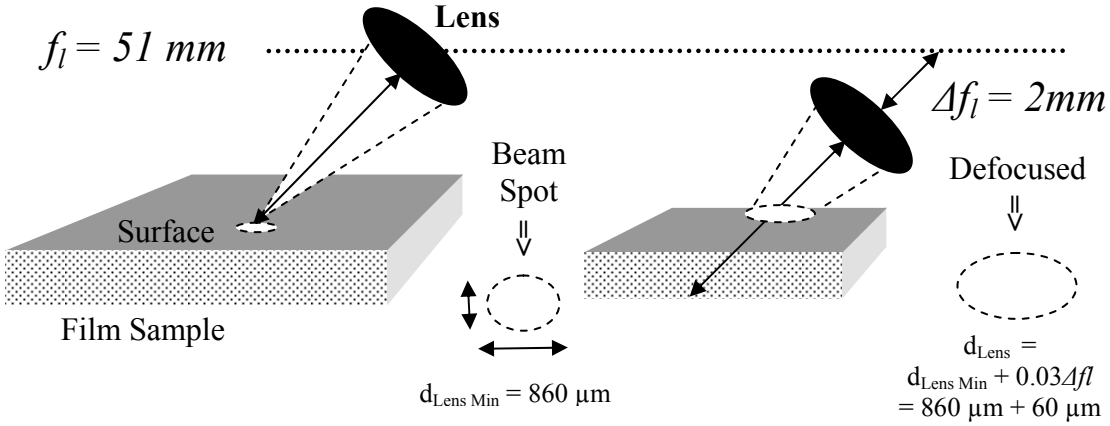

Figure 3-15: Illustration of de-focusing experiment designed to investigate optical heating at different power density.

Table 3-2: Changes in heat power density during the optical experiment.

Focus	Δfl, mm	d_{Beam}, μm	Area, 10^{-3} cm^2	Q_{AVG}, z = 500 nm 1 W/m^3	Gauss Q_{max}, z = 500 nm 1 W/m^3
Max	--	860	5.81	3.44×10^{12}	4.33×10^{12}
Step 1	2	920	6.65	3.01×10^{12}	3.76×10^{12}
Step 2	4	980	7.54	2.65×10^{12}	3.33×10^{12}
Step 3	6	1040	8.49	2.35×10^{12}	2.94×10^{12}
Step 4	8	1100	9.50	2.10×10^{12}	2.64×10^{12}

Table 3-3: Dimensions used for different regions of the FE thermal models.

Thin Film	Total Thick.	Type	d_{Cap} nm	Optical Thick. (nm)	LUT Thick.	LUT Type
M046	4.65	PbSe	-			PbSe
M047	4.37	PbSe	-			PbSe
M048	3.94	PbSe	-			PbSe
M049	3.78	PbSe	-			PbSe
M141	2.47	MQW	150	670	1.48	PbSe
M168	3.08	MQW	180	712	1.79	SL

$Pb_{0.94}Sr_{0.06}Se$/PbSe ≈ 30 nm and 10 nm respectively for a total of 800 nm. The material forming the test layer for film #M141 was PbSe, while films #M168 and #M207 were designed with multiple period SLs consisting of alternating $Pb_{0.85}Sn_{0.15}Se$ and PbSe layers. Film #M168 had three different periodicity SLs (125 pairs x 0.5 nm layers, 168 x 1.2 and 250 x 1.5 nm) with 547 interfaces over a thickness of 1.68 μm. PbSe samples were electronically characterized with Hall Effect measurements prior to PL testing. PbSe samples #M046, #M048, and #M049 had nominally similar intrinsic carrier concentrations ($n_p \approx 3 \times 10^{17}$) with mobility ($\mu_p$ = 300 $cm^2V^{-1}sec^{-1}$) at 300 K that both varied with temperature. Film #M047 was n-type ($n_e = 4 \times 10^{18}$) with μ_e = 82 $cm^2V^{-1}sec^{-1}$ at 300 K. The MQW films listed were doped with bismuth similar to film #M103 that was measured with $n_e = 4 \times 10^{18}$ and $\mu_e \approx 500$ $cm^2V^{-1}sec^{-1}$ at 300 K. The PbSe

samples that have a lower electrical conductivity should heat more than samples with higher values.

3.5.1 Spectral Analysis

The PbSe thin film emission was dramatically affected by CO_2 absorption for all room temperature measurements while MQW sample data was not, Figure 3-16. All calculations reported for PbSe films used data processed with the absorption reconstruction techniques described previously. The emission at maximum PL irradiance or focus (solid lines) was clearly shifted to higher energies with reduced intensity on the low energy side of the emission peak compared to spectra acquired when the beam was defocused (dashed lines). This is a result of both an increased area of emission on the film surface previously not emitting a PL signal and a lower overall temperature increase of the entire film as predicted by thermal modeling. However the high energy side of the PL emission peak for all films was a similar intensity for each level of irradiance at a constant total optical power. Using the EMG fit described earlier

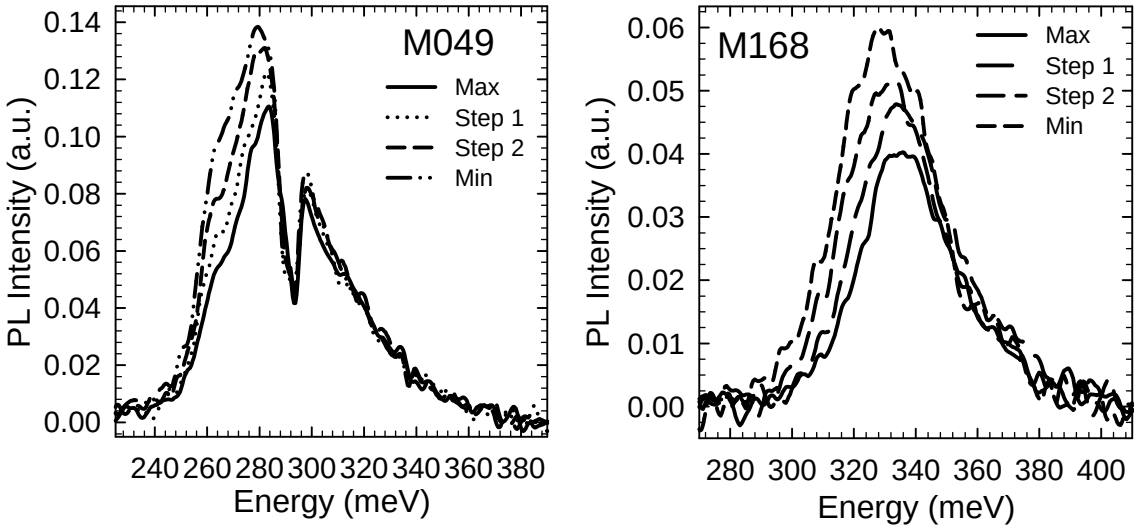

Figure 3-16: PL emission spectra for PbSe sample #M049 (left) and MQW on SL sample #M168 (right) for different "de-focused" laser settings.

film #M168 had a residue less than 6 x 10^{-7} for the data shown. Film #M049 had a residue of 7.7 x 10^{-7} for reconstructed data and 2.0 x 10^{-5} for the raw data.

The measured shift in the PL emission fit maximum for increased optical power $\Delta E_{PL}(P_{abs})$, proportional to a temperature increase $\Delta T_{PL}(P_{abs}) \equiv \Delta E_{PL}/\Delta E_g(T)$, for the maximum irradiance was significantly increased, approximately four times larger, compared to the minimum heat density as shown in Figure 3-17. The measured difference at P_{abs} = 2 W corresponds to a temperature difference of ΔT_{PL} = 7 meV/ 0.43 meVK^{-1} = 16.3 K. In addition, the PL emission peak quality typically, defined as the maximum intensity over the full-width at half-maximum (FWHM), was higher for the minimum focus settings. This indicates a decreased spread of energy (and therefore a reduced temperature differential) in the luminescent material for the larger optical beam and/or a lower overall temperature. The PL emission intensity for all films decreased at increased temperatures and increased irradiance. For the data shown above the maximum intensity decreased roughly 40% over a 30 K change in temperature at a constant optical P_{abs} = 1.9 W. The measured change at a heatsink temperature T_{HS} =

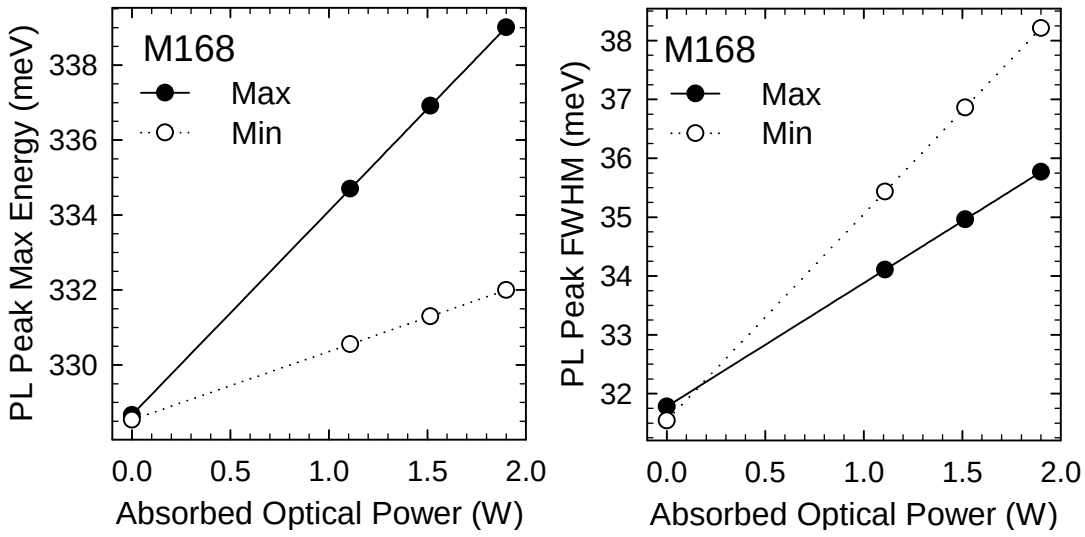

Figure 3-17: Change in the PL energy with maximum intensity and FWHM for the maximum and minimum irradiance settings.

303.15 K and P_{abs} = 1.9 W for the different focus settings was ~ 30 %. This corresponds to an estimated 22 K increase in temperature for the maximum beam focus compared to the larger surface diameter optics for film #M168.

3.5.2 Film Conductivity

The difference in thickness for PbSe thin films tested should result in less than a 0.5 K difference in the PL induced temperature change ΔT_{PL} according to the thermal modeling. Figure 3-18 shows the change in temperature at the different optical focus settings for the absorption reconstructed emission data of these films. The data show no clearly distinguishable difference in heating between the films due to overlapping measurement error bars. However, the three films tested at all irradiances had the same relative heating with the thinnest film #M049 (open triangles) having the lowest heating effect for all measurements as would be expected. The difference in the heating effect for the thickest (8.1 K/W) and thinnest film (7.4 K/W) shown at an optical focus of 980

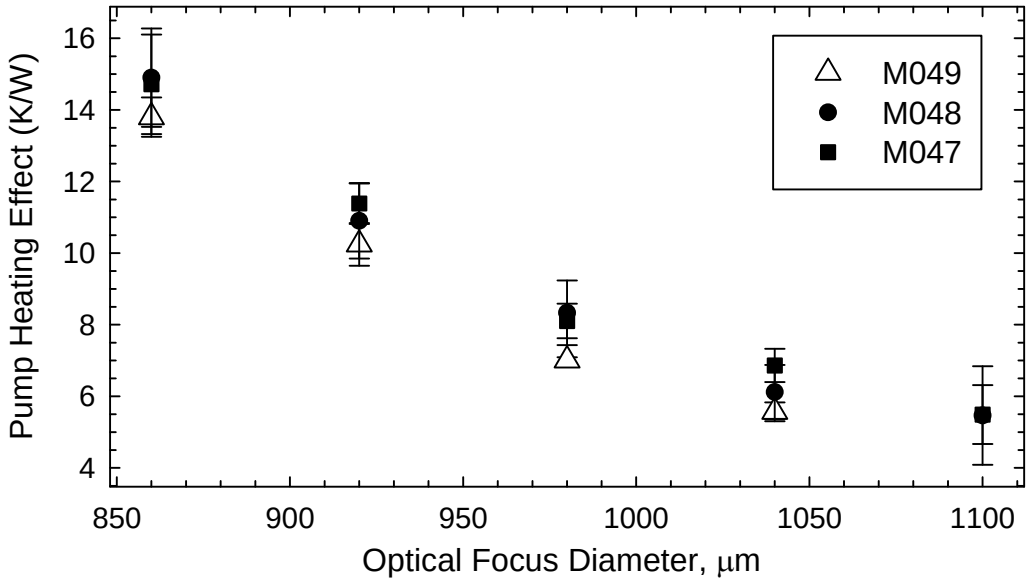

Figure 3-18: Optical heating effect in three PbSe samples with different thickness as a function of optical focusing on the surface.

μm corresponds to the difference in ΔT_{Vol} shown for the different regions of material near the surface of the FE thermal model in Figure 3-13.

The MQW samples tested showed a statistically significant variation in the PL induced temperature change, Figure 3-19, for two different samples of SL film #M168 compared to PbSe film #M141. At the greatest power density the heating effect was nearly 2X greater for the SL samples. As just shown the slight difference in thickness (< 0.6 μm) between the films should not be a factor in the measurements and the increased heating of SL films compared to PbSe is attributed to a difference in thermal conductivity, $\kappa_{SL} << \kappa_{Bulk}$. Assuming that film #M141 has a thermal conductivity nearly equal to PbSe, $\kappa_{141} \approx \kappa_{PbSe} = 2.2$ $Wm^{-1}K^{-1}$ at 300 K and using Figure 3-14, which assumes all heat is generated within 500 nm of the surface, the increased heating in film #M168 corresponds to $\kappa_{168} \approx 0.6$ $Wm^{-1}K^{-1}$. If the heat were generated further below the surface due to a smaller absorption coefficient (for example $\alpha = 1 \times 10^4$ cm^{-1}) the thermal conductivity of #M168 would be $\kappa_{168} \approx 0.4$ $Wm^{-1}K^{-1}$. However, this low a

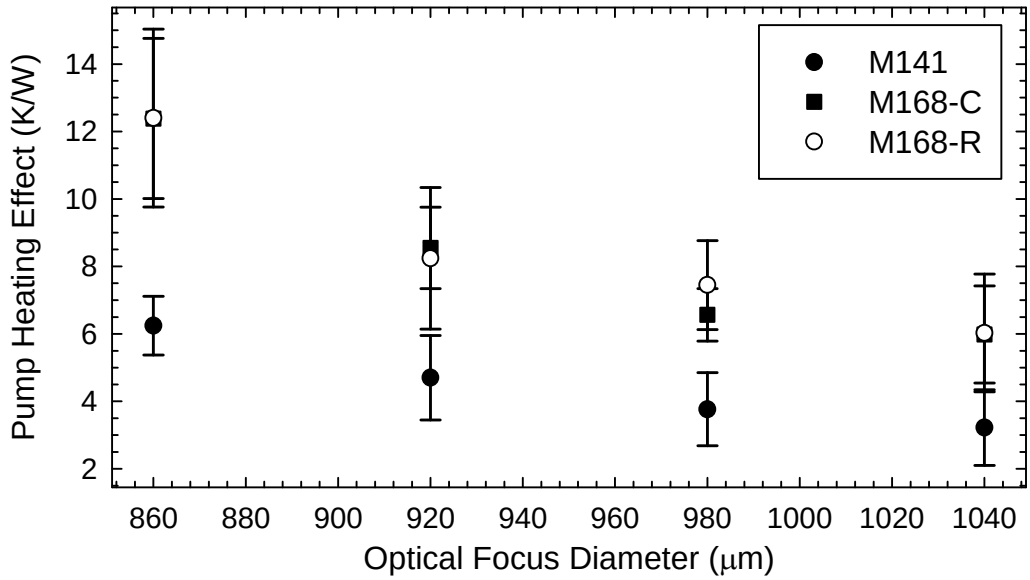

Figure 3-19: MQW measured heating effect and PL model variation with power density and the lower thermal conductivity of SLs.

value for thermal conductivity in this sample is unlikely as will be shown in the next chapter. If the heat generation in the FE was restricted to only 200 nm below the surface the PL results would correspond to $\kappa_{168} \approx 1.0$ $Wm^{-1}K^{-1}$. Since films #M168 and #M141 have a similar carrier density and mobility the difference in κ is attributed to a reduction in the lattice thermal conductivity. Increased scattering or reflection of phonons by the SL nanostructure can be responsible for this effect [12].

3.6 Summary and Conclusions

An energy transport model and novel calculation method were developed and used to measure cross-plane thermal conductivity in thin film PbSe and PbSnSe/PbSe superlattices from PL emission spectra. Evaluation of material parameters including optical absorption coefficient, thermalization lifetime, and normal band-edge carrier lifetime at 300 K were tested with thermal models of varying complexity to establish valid approximations. The energy transport model was combined with complex fitting of PL emission spectra using an asymmetric function commonly used in other forms of spectroscopy to reduce measurement error. An exponentially modified Gaussian function lowered the fit residue nearly two orders of magnitude compared to the raw data maximum or a Gaussian fit. Additional data analysis techniques to remove optical artifacts such as molecular absorption were also included.

The validity of the thermal model presented was tested under variable optical pumping densities in continuous wave PL for multiple PbSe and PbSrSe/PbSe MQW thin films. PL emission was observed for exciton generation rates covering more than three orders of magnitude with no observation of non-linearity or band-filling effects. The MQW films were analyzed with a multiple emission peak energy model for oblique

and lateral confined modes. No difference between a single envelope function and the band filling model was measured.

The energy transport model and PL analysis techniques presented were then used with an FE thermal model to calculate thin film thermal conductivity. The FE model and various assumptions were developed and tested through several *ab initio* calculations of expected temperature rises of 2 to 5 μm thick films dependent on heat distribution, film thickness, and thermal conductivity. This model was used to calculate the thermal conductivity of the films under the variable optical pumping density experiment. A bulk value of $\kappa = 2.2$ $Wm^{-1}K^{-1}$ for PbSe at 300 K was used in modeling the test layer below a MQW optical layer in sample #M141 to predict an increased heating of approximately 6 K. This was verified by PL measurements and was used as a reference comparison to MQW on SL structures in film #M168. This film showed significantly increased heating (> 2X) and therefore a much lower thermal conductivity ≈ 0.65 $Wm^{-1}K^{-1}$. The SL films tested had minimum layer thicknesses of 0.5 nm and 2 nm respectively with several hundred layer interfaces within 1.5 μm of material between the MQW and substrate that would decrease phonon transport and cross-plane thermal conductivity.

Chapter 3 References

1. R. Dalven, "A review of the semiconductor properties of PbTe, PbSe, PbS, and PbO", *Infrared Phys.*, **9**, pp. 141-184 (1969)
2. C. A. Kennedy and K. J. Linden, "Some properties of the quaternary system PbSnTeSe", *J. Appl. Phys.*, **41**(1), pp. 252-253 (1970)

3. W. W. Anderson, "Absorption constant of PbSnTe and HgCdTe alloys", *Infrared Phys.*, **20**, pp. 363-372 (1980)

4. R. Grisar, W. J. Reidel, and H. M. Preier, "Properties of diffused PbSnSe homojunction Diode Lasers", *IEEE J. Quant. Elec.*, **QE-17**(5), (1981)

5. F. Zhao, X. Lv, A. Majumdar, and Z. Shi, "Influence of mounting on continuous-wave photoluminescence from midinfrared PbSrSe/PbSe multiple quantum wells", *Appl. Phys. Lett.*, **84**(8), pp. 1251-1253 (2004)

6. D. Li, S. Mukherjee, J. Ma, G. Bi, D. Ray, F. Zhao, S. L. Elizondo, G. Yu, and Z. Shi, "Edge-Emitting Lead Salt Mid-Infrared laser Structure on BaF_2 (110) Substrate", *J. Elec. Materials*, **38**(9), pp. 1952-1955 (2009)

7. L. A. Elizondo, *Low-dimensional IV-VI Semiconductor Materials*, Ph.D. Dissertation, University of Oklahoma (2008)

8. A. D. LaLonde, Y. Pei, H. Wang, and G. J. Snyder, "Lead telluride alloy thermoelectrics", *Materials Today*, **14**(11), pp. 526-532 (2011)

9. H. Wang, Y. Pei, A. D. Lalonde, and G. J. Snyder, "Heavily doped p-type PbSe with high thermoelectric performance: an alternative for PbTe", *Adv. Materials*, **23**, pp. 1366-1370 (2011)

10. P. W. Zhu, L. X. Chen, X. Jia, H. A. Ma, G. Z. Ren, W. L. Guo, W. Zhang, and G. T. Zou, "Thermoelectric properties of PbTe prepared at high pressure and high temperature", *J. Phys.: Cond. Matter*, **14**, pp. 11185-11188 (2002)

11. J. P. Heremans, C. M. Thrush, and D. T. Morelli, "Thermopower enhancement in PbTe with Pb precipitates", *J. Appl. Phys.*, **98**, (2005)

12. Y. K. Koh, C. J. Vineis, S. D. Calawa, M. P. Walsh, and D. G. Cahill, "Lattice thermal conductivity of nanostructured thermoelectric materials based on PbTe", *Appl. Phys. Lett.* **94**, 153101 (2009)

13. L. A. Elizondo, Y. Li, A. Sow, R. Kamana, H. Z. Wu, S. Mukherjee, F. Zhao, Z. Shi, and P. J. McCann, "Optically pumped mid-infrared light emitter on silicon", *J. Appl. Phys.*, **101**, 104504, (2007)

14. F. S. Terra, M. Abdel-Rafea, and M. Monir, "Photoconductivity and electrical properties of PbSnTe thin films", *J. Mat. Sci.: Mat. Elec.*, **12**, pp. 561-567 (2001)

15. J. D. Jeffers, K. Namjou, Z. Cai, P. J. McCann, and L. Olona, "Cross-plane thermal conductivity of a PbSnSe/PbSe superlattice material", *Appl. Phys. Lett.*, **99**, 41903 (2011)

16. J. T. Verdeyen, *Laser Electronics Chapter 4:Gaussian Beams in Continuous Media*, Prentice Hall, New Jersey, USA pp. 70-88 (1981)

17. E. L. Dereniak and G. D. Boreman, *Infrared Detectors and Systems*, John Wiley and Sons, New York, USA (1996)

18. N. Suzuki, K. Sawai, and S. Adachi, "Optical properties of PbSe", *J. Appl. Phys.*, **77**(3), pp. 1249-1255 (1995)

19. C. A. Kennedy and K. J. Linden, "Some properties of the quaternary system PbSnTeSe", *J. Appl. Phys.*, **41**(1), pp. 252-253 (1970)

20. A. Fach, J. John, P. Muller, C. Paglino, and H. Zogg, "Material properties of PbSnSe epilayers on Si and their correlation with the performance of infrared photodiodes", *J. Elec. Mater.*, **26**(7), pp. 873-877 (1997)

21. Y. Gai, E. Talgorn, M. Aerts, M. T, Trinh, J. M. Schins, A. J. Houtepen, and L. D. A. Siebbeles, "Enhanced hot-carrier cooling and ultrafast spectral diffusion in strongly coupled PbSe quantum-dot solids", *Nano Lett.*, **11**, pp. 5471-5476 (2011)

22. H. Bao, B. F. Habenicht, O. V. Prezhdo, and X. Ruan, "Temperature dependence of hot-carrier relaxation in PbSe nanocrystals: an *ab initio* study", *Phys. Rev. B*, **79**, 235306, pp. 1-7 (2009)

23. W. A. Tisdale, K. J. Williams, B. A. Timp, D. J. Norris, E. S. Aydil, and X.-Y. Zhu, "Hot-electron transfer from semiconductor nanocrystals", *Science*, **328**, pp. 1543-1548 (2010)

24. S. D. Yoo and K. D. Kwack, "Theoretical calculation of electron mobility in HgCdTe", *J. of Appl. Phys.*, **81**(2), pp. 719-725 (1997)

25. User's Manual LabVIEW Version 10.0, National Instruments, Inc., Austin, Texas, USA (2010)

26. M. Yoshikawa, M. Kunzer, J. Wagner, H. Obloh, P. Schlotter, R. Schmidt, N. Herres, and U. Kaufmann, "Band-gap renormalization and band filling in Si-doped GaN films studied by photoluminescence spectroscopy", *J. Appl. Phys.*, **86**(8), pp. 4400-4403 (1999)

27. R. Rupprecht and H. Pascer, "Interpretation of magnetophotoluminescence spectra of narrow-gap IV-VI semiconductors", *Phys. Rev. B*, **50**(23), pp. 931-942 (1994)

28. F. Schwarzl, E. Kaufmann, G. Springholz, K. Koike, T. Hotei, M. Yano, and W. Heiss, "Temperature-dependent midinfrared photoluminescence of epitaxial PbTe/CdTe quantum dots and calculation of the corresponding transition energy", *Phys. Rev. B*, **78**, 165320, pp. 1-9 (2008)

29. L. S. Rothman, C .P. Rinsland, A. Goldman, S. T. Massie, D. P. Edwards, J. M. Flaud, A. Perrin, C. Camy-Peyret, V. Dana, J. Y. Mandin, J. Schroeder, A. McCann, R. R. Gamache, R. B. Watson, K. Yoshino, K. V. Chance, K. W. Jucks, L. R. Brown, V. Nemtchinov, and P. Varanasi, "The HITRAN molecular spectroscopic

database and HAWKS HITRAN atmospheric workstation: 1996 edition," *J. Quant. Spectrosc. Radiat. Transfer*, **60**, pp**.** 665–710 (1998)

30. P. J. Naish and S. Hartwell, "Exponentially modified Gaussian functions – a good model for chromatographic peaks in isocratic HPLC?", *Chromatographia*, **26**, pp. 285-296 (1988)

Chapter 4

Low Temperature Properties of Superlattices

4.1 Motivation

The temperature dependence of semiconductor thermal conductivity, k, along a specific crystal direction provides experimental evidence of quantum nanostructure theory. The relaxation time approximation of the Boltzmann transport equation [1] for atomic lattice thermal conductivity, k_{lat}, at any temperature, T, given by Eq. 4.1 is the sum over j different phonon types and is proportional to the specific heat, C_p, integrated over all phonon energies with a dimensionless value, $z = \hbar\omega/k_B T$, calculated using Plank's constant, $\hbar$, Boltzmann's constant, k_B, and the phonon angular frequency, ω.

$$k_{lat}(T) = \sum_{j} \int_{\omega} C_j(\omega, T) \mathrm{v_j}^2(\omega) \tau_j(\omega, T) \mathrm{dz} \tag{4.1}$$

The Klemens-Callaway heat conduction model assumes acoustic phonons dominate ordered energy transport moving within the crystal at an average velocity, v_{ph}, for a finite lifetime, τ_{ph}, before a scattering event and energy transfer. The "average" distance the phonon travels before scattering is referred to as the particle mean free path, $\Lambda_{ph} \equiv v_{ph} \times \tau_{ph}$. IV-VI semiconductor PbSe has a reported longitudinal acoustic (LA) phonon velocity ≈ 3 km/second depending on crystal orientation [2] with an average total lifetime $\tau_{ph} \approx 1$ picosecond [3] at 300 K that results in $\Lambda_{ph} \approx 3$ nm.

The total phonon lifetime is a combination of n distinct, independent scattering mechanisms that can be estimated [1] using Mathiessen's rule, $\tau_{tot}^{-1} = \sum \tau_n^{-1}$. The phonon lifetime in "bulk", or large, samples of PbSe between 100 K and 300 K is

dominated by inelastic Umklapp scattering [2] between two phonons that is calculated using second order perturbation theory [4] shown in Eq. 4.2 where θ_D is the Debye temperature, γ is the Grüneisen anharmonicity parameter, and M is the average atomic mass. Therefore at low temperatures ($T \leq 50$ K) most crystalline solids become more

$$\tau_{umk}^{-1} \approx \frac{\hbar\gamma^2}{Mv^2\theta_D}\omega^2 T \exp(-\theta_D / 3T) \qquad \textbf{(4.2)}$$

efficient heat conductors as the phonon lifetime increases. However, a phonon wave is the motion of atoms and the maximum value of Λ_{ph} is determined by the dimensions of the object being tested. Figure 4-1 illustrates the "size" limit of thermal conductivity with data for two different samples of PbSe reproduced from [5]. At temperatures approximately equal to 100 K both samples had a nearly identical total thermal conductivity $k_{tot} \approx 5$ $Wm^{-1}K^{-1}$. At higher temperatures the thermal conductivity of PbSe has been investigated by many other research groups more recently [1, 2, 6] and this value continues to decrease to $k_{tot} \approx 2.0$ $Wm^{-1}K^{-1}$ at 300 K that agrees with Umklapp scattering inversely proportional to temperature. However, below 40 K the thermal conductivity of the two samples shown was not similar and the larger sample, with dimensions of 5 mm x 5 mm x 70 mm, had a significantly higher maximum $k_{tot} \approx 220$ $Wm^{-1}K^{-1}$ compared to the smaller sample (2.5 mm x 3 mm x 35 mm) that had a maximum $k_{tot} \approx 92$ $Wm^{-1}K^{-1}$. At temperatures below 6 K the measured thermal conductivity decreased at a similar rate for both films. The rate of change is consistent with theoretical calculations [7] of the specific heat C_V, which is proportional to the Debye relationship $(T/\theta_D)^3$, and indicates that the phonon mean free path is a size-limited constant.

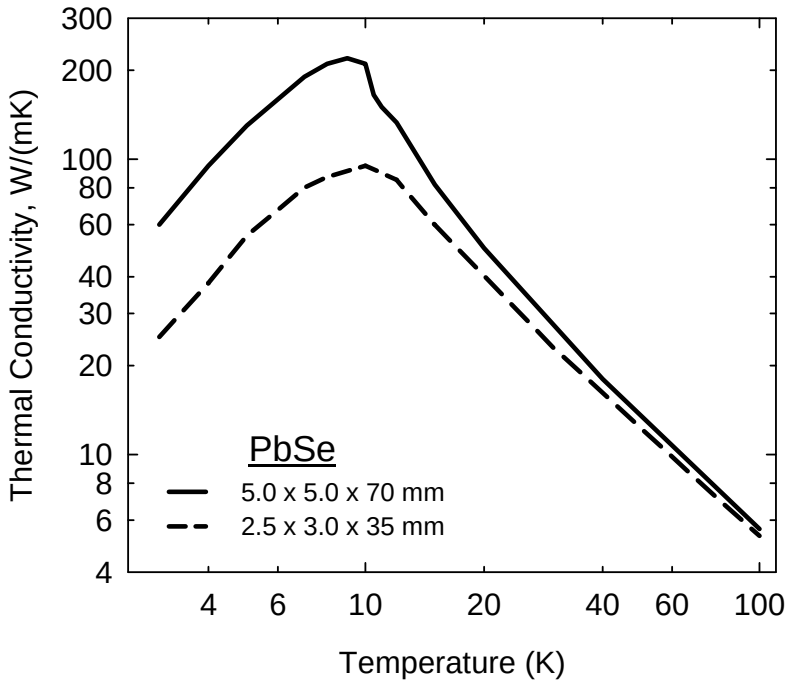

Figure 4-1: Measured thermal conductivity of two different sized samples of PbSe adapted from [5] showing reduced Umklapp scattering at low temperatures.

In addition to lattice thermal conductivity from atomic motion the movement of charge carriers, both electrons and holes with mobility, μ, contribute to thermal transport and the total thermal conductivity, $k_{tot} = k_{lat} + k_e$. The electronic carrier thermal conductivity of metals [8] is given by the Wiedemann-Franz law, Eq. 4.4, and is proportional to the electrical conductivity, σ, and the Lorentz number, L_0. The Lorentz

$$L_o = \frac{\kappa_e}{\sigma T} = \frac{\pi^2}{3}\left(\frac{k_B}{q}\right) = 2.44 \times 10^{-8} \frac{\mathrm{W\Omega}}{\mathrm{K}^2} \qquad \textbf{(4.3)}$$

number is a fundamental limit to the maximum random carrier diffusion in a 3D electron gas related to the thermal energy in the charge of an electron, q. However, for a well investigated high purity semiconductor such as silicon with an energy band-gap experimental results have indicated the material has a lower effective Lorentz number, $L^* = L_{Actual}/L_0 < 1$, that is a function of carrier concentration [9]. Several theories for calculating this value in PbSe have been proposed [10] based on different energy band

structure models that resulted in $L^* \geq 0.7$ at 300 K. In contrast the authors of [5] claimed that $L^* \leq 0.4$ for all of their PbSe samples at lattice temperatures above 100 K. Since experiments only assess k_{tot} the relative contribution of the lattice and electronic components can only be estimated from samples with different carrier concentrations.

The theory of lattice thermal conductivity based on the phonon lifetime and mean free path enables engineering material properties [11-14] through alloying, impurities, and nanostructures. Alloyed materials have increased phonon scattering compared to pure bulk materials due to differences in the mass and forces between neighboring atoms. Embedded nanoparticles [15, 16] create crystalline imperfections that reduce the phonon lifetime as a function of the size and density of the impurity. The lifetime of phonons in nanostructured materials such as alternating atomic layer superlattices (SLs) [17] is dominated by boundary scattering, τ_B, caused by a difference in elasticity between layers. The magnitude of this type of scattering [4], Eq. 4.2, is a function of layer thickness, L, phonon velocity, v, and the transmissivity, t,

$$\tau_B^{-1} = v(1-t)/L\left(\frac{3}{4}t\right), \quad t = \frac{1}{2}\left(t_{12} + t_{21}\right), \quad t_{ab} = \frac{v_b^2 \rho_b}{v_a^3 \rho_a + v_b^3 \rho_b} \tag{4.4}$$

between two layers that can be calculated using the phonon velocity and the material density, ρ. These scattering mechanisms are independent and nanostructured SL layers of ternary alloys with different nanoparticle densities can achieve a lattice thermal conductivity similar to amorphous materials [18].

The fundamental quantum physics of nanostructures with low thermal conductivity has commercial applications in solid state thermoelectric (TE) power generation and refrigeration. While the heat transport in optimized nanostructures is comparable to amorphous materials the electrical transport properties may be more

similar to crystalline materials [19]. The quality of TE materials is typically compared using the dimensionless figure of merit, *ZT*, shown in Eq. 4.5 and is a function of the Seebeck coefficient, *S*, in addition to the thermal and electrical conductivity. Values of S = 200 μV/K, σ = 4.5 x 10^4 S/m, and k_{tot} = 2.0 $Wm^{-1}K^{-1}$ that have been reported for

$$ZT \equiv \frac{S^2\sigma}{\kappa}T \qquad \textbf{(4.5)}$$

bulk PbSe at 300 K results in a ZT = 0.3 that increases at higher temperatures [20]. However, very few investigations of the TE properties of IV-VI semiconductors at lower temperatures have been published [5, 21] and none for nanostructured PbSe. This chapter presents measurements of photoluminescence (PL) emission shift for multiple quantum well (MQW) optical materials fabricated on single crystal PbSe and PbSe/PbSnSe SL material over the temperature range 100 K to 250 K. Thermal modeling of this optical heating effect indicates the SL films tested have k_{lat} values that are up to 10X lower than bulk material at 100 K. The thermal conductivity data from six thin films with different carrier profiles, measured using the Hall Effect, indicates that these nanostructured PbSe materials have a maximum estimated ZT = 1.2 at 300 K.

4.2 Experimental Procedures

The PL testing system described in Chapter 2 was modified to accommodate a liquid nitrogen (LN_2) cooled vacuum-sealed cryostat for thin film temperature control shown during a sample test in Figure 4-2. The black square on the CCD camera display is an image of the sample mounted inside the cryostat. The cryostat housing was a cube with IR transparent 1.5 inch diameter removable glass windows perpendicular to the thin film sample surface for entry of the PL stimulating laser beam and exit of the

reflected beam. At the PL laser energy (E_{las} = 1.4 eV) the normal incidence optical transmission through the calcium fluoride (CaF_2) windows was measured, T_w = 93%, with a calibrated optical power meter (Newport, Inc. model # 1816-C) and thermopile detector (model # 818P-12). The blackbody and PL emission spectrum from the PbSe film surface exited the cryostat through either a CaF_2 window with cutoff wavelength, λ_c = 7 µm, or a zinc selenide window (T_{ZnSe} = 65%, λ_c = 20 µm) [22]. More magnified images of the testing apparatus with the PL laser illuminating a PbSe thin film are shown in Figure 4-3. The CCD camera "sees" the infrared light from the laser scattered off of surfaces that appears as either purple or white dots in the images. Figure 4-3 a)

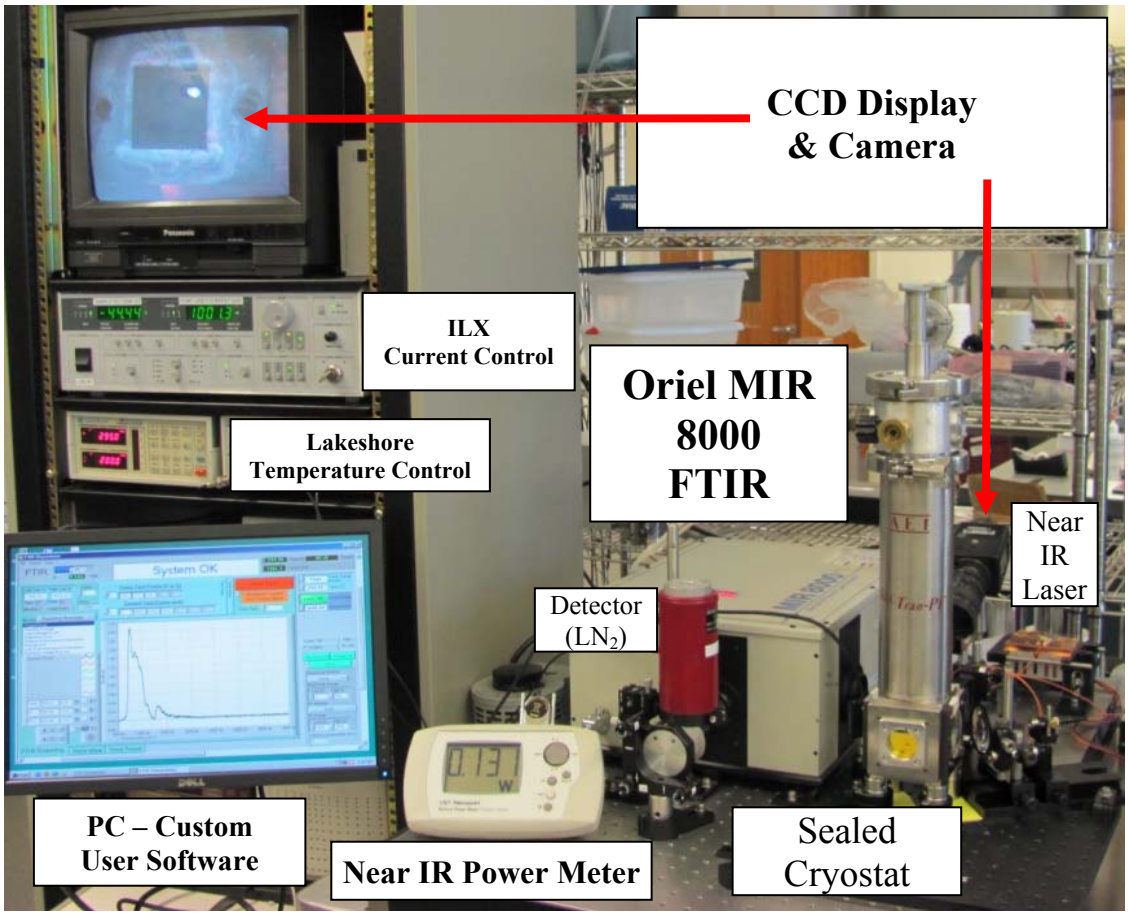

Figure 4-2: Image of the PL system for low temperature testing with a LN_2 cooled cryostat.

on the left shows the optical signal focused by a two-inch CaF_2 lens and reflected off the film surface that is visible through the glass window. Figure 4-3 b) on the right shows the reflected optical beam being measured with the power meter during testing. The samples tested were ≈ 1 cm square pieces diced or cleaved from circular 3-inch silicon wafers with IV-VI films grown using molecular beam epitaxy (MBE) with techniques detailed in references [23-24]. Film samples were then affixed by the substrate to a copper sub-mount using a eutectic gallium indium (EGaIn) [25] layer. The sub-mount was a 17 mm by 26 mm rectangular copper plate that was approximately 1 mm thick that could be attached to the temperature controlled cryostat interior mount with two #2-56 screws. The cryostat mount was constructed of copper

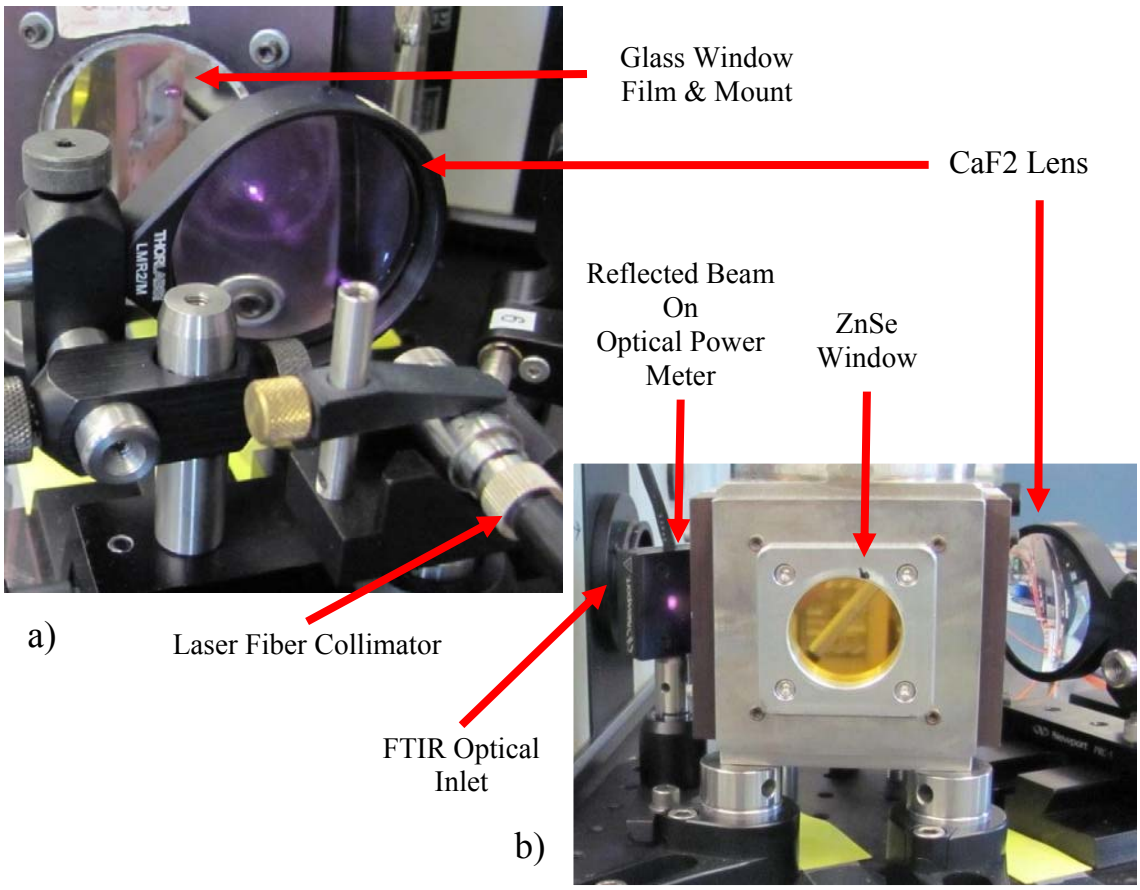

Figure 4-3: Images of the PL laser system window reflections and thin film illumination captured using a digital camera.

and temperature was stabilized with an integrated electrically resistive heating element and an external proportional, integral, and derivative (PID) control unit (Lakeshore Cryotronics, Inc. model #330) using a silicon diode temperature sensor (model #DT-570) and a 25 Watt resistive cartridge heater.

The cryostat chamber was evacuated using a mechanical vacuum pump for more than 45 minutes to lower the internal pressure below 3 x 10^{-3} Torr. During film testing the cryostat pressure was additionally maintained with a liquid nitrogen-cooled sorption pump to enable extended low temperature data acquisition. Thin films were evaluated by measuring the temperature dependent "blue-shift" of PL emission associated with optical heating, $\Delta E_{PL}(P) \equiv \Delta E/\Delta P$, for absorbed optical powers up to 2.5 W. Figure 4-4 shows the test timing and the number of heatsink temperatures that each sample was tested. As the system temperature was lowered data were acquired at each test set point (250 K, 200 K, 150 K, and 100 K) with the temperature varied ± 10 K and averaged for a single value. Data were also acquired as the system temperature was raised from a minimum value of 90 K to room temperature for a total of 30 different data sets at 12 different fixed temperatures. The spectral data acquired at each test setting consisted of four to seven optical powers for a total of more than 100 independent measurements for each film during a single test. At each test point the reflected PL laser power was measured to calculate the absorbed power with the effect of reflection losses from two glass windows taken into account. The rate of heatsink temperature change applied to thin films during testing was controlled with a custom program written using National Instruments, Inc. LabVIEW Version 7.0 development platform. Temperature range (or zone) dependent PID values were implemented to reduce thermal shock from

temperature cycling due to thermal expansion mismatch between the IV-VI materials and a CaF_2 buffer layer grown between the silicon substrate and the IV-VI films [26].

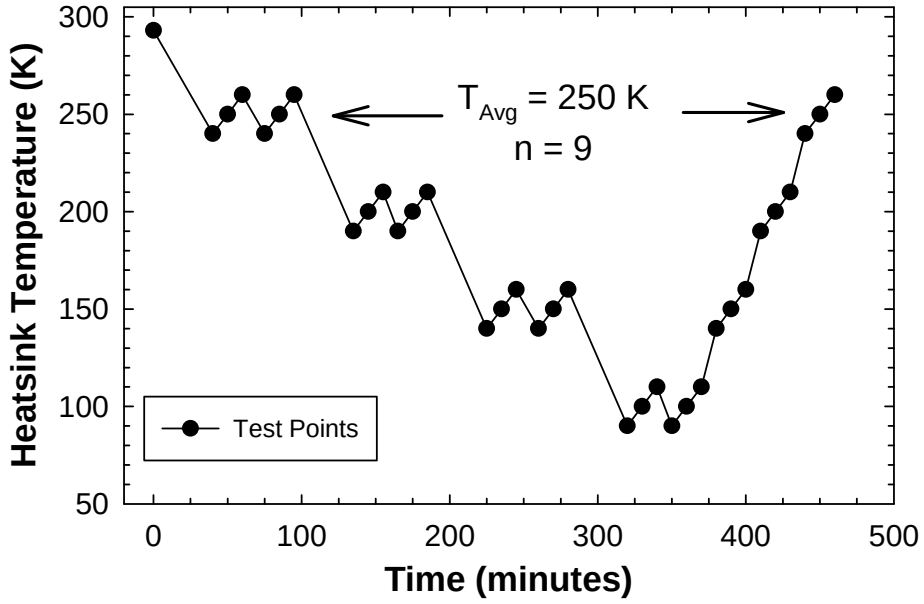

Figure 4-4: Test temperatures and data collection timing for a single thin film test.

The effect of PbSe/$Pb_{0.85}Sn_{0.15}Se$ superlattice design parameters on total material cross-plane thermal conductivity were evaluated using a matrix of thin film designs with different SL periodicity, thickness, and electrical properties. Figure 4-5 shows the SL film structure of sample #M168 compared with sample #M141 that only contained

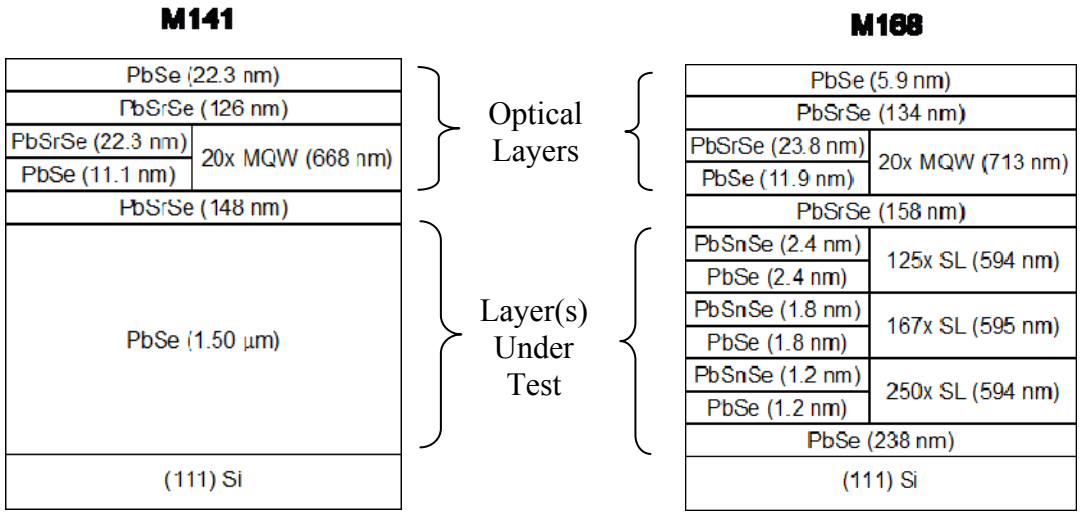

Figure 4-5: Comparison of MQW on PbSe sample #M141 with SL sample #M168.

micron of film material for all samples was a nominally similar 20-pair MQW with PbSe between the optically active upper material layers and the substrate. The top alternating PbSe/$Pb_{0.93}Sr_{0.07}Se$ layers and extended thickness PbSrSe barrier layers, $t \approx$ 150 nm, immediately above the first and below the last PbSe quantum well layer for carrier spatial confinement. The MQW design creates confined electron energy levels blue-shifted approximately 12 meV from both PbSe band edges with L-valley band degeneracy removed [23]. For SL sample #M168 the approximately 2.1 μm of material below the optical layers, labeled the layer under test (LUT), contained three different SL types each ≈ 600 nm thick. The layers of each SL type were 2.4 nm, 1.8 nm, and 1.2 nm thick with 125, 167 and 250 pairs respectively. Table 4-1 contains a summary of four other SL samples that contained either 5 or 7 different SL types with different layer thicknesses. Additional sample details are contained in Appendix B.

Table 4-1: Summary of MQW on SL sample design thickness.

Sample ID #	# SL Types	SL Layer Thickness (nm)			# Layers	LUT Thick	Average Thickness
		Min	Max	Total			
M168	3	1.2	2.4	600	1084	1.79 μm	1.65 nm
M211	5	1.0	5.0	300	686	1.68 μm	2.45 nm
M212	5	0.5	2.5	300	1370	1.69 μm	1.24 nm
M213	7	0.5	2.0	200	1374	1.56 μm	1.13 nm
M214	7	1.5	3.0	200	654	1.72 μm	2.64 nm

4.3 Low Temperature Testing Results

The electronic properties of all samples were characterized in the temperature range from 300 K to 100 K with Hall effect measurements prior to PL testing. Samples #M141 and #M168 could not be accurately tested because the upper MQW layers were

undoped p-type and the lower layers were doped n-type with bismuth that created a pn-junction ≈ 1 μm below the surface. However, sample #M103 was doped uniformly with bismuth using the same MBE growth conditions as the lower layers of samples #M141 and #M168 and should therefore have approximately the same electronic properties. The temperature dependent carrier concentration, n, and mobility, μ, of sample #M103 and the undoped SL samples are summarized in Table 4-2. The carrier concentration of the undoped SL samples at 250 K is 2.61 ± 0.13 holes cm^{-3} that decreases to 1.49 ± 0.13 holes cm^{-3} due to carrier freeze out. The mobility of the carriers in these samples increases more than 10X as the lattice temperature is decreased from 250 K to 100 K due primarily to a reduced Auger scattering [27]. The majority carrier concentration (electrons indicated by the negative sign) in the intentionally doped sample #M103 is 20X greater than the undoped samples and increases as the temperature is lowered. The mobility of the electrons in this sample increases only 5X as the temperature is lowered to 100 K. The Hall effect data can be used to estimate the electrical conductivity [10] of these samples with the equation, $\sigma \approx n\ \mu\ q$, where q is the charge of an electron and is

Table 4-2: Measured temperature dependence of the carrier concentration and mobility of PbSe samples using the Hall Effect.

Sample ID #	**T = 250 K**		**T = 200 K**		**T = 150 K**		**T = 100 K**	
	μ, cm^2/Vs	**n, 10^{17} cm^{-3}**	**μ, cm^2/Vs**	**n, 10^{17} cm^{-3}**	**μ, cm^2/Vs**	**n, 10^{17} cm^{-3}**	**μ, cm^2/Vs**	**n, 10^{17} cm^{-3}**
M103	1710	-55.7	2530	-56.5	3792	-56.7	6697	-59.3
M211	1022	2.46	2135	1.87	4514	1.59	11540	1.46
M212	1278	2.76	2711	2.22	5860	1.98	15070	1.90
M213	1140	2.65	2405	2.05	5225	1.75	14110	1.60
M214	747	2.55	1535	1.76	3291	1.34	8839	1.01

equal *to* 1.602 x 10^{-19} Coulombs. Figure 4-6 a) shows the electrical conductivity of sample #M103 and SL sample #M212. This data is combined with the relative Lorenz number calculated using the single parabolic band model and the Wiedemann-Franz law to estimate the electronic component of thermal conductivity for doped samples #M141 and #M168 compared to an undoped sample in Figure 4-6 b).

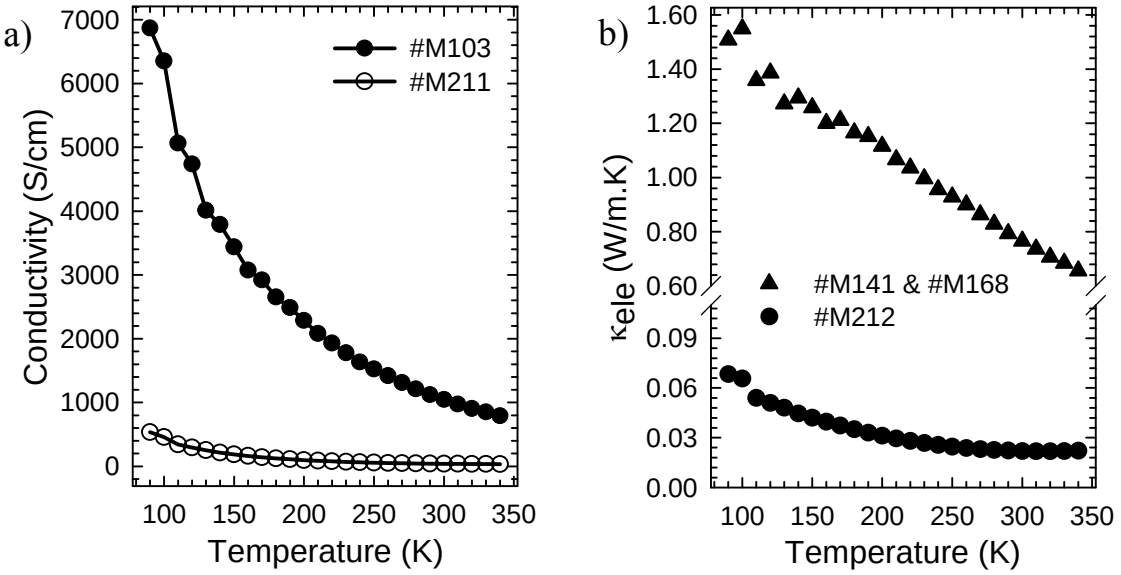

Figure 4-6: a) Measured electrical conductivity of different samples from 90 K to 340 K and b) calculated electronic thermal conductivity of similar samples.

Initial PL testing of samples was completed with PL emission exiting the cryostat through a ZnSe window. The blackbody emission of the tested samples verified that this system operated similarly to the thermoelectric cooled system described in Chapter 2. For all subsequent testing PL emission from samples exited the cryostat through the CaF_2 window that absorbed all blackbody radiation. In the previous chapters PL characterization of IV-VI semiconductor samples at 300 K showed differences in the measured $\Delta E_{PL(P)}$, and therefore thermal conductivity, between PbSe sample #M141 and PbSe/PbSnSe SL sample #M168 [28]. However, most MQW on SL samples had low intensity PL emission at or above 300 K that could

not be analyzed. Figure 4-7 a) shows the PL spectra of SL sample #M214 at lower heatsink temperatures for a constant absorbed optical power, P_{abs} = 2.4 W. Figure 4-7 b) shows the change in PL emission as a function of absorbed power at a fixed film heatsink temperature of 150 K. The shift of the PL spectrum energy with maximum intensity (E_{max}) was determined using a single peak exponentially modified Gaussian (EMG) fit with molecular absorption corrected by techniques described in the previous chapter. The largest fit error occurred at a heatsink temperature of 200 K where E_{max} coincides with atmospheric gas CO_2 absorption at 290 meV. All other spectral data from the MQW on SL films exhibited a similar asymmetric intensity distribution with a larger portion of the optical power on the high energy side of E_{max}. The linear least squares (LLS) fit of E_{max} as a function of P_{abs} for the data shown resulted in a value of $\Delta E_{PL}(P)$ = 3.22 meV/Watt with fit accuracy metric R^2 = 0.987.

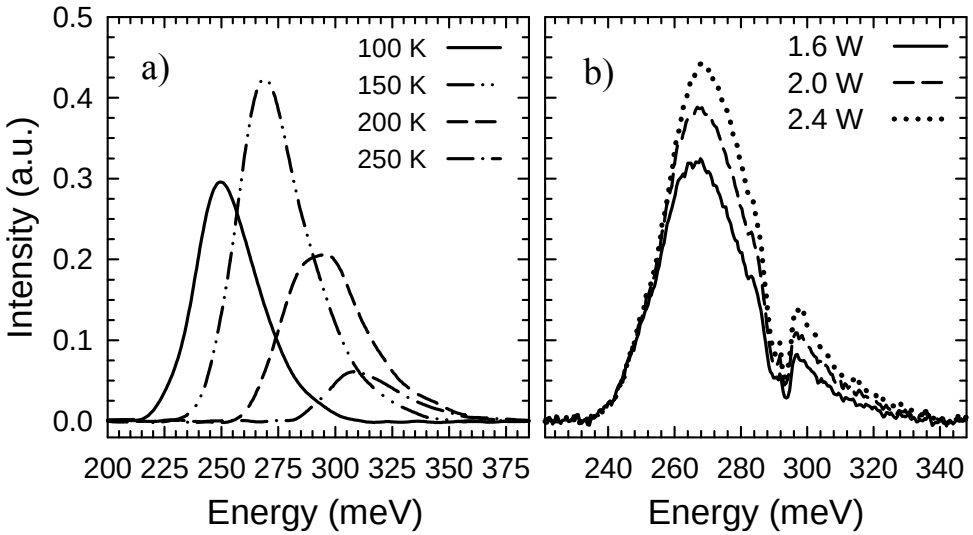

Figure 4-7: PL emission spectra measured for thin film #M214 for a) different heatsink temperatures and b) different absorbed optical powers.

The shift of PL emission maximum energy as a function of temperature, $\Delta E_{PL}(T)$, for a constant absorbed optical power ≈ 2.5 Watts for all MQW on SL samples is shown in Figure 4-8. Table 4-3 summarizes the slope, intercept, and R^2-value of an

LLS fit of the data for these samples and includes data for MQW on PbSe sample #M141. The shift of PL emission energy with heatsink temperature is used to convert the shift of PL emission energy with increased optical power into the optical heating effect, $HE \equiv \Delta E_{PL}(P)/\Delta E_{PL}(T)$ with units K/Watt. The MQW on SL films had an average $\Delta E_{PL}(T)$ = 0.43 ± 5% meV/K similar to the value reported by others [24]. In addition to similar $\Delta E_{PL}(T)$ values each MQW on SL sample that was tested exhibited a similar change in PL intensity as shown in Figure 4-9 a). The measured PL emission intensity increased as the sample heatsink temperature was lowered from 260 K to 150 K. The PL intensity then decreased at lower temperatures at nearly the same rate of 1 % per degree. The only significant difference in the PL emission of the MQW on SL samples was the change in the full-width at half-maximum (FWHM) of the PL emission peak at different heatsink temperatures shown Figure 4-9 b). The FWHM decreases approximately 15% for undoped SL samples but decreased 38% for sample #M168 at the lowest tested temperature. The FWHM of PL emission is a function of the absolute

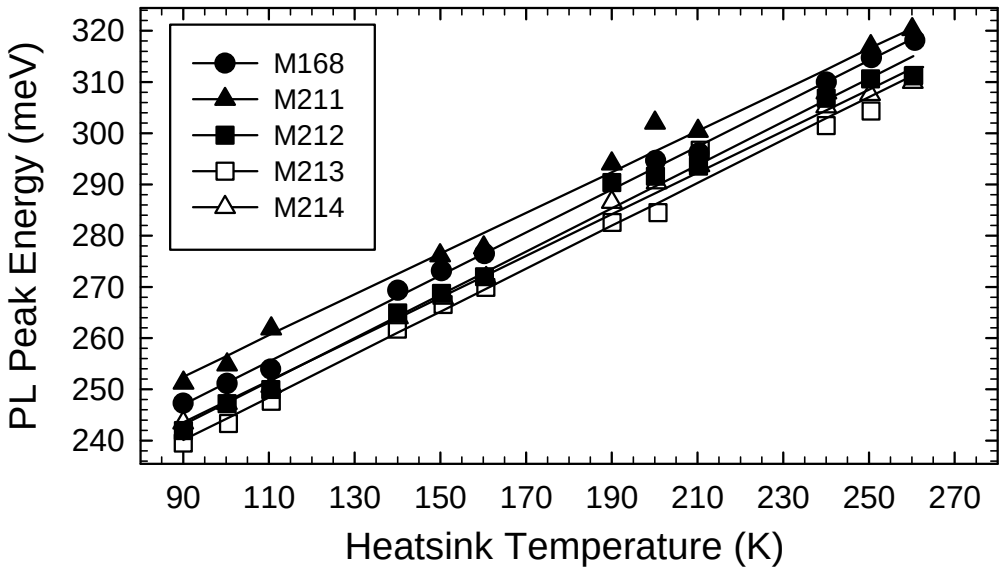

Figure 4-8: Measured change in the energy of the maximum intensity PL emission from PbSrSe/PbSe MQW on SL samples from 90-260 K.

Table 4-3: MQW sample bandgap temperature dependence fitting results.

Film-Sample	$\Delta E_{PL}(T)$ (meV/K)	Intercept (meV)	R^2
M148-H1	0.488	180.03	0.9895
M168-C	0.417	205.17	0.9985
M211-R	0.423	208.66	0.9976
M212-R	0.456	200.82	0.9977
M213-R	0.426	191.50	0.9976
M214-R	0.406	200.89	0.9962

lattice temperature due to the Fermi-Dirac distribution of carriers and energy level occupancy [29] but is also a function of the temperature difference in the volume of material where PL emission originates. The larger decrease in the FWHM of PL emission from sample #M168 compared to other samples is attributed to a smaller temperature gradient within the MQW region that would only occur if the thermal conductivity of the sample was decreasing more dramatically at lower temperatures.

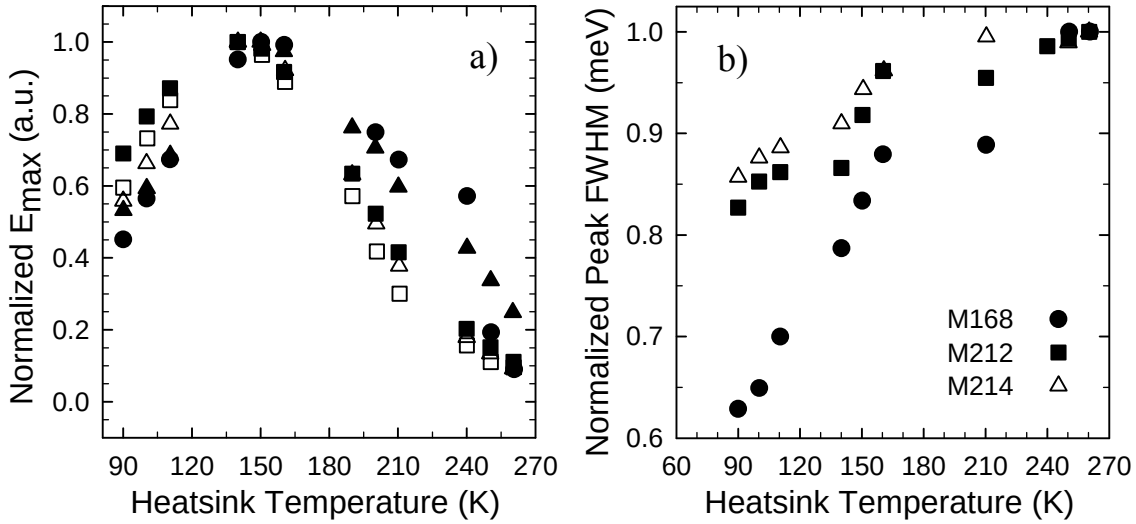

Figure 4-9: PbSrSe/PbSe MQW PL data from 90-260 K a) emission intensity and b) normalized emission FWHM.

The optical heating effect for the different samples tested as a function of temperature is shown in Figure 4-10. The undoped SL samples are shown on the left and the intentionally doped samples are shown on the right. The undoped samples

show no significant change in optical heating at lower temperatures. The slight decrease (≈ 13 %) in optical heating for sample #M213 may be due to noise in the PL spectra since the PL intensity of this sample at 250 K was significantly lower than all other samples that were tested. Both doped samples exhibited a more dramatic decrease in optical heating at lower heatsink temperatures. The optical heating in sample #M141 without a SL nanostructure, decreased more than 50%.

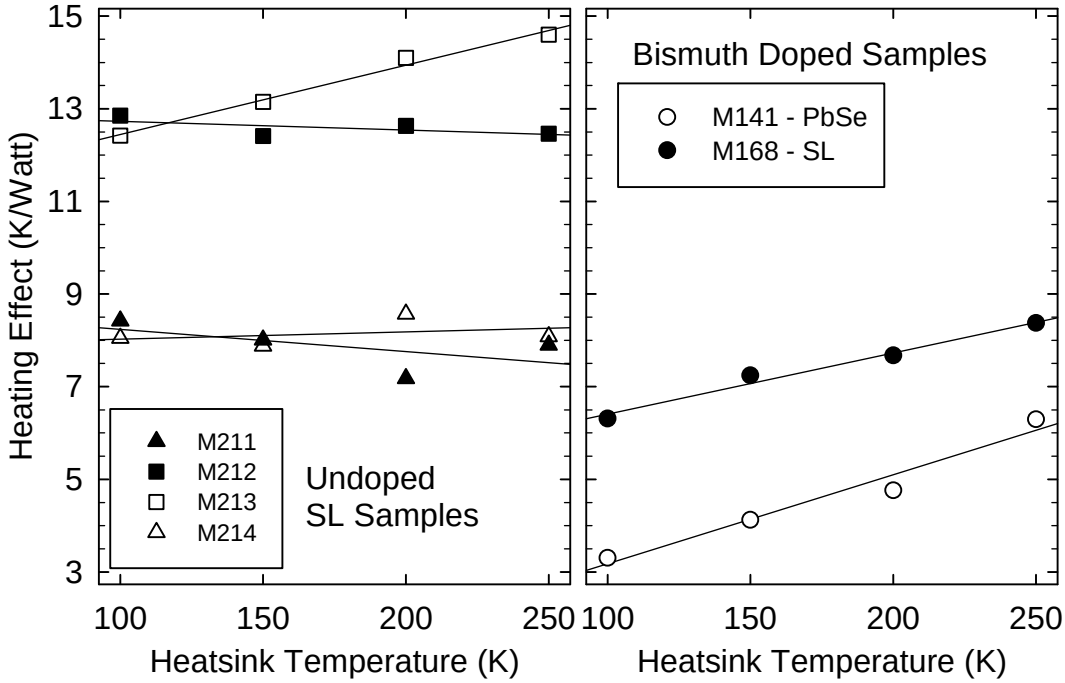

Figure 4-10: The optical heating calculated from the shift of PL spectra for different samples as a function of temperature: a) undoped samples and b) doped samples.

4.4 Thermal Conductivity Results

The optically induced PL heating effect was converted to thermal conductivity using Tera Analysis, Inc. Quickfield Version 5.0 finite element (FE) software. The thermal model that was used is described in Chapter 3 and has multiple material layers including the silicon substrate, copper sub-mount, and a layer of either EGaIn or pure indium used to attach the substrate to the copper sub-mount. The change in thermal

conductivity for these materials as a function of temperature from different reference sources is summarized in Table 4-4. The thermal model for each sample was evaluated at the given temperatures with directional thermal conductivity, or anisotropy, taken in account. The in-plane SL layer thermal conductivities, $k_{//}$, were set to the value of bulk PbSe and only the cross-plane thermal conductivity, $k_{\perp}$, was allowed to vary as the data fit parameter. The thermal model in-plane power distribution used was Gaussian with 95% of the total optical power within 1 mm of the beam spot maximum on the film surface. This value was determined by comparison of the measured heating effect and results of the room temperature system optical power density experiment in Chapter 3.

Table 4-4: The thermal conductivity of different materials used in the FE model of the PL system at different test temperatures.

Material	**Thermal Conductivity, Watts meter^{-1} Kelvin^{-1}**					**Refs.**
Temperature	**300 K**	**250 K**	**200 K**	**150 K**	**100 K**	
Copper	393	425	465	515	600	12, 8, 30
Silicon	141	185	275	420	900	7, 31
In	350	365	385	435	500	32
GaIn	40	42	46	52	80	33, 34
PbSe	2.2	2.5	2.9	3.8	6	2, 5, 6, 19

The calculated total cross-plane thermal conductivity for all tested samples is shown in Figure 4-11. The right graph shows that both samples that were doped with an n-type carrier concentration, $n \approx 6 \times 10^{18}$ cm^{-3}, had increased thermal conductivity at lower temperatures. The total thermal conductivity of sample #M168 increased 0.6 Wm^{-1}K^{-1} that is nearly equal to the expected change in the electronic component of thermal conductivity calculated previously, $\Delta k_e \approx 0.54$ Wm^{-1}K^{-1}, and shown in Figure 4-6. It should be noted that the Hall effect data represents in-plane charge carrier

transport properties and that the cross-plane transport through the superlattice structure may be different [17, 18]. Sample #M141 exhibited an even greater increase in total thermal conductivity $\Delta k_{tot} \approx 2.4$ $Wm^{-1}K^{-1}$ that indicates that the lattice thermal conductivity of this sample also increased as would be expected due to reduced Umklapp scattering, Eq. 4.2, in the bulk PbSe layer beneath the MQW optical layers. In contrast the total thermal conductivity of the undoped SLs shown in the left graph had no significant variation in thermal conductivity at any temperature that indicates boundary scattering is the dominant phonon scattering mechanism. The expected increase in the electronic component of thermal conductivity for these SL films was too small to be detected by the PL measurement system, $k_e \leq 0.06$ $Wm^{-1}K^{-1}$ at 100 K. Figure 4-12 shows just the lattice component of thermal conductivity for all of the samples. The solid line indicates an increase in lattice thermal conductivity that is inversely proportional to temperature. The lattice thermal conductivity of samples #M212 and #M213, $k_{lat} \approx 0.4$ $Wm^{-1}K^{-1}$, is near the theoretical limit for amorphous

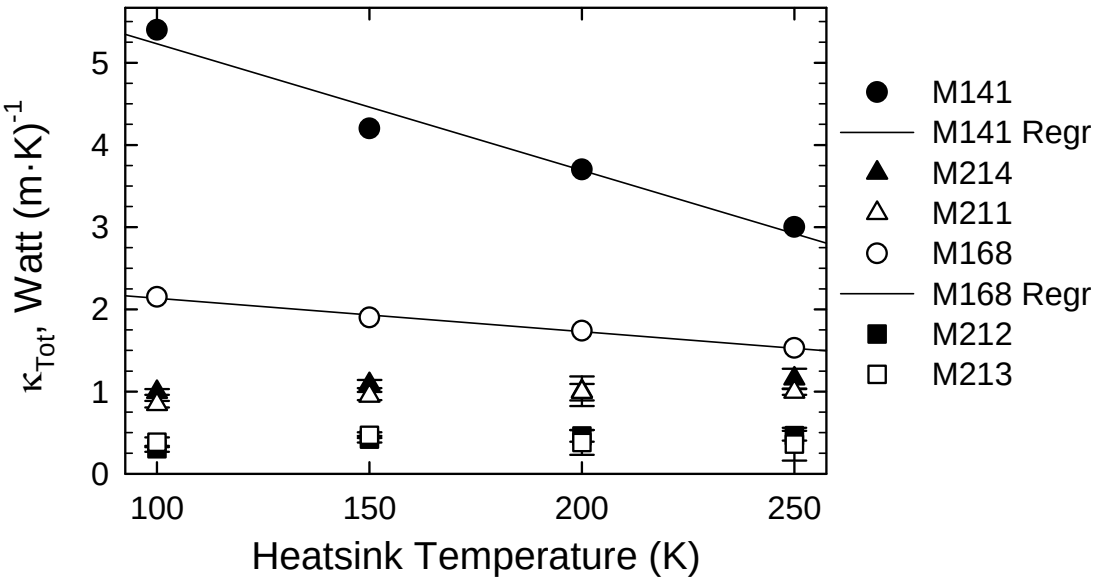

Figure 4-11: The total thermal conductivity of different SL samples compared to sample #M141 with a single PbSe test layer (lines to guide the eye).

materials [36] yet these samples retain crystalline electronic transport properties. This agrees well with the results of other IV-VI semiconductor nanostructured SL material [35] in the temperature range from 300 K to 700 K. *Androulakis and coworkers* fabricated periodic structures of PbSnTe and PbS with spinodal decomposition that resulted in with alternating material layers that were in the range of 2-5 nm thick. The lattice thermal conductivity reported for different samples ranged from 0.4 $Wm^{-1}K^{-1}$ to 1.1 $Wm^{-1}K^{-1}$ based on the stoichiometric ratio of growth components that determined the layer thickness. In addition the lattice thermal conductivity their samples did not change significantly with temperature. Figure 4-13 shows the lattice thermal conductivity as a function of the average layer thickness for the entire structure for the SL samples tested for this research. The thermal conductivity is highly linear and agrees with the equation for the phonon lifetime due to boundary scattering, Eq. 4.4. This trend is consistent for a heatsink temperature of 250 K and 100 K with an LLS fit quality of R^2 = 0.928 and R^2 = 0.956 respectively. This data contradicts the report of

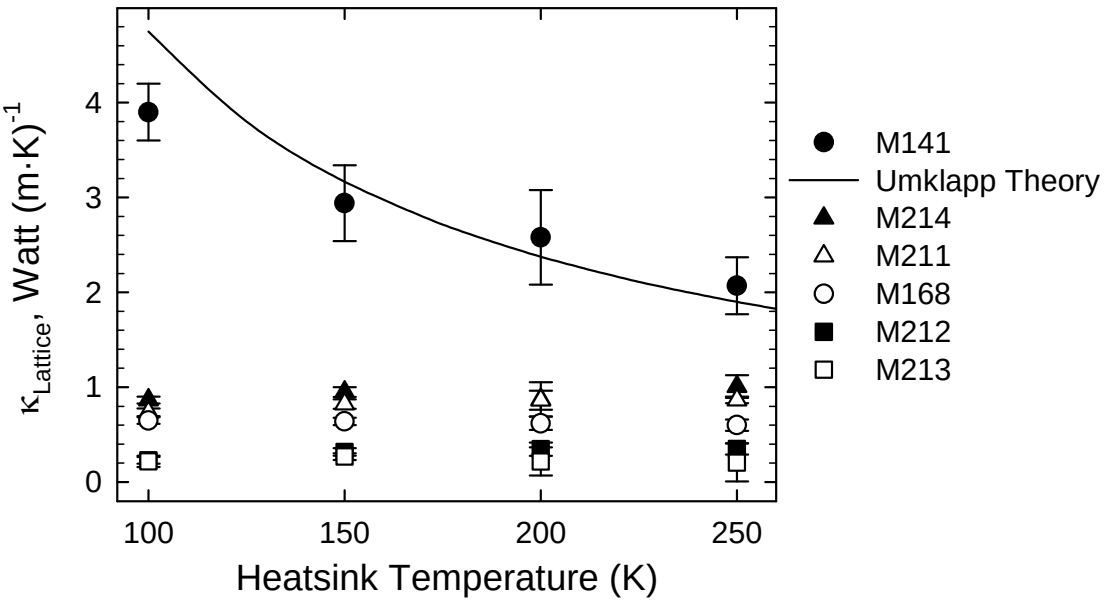

Figure 4-12: Lattice thermal conductivity from 250 K to 100 K for MQW on PbSe and MQW on SL thin films.

[17] that showed that the lowest lattice thermal conductivity, $k_{lat} \approx 0.33$ $Wm^{-1}K^{-1}$, for PbTe/PbSeTe SLs occurred for layers that were 7 nm thick and k_{lat} increased for thinner layers. However, these SL materials were grown by thermal evaporation and the epitaxial layers exhibited "kinks" attributed to "subsurface polishing damage" to the BaF_2 substrate during preparation.

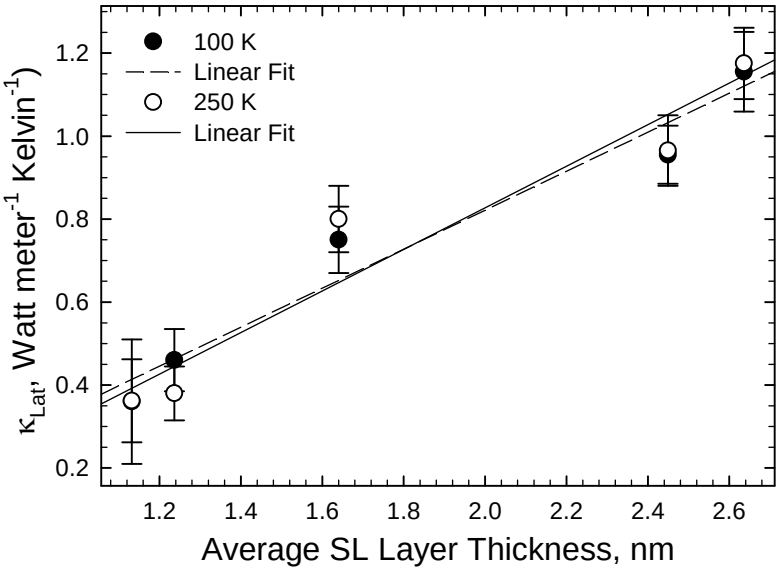

Figure 4-13: Total thermal conductivity as a function of heterojunction per distance for intrinsic and doped MQW films.

4.5 Summary and Conclusions

The temperature dependence of bulk nanostructured IV-VI semiconductor MBE-grown materials was investigated with a PL induced heating effect experiment analyzed with FE thermal modeling. A custom testing apparatus using a liquid nitrogen cooled cryostat was developed to precisely control film temperature across a large temperature range 90 K to 320 K. Data collection was automated with a custom software program using a standard computer serial bus interface to control multiple instruments including a PID temperature controller. This software included advanced

timing control to manage the thermal stress applied to films due to rapid cooling and heating during testing. Analysis of the PL emission from several MQW on SL films provided insight into electrical and thermal energy transport in these nanostructures. Both the intensity and distribution of PL emission over a broad temperature range was documented. In addition the measured PL emission FWHM for un-doped MQW on SL films #M211, #M212, #M213, and #M214 decreased linearly with temperature at approximately the same value irrespective of intensity changes. However, for film #M168 the FWHM decreased more drastically than all other films indicating less heating at lower temperatures and therefore a higher thermal conductivity than un-doped MQW on SL films.

The thermal conductivity of all films, extrapolated from the measured PL emission shifts with a FE thermal model, was clearly related to both electronic carrier properties and physical film dimensions. Both film samples with doped n-type carrier concentrations had decreased heating and higher thermal conductivity compared to un-doped films at all temperatures. The thermal conductivity of these two films (#M168 and #M141) increased with temperature from 1.5 $Wm^{-1}K^{-1}$ and 3.0 $Wm^{-1}K^{-1}$ at 250 K to 2.2 $Wm^{-1}K^{-1}$ and 5.4 $Wm^{-1}K^{-1}$ at 100 K respectively. Assuming a nominal Seebeck coefficient as reported elsewhere [21] and that the cross-plane electrical conductivity of film #M168 is reduced from measured Hall effect values by 20% this films exhibits a $ZT \approx 0.77$ at 250 K that reduces to $ZT \approx 0.21$ at 100 K. These ZT values correspond to a theoretical maximum temperature difference $\Delta T \equiv (T_H - T_C) = z(T_C^2)/2$ for a TE cooling device [37] of $\Delta T_{250K} = 56$ K and $\Delta T_{100K} = 8$ K.

The SL films with similar undoped p-type carrier concentrations had a total thermal conductivity at a heatsink temperature of 250 K: #M211 (k_{tot} = 1.15 $Wm^{-1}K^{-1}$), #M212 (k_{tot} = 0.44 $Wm^{-1}K^{-1}$), #M213 (k_{tot} = 0.42 $Wm^{-1}K^{-1}$), and #M214 (k_{tot} = 0.94 $Wm^{-1}K^{-1}$). These films exhibited little or no change in optical heating during PL measurements, and therefore thermal conductivity, over the temperature range 100 K to 250 K. The difference in total thermal conductivity between these films and doped SL film #M168 is explained by differences in the electrical conductivity calculated from Hall effect measurements. The Hall effect data were used with a Lorenz number, calculated using a parabolic band approximation developed by others, to estimate the cross-plane thermal conductivity from electrical carriers (k_e) using the Wiedemann-Franz law. The electronic component of thermal conductivity was subtracted from the total thermal conductivity to estimate the lattice thermal conductivity for all samples. The lattice thermal conductivity was a nearly linear function (R^2 = 0.95) of the average layer thickness in the SLs between the optically active MQW layers and the silicon substrate at all test temperatures. No difference in the measured k_{lat} based on the number of SL pairs (30 for the thickest layers of 5 nm and 300 for the thinnest layers of 0.5 nm) or number of SL types (3, 5, or 7) that may have indicated any phonon wave reflection effects [38] were readily observed.

Chapter 4 References

1. C. M. Bhandari, *"Chapter 14: Size Effects on Thermal Transport"*, *Thermoelectrics Handbook: Macro to Nano (Ed. D. M. Rowe)*, Taylor and Francis, Boca Raton, pp. 1-10 (2006)

2. H. Wang, Y. Pei, A. D. Lalonde, and G. J. Snyder, "Heavily doped p-type PbSe with high thermoelectric performance: an alternative for PbTe", *Adv. Materials*, **23**, pp. 1366-1370 (2011)

3. Z. Tian, J. Garg, K. Esfarjani, T. Shiga, J. Shiomi, and G. Chen, "Phonon conduction in PbSe, PbTe, and $PbTe_{1-x}Se_x$ from first principle calculations", *Phys. Rev. B*, **85**, 184303 (2012)

4. J. He, S. N. Girard, M. G. Kanatzidis, and V.P. Dravid, "Microstructure-lattice thermal conductivity correlation in nanostructured $PbTe_{0.7}S_{0.3}$ thermoelectric materials", *Adv. Func. Mater.*, **20**, pp. 764-772 (2010)

5. S. S. Shalyt, V. M. Muzhdaba, and A. D. Galetskaya, "Lattice and electronic thermal conductivity of PbTe, PbSe, and PbS", *Soviet Phys. – Solid State*, **10**(5), pp. 1018-1024 (1968)

6. A. A. El-Sharkawy, A. M. Abou El-Azm, M. I. Kenawy, A. S. Hillal, and H. M. Abu-Basha, "Thermophysical properties of polycrystalline PbS, PbSe, and PbTe in the temperature range 300-700K", *Int. J. Thermophys.,* **4**(3), pp. 261-269 (1983)

7. H. Romero, M. Cardona, R. K. Kremer, R. Lauck, G. Siegle, J. Serrano, and X. C. Gonze, "Lattice properties of Pb*X* (*X* = S, Se, Te): Experimental studies *ab initio* calculations including spin-orbit effects", *Phys. Rev. B*, **78**, 224302 (2008)

8. E. C. Svensson, B. N. Brockhouse, and J. M. Rowe, "Crystal dynamics of copper", *Phys. Rev.*, **155**(3), pp. 619-632 (1967)

9. A. J. Minnich, M. S. Dresselhaus, Z. F. Ren, and G. Chen, "Bulk nanostructured thermoelectric materials: current research and future prospects", *Energy Environmental Science*, **2**, pp. 466-479 (2009)

10. J. Androulakis, D.-Y. Chung, X. Su, L. Zhang, C. Uher, T. C. Hasapis, E. Hatzikraniotis, K. M. Paraskevopoulos, M. G. Kanatzidis, "High-temperature charge and thermal transport properties of the n-type thermoelectric material PbSe", *Phys. Rev. B*, **84**, 155207 (2011)

11. M. G. Holland, "Analysis of lattice thermal conductivity", *Phys. Rev.*, **132**(6), pp. 2461-2471 (1963)

12. P. Lindenfeld and W. B. Pennebaker, "Lattice conductivity of copper alloys", *Phys. Rev.*, **127**, No. 6, pp. 1881-1889 (1962)

13. D. G. Cahill, K. E. Goodson, and A. Majumdar, "Thermometry and Thermal Transport in Micro/Nanoscale Solid-State Devices and Structures", *ASME J. Heat Transfer*, **124**(2), pp. 223-241, (2002)

14. R. Kim, S. Datta, and M. Lundstrom, "Influence of dimensionality on thermoelectric device performance", *J. Appl. Phys.*, **105**, 034506 (2009)

15. J. Martin, G. S. Nolas, W. Zhang, and L. Chen, "PbTe nanocomposites synthesized from PbTe nanocrystals", *Appl. Phys. Lett.*, **90**, 222112 (2007)

16. B. Zhang, J. He, X. Ji, and T. M. Tritt, "Size-selective high-yield growth of lead telluride (PbTe) nanocrystals using a chemical vapor deposition technique", *Appl. Phys. Lett.*, **88**, 043119 (2006)

17. J. C. Caylor, K. Coonley, J. Stuart, T. Colpitts, and R. Venkatasubramanian, "Enhanced thermoelectric performance in PbTe-based superlattice structure from reduction of lattice thermal conductivity", *Appl. Phys. Lett.*, **87**, 023105 (2005)

18. Y. K. Koh, C. J. Vineis, S. D. Calawa, M. P. Walsh, and D. G. Cahill, "Lattice thermal conductivity of nanostructured thermoelectric materials based on PbTe", *Appl. Phys. Lett.* **94**, No. 153101 (2009)

19. M. Zebarjadi, K. Esfarjani, A. Shakouri, J.-H. Bahk, Z. Bian, G. Zeng, J. Bowers, H. Lu, J. Zide, and A. Gossard, "Effect of nanoparticle scattering on thermoelectric power factor", *Appl. Phys. Lett.*, **94**, No. 202105 (2009)

20. D. Parker and D. J. Singh, "High temperature thermoelectric performance of heavily doped PbSe", *Phys. Rev. B*, **82**, No. 035204 (2010)

21. V. Jovovic, S. J. Thiagarajan, J. P. Heremans, T. Komissarova, D. Khokhlov, and A. Nicorici, "Low temperature thermal, thermoelectric, and thermomagnetic transport in indium rich $Pb_{1-x}Sn_xTe$ alloys", *J. Appl. Phys.* **103**, No. 053710 (2008)

22. R. Kamana, *Development of an Instrument for Sensitive Measurement of Mid-Infrared Radiation*, Master's Thesis, University of Oklahoma (2006)

23. L. A. Elizondo, Y. Li, A. Sow, R. Kamana, H. Z. Wu, S. Mukherjee, F. Zhao, Z. Shi, and P. J. McCann, "Optically pumped mid-infrared light emitter on silicon", *J. Appl. Phys.*, **101**, No. 104504, (2007)

24. P. J. McCann, K. Namjou, and X. M. Fang, "Above-room temperature continuous-wave mid-infrared photoluminescence from PbSe/PbSrSe quantum wells", *Appl. Phys. Lett.*, **75**, No. 23, pp. 3608-3610 (1999)

25. M. D. Dickey, R. C. Chiechi, R. J. Larsen, E. A. Weiss, D. A. Weitz, and G. M. Whitesides, "Eutectic Gallium-Indium (EGaIn): a liquid metal alloy for the formation of stable structures in microchannels at room temperature", *Adv. Functional Materials*, **18**, pp. 1097-1104 (2008)

26. H. Zogg, S. Blunier, A. Fach, C. Maissen, P. Muller, S. Teodoropol, V. Meyer, G. Kostorz, A. Dommann, and T. Richmond, "Thermal-mismatch-strain relaxation in epitaxial CaF2, BaF2/CaF2, and PbSe/BaF2/CaF2 layers on Si(111) after many temperature cycles", *Phys. Rev. B*, **50**, No. 15 (1994)

27. T. X. Hoai, K. H. Herrmann, and D. Genzow, "A new attempt for understanding temperature-dependent thresholds in lead salt injection lasers", *Physica Status Solidus (a)*, **64**, pp. 239-248 (1981)

28. J. D. Jeffers, K. Namjou, Z. Cai, P. J. McCann, and L. Olona, "Cross-plane thermal conductivity of a PbSnSe/PbSe superlattice material", *Appl. Phys. Lett.*, **99**, No. 41903 (2011)

29. W. B. Joyce, "Expression for the Fermi energy in narrow-gap semiconductors", *IEEE J. Quantum Elec.*, **QE-19**, No. 11, pp. 1625-1627 (1983)

30. G. K. White, "The thermal and electrical conductivity of copper at low temperatures", *Australian J. Physics*, **6**, No. 4, pp. 397-404 (1953)

31. P. D. Maycock, "Thermal conductivity of silicon, germanium, III-V compounds, and III-V alloys", *Solid State Elec.*, **10**, pp. 161-168 (1967)

32. G. Partridge, "Ceramic materials possessing high thermal conductivity", *Adv. Materials*, **4**, No. 1, pp. 51-54 (1992)

33. V. V. Kosarev, P. V. Tamarin, and S. S. Shalyt, "Thermal conductivity of indium antimonide at low temperatures", *Physica Stat. Solid. (B)*, **44**, pp. 525-534 (1971)

34. R. J. Sladek, "Thermal conductivity of indium-thallium alloys at low temperatures", *Phys. Rev.*, **97**, No. 4, pp. 902-915 (1955)

35. J. Androulakis, C.-H. Lin, H.-J. Kong, C. Uher, C.-I. Wu, T. Hogan. B. A. Cook, T. Caillat, K. N. Paraskevopoulos, and M. G. Kanatzidis, "Spinodal decomposition and nucleation and growth as a means to bulk nanostructured thermoelectrics: enhanced performance in Pb1-xSnxTe-PbS", *J. Am. Chem. Soc.*, **129**, pp. 9780-9788 (2007)

36. C. Chiritescu, C. Mortensen, D. G. Cahill, D. Johnson, and P. Zschack, "Lower limit to the lattice thermal conductivity of nanostructured Bi_2Te_3-based materials", *J. Appl. Phys.*, **106**, No. 073503 (2009)

37. D. M. Rowe, *"Chapter 1: General Principles and Basic Considerations"*, *Thermoelectrics Handbook: Macro to Nano (Ed. D. M. Rowe)*, Taylor and Francis, Boca Raton, pp. 1-15 (2006)

38. M. Maldovan, "Narrow low-frequency spectrum and heat management by thermocrystals", *Phys. Rev. Lett.* **110**, 025902 (2013)

Chapter 5

PbSe/PbSnSe Acoustic Distributed Bragg Reflectors

5.1 Motivation

Quantum mechanics treats photon, electron, and phonon propagation with a particle-wave duality that mathematically results in interference effects when the particle wavelength is similar to the structural periodicity of the materials. The distributed Bragg reflector (DBR) uses the repetitive difference of the index of refraction, n, between two materials fabricated in thin alternating layers that are stacked in pairs to enhance the reflectivity of macrostructures for waves of a particular wavelength [1, 2]. Figure 5-1 shows DBRs used to create the high reflectivity mirrors at either end of a single material gain medium similar to the diagram of a vertical cavity surface emitting laser (VCSEL) [3, 4] or an acoustic micro-cavity (AMC) [5]. These devices are designed for a target wavelength ($\lambda_0 = hc_{vac}/E_0$) that determines the optimized thickness of each layer in a pair. The reflectivity of an optical DBR is

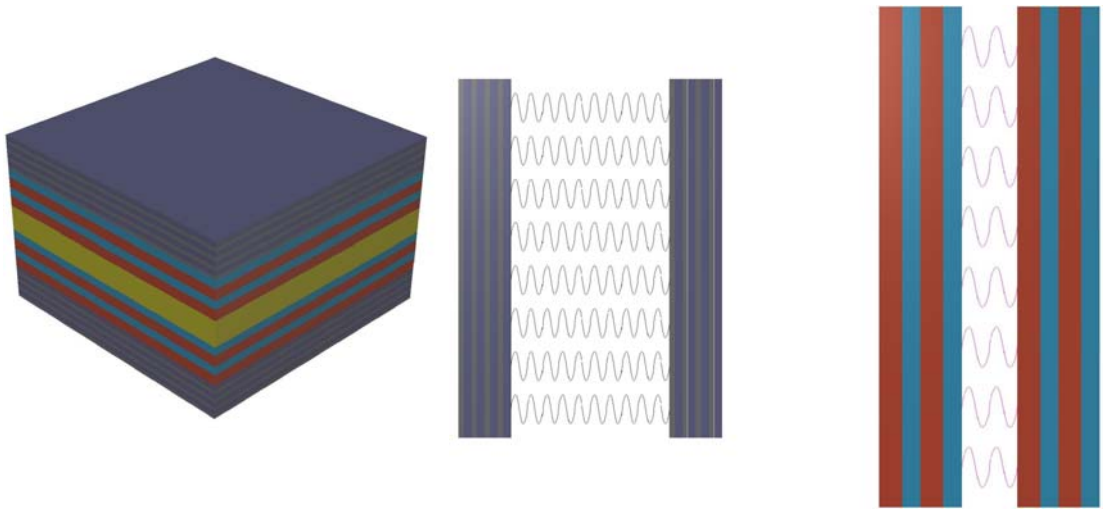

Figure 5-1: Diagram of a gain medium surrounded by two different types of DBRs with different thickness layers that reflect different particle wavelengths.

determined by the number of pairs and the difference between two material parameters: n and either the electric field permittivity, ε, or the magnetic permeability, μ. A high contrast between these parameters in each DBR layer increases the reflectivity of each pair and minimizes the total mirror thickness required to achieve a given reflectivity. The mid-IR VCSELs reported in [4] were fabricated using IV-VI semiconductor lead selenide (PbSe) as the gain medium with three-pair DBR mirrors using alternating layers of BaF_2 and PbSrSe. The reflectivity of the top and bottom mirror was set by varying the percentage, x, of strontium in $Pb_{1-x}Sr_xSe$ layers.

Researchers have proposed that optical wave theory analogs can be applied to atomic crystal waves or phonons to design and create an "acoustic laser" [6-7]. Several applications in medical imaging and treatment would benefit from high power, single frequency, and focused sonic waves [8-10]. Table 5-1 contains a summary of acoustic DBR devices demonstrating enhanced phonon populations with the relevant material properties compared to PbSe. This experimental evidence was predicted by the acoustic mismatch model (AMM) outlined by *Mizuno and Tamura* [16] who showed that GaAs/AlAs acoustic DBR structures needed a layer thickness $d_{SL} \leq 10$ nm for confinement of the high energy longitudinal acoustic phonon (sound wave). The AMM calculation is based on differences in the material density (ρ) and LA phonon velocity (V_T) between two layers. The AMC device structure used for phonon confinement experiments typically employs optical stimulation and excited carrier decay to create additional phonons in the gain media requiring multiple cavities as shown in Figure 5-1. The effects can be observed with Raman spectrometers measuring the in-elastically scattered pump light or an additional probe beam. The Raman spectra of AMCs have

Table 5-1: Relevant acoustic DBR material parameters for phonon wave reflection.

Materials		Ref	Thick.		Layer	Acoustic Properties			
			1	2	Pairs	ρ_1	$V_{T,1}$	ρ_2	$V_{T,2}$
Layer 1	Layer 2		nm		#	g/cm^3	km/s	g/cm^3	km/s
AlAs	GaAs	11	7.4	3.8	12	5.360	5.61	3.96	5.35
AlAs	GaAs	12	6.1	2.4	11	5.360	5.61	3.96	5.35
$BaTiO_3$	$SrTiO_3$	13	2	5	10	--	5.42	--	7.85
Si	$Si_{0.4}Ge_{0.6}$	14	8	4	20	2.39	8.43	4.25	5.82
PbSe	$Pb_{0.93}Sr_{0.07}Se$	15	N/A: Calculations			8.274	4.02	7.822	4.20
PbSe	$Pb_{0.85}Sn_{0.15}Se$	15				8.274	4.02	7.854	4.25

clearly demonstrated enhancement of single wavelength zone-center, dispersion-less high energy acoustic phonons. However, it is still unclear whether low energy acoustic phonons have similar properties or if these quasi-particles exhibit behavior analogous to differences in radio wave transmission compared to photons or x-rays.

In addition to the development of novel devices, the acoustic DBR, also called superlattices (SLs) to denote a fundamental difference in the governing physics, have been shown to alter the thermoelectric (TE) properties of materials. The lattice thermal conductivity, k_{lat}, of a material is proportional to the lifetime, τ_{ph}, or mean free-path, Λ_{PH}, of acoustic phonons that are scattered at the interface (boundary) between two materials. Therefore nanostructured bulk materials can be designed with SLs consisting of several hundred interfaces, each separated by several nanometers, in a much thicker composite material that has a low thermal conductivity. The diffuse mismatch model (DMM) assumes phonons scatter due to differences in lattice periodicity [17] where the magnitude of phonon scattering is dependent on several material properties including the interface roughness [18]. These factors combined with the difficulty in fabricating

ideal atomic monolayer SLs has led to debate in the scientific literature over the theoretical possibilities for reduction of k_{lat} due to coherent effects resulting in phonon reflection in nanostructured materials. While no clear evidence of phonon coherence being observed in thermal conductivity measurements exists to date [19-21], the potential benefits of optimization of TE materials merits further investigation. More recent research into SL material with alternating layers of isotopic silicon [22] may address the complexity of isolating a single phonon scattering mechanism amongst several since the only difference between SL layers is atomic mass.

This chapter presents novel calculations and design theory for acoustic DBR material with enhanced TE performance using superlattices of PbSe/PbSnSe. There is a brief review of the important material parameters used in optical, electrical, and acoustic wave theory. A numerical method for calculation of electron transmission in SLs available in the literature is adapted for optical DBRs to establish basic design theory and material system comparisons. Similar techniques for coherent acoustics are then employed to present the first known analysis of this type for IV-VI semiconductors. These theoretical calculations are discussed with respect to experimental results of thermal transport properties for several thin films with varying complex SL designs that were characterized using a photoluminescence technique. The section will conclude with optimized film designs rules for nanostructured thin films that maximize cross-plane TE performance.

5.2 Material Parameters in PbSe/SnSe Superlattices

IV-VI semiconductor bulk material properties have been measured experimentally by several groups [23-25]. Research on PbSe for room temperature

long-wavelength optical detectors has provided the following information: a temperature dependent band structure that has a direct gap along the <111> crystal axes at the L-point in reciprocal with $E_g(300\ K) \approx 280$ meV, a relative permittivity or dielectric constant, $\varepsilon_R = 227$, an absorption coefficient for 900 nm photons, $\alpha = 1 \times 10^5$ cm^{-1}, and an index of refraction, $n = 5.0$. The material properties can be tailored to applications by the introduction of a small percentage, x, of elements such as strontium or tin to make ternary $Pb_{1-x}Sr_xSe$ [4] or $Pb_{1-x}Sn_xSe$ [26]. Figure 5-2 shows the rock-salt crystal structure indicating the different directional axes for these materials. The ternary compound $Pb_{0.85}Sn_{0.15}Se$ has smaller bandgap energy while that of $Pb_{0.93}Sr_{0.07}Se$ is greater than that of bulk PbSe. Researchers have clearly demonstrated the effect of dimensional confinement on energy levels in nanostructures such as a SL or a multiple quantum well (MQW). A PbSrSe/PbSe/PbSrSe MQW film oriented in the <111> crystal direction shows the presence of at least two quantized energy levels due to carriers with different effective masses [27]. PbSe has 4-fold degenerate valleys at the L-point in reciprocal space that separate into different oblique and longitudinal energy

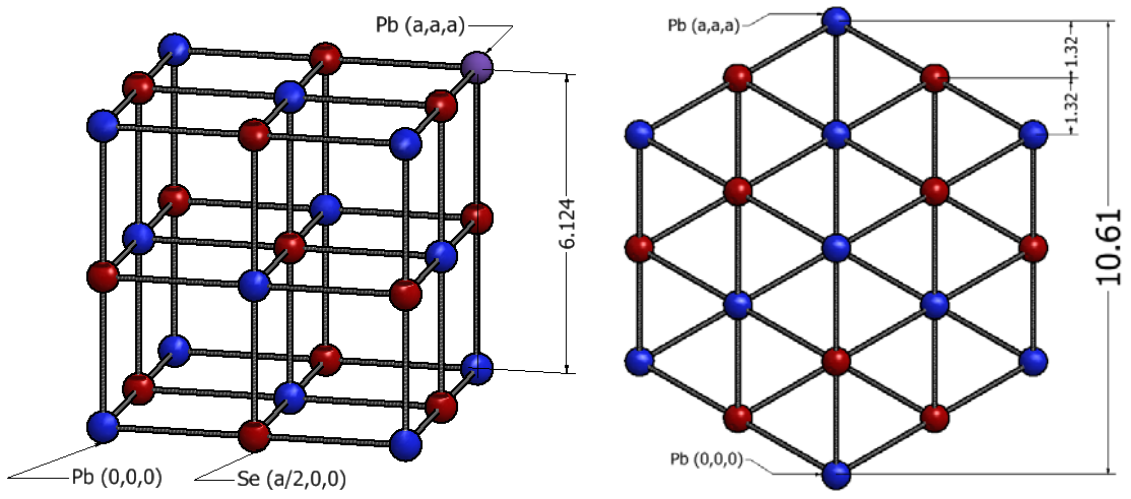

Figure 5-2: Rock salt crystal structure and directional orientation for PbSe/PbSnSe thin film SLs.

levels when dimensional confinement in a <111>-oriented plane is implemented. It is also well understood that this quantization of energy levels reduces Auger scattering and increases the electron lifetime.

In addition to the optoelectronic properties the quantum mechanical properties of phonons for PbSe including the bulk modulus, or Young's modulus parameters, used to calculate the material stiffness has been well investigated [28-33]. The importance of the phonon energy dispersion relation, Figure 5-3, and the density of states (DOS) in calculations of TE performance for PbSe has been completed using theoretical models such as the constant gradient approximation and spin-orbit interaction [34]. First principles calculations of phonon transport properties indicated the lifetime of acoustic phonons at 300 K is $\tau_{ph} \leq 100$ ps with an average $\Lambda_{ph} \approx 3$ nm [35].

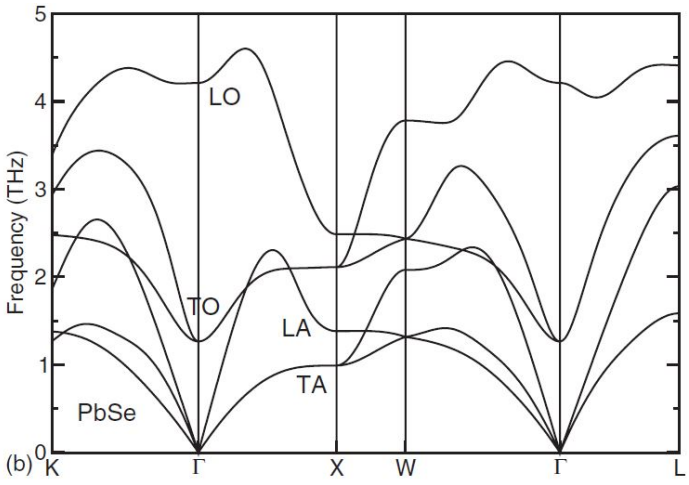

Figure 5-3: Phonon energy dispersion for PbSe from literature [33].

5.3 Transfer matrix method for Light Waves

In order to understand the effect of wave transmission and reflection through an interface of dissimilar media Maxwell's equations for electromagnetic waves in one dimension has been thoroughly investigated. In the direction perpendicular to the

alternating stacks forming the superlattice of an optical DBR the wave equation for the optical and electro-magnetic fields in each material must match at the boundary. The differential form of the equation for a photon wave is shown in Eq. 5.1. The first order differential equation includes the angular frequency of the optical wave, ω, adjusted by

$$\frac{\partial \psi_Z}{\partial x^2} + \left(\frac{\omega^2}{c_{vac}^2} n_{med}^2 - \beta^2 \right) \psi_Z = 0 \tag{5.1}$$

the speed of the light in the medium, $c_{med} = c_{vac}/n_{med}$. Combined with a similar form for the transverse magnetic (TM) field, H with proper normalization ($\eta_0 = \mu_0/\varepsilon_0$), a linear set of equations governing the optical EM wave is given by Eq. 5.2. The wave vector

$$\begin{pmatrix} \Psi_z \\ \eta_0 H_y \end{pmatrix} = \begin{pmatrix} Ae^{ik_l x} + Be^{-ik_l x} \\ \frac{-kc}{\omega \mu_r} \left(Ae^{ik_l x} - Be^{-ik_l x} \right) \end{pmatrix} \tag{5.2}$$

relation, neglecting phase, is given by $k = \omega/v_{wave}$ and the TM equation is adjusted by the material's relative magnetic permeability. These equations can be used with the numerical techniques shown in [1] to define a layer propagation matrix, P_l, which can be used to describe the entire structure for a TM polarized optical wave, Eq. 5.3. This

$$P_l = \begin{pmatrix} \cos(k_l d_l) & i \frac{\omega \mu_{rl}}{c k_l} \sin(k_l d_l) \\ i \frac{c k_l}{\omega \mu_{rl}} \sin(k_l d_l) & \cos(k_l d_l) \end{pmatrix}, \quad M^p = P_1 P_3 P_4 ... P_l ... P_n \tag{5.3}$$

normalized linear equation can be applied to optical DBRs with n layers to form a simple equation describing the effect of the entire structure on both wave equations with a single 2x2 matrix as shown in Eq. 5.4. These linear numerical methods can be implemented using computer techniques such as the National Instruments LabVIEW Version 2011 software development environment [36]. It has been shown in great

detail through analysis of these equations that when DBRs are designed for a particular wavelength the thickness of each layer with maximum reflectance occurs when $d = \lambda_{medium}/4$ where the wavelength in the medium is that of the incoming wave in a vacuum

$$\begin{pmatrix} A_1 \\ B_1 \end{pmatrix} = M_{1,n} \begin{pmatrix} A_n \\ B_n \end{pmatrix}$$

$$M_{1,n}^{TE} = \frac{1}{2} \begin{pmatrix} 1 & -\dfrac{\omega\mu_{r1}}{ck_1} \\ 1 & \dfrac{\omega\mu_{r1}}{ck_1} \end{pmatrix} \begin{pmatrix} M_{11}^{P} & M_{12}^{P} \\ M_{21}^{P} & M_{22}^{P} \end{pmatrix} \begin{pmatrix} 1 & \dfrac{1}{ck_n} \\ -\dfrac{ck_n}{\omega\mu_{rn}} & \dfrac{ck_n}{\omega\mu_{rn}} \end{pmatrix} \quad \textbf{(5.4)}$$

adjusted by the index of refraction. The overall design of a DBR mirror using two different material systems is shown in Figure 5-4. These two designs are optimized for photons with λ_{air} = 1 μm and show the differences in the material systems. The larger difference in refractive index between layers of silicon and silicon dioxide (SiO_2), $\Delta n \approx$ 56 %, compared to that between gallium arsenide (GaAs) and aluminum arsenide (AlAs), $\Delta n \approx$ 15 %, requires significantly fewer mirror pairs ($\approx 5 < 22$) to achieve the same total 99.9% reflectivity. However, since SiO_2 has a much lower index of refraction (n = 1.5) than the other materials ($n \geq 3$) these layers must be thicker. This

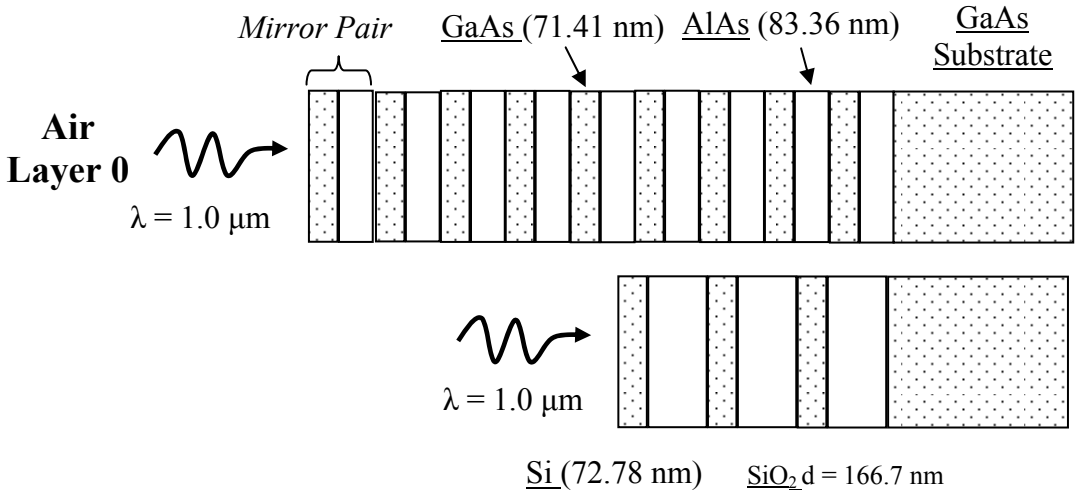

Figure 5-4: Bragg reflector design difference in materials for incident light.

system of linear equations can be reduced to a simple transmittance and reflectance ($T = 1-R$) for photons in SLs as a function of the wave energy, wave vector, and matrix elements and determinants. Figure 5-5 shows these techniques applied to calculating optical DBR reflectance for different materials. In addition to a greater reflectivity at the design wavelength with a fewer number of mirror pairs (or total thickness) for the Si/SiO_2 mirrors the central optical "stop-band" ($\Delta\lambda$) is much wider emphasizing the importance of contrast in the index of refraction (optical wave speed) and the EM field impedance in each material.

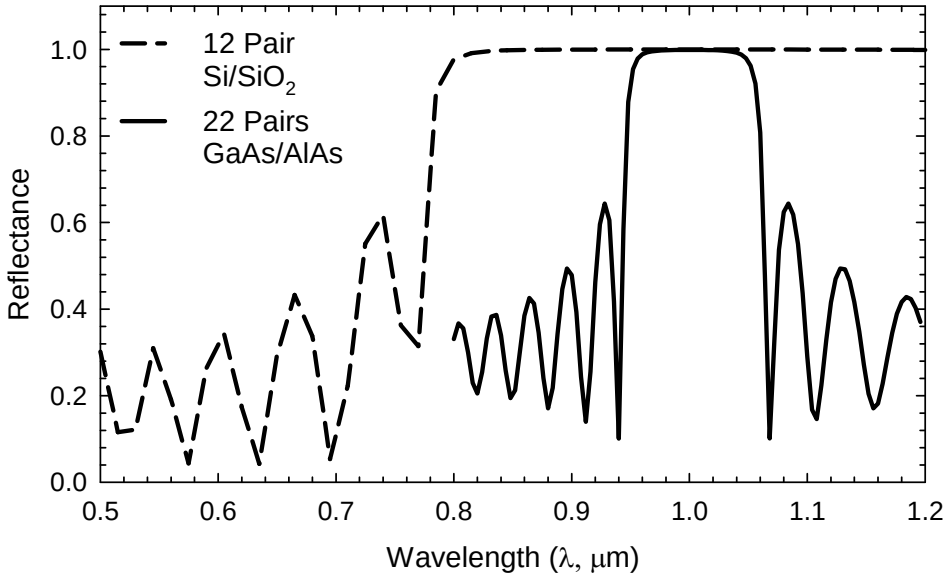

Figure 5-5: Calculated reflection coefficient for multiple pairs of acoustic Bragg reflectors for phonon waves of various energy.

5.4 Transfer matrix method for Phonon Waves

The design of acoustic DBRs for phonon waves cannot use the transverse electro-magnetic field equation in order to solve for the two unknowns (A and B) in the solutions of Eq. 5.2. Therefore the governing equations for AMM theory and calculations [16] require conservation of the real force associated with atomic lattice

displacement in an elastic continuum or the stress, *S*. Eq. 5.6 shows these equations and the propagation matrix for a single layer, *l*, describing phonon wave motion. The stress is a function of the wave frequency, the material density, and phonon velocity.

$$\begin{pmatrix} \Psi_l \\ S_l \end{pmatrix} = \begin{pmatrix} Ae^{ik_l x} + Be^{-ik_l x} \\ i\omega\eta_l\left(Ae^{ik_l x} - Be^{-ik_l x}\right) \end{pmatrix} \Rightarrow P_l = \begin{pmatrix} \cos(k_l d_l) & \frac{1}{\omega\eta}\sin(k_l d_l) \\ -\omega\eta\sin(k_l d_l) & \cos(k_l d_l) \end{pmatrix} \quad \textbf{(5.5)}$$

The latter two properties can be grouped in a single term: the acoustic impedance, $\eta \equiv \rho/v_{ph}$. This term is analogous to the optical index of refraction and describes the relative change in acoustic wave speed between two materials. Since the stress is real the equation must be scaled by an imaginary number, $i^2 = -1$, that results in a different form for the combined layer propagation matrix, shown in Eq. 5.7, compared to the

$$P_l P_m = \begin{pmatrix} \cos(L)\cos(M) - \frac{\eta_l}{\eta_m}\sin(L)\sin(M) & \sin(L)\cos(M) - \frac{\eta_l}{\eta_m}\cos(L)\sin(M) \\ -\sin(L)\cos(M) - \frac{\eta_m}{\eta_l}\cos(L)\sin(M) & \cos(L)\cos(M) - \frac{\eta_m}{\eta_l}\sin(L)\sin(M) \end{pmatrix} \quad \textbf{(5.6)}$$

optical method described previously. The capital letters L and M represent the product of the wave vector, k_{ph}, and thickness, *d*, in either of the two material layers (*l* or *m*). *Mizuno and Tamura* simplified the system into a single equation for the reflectance of the entire DBR stack, Eq. 5.8, where *a*, *b*, *c*, and *d* represent different calculations on

$$T = \frac{4(\eta_l/\eta_m)}{(a(\eta_l/\eta_m) - b(\eta_l/\eta_m))^2 + (c + d(\eta_l/\eta_m))^2} \quad \textbf{(5.7)}$$

the propagation matrix detailed in the paper. This technique predicted that a GaAs-AlAs acoustic DBR with ≈ 1 nm thick layers could be used to reflect phonons with a frequency approximately 1 THz or less. This technique and this material system were subsequently employed by researchers to design and demonstrate the acoustic

microcavity as detailed in Table 5-1. In addition to difference in the wave function and normalization techniques between optical and acoustic DBRs the behavior of phonons and solutions of the previous equations shown reflectance is maximized when each layer thickness is designed with the relationship, $d_{layer} = \lambda_{ph}/2$.

5.4.1 Reflection Coefficient, Filtering, and Design Considerations

The publications on AMC research contain a variety of calculations for the reflectance of acoustic DBRs based on the thickness of each material layer and the number of pairs as shown in Figure 5-6. As with optical DBRs and the index of refraction, the contrast in the acoustic impedance between the two materials used for the mirror layers determines both the maximum reflectance and the stop-band width. As also shown these structures exhibit enhanced reflectance for waves with an energy that are integer multiples of the lowest, $E = nE_0$. The AlAs/GaAs materials have a difference $\Delta\eta \approx 15\%$ [?] and ACM devices have been fabricated with mirrors having 20 or fewer pairs. Since these materials have similar crystal structure they can be fabricated on one

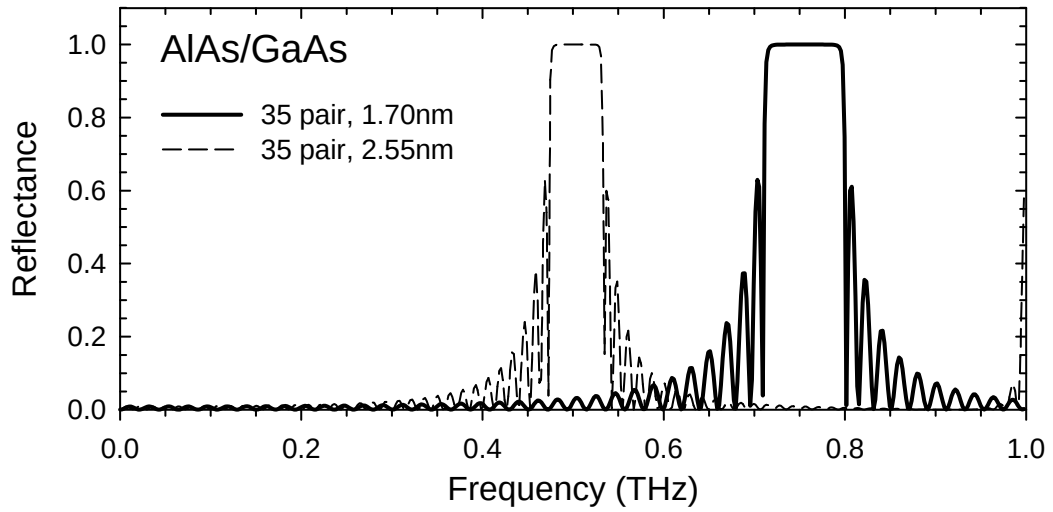

Figure 5-6: Calculated reflection coefficient for different thickness AlAs/GaAs acoustic DBRs.

another using a variety of techniques and therefore no one has reported on the use of ternary materials since the difference in η between layers would be reduced requiring an overall thicker device with a more narrow energy range reflected. Figure 5-7 shows the combination of two different SLs with a different layer thickness fabricated on top of each other to form a composite mirror capable of reflecting multiple energies. It should also be noted that each SL type with a different thickness continues to have enhanced reflectance at integer multiples of each design frequency, and two or SLs reflect a more broad range of the phonon spectrum and create a denser "comb" filter that blocks a greater percentage of the total spectral power density.

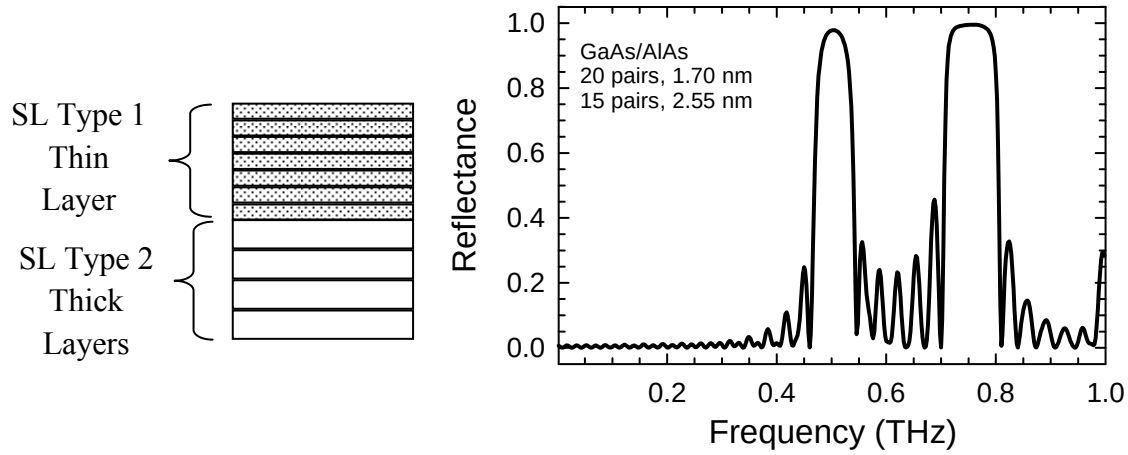

Figure 5-7: Diagram of a single film with a combination of multiple acoustic DBRs with different layer thickness and the calculated reflectance.

5.4.2 PbSe/PbSnSe Material Modeling

Using the material parameters of Table 5-1 to calculate the acoustic impedance mismatch between the layers of a PbSe/$Pb_{0.85}Sn_{0.15}Se$ SL the difference is relatively small ($\Delta\eta \approx 4\%$). Figure 5-8 shows the difference in the lowest energy reflectance for two different acoustic DBR thicknesses of PbSe/PbSnSe. The thicker 2.4 nm layers have a lower energy reflection peak while the 1.2 nm layers reflects a wave energy

twice as large with a wider energy peak. Figure 5-9 shows the lowest energy with maximum reflectance as a function of mirror layer thickness. These energies are shifted for similar thickness layers compared to the theoretical calculations of GaAs/AlAs DBR systems where the materials are less dense and the phonon velocity is slightly larger. It should be noted that in these calculations both film layers were the same, not following the λ/2 design principle requires a 10 % thicker PbSnSe layer in order to maximize the

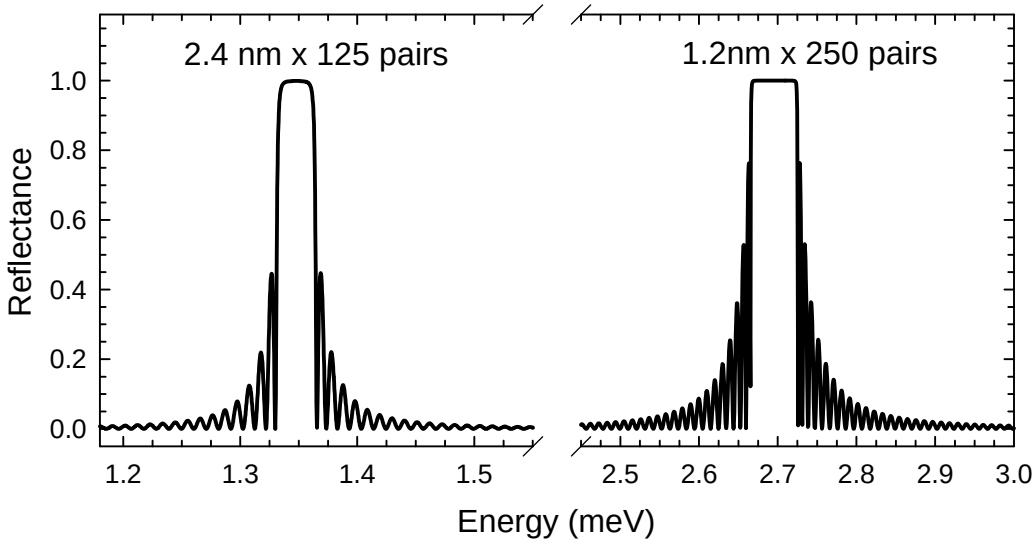

Figure 5-8: Calculated reflectance at the lowest energy for two different thickness layers for PbSe/PbSnSe acoustic Bragg reflectors.

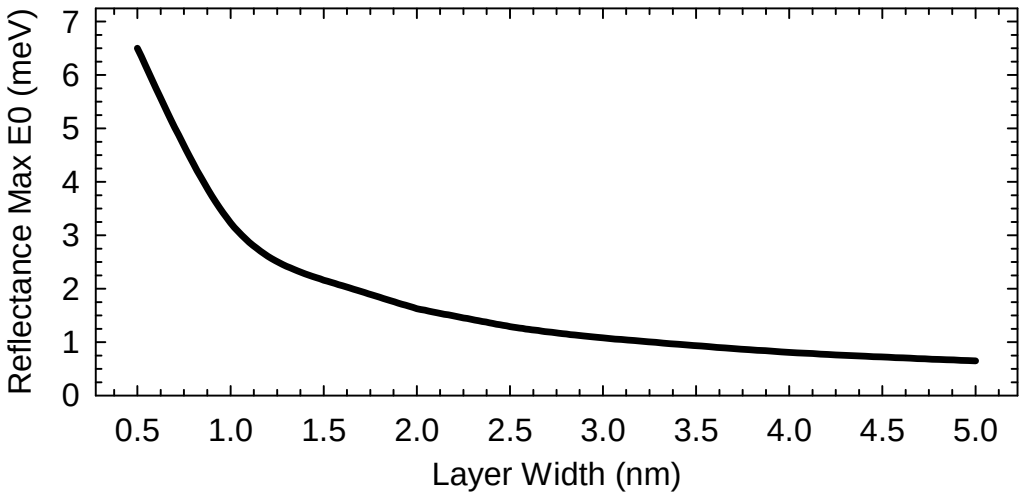

Figure 5-9: The lowest energy phonon waves with a non-zero reflectance maximum for PbSe/PbSnSe acoustic DBR layer thickness.

reflectance. This non-ideal design creates a slight anti-symmetry in the reflectance peak shape with a decreased magnitude on the low energy side of the peak center. Figure 5-10 shows the maximum reflectance for the lowest energy phonon for a varying number of SL pairs. For nearly all mirror designs the number of pairs required was greater than 50 to achieve 90 % reflectance while more than 150 DBR pairs has a reflectance above 99.9 %. As would be expected this ternary material system SL requires a significantly larger number of pairs than the GaAs/AlAs AMC devices due to a lower contrast in acoustic impedance.

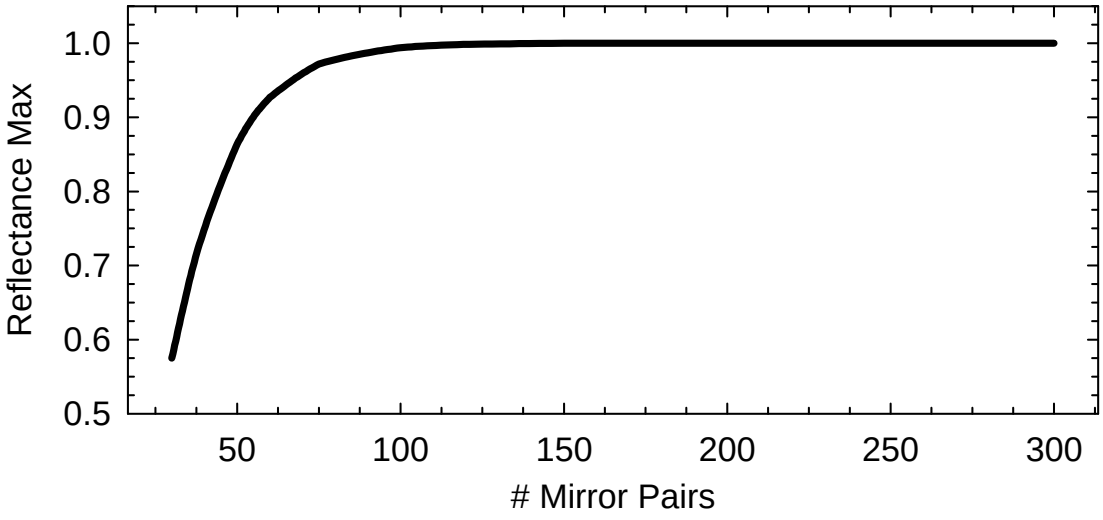

Figure 5-10: The number of mirror pairs and reflectivity of acoustic DBRs of PbSe/PbSnSe with 0.5 nm layers.

5.5 Theory of Heat Transport in Phonons

The economic and social importance of TE materials is largely due to potential applications in "green" energy production using a solid-state device. In order to compete on a "cost-per-Watt" basis with current fossil-fuel technology efficient conversion of the energy associated with light in photovoltaic cells and a temperature differential in Peltier devices must be increased [37]. Historical reviews of heat

transport theory and the various mechanisms involved in thin film TE performance are readily available in the literature [38]. The most common engineering approach to improving the thermopower figure of merit, $ZT = T(S^2\sigma)/(k_{lat} + k_e)$, in nano-structured materials is through reduction of k_{lat} by increased phonon scattering that lowers τ_{ph} effectively limiting Λ_{ph} with the "size effect". Most scattering mechanisms typically have an energy dependence resulting in limited effects on long-wavelength phonons. However the most well accepted heat transport theory from the Debye-Peirls and Callaway models of particle behavior attributes thermal conductivity to these same low energy acoustic branch phonons with long mean free paths. Figure 5-11 shows the *ab initio* calculated phonon DOS for PbSe from [33]. This function is convolved with the Bose-Einstein distribution to determine the occupation probability of phonons at a particular energy. These models are typically verified by measuring the temperature dependence of thermal conductivity. Above room temperature ($\geq$ 300 K) anomalies in this theory have been observed by *Androulakis et al* [39] who suggested k_{lat} for highly doped PbSe was also due to optical phonon interaction with excited electronic carriers. At lower temperatures the term phonon "freeze-out" is used to describe a decrease in the total free particle population at higher energies. However this apparent reduction of phonons for thermal transport is offset by less phonon-phonon scattering that increases τ_{ph} and the mean free-path that phonons travel before scattering. Therefore the thermal conductivity in bulk PbSe increases dramatically (100X) as the material temperature is lowered from 300 K down to 20 K [28]. To date most published results from SL films [38, 40] have shown this increase of k_{lat} does not occur at lower temperatures and optimized TE materials have thin SL layers.

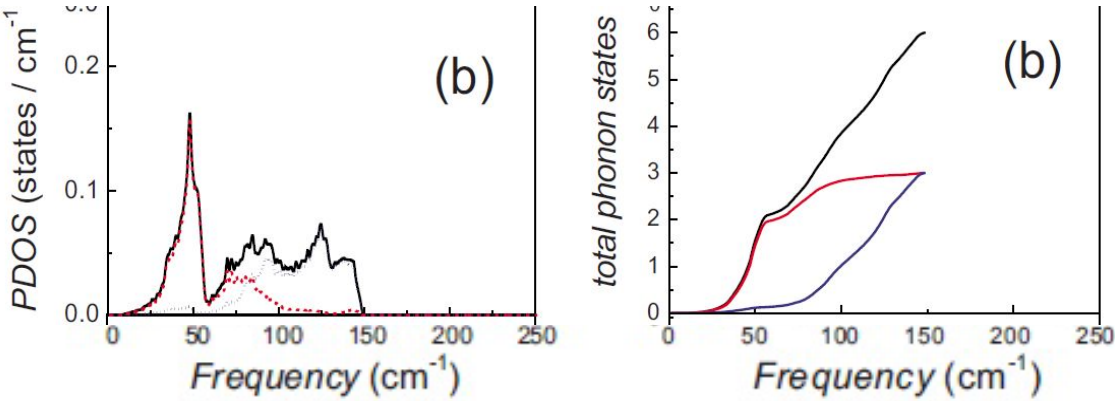

Figure 5-11: Calculated phonon DOS for PbSe from [33].

5.5.1 Thermal Conductivity Measurements for SLs

Figure 5-12 shows the optical and acoustic nano-structure designs of several PbSe/PbSrSe MQW and PbSe/PbSnSe SL thin films fabricated by molecular beam epitaxy (MBE) on silicon wafers using techniques detailed previously in the literature [27]. The films shown contain several structural differences including the average SL layer thickness (d_{avg}), the maximum SL layer thickness (d_{max}), and the number of

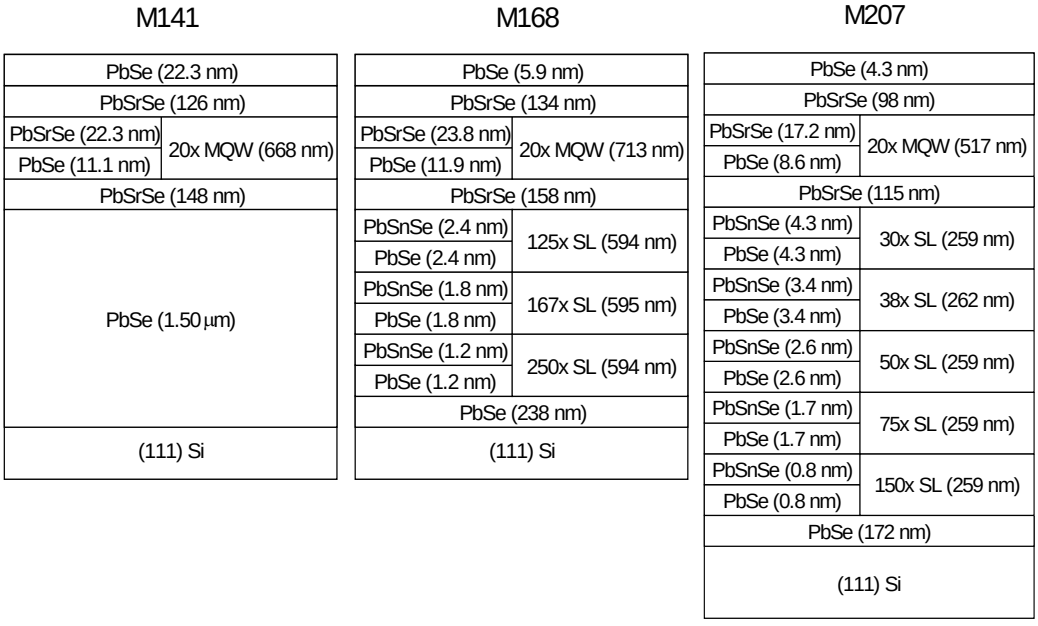

Figure 5-12: Comparison of SL films fabricated and characterized with different layer thickness and number of pairs.

multiple SL layer thickness (SLx) fabricated in a single structure. These films were characterized over a broad temperature range in Chapter 4 and Figure 5-13 shows the calculated lattice thermal conductivity of these films shown at 250 K. Carrier doped SL film #M168 and similarly fabricated but un-doped SL films #M211-M214 exhibited a reduced $k_{lat} \propto 1/d_{avg}$ compared to bulk PbSe (film #M141) at all temperatures. It should be noted that film #M168 exhibited a much higher k_{tot} during thermal characterization that was attributed to the electronic transport component and a different electronic carrier concentration. Since the total phonon lifetime is a statistical combination of different mechanisms it is impossible to isolate the effects of a single type of scattering (diffuse or acoustic) with the experiments used. However, these SL films also possess the properties of acoustic DBRs that mathematically results in coherent effects and enhanced reflectance of phonons within a limited range of energies. While there may not be a real-world physical effect on low energy phonons there is likely a limited effect on higher energy acoustic phonons and the optical branches. However, the general

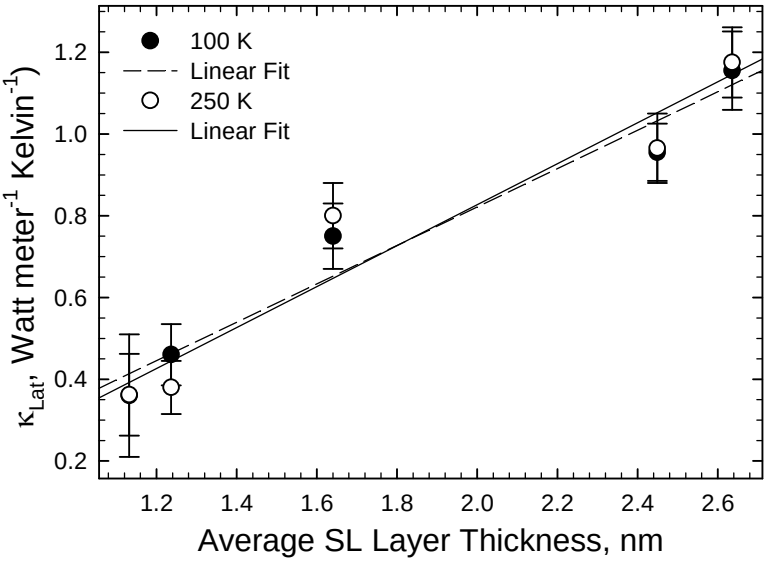

Figure 5-13: Lattice thermal conductivity calculated from PL measurements for different SL films at 250 K and 100 K.

DBR principles discussed indicate multiple SLs films should enhance total phonon scattering across a wide energy range of the phonon DOS and films with thicker SL pairs should reflect a greater percentage of lower energy acoustic branch phonons.

5.5.2 Discussion of Thermal Characterization and Acoustic Reflection

The SL structural designs for the different thin films tested for this research are summarized in Table 5-2 and detailed in Appendix B. The SL films had three, five, or seven different layer thicknesses with each type having a different number of pairs in order to maintain a similar total film thickness for direct comparison of the data acquired in the measurement technique used. All films possessed a nominally similar thinnest SL layer, d_{min} = 1.0 ± 0.5 nm, while the thickest SL had layers d_{max} = 5.0 nm. Since the crystal structure of these materials is intertwined single element simple cubic the distance between atomic planes in the transverse <111> direction for these films is approximately 1.3 Å. Therefore the thinnest layers that were fabricated, d_{min} = 0.5 nm, were ≈ 2-3 atomic monolayers while the thickest SL layer was 30 atomic layers. All films had symmetrically thick layers in the SL pairs ($d_1 = d_2$). Films #M211 and #M212 both have the same number of SLs (5) but a different combination of SL layer thicknesses resulting in a different average layer thickness. Films #M213 and #M214 were designed with an average layer thickness similar to a corresponding SL5 film but with more layer thicknesses (7) that limited each SL type to fewer pairs and a lower reflectivity for each mirror. Figure 5-14 shows the different low energy reflectance peaks calculated for several of the films analyzed. Films #M211 and #M214 with the thicker maximum SL layers would theoretically exhibit coherent reflection for lower energy phonons in the acoustic branches while having a nearly identical high energy

Table 5-2: SL layer thickness estimated from design and total sample thickness.

Film ID #	SL1		SL2		SL3		SL4		SL5		SL6		SL7		Avg. Thick. nm
	nm	#	nm	#	nm	#	nm	#	nm	#	nm	#	nm	#	
M168	1.2	250	1.8	167	2.4	125									1.65
M211	1.1	150	2.2	75	3.4	50	4.5	38	5.6	30					2.45
M212	0.6	300	1.1	150	1.7	100	2.3	75	2.8	60					1.24
M213	0.6	200	0.8	133	1.1	100	1.4	80	1.7	67	1.9	57	2.2	50	1.13
M214	1.9	67	2.2	57	2.5	50	2.8	44	3.1	40	3.4	36	3.7	33	2.64

reflectance due to similar minimum thickness layers compared to film #M212. However the thicker SL layer design resulted in fewer mirror pairs and a reduced reflectance as shown in Figure 5-15. The trade-off between these two factors results in a nearly identical expected improvement in k_{lat} from coherent effects on acoustic phonons. This was calculated by numerically integrating the reflectance across the entire phonon energy spectrum and neglecting the DOS for PbSe. All films tested and analyzed had a predicted coherent enhancement from reflection of phonon waves up to 50 meV using a distributed Bragg structure between R_{max} = 9.0 % and R_{min} = 7.8 % for

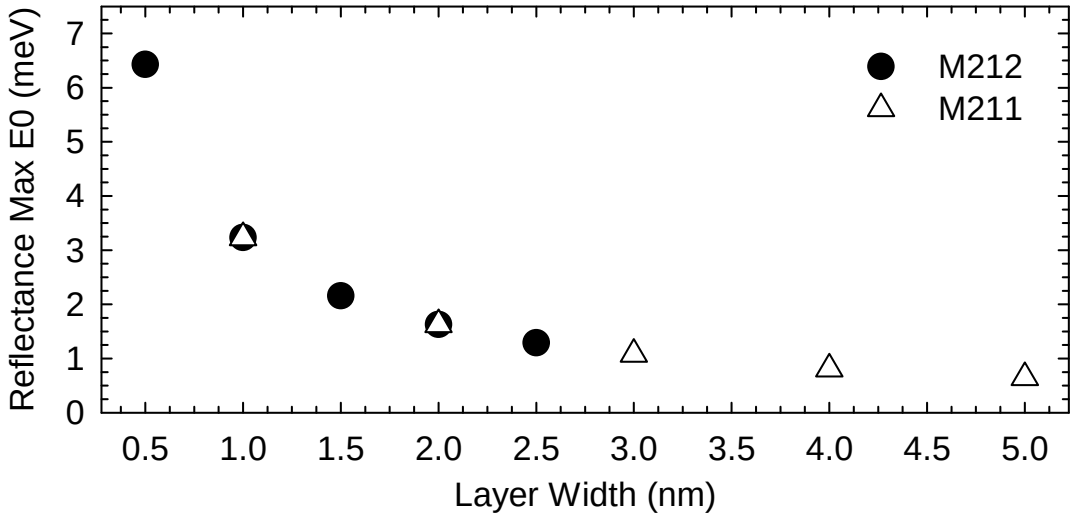

Figure 5-14: Comparison of the phonon energy reflected by the different SL layer thicknesses for films #M211 and #M212.

films #M214 and #M212 respectively. This value increased slightly for SL films with thicker layers in the low energy acoustic phonon range ($E_{ph} \leq 10$ meV). However at the testing temperatures and with the calculated measurement noise level, see Chapter 2 and the error bars of Figure 5-13, a difference of ≈ 1 % could not be detected in the data. In addition since diffuse scattering clearly dominates thermal transport ($\tau_{dif} << \tau_{coh}$) in these structures and coherent effects would only constitute a small portion of the reduction in total phonon lifetime. Therefore the total expected difference in k_{lat} between films in the tested temperature range is estimated to be less than 0.01 %. However at significantly higher (700 K) or lower (10 K) temperatures when the phonon DOS distorts the differences in acoustic reflection could become apparent.

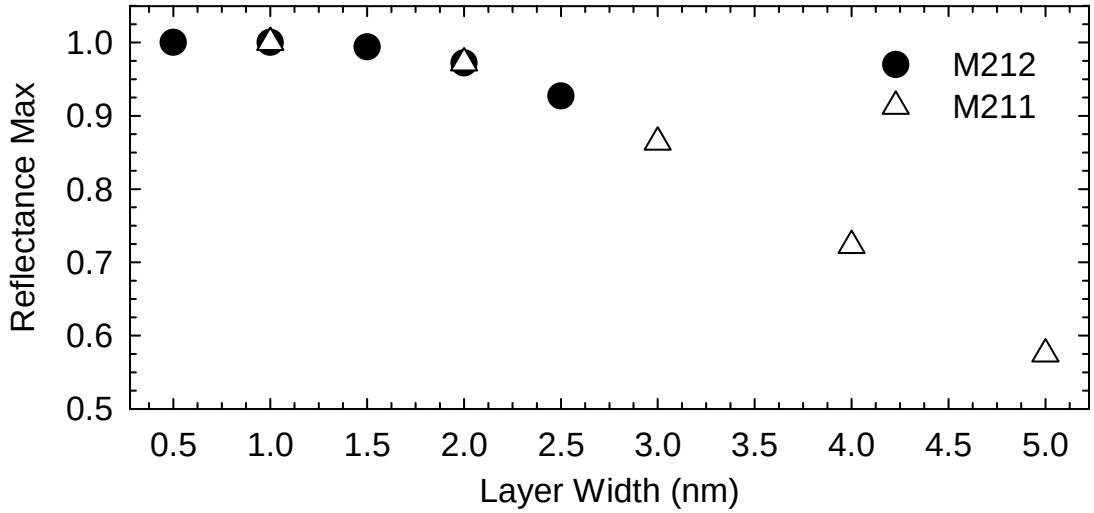

Figure 5-15: Comparison of the reflectance for the different SL layer thicknesses for films #M211 and #M212.

5.6 Summary and Conclusions

The first analysis of acoustic distributed Bragg reflectors using ternary IV-VI semiconductors was presented. The well accepted diffuse mismatch model predicts all

phonons are scattered at material interfaces due to difference in crystal structure. This has led to the development of novel nano-structured SL material with thin layers and a reduced lattice thermal conductivity. An additional coherent effect on phonon motion in SL films has been widely discussed in the literature as a potential design route for both optimizing *ZT* in composite TE materials or enhancing device capabilities such as lower/higher temperature operation. Multiple researchers have experimentally demonstrated acoustic micro-cavities using several material systems to fabricate acoustic DBRs capable of reflecting high energy zone center phonons. However it still remains unclear whether low energy acoustic phonons are affected by these periodic structures with a thickness much smaller than the phonon wavelength.

The different acoustic material parameters necessary for designing PbSe/$Pb_{0.85}Sn_{0.15}Se$ SL structures were provided and compared to the more well developed material systems such as GaAs/AlAs. A numerical method using linear solutions to wave equations developed in the literature as a generic approach for calculating electron transmission through SL films was adapted to calculate photon transmission. The energy dependent reflectance plots of different thickness SL layers were reviewed to establish the engineering design considerations for maximizing DBR reflectance while minimizing film thickness. These results were compared to the acoustic mismatch model for calculating acoustic DBRs to reflect phonon waves in SL layers thinner than 5 nm and up to 300 mirror pairs. These calculations indicated that at least 150 mirror pairs were necessary to achieve 99.9% reflectivity.

These principles were applied to analysis of several MBE grown thin films fabricated with complex optical and acoustic structures for thermoelectric property

characterization. The temperature dependence of bulk nanostructured IV-VI semiconductor thermal conductivity investigated with a PL induced heating effect experiment previously showed a linear relationship with respect to average SL layer thickness. Additionally these film designs were crafted to have different coherent phonon effects and reflect different amounts of the total phonon energy spectrum by altering the layer thickness, the number of different layer thickness types, and the number of SL pairs in each film. Calculations predicted all films reflected between 8 % and 9 % of the total phonon energy range. However in the tested temperature range (100 K to 350 K) the average phonon mean free path is less than 10 nm and these acoustic structures would have limited effect compared to diffuse properties.

Chapter 5 References

1. M. Born and E. Wolf, *Principles of Optics (7th Edition),* Cambridge University Press, Cambridge, UK (1999)

2. P. Yeh, A. Yariv, and C.-S. Hong, "Electromagnetic propagation in periodic stratified media. I. General theory", *J. Opt. Soc. Am.*, **67**(4), pp. 423-438 (1977)

3. B. Lambert, Y. Toudic, Y. Rouillard, M. Gauneau, M. Baudet, F. Alard, I. Valiente, and J. C. Simon, "High reflectivity 1.55 μm (Al)GaAsSb/AlAsSb Bragg reflector lattice matched on InP substrates", *Appl. Phys. Lett.*, **64**(4), pp. 442-444 (1995)

4. Z. Shi, G. Xu, P. J. McCann, X. M. Fang, N. Dai, C. L. Felix, W. W. Bewley, I. Vurgaftman, and J. R. Meyer, "IV-VI compound midinfrared high-reflectivity mirror and vertical-cavity surface-emitting lasers grown by molecular beam epitaxy", *Appl. Phys. Lett.*, **76**(25), pp. 3688-3690 (2000)

5. A. Fainstein, B. Jusserand, V. Thierry-Mieg, "Raman scattering enhancement by optical confinement in a semiconductor planar microcavity", *Phys. Rev. Lett.*, **75**(20), pp. 3764-3767 (1995)

6. S. T. Zavtrak, "Acoustic laser with dispersed particles as an analog of a free-electron laser", *Phys. Rev. E*, **51**(3), pp. 2481-2485 (1995)

7. J. Chen and J. B. Khurgin, “Feasibility analysis of phonon lasers”, *IEEE J. Quantum Elec.*, **39**(4), pp. 600-607 (2003)

8. P. V. Chitnis, H.-P. Brecht, R. Su, and A. A. Oraevsky, “Feasibility of optoacoustic visualization of high-intensity focused ultrasound-induced thermal lesions in live tissue”, *J. Biomedical Opt.*, **15**(2), 021313 (2010)

9. W. Yang, S. Zhang, W. Li, Yaq. Chen, H. Lu, W. Chen, and Yaz. Chen, “Partial dependence of breast tumor malignancy on ultrasound image features derived from boosted trees”, *J. Electronic Imaging*, **19**(2), 023004 (2010)

10. E. M. Boctor, P. Stolka, H.-J. Kang, C. Clarke, C. Rucker, J. Croom, E. C. Burdette, and R. J. Webster III, “Precisely shaped acoustic ablation of tumors utilizing steerable needle and 3D ultrasound image guidance”, *Proc. SPIE: Medical Imaging 2010*, **7625**, 7652N-1 (2010)

11. I. Camps, S.S. Makler, H. M. Pastawski, and L. E. F. Foa Torres, “GaAs-$Al_xGa_{1-x}As$ double-barrier heterostructure phonon laser: A full quantum treatment”, *Phys. Rev. B*, **64**, 125311 (2001)

12. M. Trigo, A. Bruchhausen, A. Fainstein, B. Jusserance, and V. Thierry-Mieg, “Confinement of acoustical vibrations in a semiconductor planar phonon cavity”, *Phys. Rev. Lett.*, **89**(22), 227402 (2002)

13. A. Soukiassian, W. Tian, D. A. Tenne, X. X. Xi, D. G. Schlom, N. D. Lanzillotti-Kimura, A. Bruchhausen, A. Fainstein, H. P. Sun, X. Q. Pan, A. Cros, and A. Cantarero, “Acoustic Bragg mirrors and cavities made using piezoelectric oxides”, *Appl. Phys. Lett.*, **90**, 042909 (2007)

14. Y. Ezzahri, S. Grauby, J. M. Rampnoux, H. Michel, G. Pernot, W. Claeys, S. Dilhaire, C. Rossignol, G. Zeng, and A. Shakouri, “Coherent phonons in Si/SiGe superlattices”, *Phys. Rev. B*, **75**, 195309 (2007)

15. I. I. Zasavitskii, E. A. Silva, E. Abramof, and P. J. McCann, “Optical deformation potential for PbSe and PbTe”, *Phys. Rev. B*, **70**, 115302 (2004)

16. S. Mizuno and S.-i. Tamura, “Theory of acoustic-phonon transmission in finite-size superlattice systems”, *Phys. Rev. B*, **45**(2), pp. 734-741 (1992)

17. P. E. Hopkins, J. C. Duda, C. W. Petz, and J. A. Floro, “Controlling thermal conductance through quantum dot roughening at interfaces”, *Phys. Rev. B*, **84**, 035438 (2011)

18. F. Gather, C. Heiliger, and P. J. Klar, “Modeling of interface roughness in thermoelectric composite materials”, *J. Phys.: Cond. Matter*, **23**, 335301 (2011)

19. J. C. Caylor, K. Coonley, J. Stuart, T. Colpitts, and R. Venkatasubramanian, "Enhanced thermoelectric performance in PbTe-based superlattice structure from reduction of lattice thermal conductivity", *Appl. Phys. Lett.*, **87**, 023105 (2005)

20. W. S. Capinski, H. J. Maris, T. Ruf, M. Cardona, K. Ploog, and D. S. Katzer, "Thermal-conductivity measurements of GaAs/AlAs superlattices using a picosecond optical pump-and-probe technique", *Phys. Rev. B*, **59**(12), pp. 8105-8113 (1999)

21. J. C. Duda, T. S. English, E. S. Piekos, W. A. Sofa, L. V. Zhigilei, and P. E. Hopkins, "Implications of cross-species interactions on the temperature dependence of Kapitza conductance", *Phys. Rev. B*, **84**, 1933301 (2011)

22. G. Bastuan, A. Vogelsang, and C. Schiffmann, "Isotopic superlattices for perfect phonon reflection", *J. Electronic Materials*, **39**(9), pp. 1769-1771 (2010)

23. R. Dalven, "A review of the semiconductor properties of PbTe, PbSe, PbS, and PbO", *Infrared Physics*, **9**, pp. 141-184 (1969)

24. N. Suzuki, K. Sawai, and S. Adachi, "Optical properties of PbSe", *J. Appl. Phys.*, **77**(3), pp. 1249-1255 (1995)

25. A. Rogalski, J. Antoszewski, and L. Faraone, "Third generation infrared photodetector arrays", *J. Appl. Phys.*, **105**, 091101 (2009)

26. S. L. Elizondo and Z. Shi, "One-dimensional analysis of N-on-p $Pb_{1-x}Sn_xSe$ compositionally graded heterojunction photodetectors", *J. Appl. Phys.*, **101**, 114510 (2007)

27. L. A. Elizondo, Y. Li, A. Sow, R. Kamana, H. Z. Wu, S. Mukherjee, F. Zhao, Z. Shi, and P. J. McCann, "Optically pumped mid-infrared light emitter on silicon", *J. Appl. Phys.*, **101**, 104504 (2007)

28. S. S. Shalyt, V. M. Muzhdaba, and A. D. Galetskaya, "Lattice and electronic thermal conductivity of PbTe, PbSe, and PbS", *Sov. Phys. – Solid State*, **10**(5), pp. 1018-1024 (1968)

29. C. A. Kennedy and K. J. Linden, "Some properties of the quaternary system PbSnTeSe", *J. of Appl. Phys.*, **41**(1), pp. 252-253 (1970)

30. R. Grisar, W. J. Reidel, and H. M. Preier, "Properties of diffused PbSnSe homojunction Diode Lasers", *IEEE J. Quant. Elec.*, **QE-17**(5), pp. 586-592 (1981)

31. P. Giannozzi, S. de Gironcoli, P. Pavone, and S. Baroni, "*Ab initio* calculation of phonon dispersions in semiconductors", *Phys. Rev. B*, **43**(9), pp. 43-54 (1991)

32. A.-I. Yang, H.-Z. Wu, Z. F. Li, D. J. Qiu, Y. Chang. J. F. Li, P. J. McCann, and X. M. Fang, "Raman scattering study of PbSe grown on (111) BaF_2 substrate", *Chinese Phys. Lett.*, **17**(8), pp. 606-609 (2000)

33. Y. Zhang, X. Ke, C. Chen, J. Yang, and P. R. C. Kent, "Thermodynamic properties of PbTe, PbSe, and PbS: First-principles study", *Phys. Rev. B*, **80**, 023404 (2009)

34. H. Romero, M. Cardona, R. K. Kremer, R. Lauck, G. Siegle, J. Serrano, and X. C. Gonze, "Lattice properties of Pb*X* (*X* = S, Se, Te): Experimental studies *ab initio* calculations including spin-orbit effects", *Phys. Rev. B*, **78**, 224302 (2008)

35. Z. Tian, J. Garg, K. Esfarjani, T. Shiga, J. Shiomi, and G. Chen, "Phonon conduction in PbSe, PbTe, and PbTe1-xSex from first principle calculations", *Phys. Rev. B*, **85**, 184303 (2012)

36. National Instruments LabVIEW Version 2011, Austin, Texas, USA

37. M. S. Dresselhaus, G. Chen, M. Y. Tang, R. Yang, H. Lee, D. Wang, Z. Ren, J.-P. Fleurial, and P. Gogna, "New directions for low-dimensional thermoelectric materials", *Adv. Materials*, **19**, pp. 1043-1053 (2007)

38. D. G. Cahill, K. E. Goodson, and A. Majumdar, "Thermometry and Thermal Transport in Micro/Nanoscale Solid-State Devices and Structures", *ASME J. Heat Transfer*, **124**(2), pp. 223-241 (2002)

39. J. Androulakis, D.-Y. Chung, X. Su, L. Zhang, C. Uher, T. C. Hasapis, E. Hatzikraniotis, K. M. Paraskevopoulos, M. G. Kanatzidis, "High-temperature charge and thermal transport properties of the n-type thermoelectric material PbSe", *Phys. Rev. B*, **84**, 155207 (2011)

40. Y. K. Koh, C. J. Vineis, S. D. Calawa, M. P. Walsh, and D. G. Cahill, "Lattice thermal conductivity of nanostructured thermoelectric materials based on PbTe", *Appl. Phys. Lett.* **94**, 153101 (2009)

Chapter 6

Summary and Future Investigations

6.1 Summary of Results

This dissertation described research on the measurement, and analysis of the thermal conductivity of IV-VI semiconductor nanostructures for high-performance solid state thermoelectric power generation and refrigeration devices. Figure 6-1 shows the first experimental measurements of cross-plane lattice thermal conductivity in superlattice (SL) material composed of PbSe and $Pb_{0.85}Sn_{0.15}Se$ layers in the temperature range from 100 K to 300 K. The results show that the lattice thermal conductivity, k_{lat}, of nanostructured materials is much lower than the values for bulk

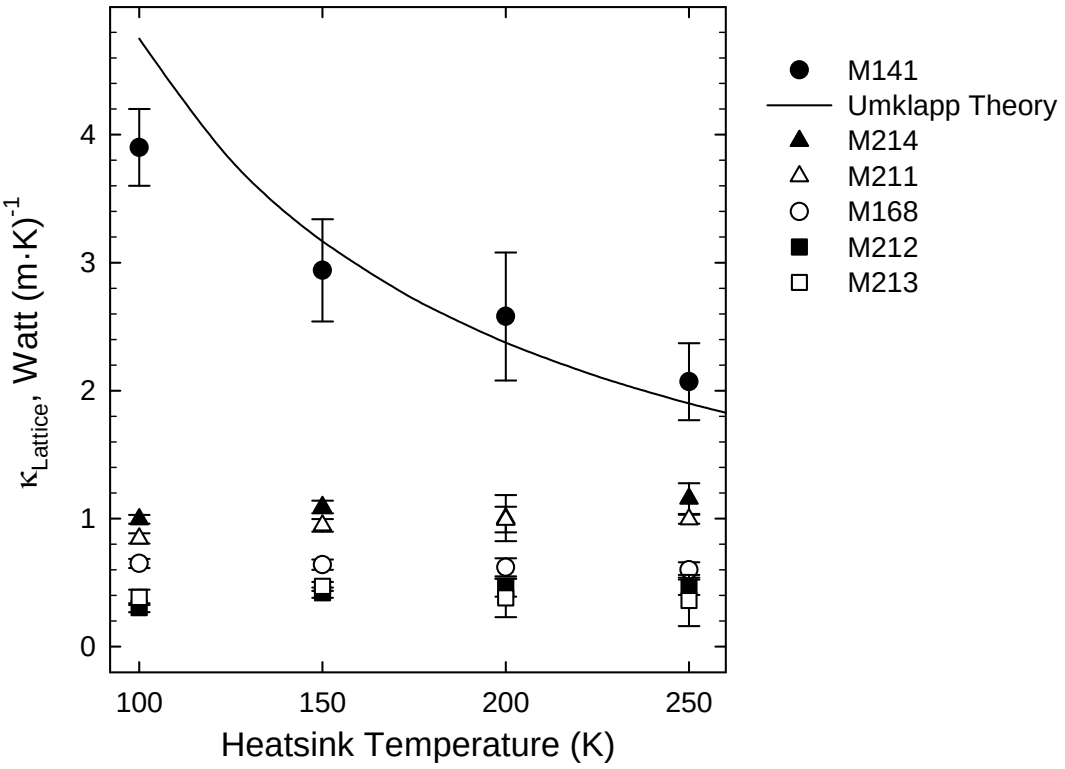

Figure 6-1: Lattice thermal conductivity of nanostructured thin films fabricated and characterized in this research compared to film #M141 with a single layer of PbSe.

PbSe. Diffuse interface scattering of phonons is believed to be responsible for this effect [1-4]. This conclusion is based on the measurements of samples from five different SL materials that indicated the lattice thermal conductivity was a function of the average SL layer thickness. Film #M214, which was fabricated with 654 SL layers in 1.72 μm of material (d_{avg} = 2.64 nm), had the highest lattice thermal conductivity of k = 1.2 ± 0.2 $Wm^{-1}K^{-1}$. Film #M213, which was fabricated with 1374 SL layers in 1.56 μm of material (d_{avg} = 1.13 nm), had the lowest lattice thermal conductivity of 0.45 ± 0.1 $Wm^{-1}K^{-1}$. The lowest possible thermal conductivity for IV-VI material, amorphous PbSe is estimated to be 0.35 $Wm^{-1}K^{-1}$ [5].

The thermal conductivity data obtained in this research can be combined with low temperature Hall effect characterization of electrical conductivity, σ, and estimates for the Seebeck coefficient to calculate the thermoelectric figure of merit, $ZT = S^2\sigma T/k$. The Seebeck coefficient, S, for these materials was estimated using published reports for similar materials. Values range between 100-200 μV/K [6, 7] depending on doping levels. Sample #M212, with $\sigma_{300K} \approx 3.5 \times 10^3$ S/m and $\sigma_{100K} \approx 4 \times 10^4$ S/m, had an estimated ZT_{300K} = 0.09 and ZT_{100K} = 0.08. Intentionally doped SL film #M168, with an estimated electron concentration $n \approx 6 \times 10^{18}$ that was measured in a similarly grown film, had ZT_{300K} = 1.2 and ZT_{100K} = 0.21. The highest reported value for optimized bulk PbSe materials at 300 K is ZT = 0.4 [5, 8]. This nearly 3X improvement in the figure of merit justifies effort for development of thermoelectric modules fabricated from IV-VI semiconductor nanostructures.

Chapter 1 described energy transport in nanostructured solid state materials using a mixed quantum and macro physics approach. The chemical properties of IV-VI

semiconductors were then reviewed to outline the molecular beam epitaxy (MBE) fabrication of composite PbSe, PbSrSe, and PbSnSe films approximately 5 μm thick with SL nanostructure layers as thin as 1 nm. This chapter next described the growth techniques used to fabricate more than 100 thin films with different material properties including carrier dopant concentration and optical multiple quantum well (MQW) structures. The films were characterized with multiple techniques including scanning electron microscopy (SEM), X-ray diffraction (XRD), and the Hall effect.

Chapter 2 outlined a novel, non-contact characterization technique to obtain cross-plane thermal conductivity. This included measuring photoluminescence (PL) spectra from IV-VI semiconductor material at heatsink temperatures from 290 K to 330 K with different amounts of incident optical power. The system employed a 1.4 eV diode laser with manually controlled focus and total power up 4-Watt to stimulate PL in both bulk PbSe and PbSe/PbSrSe MQW materials. The procedure was optimized by analyzing more than 10,000 individual data points that were collected with custom automated testing software. Chapter 3 described the techniques used to extract thermal conductivity from these data by analyzing the "blue-shift" of the measured PL emission for different optical powers. The magnitude of the PL blue-shift, which is proportional to the magnitude of the temperature increase, was determined using custom software that employed advance digital filters and curve-fitting. Finite element (FE) thermal modeling was then used to obtain thermal conductivity from the temperature increase data for the different materials tested.

Chapter 4 contains measurements of electrical and thermal conductivity for different materials at heatsink temperatures as low as 90 K. PL data collection and

accuracy were optimized with custom software that implemented an adaptive zone-dependent proportional, integral, and derivative (PID) control algorithm to rapidly change the heatsink temperature. Material samples with similar MQW optical layers but different SL designs exhibited clear differences in the magnitude of the blue-shift of PL spectra for increased optical power. The lattice and carrier components of the total thermal conductivity for different materials were estimated using the Wiedemann-Franz law and a Lorentz number that was calculated from the measured carrier concentrations.

Chapter 5 applies acoustic wave theory to the analysis of lattice thermal conductivity of PbSe/PbSnSe SL materials. The chapter details a numerical method to calculate the potential effect on phonons from acoustic distributed Bragg reflectors (aDBRs) using the acoustic mismatch model (AMM) [9]. Finally, the magnitude of aDBR reflection as a mechanism for reducing k_{lat} was compared to diffuse phonon scattering [10, 11] and discussed as a function of material temperature and the phonon energy distribution.

6.1.1 PL Characterization and Thermal Modeling

The experimental design and numerical techniques presented for measuring thermal conductivity in PbSe, PbSrSe, and PbSnSe materials grown on industry standard silicon substrates using laser induced PL spectra represents a significant contribution to science. This technique that had been used previously to estimate differences in optical heating based on material mounting [12] and the wavelength of the PL pump laser [13] was optimized through an iterative, data intensive process. The most important experimental technique developed was the use of eutectic indium gallium (EGaIn) for bonding material samples to a temperature controlled heatsink with

a low thermal contact resistance (TCR). This material was used to easily bond samples to a copper sub-mount at room temperature on a standard work surface with precision control. This technique was more simple and repeatable than using pure indium that has a melting point of 156 °C and requires a hot-plate or similar heating mechanism. Experimental results from different samples of the same semiconductor material mounted with different bonding materials showed EGaIn had a lower TCR than both double-sided tape and black wax. Analysis of the same group of semiconductor materials over a three year period showed a minimum time of 24 hours to establish the lowest TCR sample mounting with EGaIn.

A second significant source of variation in the heating effect during PL experiments, optical alignment, was quantified in this research. An experiment was designed and executed to manipulate the surface area illuminated by the PL pump laser. The lens used to focus the collimated infrared beam generated by the fiber optic laser was displaced in 2 mm steps along the optical axis that increased the full-width at half-maximum (FWHM) of the optical power distribution by approximately 80 μm. Sample #M168 heated 12 K/Watt for the most focused PL laser signal that was twice as large as film #M141. When the optical lens was defocused 2 mm from the optimum distance from the sample surface the heating effect for #M168 decreased more than 35% and the difference between this sample and sample #M141 decreased to 4 K/W.

In addition to mechanical procedures, this research outlined several advanced digital signal processing (DSP) techniques for more accurate analysis of the PL spectra from different material samples. The DSP steps included a zero-phase infinite impulse response (IIR) smoothing filter, calculations to remove optical artifacts including open-

air molecular absorption, and PL peak emission fitting using an exponentially modified Gaussian (EMG) function with a non-linear Levenberg-Marquardt routine. The IIR smoothing filter implemented had a significantly lower group delay than traditional low-pass filters. The EMG fit was essential in reducing the effect of optical cavity fringes on the calculation of the PL peak maximum. Results from more than 90 tests on a single film sample showed the minimum measurement noise was ± 1 K. Figure 6-2 shows an SEM image of single crystal PbSe film #M199 with the results for optical heating measured in additional PbSe films with varying thickness. The data, which are an average of three experiments for each sample at 300 K, illustrates the precision of the procedure that was developed. The trend line indicates a small difference in optical heating between samples with a difference in thickness less than 1 μm. The analysis of PL spectra also agreed with pyrometry calculations of optical heating using the low energy blackbody power emitted by these materials during PL characterization. PL and

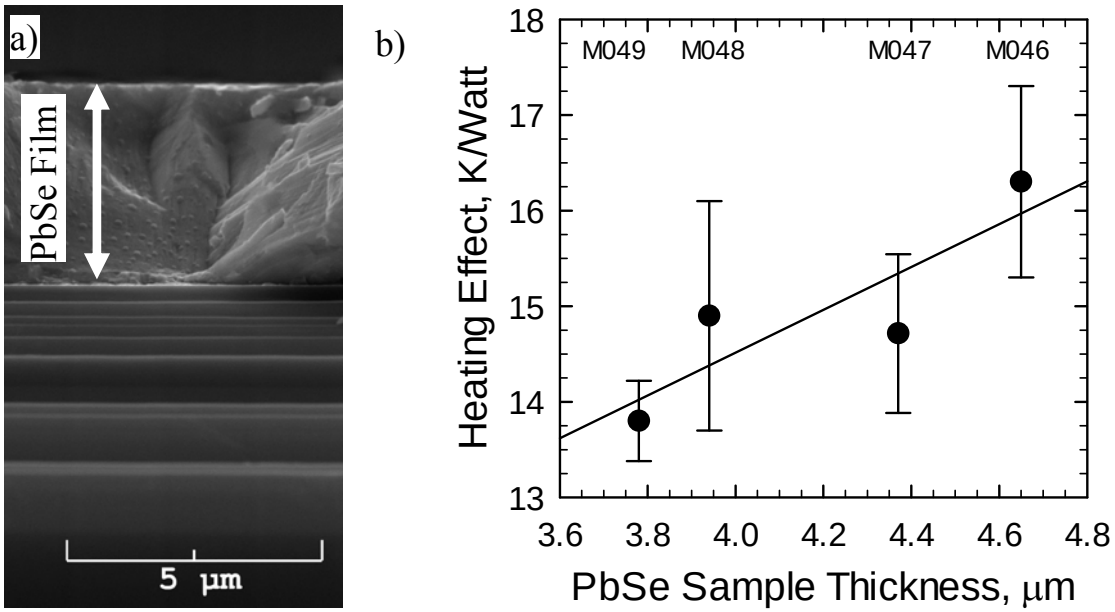

Figure 6-2: a) SEM image of approximately 4 μm thick PbSe film #M199 and b) the optical heating effect calculated from measurements of the blue-shift in PL energy for PbSe films with similar thickness.

blackbody calculations indicated SL samples #M168 and #M207 heated at a rate of 12 K/Watt while sample #M141 with a 1.5 μm layer of PbSe heated at a rate of 10 K/Watt.

The experimental results of a PL emission blue shift and therefore a temperature increase for a given amount of optical power were used with FE analysis software to calculate the cross-plane thermal conductivity of individual films. The FE model was developed using published reports of the optical absorption coefficient [14], the time-scale for exciton thermalization [15], and carrier behavior in MQW structures [16]. Based on these data the FE model restricted all heat generation to within 500 nm of the material surface. The thermal conductivity of the SL region of the model was then adjusted until the average lattice temperature of the MQW material matched the temperature increase measured in the PL emission blue-shift. Nanostructured SL samples #M168 and #M207 had a total thermal conductivity $k_{tot} \approx 1$ $Wm^{-1}K^{-1}$ at 300 K, half that for film #M141 with a single layer of PbSe and $k_{tot} = 2$ $Wm^{-1}K^{-1}$.

6.1.2 Thermal and Electrical Material Properties

The focus of this research was the lattice thermal conductivity of nanostructures; however, this property cannot be measured independently from the electronic thermal conductivity, k_e. The PL technique used, as with all measurements of thermal conductivity [17, 18], assesses the total thermal conductivity of samples, $k_{tot} = k_{lat} + k_e$. Figure 6-3 shows the variation in total thermal conductivity and electrical conductivity as a function of temperature for two samples with similar SL layer thicknesses. Figure 6-3 a) shows the total thermal conductivity for sample #M168 increases to 2.2 $Wm^{-1}K^{-1}$ when the material is cooled to 100 K and sample #M211 has $k_{tot} \approx 1.1$ $Wm^{-1}K^{-1}$ at all temperatures. Figure 6-3 b) shows the electrical conductivity calculated from Hall

effect measurements for sample #M211 and sample #M103 that was fabricated similar to sample #M168. Sample #M211 had a p-type carrier concentration $n_p \approx 4 \times 10^{17}$ cm^{-3} at 300 K. Sample #M103 was intentionally doped with bismuth to be n-type with a carrier concentration of $n_e \approx 6 \times 10^{18}$ cm^{-3}, similar to the value expected for the SL region of sample #M168. However, Hall effect measurements of sample #M168 were inaccurate because the MQW region was not doped with bismuth and therefore formed a pn-junction approximately 1 μm below the surface.

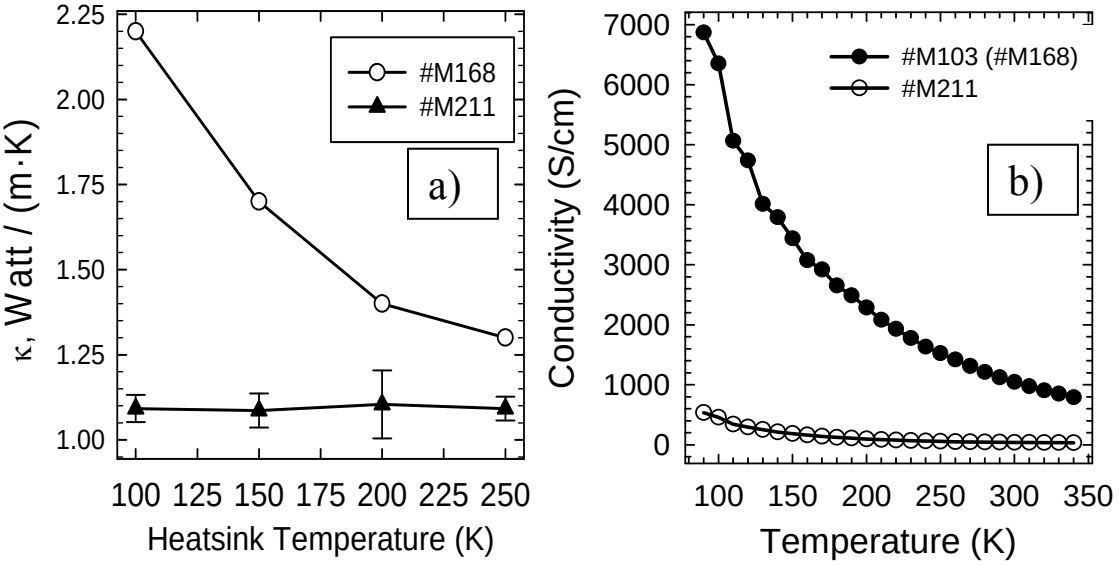

Figure 6-3: The temperature dependent measurement of a) the total thermal conductivity and b) electrical conductivity for two nanostructures with different carrier concentrations.

The difference in total thermal conductivity between the two samples correlates with the difference in electrical conductivity. The magnitude of k_e in semiconductors can be calculated from the electrical conductivity and the Lorentz number using the Wiedemann-Franz law, $k_e = L_0 \sigma T$. For semiconductors L_0 is replaced by a reduced Lorentz number ($L_R \leq L_0$) that is proportional to the carrier concentration and mobility. Different theories for calculating L_R from the band structure of PbSe have been

investigated with various doping concentrations [19]. The results indicated that $L_R \geq 0.8L_0$ at 300 K, and this value increases at lower temperatures. Therefore the electronic thermal conductivity of sample #M168 would theoretically increase 0.8 $Wm^{-1}K^{-1}$ from 250 K to 100 K that matches the measured change in total thermal conductivity. The electronic thermal conductivity of sample #M211 would only increase 0.07 $Wm^{-1}K^{-1}$ and would result in a change in optical heating below the measurement noise.

6.1.3 Nanostructure Engineering Design

The final significant contribution to science presented in this dissertation was conclusive evidence of the SL layer thickness required to alter lattice thermal conductivity. Previous experimental data for PbTe nanoparticle SLs have shown no significant reduction in thermal conductivity, or the corresponding improvement in *ZT*, for material with SL layers thicker than 5 nm [7, 11]. These results are consistent with theoretical calculations of the phonon properties for PbSe [10] that led the authors to conclude that SL "layers must be less than 10 nm thick" to affect the lattice thermal conductivity at 300 K. However, the numerical results indicated that the phonon lifetime was approximately $\tau = 1$ picosecond and the average phonon velocity was $v = 3$ km/second that corresponds to a phonon mean free path, $\Lambda \equiv \tau v = 3$ nm. Since the total phonon lifetime is a combination of multiple physical processes and is dominated by Umklapp scattering for bulk materials [20] the increase in boundary scattering for SL material must be significant to further reduce Λ. The magnitude of boundary scattering can be calculated using the difference in acoustic impedance for the different materials and the individual layer thickness [10]. Therefore SL material with the thinnest layers

would have the lowest lattice thermal conductivity. The samples analyzed in this research all had an average layer thickness less than 3 nm. Figure 6-4 shows lattice thermal conductivity as a function of average layer thickness for different samples with similar electrical conductivity at both 250 K and 100 K. None of the films tested exhibited any significant temperature dependence for the thermal conductivity that is consistent with a constant phonon mean free path. Since Umklapp scattering is proportional to temperature another mechanism is holding the phonon lifetime constant.

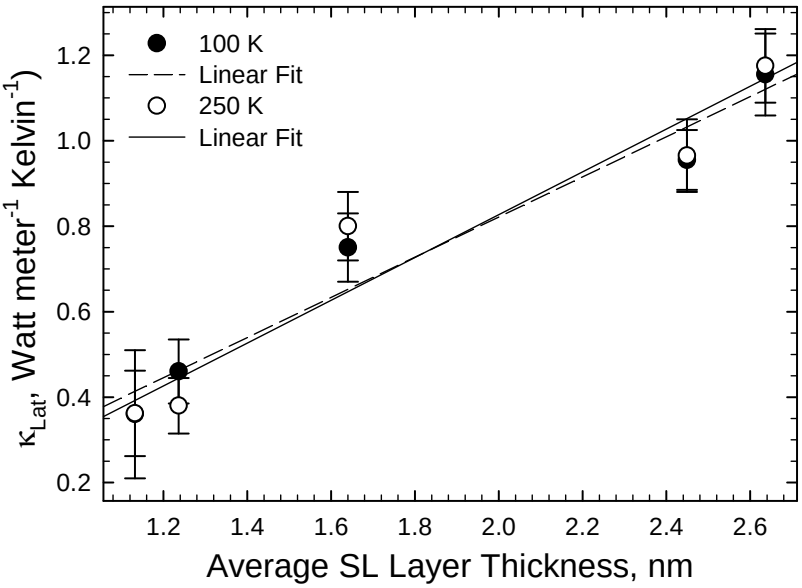

Figure 6-4: Thermal conductivity for different SL samples plotted as a function of the average layer thickness at 100 K and 250 K.

In addition to diffuse boundary scattering, phonon waves are susceptible to reflection from aDBR structures. The SL films analyzed in this research were designed with multiple periods or thicknesses that had the potential to reflect different phonon energies and further reduce lattice thermal conductivity. Sample #M168 had three different SL periods: 0.6 nm, 1.2 nm, and 1.8 nm with an average layer thickness of 1.4 nm. Sample #M211 had seven different SL periods between 0.5 nm and 2.5 nm with an average layer thickness of 1.2 nm. However, no experimental results indicated any

difference in thermal conductivity measurements for films other than electrical conductivity and the average SL layer thickness. The AMM model used to calculate the affect of the aDBR structures for the different SL samples indicated that 60 pairs of alternating layers were needed for 90 % reflectance. Therefore the thinnest SL layers, which were ≈ 0.5 nm, would require an aDBR structure with a total thickness significantly greater than the phonon mean free path for the temperature range tested.

6.2 Recommendations for Future Research

This research contains the first reported measurements and calculations of the thermoelectric properties of nanostructured IV-VI semiconductors from 100 K to 300 K. Most published research on similar materials has focused on the temperature range from 300 K to 1000 K [21-23]. This is due to the behavior of bulk materials PbTe and PbSe that have a maximum $ZT \approx 1$ above 700 K and applications in TE power generation from waste heat recovery. Research on TE materials at lower temperatures has shown that $Bi_xSb_{2-x}Te_3$ has a maximum bulk $ZT \approx 1$ at 400 K [24]. A significant application of TE materials in this temperature range is for refrigeration devices to lower the operating temperature of infrared detectors and lasers. Currently TE refrigeration devices fabricated from bulk materials with $ZT < 0.5$ are commercially available but are limited to reducing the temperature of electronics to approximately 200 K using 4-6 cooling stages stacked upon each other [25]. The IV-VI semiconductor nanostructured materials analyzed in this research, in particular sample #M168 with a calculated $ZT = 1.2$ at 300 K, greater than bulk BiSbTe, could be used to fabricate a standard TE "unipole" module as shown in Figure 6-5. This common structure has two "legs" that are constructed from materials with a different majority

carrier type: *p* and *n* that are connected on one end with a metallic conductor. Multiple unipoles operating in parallel can be assembled between two ceramic plates providing the device a mechanically sturdy surface to contact the hot and cold objects. The theoretical efficiency of a TE module has been calculated by different methods [25]. A TE refrigeration module with $ZT = 1.2$ could achieve a temperature differential of 80 K. However, real TE devices are affected by parasitic wire bonding resistances and other factors that reduce efficiency and therefore further research is needed.

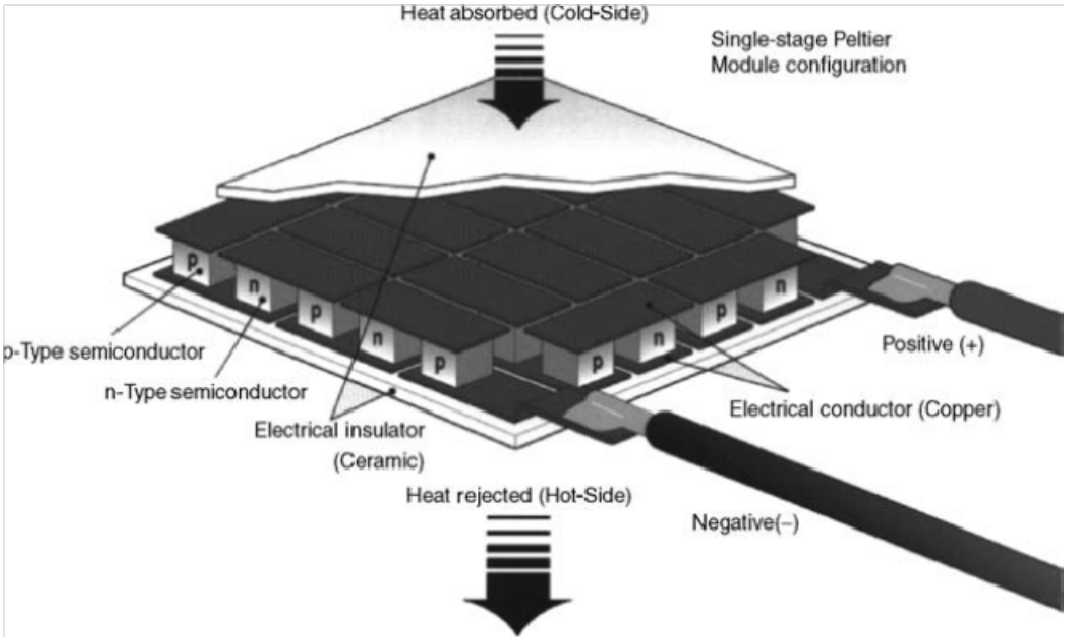

Figure 6-5: Standard TE module design taken from reference [25] using multiple unipoles operating in parallel between two ceramic plates.

In addition to room-temperature multipurpose TE refrigeration modules research on complex device designs with mid-IR PbSe detectors integrated on SL material could be attempted. Mid-IR HgCdTe detectors operating at temperatures below 100 K have been used extensively for gas phase spectroscopy [26] and were used to detect PL during this research performance. The performance of these devices as with PbSe detectors increases dramatically at lower temperatures [27]. However, the TE

properties of PbSe at low temperatures as shown in this dissertation could enable a device to be constructed similar to Figure 6-6 that could achieve a lower heatsink temperature than current solid state cooling devices. This monolithic device structure could be fabricated using multiple steps of photolithography and etching.

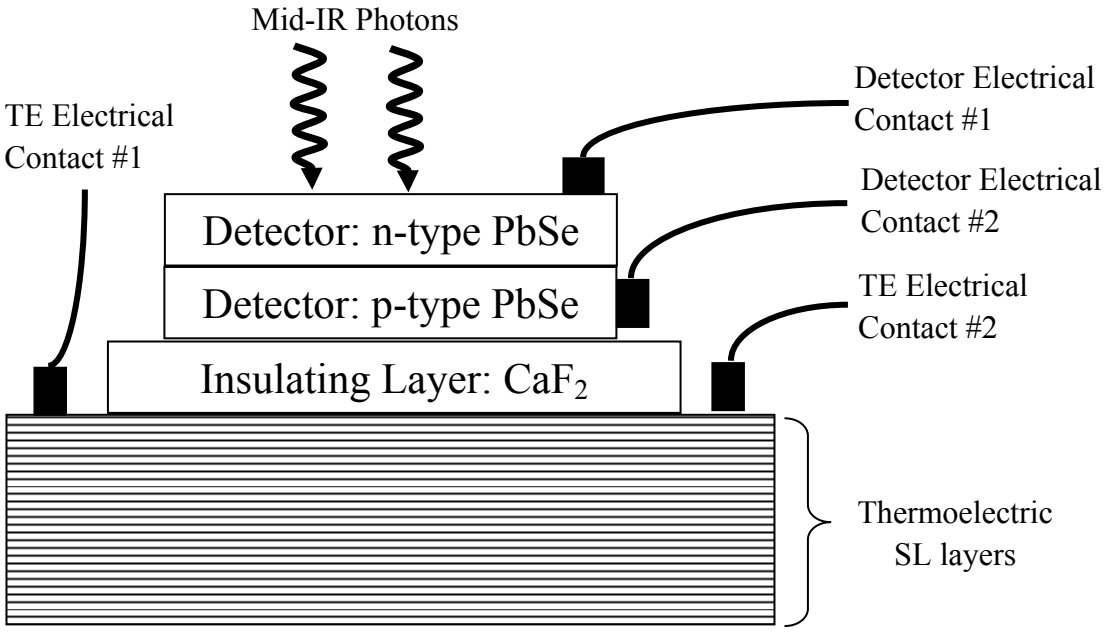

Figure 6-6: Prototype design for a mid-IR detector integrated on a PbSe/PbSnSe SL material for TE cooling.

6.2.1 Additional Experiment Optimization

The experimental techniques used to acquire and analyze PL data were optimized throughout this research; however, the testing apparatus and equipment could be improved. In particular a system could be designed that would not have molecular absorption affecting the PL spectra that would eliminate the need for custom software to filter this effect. Absorption of the infrared optical signal by gaseous carbon dioxide and water could be significantly reduced by performing experiments in either a vacuum or a purge gas. Preliminary experiments purging the interior of the Fourier transform

infrared (FTIR) spectrometer with a constant flow of ultra high purity nitrogen reduced the amplitude of the CO_2 absorption feature at 280 meV by nearly 50%. However the length of experiments and the flow rate of nitrogen required quickly depleted the gas supply and the continued expense would be impractical. In addition, a large portion of the optical path occurs outside of the FTIR so a significant amount of absorption would still occur. However, if the entire optical system were enclosed by a hermetically sealed chamber with an electrical feed-through a vacuum pump could be used to perform experiments at a reduced pressure.

The PL system with a thermoelectric module to maintain the sample heatsink temperature described in Chapter 2 could be improved by confining the mount in a vacuum chamber or cryostat with infrared transparent windows. The system was operated from 290 K up to 330 K, but was also capable of operating below room temperature. However, condensation formed on the sample surface when the heatsink temperature was reduced below 290 K and damaged the sample. If both the sample and TE module were confined in a vacuum or nitrogen environment, similar to the low temperature cryostat described in Chapter 4, the test range could be increased more than 2X. In addition to confining the sample and heatsink temperature control apparatus in a cryostat the PL pump laser should also be located in the vacuum chamber.

The accuracy of the thermal modeling in this research could be improved with use of three-dimensional FE analysis software designed specifically for nanostructure simulations. An FE model developed using Solid Works thermal analysis package is shown in Figure 6-7. The results presented were obtained with software that used a two-dimensional model and calculated the third dimension as either an infinite plane or

by revolving the model around a fixed axis. Treating the 2D model as a circularly symmetric cross-section generated slightly different results than the infinite plane approach and is more representative of the actual heat distribution that occurs when the PL beam is focused on the sample surface. However, since the PL laser beam is at an angle with respect to the surface the heat distribution is not symmetric and forms an ellipse on the surface this could be more accurately represented in a 3D model. The commercial software package shown was not used because of significant problems that occurred when simulating nanostructures. The large scale differences in sample thickness, less than 5 μm, compared the in-plane dimensions, ≈ 1 cm, caused the software to "crash" and routinely provide false results. In addition this software did not allow the heat source to be modeled as function of spatial coordinates. The extreme

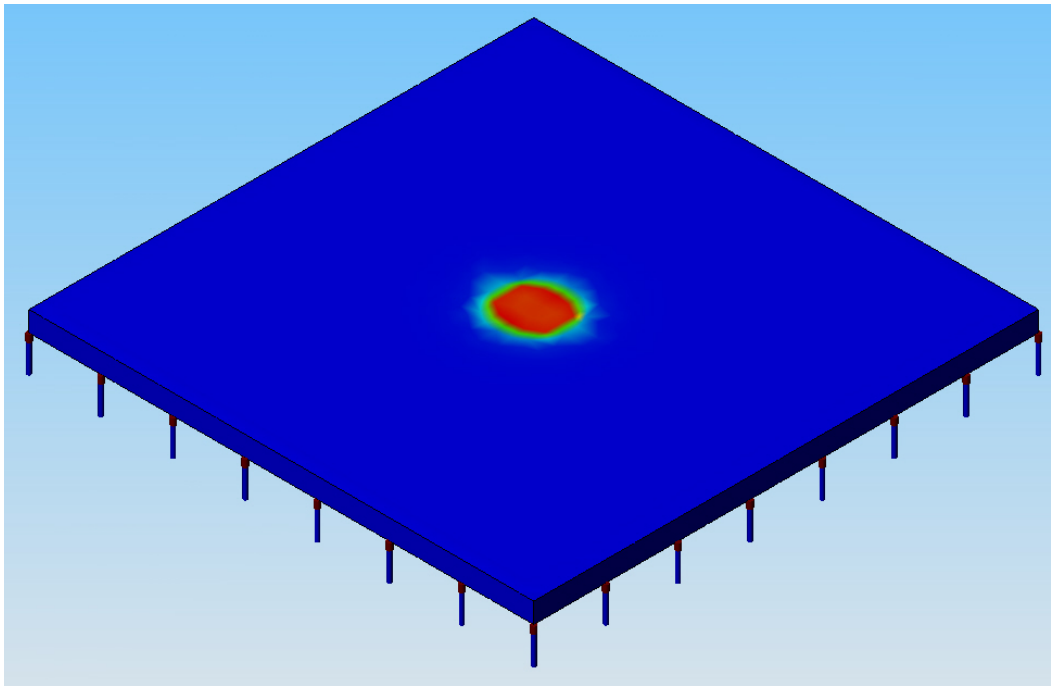

Figure 6-7: Three-dimensional thermal modeling software for PL characterization analysis that shows localized heating immediately beneath the pump laser.

requirements of these nanostructure experiments may require custom FE analysis

software for the most accurate calculations. In addition to improved accuracy custom FE software would enable heat transport to be calculated using probabilistic quantum behavior such as Monte Carlo modeling.

6.2.2 Evidence of Phonon Reflection

While this research did not demonstrate clear evidence for phonon reflection affects the theoretical possibility of reflecting low energy acoustic phonons should be investigated further. The possibility of altering bulk thermal conductivity through reflection of phonons using periodic structures has been discussed in the literature for more than 20 years [28]. To date no experimental evidence of this effect has been observed [3], and the magnitude of reflection may be insignificant compared to phonon scattering as shown in Chapter 5. However, the precise control and calculations of reflection compared to the random probability of scattering has led to continued research on new approaches and materials [29]. Therefore, demonstration of phonon reflection in low thermal conductivity nanostructures would be a significant experimental and theoretical accomplishment.

Two modifications of the research presented in this dissertation may enable this to occur: measurement of thermal conductivity at lower temperatures and additional SL film designs. Since the aDBR structures must be must be a minimum of 60 nm thick for 90 % reflectance the material temperature must be low enough for the bulk phonon mean free path to be increased to this distance. This could be accomplished with a liquid helium compressor and cryostat that can achieve a temperature as low as 4 K. However, the PL intensity from the MQW samples tested would not be sufficient at this

temperature for these types of thermal conductivity measurements and another technique such as thermoreflectance [18] would have to be used.

In addition to lower temperature measurements a different SL design may be necessary to isolate phonon reflection and scattering effects. The tested samples were fabricated for maximum cross-plane electrical conductivity using a design commonly referred to as a graded superlattice [30]. The SL structures had 3, 5, and 7 different layer thicknesses however k_{tot} was only a function of the average layer thickness. Since all samples would theoretically reflect a similar percentage of the phonon energy spectrum, between 7% and 9%, it would be impossible to distinguish between them. Therefore a sample with a random distribution of SL layers with different thicknesses could be compared to a regular SL design as shown in Figure 6-8. Both film designs have a similar average nanostructure layer thickness but the randomly arranged film would reflect less than 1 % of the phonon energy spectrum as calculated by the AMM technique. In addition to randomly arranged nanostructures samples with different concentrations of tin in the ternary layers of the SL could be compared. An increased

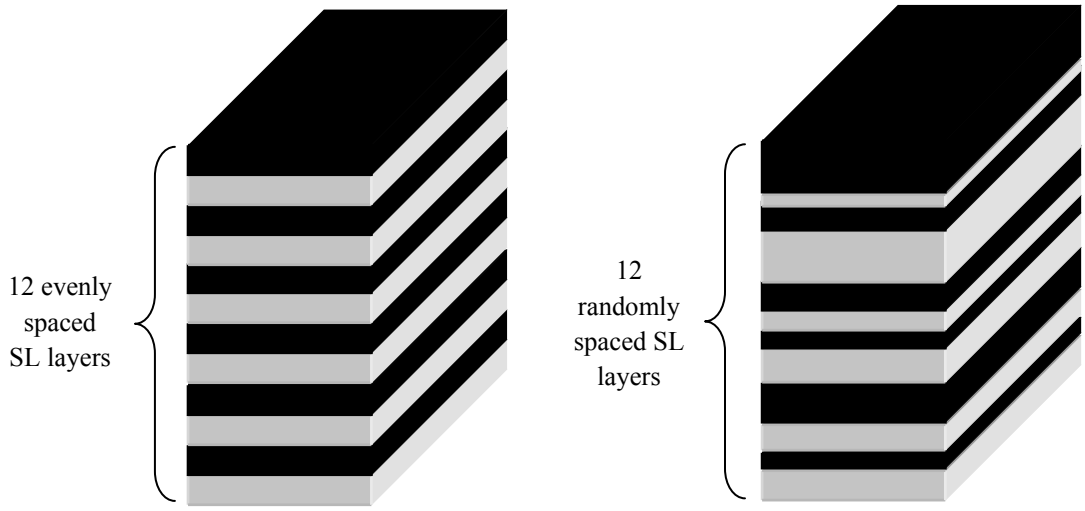

Figure 6-8: SL film designs with the same average layer thickness but significantly different periodicity.

tin concentration in the SL layers would increase both the difference in material stiffness (ΔC) and the acoustic impedance mismatch ($\Delta \eta$).

6.2.3 New Characterization Techniques

The electronic material characterization of the films presented during this research used standard four-probe geometry to assess the Hall resistance in a varying magnetic field that is then normalized to the cross-plane thickness. These results were used to calculate both the electronic thermal conductivity and *ZT* at various temperatures for the different samples. However, this number may not represent the actual cross-plane electrical conductivity of the SL films as illustrated by Figure 6-9. The SL layers have different electrical properties that create band-edge discontinuities and form "barriers" that may impede carrier movement in the cross-plane direction. However, these same periodic structures create discrete confined energy levels within the quantum well that reduces the potential for phonon scattering and increases excited

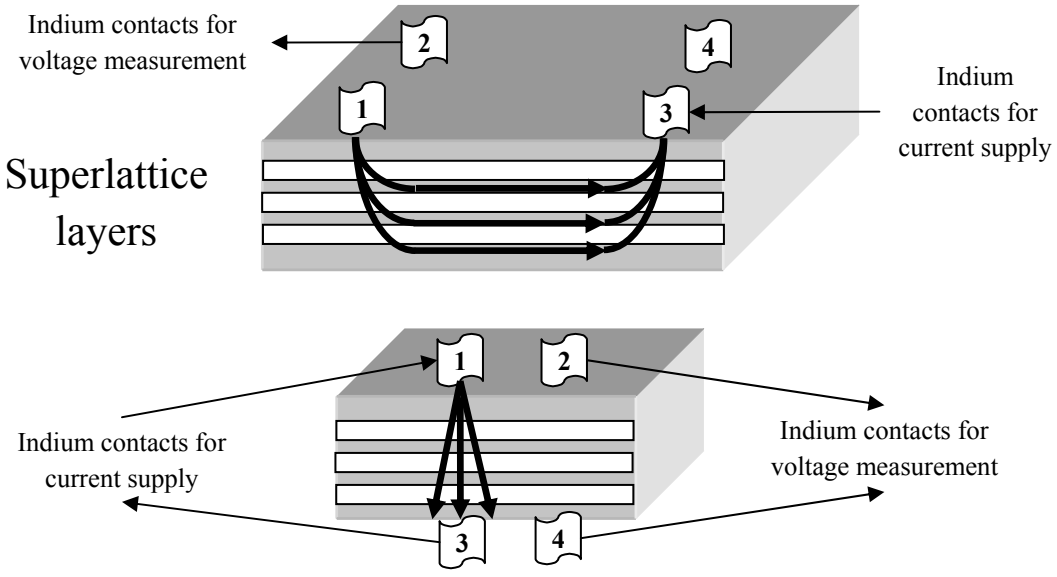

Figure 6-9: Cross-plane electrical conductivity apparatus design and prototype for thin films bonded to copper bars.

carrier lifetime. Therefore the electrical conductivity should be measured across the periodic structure with electrical contacts on the top and bottom layers of the SL.

The single optical beam PL measurement employed in this research was sufficient to assess differences in optical heating for the IV-VI semiconductor samples tested. The technique used a single numerical value for the blue-shift of the PL spectrum energy with maximum intensity as a representation of the average temperature change from the entire volume of material emitting PL. However, the FE model results show that the temperature of this volume of material varies both as a function of depth from the surface and in-plane as shown by the isotherm plots in Figure 6-10. The FE model in Figure 6-10 a) assumes the heat is generated by a 1 Watt PL pump laser that is focused to a Gaussian in-plane distribution with a FWHM of 250 μm. The average lattice temperature of the outlined volume of material, which is equivalent to the MQW material of the tested samples, is 10° C above the heatsink temperature if the thermal conductivity is 2.2 $Wm^{-1}K^{-1}$. Figure 6-10 b) shows a second FE model with the heat source distributed with a FWHM of 300 μm. The average lattice temperature of the outlined region is also 10° C above the heatsink temperature but for this to occur the thermal conductivity of the material must be 2.0 $Wm^{-1}K^{-1}$. However, the temperature isotherms show that the surface temperature at the same distance from the center of the FE model is different. The small difference in optical heat distribution cannot be easily detected using standard techniques such as the knife-edge or pin-hole characterization used in Chapter 2. Therefore if the lattice temperature could be measured at multiple points on the sample that are a different distance from the heat source the FE model results for thermal conductivity could be more accurate. A differential temperature

measurement along the length of a nanowire is now considered the standard technique for measuring thermal conductivity in these types of structures [31]. The first data published for silicon nanowires varied from 600 $Wm^{-1}K^{-1}$ to 3600 $Wm^{-1}K^{-1}$ [32-34] due largely to variations in TCR between the nanowire and measurement apparatus. However, comparing the temperature increase from a laser at either end of the nanowire can be mathematically proven to eliminate the TCR of bonding materials and sub-mounts from the calculation [31].

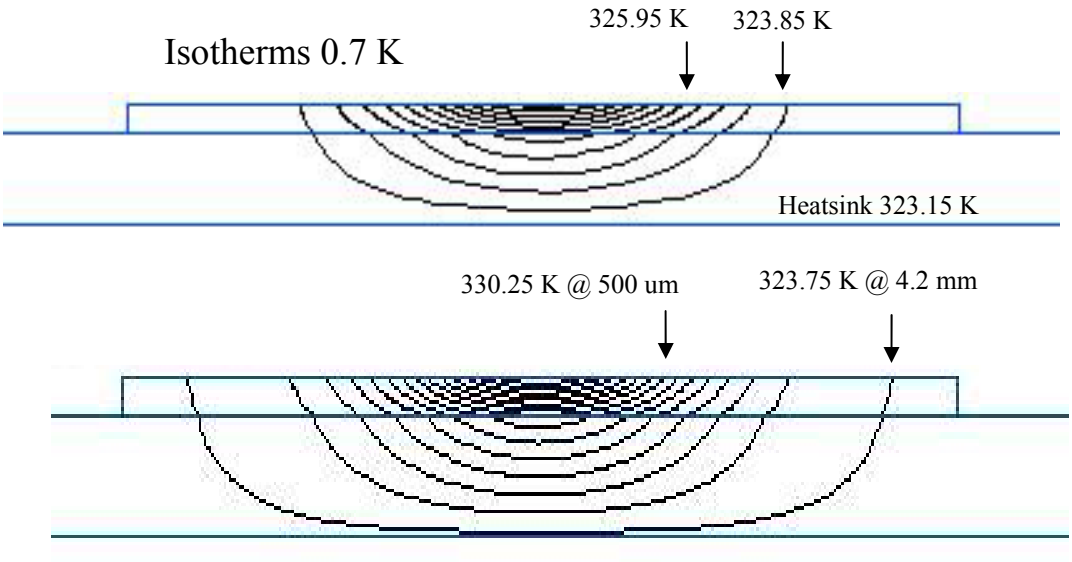

Figure 6-10: Thermal model isotherm plots with different heat distributions: upper plot has a greater heat density and higher thermal conductivity but the same average temperature increase as the lower plot.

A novel approach to implement this for thin film PL measurements would be to decouple the laser signal that stimulates PL photons from the laser signal that creates the optical heating effect. This could be accomplished using two lasers commonly referred to as "pump" and "probe" configuration with one laser being moved on the sample surface and multiple measurements being taken. This concept is illustrated by Figure 6-11. This pump-and-probe approach has been successfully implemented for

other thermal conductivity measurements such as transient thermoreflectance [18]. This procedure uses one laser to heat the sample and measures the power of second laser at normal incidence to the sample surface that is pulsed at a very high rate. The pulsed optical signal increases the signal-to-noise ratio of the detection system by shifting measurements to a high frequency. This same technique could be used in a PL system with a pulsed-mode laser and second harmonic detection with a step-scan FTIR.

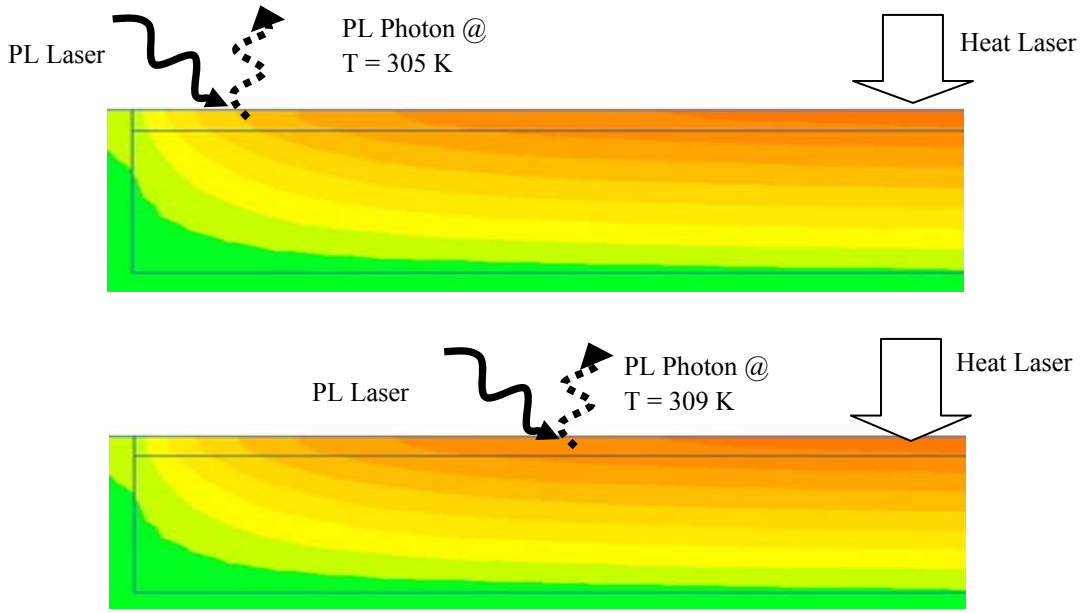

Figure 6-11: Two laser pump-and-probe approach to PL characterization of temperature for calculating thermal conductivity with the distance between the heat pump and PL probe being changed.

Chapter 6 References

1. M. G. Holland, "Analysis of lattice thermal conductivity", *Phys. Rev.*, **132**(6), pp. 2461-2471 (1963)

2. D. G. Cahill, "Heat transport in dielectric thin films and at solid-solid interfaces", *Microscale Thermophysical Engr.*, **1**(3), (1997)

3. D. G. Cahill, K. E. Goodson, and A. Majumdar, "Thermometry and Thermal Transport in Micro/Nanoscale Solid-State Devices and Structures", *ASME J. Heat Transfer*, **124**(2), pp. 223-241, (2002)

4. C. M. Bhandari, *"Chapter 14: Size Effects on Thermal Transport"*, *Thermoelectrics Handbook: Macro to Nano (Ed. D. M. Rowe)*, Taylor and Francis, Boca Raton, pp. 1-10 (2006)

5. H. Wang, Y. Pei, A. D. Lalonde, and G. J. Snyder, "Heavily doped p-type PbSe with high thermoelectric performance: an alternative for PbTe", *Adv. Materials*, **23**, pp. 1366-1370 (2011)

6. V. Jovovic, S. J. Thiagarajan, J. P. Heremans, T. Komissarova, D. Khokhlov, and A. Nicorici, "Lowe temperature thermal, thermoelectric, and thermomagnetic transport in indium rich $Pb_{1-x}Sn_xTe$ alloys", *J. Appl. Phys.* **103**, 053710 (2008)

7. J. Androulakis, C.-H. Lin, H.-J. Kong, C. Uher, C.-I. Wu, T. Hogan. B. A. Cook, T. Caillat, K. N. Paraskevopoulos, and M. G. Kanatzidis, "Spinodal decomposition and nucleation and growth as a means to bulk nanostructured thermoelectrics: enhanced performance in Pb1-xSnxTe-PbS", *J. Am. Chem. Soc.*, **129**, pp. 9780-9788 (2007)

8. D. Parker and D. J. Singh, "High temperature thermoelectric performance of heavily doped PbSe", *Phys. Rev. B*, **82**, 035204 (2010)

9. S. Mizuno and S.-i. Tamura, "Theory of acoustic-phonon transmission in finite-size superlattice systems", *Phys. Rev. B*, **45**(2), pp. 734-741 (1992)

10. J. He, S. N. Girard, M. G. Kanatzidis, and V.P. Dravid, "Microstructure-lattice thermal conductivity correlation in nanostructured $PbTe_{0.7}S_{0.3}$ thermoelectric materials", *Adv. Func. Mater.*, **20**, pp. 764-772 (2010)

11. Y. K. Koh, C. J. Vineis, S. D. Calawa, M. P. Walsh, and D. G. Cahill, "Lattice thermal conductivity of nanostructured thermoelectric materials based on PbTe", *Appl. Phys. Lett.* **94**, 153101 (2009)

12. F. Zhao, X. Lv, A. Majumdar, and Z. Shi, "Influence of mounting on continuous-wave photoluminescence from midinfrared PbSrSe/PbSe multiple quantum wells", *Appl. Phys. Lett.*, **84**(8), pp. 1251-1253 (2004)

13. P. J. McCann, P. Kamat, Y. Li. A. Sow, H. Z. Wu, G. Belenky, L. Shterengas, J. G. Kim, and R. Martinelli, "Optical pumping of IV-VI semiconductor multiple quantum well materials using a GaSb-based laser with emission at $\lambda = 2.5$ μm", *J. Appl. Phys.*, **97**, 053103 (2005)

14. N. Suzuki, K. Sawai, and S. Adachi, "Optical properties of PbSe", *J. Appl. Phys.*, **77**(3), pp. 1249-1255 (1995)

15. H. Bao, B. F. Habenicht, O. V. Prezhdo, and X. Ruan, "Temperature dependence of hot-carrier relaxation in PbSe nanocrystals: an *ab initio* study", *Phys. Rev. B*, **79**, 235306 (2009)

16. L. A. Elizondo, Y. Li, A. Sow, R. Kamana, H. Z. Wu, S. Mukherjee, F. Zhao, Z. Shi, and P. J. McCann, "Optically pumped mid-infrared light emitter on silicon", *J. Appl. Phys.*, **101**, 104504 (2007)

17. A. Jain and K. E. Goodson, "Measurement of the Thermal Conductivity and Heat Capacity of Freestanding Shape Memory Thins Films Using the 3ω Method", *ASME J. Heat Transfer*, **130**, 102402 (2008)

18. C. A. Paddock and G. L. Eesley, "Transient Thermoreflectance from Thin Metal Films", *J. Appl. Phys.*, **60**, pp. 285-290, (1986)

19. J. Androulakis, D.-Y. Chung, X. Su, L. Zhang, C. Uher, T. C. Hasapis, E. Hatzikraniotis, K. M. Paraskevopoulos, M. G. Kanatzidis, "High-temperature charge and thermal transport properties of the n-type thermoelectric material PbSe", *Phys. Rev. B*, **84**, 155207 (2011)

20. H. Romero, M. Cardona, R. K. Kremer, R. Lauck, G. Siegle, J. Serrano, and X. C. Gonze, "Lattice properties of Pb*X* (*X* = S, Se, Te): Experimental studies and *ab initio* calculations including spin-orbit effects", *Phys. Rev. B*, **78**, No. 224302 (2008)

21. J. Martin, G. S. Nolas, W. Zhang, and L. Chen, "PbTe nanocomposites synthesized from PbTe nanocrystals", *Appl. Phys. Lett.*, **90**, 222112 (2007)

22. J. P. Heremans, C. M. Thrush, and D. T. Morelli, "Thermopower enhancement in PbTe with Pb precipitates", *J. Appl. Phys.*, **98**, 063703 (2005)

23. B. Zhang, J. He, T. M. Tritt, and A. Kumbhar, "Controlled two-dimensional coated nanostructures for bulk thermoelectric composites", *Appl. Phys. Lett.*, **88**, 043119 (2006)

24. B. Poudel, Q. Hao, Y. Ma, Y. Lan, A. Minnich, B. Yu, X. Yan, D. Wang, A. Muto, D. Vashaee, X. Chen, J. Liu, M. S. Dresselhaus, G. Chen, and Z. Ren, "High-thermoelectric performance of nanostructured bismuth antimony telluride bulk alloys", *Science*, **320**, pp. 634-639 (2008)

25. D. M. Rowe, *"Chapter 1: General Principles and Basic Considerations"*, *Thermoelectrics Handbook: Macro to Nano (Ed. D. M. Rowe)*, Taylor and Francis, Boca Raton, pp. 1-15 (2006)

26. J. Jeffers, C. Roller, K. Namjou, M. A. Evans, L. McSpadden, J. Grego, and P. J. McCann, "Real-time diode laser measurements of vapor phase benzene", *Analytical Chem.*, **76**(2), pp. 424-432 (2003)

27. A. Rogalski, J. Antoszewski, and L. Faraone, “Third generation infrared photodetector arrays”, *J. Appl. Phys.*, **105**, 091101 (2009)

28. M. Maldovan, “Narrow low-frequency spectrum and heat management by thermocrystals”, *Phys. Rev. Lett.* **110**, 025902 (2013)

29. G. Bastain, A. Vogelsang, and C. Schiffmann, “Isotopic superlattices for perfect phonon reflection”, *J. Elec. Mater*. **39**(9), 1769 (2010).

30. S. Wang and N. Mingo, “Tailoring interface roughness and superlattice period length in electron-filtering thermoelectric materials”, **79**, 115316 (2009)

31. Q. Li, C. Liu, X. Wang, and S. Fan, “Measuring the thermal conductivity of individual carbon nanotubes by the Raman shift method”, *Nanotechnology*, **20**, 145702 (2009)

32. A. I. Hochbaum, R. Chen, R. D. Delgado, W. Liang, E. C. Garnett, M. Najarian, A. Majumdar, and P. Yang, “Enhanced thermoelectric performance of rough silicon nanowires”, *Nature*, **45**, pp. 163-168 (2008)

33. P. Kim, L. Shi, A. Majumdar, and P. L. McEuen, “Thermal transport measurements of individual multiwalled nanotubes”, *Phys. Rev. Lett.*, **87**(21), pp. 5502-5505 (2001)

34. H.-Y. Chiu, V. V. Deshpande, H. W. Ch. Postma, C. N. Lau, C. Miko, L. Forro, and M. Bockrath, “Ballistic phonon thermal transport in multiwalled carbon nanotubes”, *Phys. Rev. Lett.*, **95**, 226101 (2005)

Appendix A

Selected Custom Software

Molecular Beam Epitaxy Software

This software is similar to "C". However, the programmer cannot define libraries or methods. The same variable name cannot be used in different functions. For example "i" cannot be declared and used as a loop counter in two different functions. Therefore code must be re-typed where it is used and a second use of the next function in a growth recipe must be a separate text file with the variable declarations removed. I apologize for the complicated "run-on" code segment below.

Created: August 2009
Modified: December 2009

Original Language: Text Editor Proprietary Script Language (Molly 2000)
Software Development Environment Company: Veeco, Inc.

```
/*************************************************
/ Arrhenius Plot for multiple material "load cells"
/ J. Jeffers Created: 7/31/2009 Modified: 12/1/2009
/
/ Description: This program operates the shutters of
/   multiple material cells while reading the Beam
/   Flux Monitor (BFM) to calculate the beam flux
/   for each cell over a range of temperatures.
/
/   It generates an Arrhenius plot of log10(P) = m(1/T) + b.
/
/   LLS Fit -> m = ( (n SumXY) - (SumX SumY))/ (n SumX^2 - (SumX)^2)
/            b = ((SumY SumX^2) - SumX SumXY) / ( (n SumX^2) - (SumX)^2
/
/   Order of Cells:
/      1. Bi2Se3  2. PbSe  3. SnSe  4. Se
/      5. CaF2    6. BaF2  7. PbTe  8. Ag
/************************************************/
#include <gauges.h>
#include <cells.h>

int i,j,k;
double x,y,z;
string a,b;

string timeNow;
int timeNowNum;
string startTime;
int startTimeNum;
```

```
double progSleepTime;

int exitProg = 0;
int pauseLoop = 0;
int redoLoop = 0;
int cellLoop = 0, numCells = 0, cellChoice[8];


// Give names for each cell by order of fluxes ************
string name[8];
name[0] = "Bi2Se3";
name[1] = "PbSe";
name[2] = "SnSe";
name[3] = "Se";
name[4] = "CaF2";
name[5] = "BaF2";
name[6] = "PbTe";
name[7] = "Ag";

int nameSelect[8];

cell names[8];
names[0] = Bi2Se3_zone;
names[1] = PbSe_zone;
names[2] = SnSe_zone;
names[3] = Se_zone1;
names[4] = CaF2_zone1;
names[5] = BaF2_zone1;
names[6] = PbTe_zone;
names[7] = Ag_zone;

// Variables for numeric calculations **********************
double tSetPoint;
double tempStableWaitTime = 600; // Default 600 seconds (10 minutes)

double bkgPress;

double shutterOpenTime = 180; // Default 180 seconds (3 minutes)

double beamFlux, BEP;
double BEPArray[8];

double tempCell;
int rampSteps[8];
double rampTemp[64];
```

```
double targetFlux[8];
double targetTemp;

double sumX;
double sumX2;
double sumY;
double sumXY;

double slopeM, interceptB;

int aboveMin = 0, belowMax = 0;

// Open or create output log file ****************************
int fd;
string fileName;

string timeLog;
string month;
string year;
string day;
string hour;
string minute;
string second;
int monthNum;
string monthNames[12];

monthNames[0] = "Jan";
monthNames[1] = "Feb";
monthNames[2] = "Mar";
monthNames[3] = "Apr";
monthNames[4] = "May";
monthNames[5] = "Jun";
monthNames[6] = "Jul";
monthNames[7] = "Aug";
monthNames[8] = "Sep";
monthNames[9] = "Oct";
monthNames[10] = "Nov";
monthNames[11] = "Dec";

// Change directory to where files are stored
chdir("/Documents and Settings/mbe/Desktop/Log Files");

timeLog = mctime(time(0));
echo (timeLog);
month = __Mid(timeLog,5,3);
j = 0;
```

```
for (i = 0; i < 12; ++i)
{
  if (strcmp(month,monthNames[i]) == 0)
    j = i + 1;
}
if (j < 10)
  month = "0" + itoa(j);
else
  month = itoa(j);

year = __Right(timeLog,4);
day = __Mid(timeLog,9,2);
hour = __Mid(timeLog,12,2);
minute = __Mid(timeLog,15,2);
second = __Mid(timeLog,18,2);

fileName = "BEP Flux Log ";
fileName = fileName + year+"_"+month+"_"+day+"_"+hour;
fileName = fileName + "_" + minute + "_" + second+".txt";

echo (fileName);

fd = open (fileName, O_WRONLY | O_CREAT);
if (fd < 0)
{
  echo("Couldn't open output file");
  exit(EXIT_FAILURE);
}
fdecho( fd, "This log created on ", timeLog);
close(fd);

// Prompt user for cells to calculate the beam flux for ***
pauseLoop=1;
while (pauseLoop)
{
  redoLoop = 1;
  while(redoLoop)
  {
    cellLoop = 1;
    while (cellLoop)
    {
      echo ("");
      echo ("Choose Source Cell to generate Arrhenious plot for:");
      echo ("");
      echo ("1. Bi2Se3  2. PbSe  3. SnSe  4. Se");
      echo ("5. CaF2    6. BaF2  7. PbTe  8. Ag");
```

```
echo ("9. Start");
echo ("X. Exit");
echo ("");
echo ("You have ", numCells, " cells selected.");

for (i = 0; i < numCells; ++i)
{
  echo (name[cellChoice[i]]);
}
echo ("");

a = input ();

if (a == "X" || a == "x")
{
  echo ("Exit? [Y or N]");
  b = input();
  if (b == "Y" || b == "y")
  {
    exitProg = 1;
    cellLoop = 0;
    redoLoop = 0;
    pauseLoop = 0;
  }
}

else if ( atoi(a) < 1  || atoi(a) > 9)
{
  echo("Invalid entry");
}

else if ( a == "9" )
{
  echo ("Start program with selected cells? [Y or N]");
  b = input();
  if (b == "Y" || b == "y")
  {
    cellLoop = 0;
    redoLoop = 0;
  }
}

else
{
  cellChoice[numCells] = atoi(a) - 1;
  echo("You chose ", name[cellChoice[numCells]], ".  Is that correct? [Y or N]");
```

```
          b = input();

          if (b == "Y" || b == "y")
          {
            ++numCells;
          }
        }
      }
    }

    if (!exitProg)
    {
      for (j = 0; j< numCells; ++j)
      {
        redoLoop = 1;
        while (redoLoop)
        {
          echo ("Choose temperature setpoints for ", name[cellChoice[j]], " Arrhenius
plot:");
          echo ("Enter number of temperature setpoints:");
          rampSteps[j] = atoi(input());

          if (rampSteps[j] > 8 || rampSteps[j] <0)
          {
            echo("Invalid entry!  Please enter a number between 1 and 8.");
          }
          else
          {
            for (i = 0; i < rampSteps[j]; ++i)
            {
              echo ("Enter temperature #", i+1, ":");
              rampTemp[j * 8 + i] = atoi(input());
            }

            echo ("Enter target flux for ", name[cellChoice[j]], " :");
            b = input();
            targetFlux[j] = atof(b);

            echo (" ");
            echo("You chose ", rampSteps[j], " temperature points:");

            for (i = 0; i < rampSteps[j]; ++i)
            {
              echo("Temperature #", i+1, " = ", rampTemp[j * 8 + i]);
            }
            echo ("Target Flux = ", targetFlux[j]);
```

```
            echo (" ");

            echo("Is this corrrect? [Y or N]");
            b = input();
            if (b == "Y" || b == "y")
            {
            redoLoop = 0;
            }
          }
        }
      }

      redoLoop = 1;
      while (redoLoop)
      {
        echo ("Enter the shutter open time in minutes [default = 3 minutes] = ");
        b = input();
        if (b != "")
        {
          shutterOpenTime = atoi(b) * 60;
        }

        echo ("Enter the temperature stabilization wait time in minutes [default = 10
minutes] = ");
        b = input();
        if (b != "")
        {
          tempStableWaitTime = atoi(b) * 60;
        }
        echo("Shutter Open = ", shutterOpenTime / 60);

        echo(" ");
        echo("Shutter Open = ", shutterOpenTime / 60, " minutes");
        echo("Stabilize Time = ", tempStableWaitTime / 60, " minutes");
        echo( "Is this correct? [Y or N]");
        b = input();
        if (b == "Y" || b == "y")
        {
          redoLoop = 0;
        }
      }

// Enter the start time for the program ************************************
      redoLoop = 1;
      while (redoLoop)
      {
```

```
    echo(" ");
    echo ("Enter start time for Arrhenius Plot (military time format NO colon =>
0615)");
    echo ("To start now hit enter key.");

    b = input();

    if ( b != "")
    {
      startTimeNum = atoi(__Left(b,2))*3600 + atoi(__Right(b,2))*60;

      timeNow = mctime(time(0));
      hour = __Mid(timeNow,12,2);
      minute = __Mid(timeNow,15,2);
      timeNowNum = atoi(hour)*3600 + atoi(minute)*60;

      if (startTimeNum >= timeNowNum)
      {
        progSleepTime = startTimeNum - timeNowNum;
      }
      else
      {
        progSleepTime = 86400 - timeNowNum + startTimeNum;
      }

      echo ("Program will sleep for ", progSleepTime/60, " minutes.");
      echo("Is this corrrect? [Y or N]");
      b = input();

      if (b == "Y" || b == "y")
      {
         redoLoop = 0;
      }
    }
    else
    {
      progSleepTime = 0;
      echo ("Start program? [Y or N]");
      b = input();
      if (b == "Y" || b == "y")
      {
         redoLoop = 0;
      }
    }
  }
```

```
    if (progSleepTime != 0)
    {
      echo ("Program going to sleep mode for ", progSleepTime/60, " minutes at ",
mctime(time(0)));
      sleep (progSleepTime);
    }

// Start the Arrh plot ************************************************

    for (j = 0; j < numCells; ++j)
    {
      for (i = 0; i < rampSteps[j]; ++i)
      {
        echo ("Setting temperature "," for ", name[cellChoice[j]], " on step ", i+1, " to ",
rampTemp[j*8+i], " C");

        set_temp(names[cellChoice[j]],rampTemp[j*8+i]);

        echo ("Waiting for temperature to ramp");
        echo ("Started wait at ", mctime(time(0)));
        k = 1;
        while (k)
        {
          tempCell = temp(names[cellChoice[j]]);
          if (tempCell - setp(names[cellChoice[j]]) < 1)
          {
            k = 0;
          }
          sleep (5);
        }

        echo ("");
        echo ("Waiting ", tempStableWaitTime," seconds for temperature to stabilize");
        echo ("Started wait at ", mctime(time(0)));
        sleep(tempStableWaitTime);

        echo ("Acquiring background pressure for ", name[cellChoice[j]]);

        bkgPress = reading(BFM);
        for (k=0; k<9; ++k)
        {
          sleep (1);
          bkgPress += reading(BFM);
        }
        bkgPress = bkgPress/10;
        echo ("Background Pressure = ", bkgPress);
```

```
// Open shutter, wait 3 minutes, measure BFM
        shopen(names[cellChoice[j]]);
        echo (name[cellChoice[j]], " shutter OPEN at ", mctime(time(0)));
        sleep (shutterOpenTime);

        beamFlux = reading(BFM);
        for (k=0; k<9; ++k)
        {
          sleep (1);
          beamFlux += reading(BFM);
        }
        beamFlux = beamFlux/10;
        echo ("Beam Flux = ", beamFlux);

        shclose(names[cellChoice[j]]);
        echo (name[cellChoice[j]], " shutter CLOSED ", mctime(time(0)));

        BEP = beamFlux - bkgPress;
        echo ("BEP = ", BEP);

        fd = open (fileName, O_RDWR | O_APPEND);

        fdecho( fd, "");
        fdecho( fd, "Cell temperature ", name[cellChoice[j]],": Set = ",
rampTemp[j*8+i], " Actual = ", temp(names[cellChoice[j]]));
        fdecho( fd, name[cellChoice[j]]," Bkg: ", bkgPress, " ", name[cellChoice[j]], "
Flux: ", beamFlux, " ", name[cellChoice[j]], " BEP: ", BEP);

        close(fd);

        BEPArray[i] = BEP;
      }

// Sum the LLS fit variables for plotting
      for (k=0; k<rampSteps[j]; ++k)
      {
        sumX = sumX + (1/rampTemp[j*8+k]);
        sumX2 = sumX2 + ((1/rampTemp[j*8+k]) * (1/rampTemp[j*8+k]));
        sumY = sumY + log10(BEPArray[k]);
        sumXY = sumXY + (1/rampTemp[j*8+k]) * log10(BEPArray[k]);
      }

      slopeM = ((rampSteps[j] * sumXY) - (sumX * sumY))/((rampSteps[j] * sumX2) -
(sumX * sumX));
```

```
        interceptB = ((sumY * sumX2) - (sumX * sumXY))/((rampSteps[j] * sumX2) -
(sumX * sumX));

        fd = open (fileName, O_RDWR | O_APPEND);

        fdecho( fd,"");
        fdecho( fd, name[cellChoice[j]]," m: ", slopeM, " ", " b: ", interceptB);

// Find the tempearture for target flux;
        targetTemp = slopeM / (log10(targetFlux[j]) - interceptB);
        echo("");
        echo( " Target Temeprature for (Flux = ", targetFlux[i], ") => ", targetTemp);
        fdecho( fd," Target Temeprature for (Flux = ", targetFlux[j], ") => ", targetTemp);

        close(fd);

// Check that answer is within ramp range of Temps and set cell to target
        for (k = 0 ; k < rampSteps[i]; ++k)
        {
          if (targetTemp > rampTemp[j*8+k])
          {
            aboveMin = 1;
          }
          if (targetTemp < rampTemp[j*8+k])
          {
            belowMax = 1;
          }
        }
        if (belowMax && aboveMin)
        {
          echo("Setting ", names[cellChoice[j]], "temperature to target = ", targetTemp, "
C");
          set_temp(names[cellChoice[j]],targetTemp);
        }
        else
        {
          echo("Invalid target temperature leaving cell temperature alone");
        }
      }
    }
}

close(fd);
```

```
/*************************************************
/ CAR_Heater Cool Down Wait Step
/ J. Jeffers Created: 8/6/2009
/
/ Description: This program reads the CAR (substrate)
/   temperature and waits until it hits the target
/   temperature.  It then closes the Se shutter.
/************************************************/
#include <gauges.h>
#include <cells.h>

// variables all ready declared in previous code

echo("Waiting for CAR to cool down to 190");
i=1;
while (i)
{
  tempCAR = temp(CAR_Heater);
  if (tempCAR < 190)
  {
    i = 0;
  }
  sleep (5);
}

shclose(Se_zone1);
```

Photoluminescence Test Software

LabVIEW Function: FTIR Characterize.vi

Description:
This software allows the user to control the temperature, injection current, and data acquisition settings for the photoluminescence system described in this dissertation. There are 49 declared variables that includes data structures containing multiple primitive type variables. The software implements a run-time menu with traditional "File", "View", and "Help" menus.

The image below is the virtual instrument (VI) user interface front panel for the top-level main function.

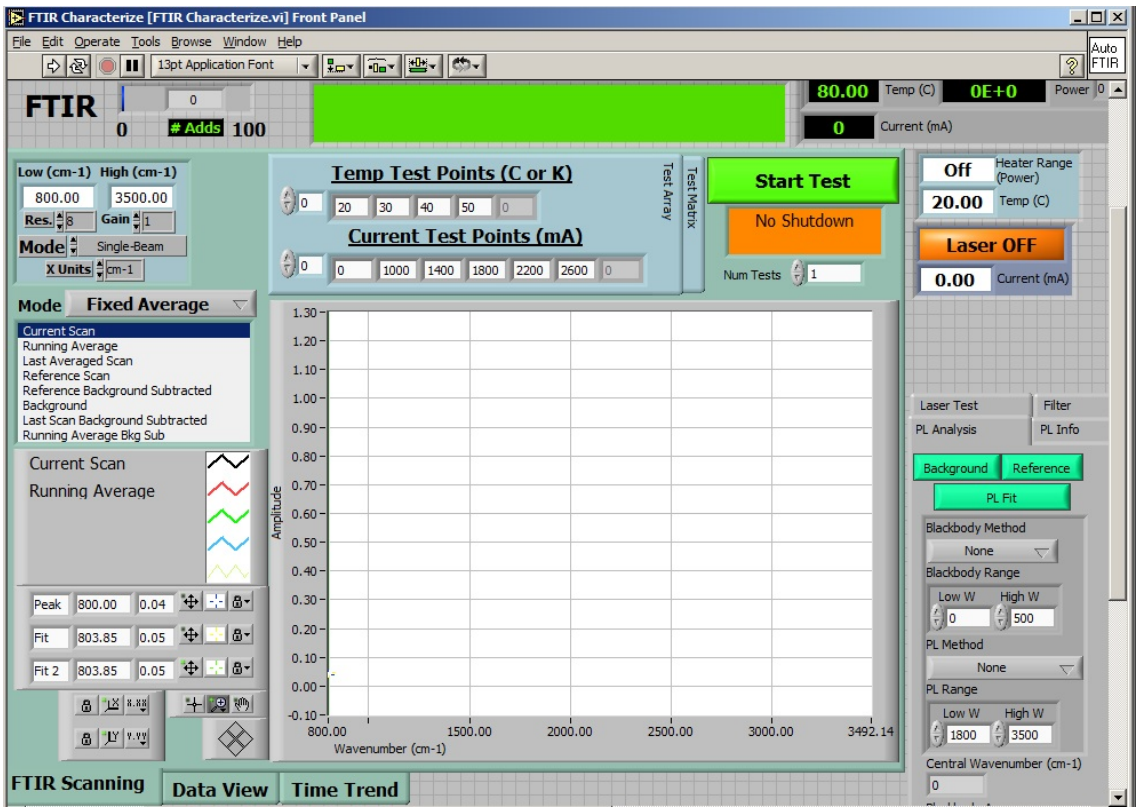

The image below is the visual software code block diagram. The structures shown are a custom programming style for real-time data acquisition on a standard personal computer Windows operating system.

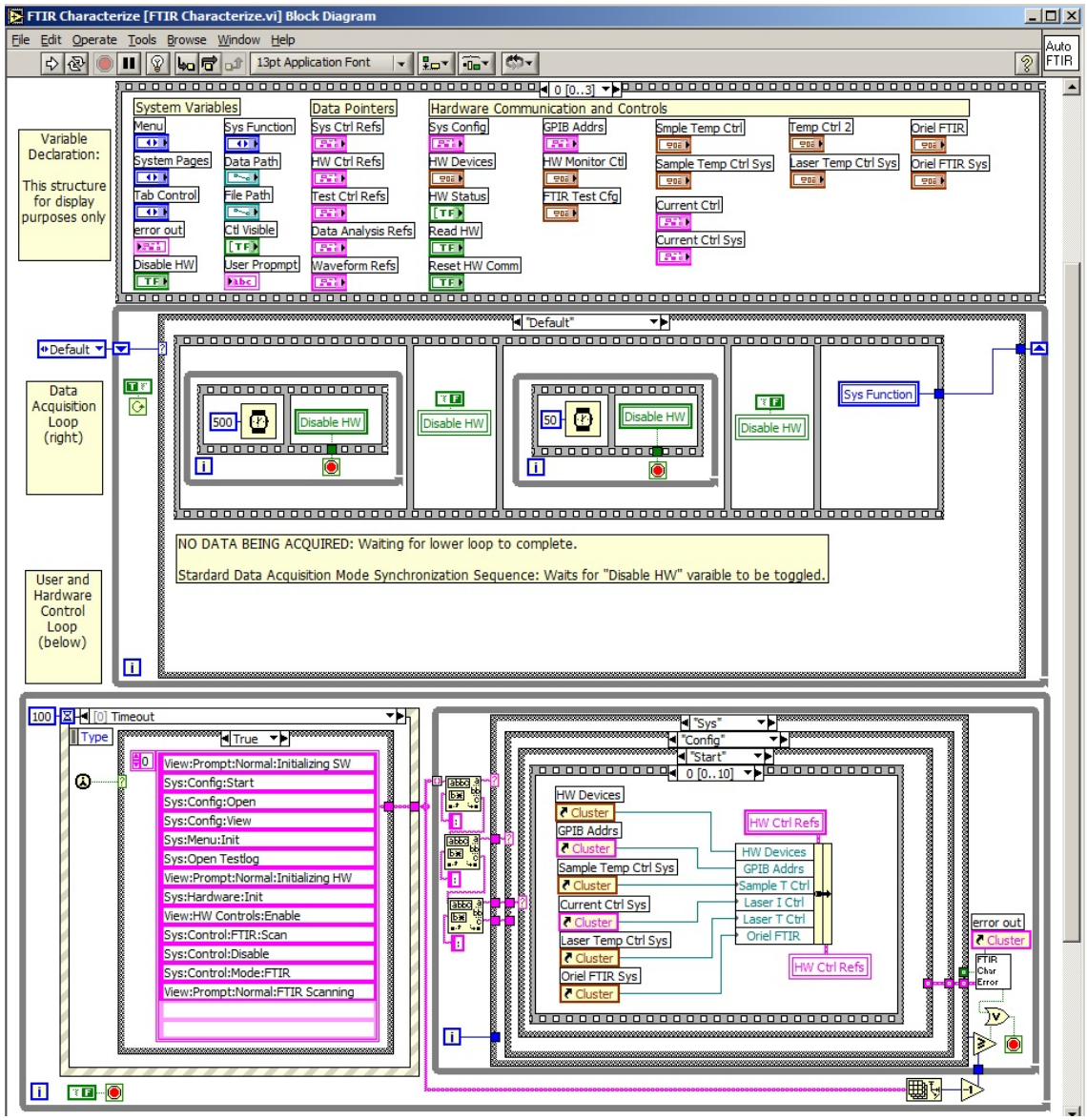

Code Segment Description: The event structure in the lowest continuous loop "User and Hardware Control" in the previous image handles all user input. There are 2 system events and 18 independent user actions. Shown below is the user action for starting a PL test. The grey box to the right shows a complete list of events. There are four actions the software completes for this event.

1. Disable all hardware control or data acquisition while variables are changed
2. Notify user of software status
3. Modify the screen objects that the user can change based on software mode
4. Prompt user to input the required information to begin a test

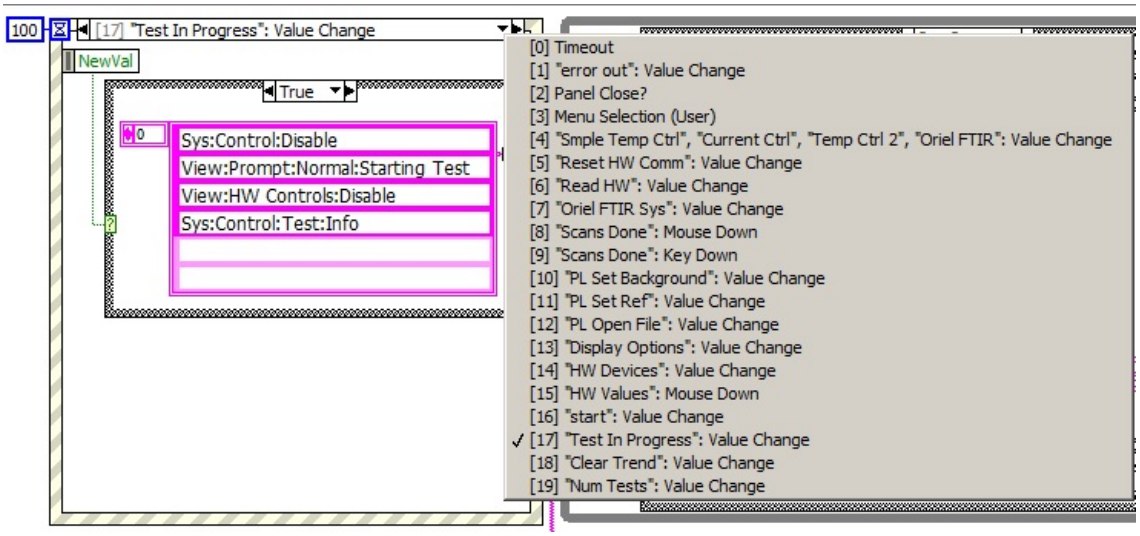

Code Segment Description: The event structure in the lowest continuous loop handles all user input. There are 2 system events and 18 independent user actions. Shown below is the user action for starting a PL test. The grey box to the right shows a complete list of events. There are four actions the software completes for this event.

1. Disable all hardware control or data acquisition while variables are changed
2. Notify user of software status
3. Modify the screen objects that the user can change based on software mode

LabVIEW Function: Auto FTIR Hardware

Description: This VI is the only access point for changing the settings of any OEM hardware devices used in the automated FTIR system. The hardware "Read" functions may appear in higher levels of software. Synchronization is maintained in the individual device software. There are four possible hardware devices that can be configured for the different commercial products listed below.

1. Temperature control unit #1 (for device under test)
    a. ILX Lightwave Model #3752
    b. ILX Lightwave Model #3900
    c. Lakeshore Cryotronics Model #330
    d. Lakeshore Cryotronics Model #331
    e. Stanford Research System Model #501
2. Temperature control unit #2 (for photoluminescence pump laser)
    a. ILX Lightwave Model #3752
    b. ILX Lightwave Model #3900
3. Laser current supply
    a. ILX Lightwave Model #3232
    b. ILX Lightwave Model #3900 (1000 mA, 4000 mA, and 8000 mA)
4. Oriel MIR8000 Fourier Transform Infrared (FTIR) Spectrometer

VI Hierarchy

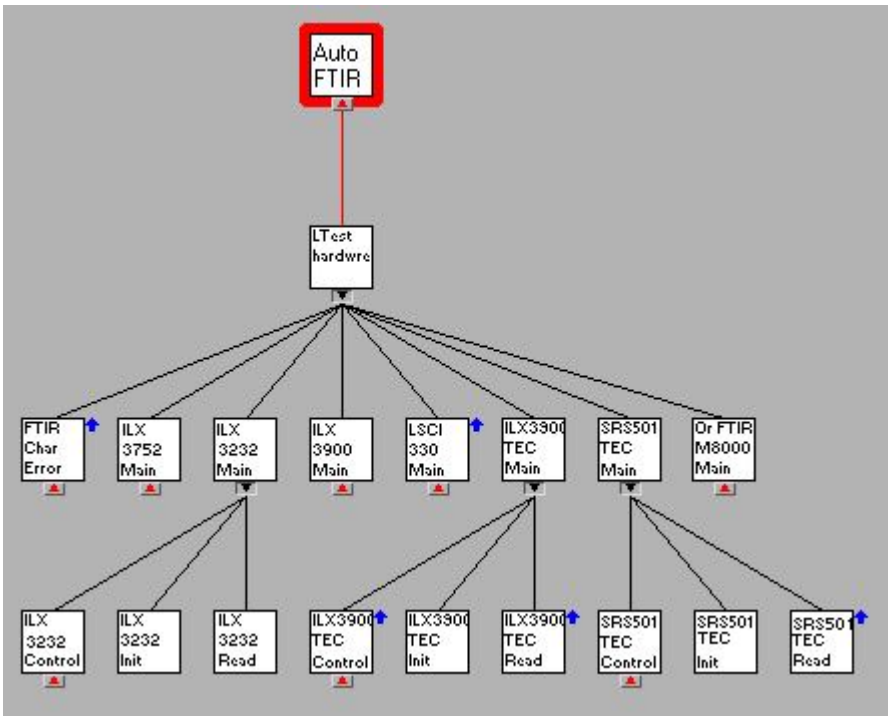

LabVIEW Function: SRS 501 Thermoelectric Cooler Main

Description: All hardware control software using the General Purpose Interface Bus (GPIB) has three sub-VIs: 1) Init, 2) Control or Load, and 3) Read. The Init function creates and maintains a semaphore for synchronizing access to the Read function from different parent callers. GPIB communications uses the LabVIEW VISA serial protocol with ASCII text commands that are listed in italics below. The set routine uses ASCII numbers with *X* representing a numeral and a period indicating floating point.

1. Initialize Routine
    a. Clear GPIB Communications (1256 byte read with 125 ms timeout)
    b. Read maximum Temperature setting: *TMAX?*
    c. Check for temperature sensor error: *TSNS?*
    d. Read maximum TEC Power limit (voltage): *TVLM?*
    e. Read maximum TEC Power limit (current): *TILM?*
2. Read Routine
    a. Temperature setpoint: *TEMP?*
    b. Thermoelectric cooler status (ON/OFF): *TEON?*
    c. Thermoelectric cooler current: *TEMP?*
    d. Thermoelectric cooler voltage: *TEMP?*
    e. Actual temperature sensor reading: *TTRD?*
    f. Control Proportional (P) gain setting: *TPGN?*
    g. Control Integral (I) gain setting: *TIGN?*
    h. Control Derivative (D) gain setting: *TDGN?*
3. Control/Load Routine
    a. Temperature setpoint: *TEMP XXX.XX*
    b. Thermoelectric cooler status (ON/OFF): *TEON X*
    c. Control Proportional (P) gain setting: *TPGN XXX.XX*
    d. Control Integral (I) gain setting: *TIGN XXX.XX*
    e. Control Derivative (D) gain setting: *TDGN XXX.XX*

Data Structure for Temperature Control

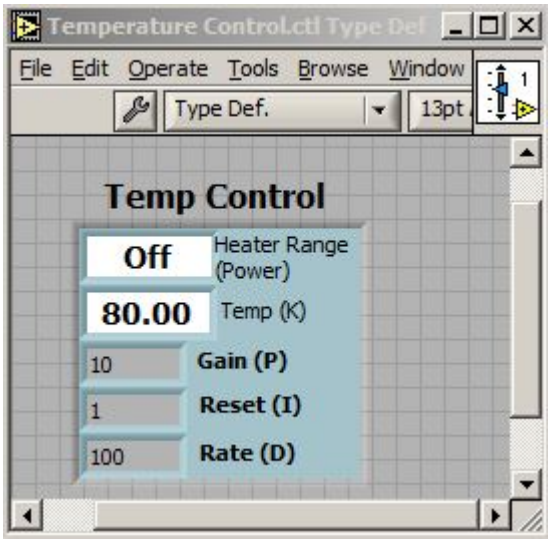

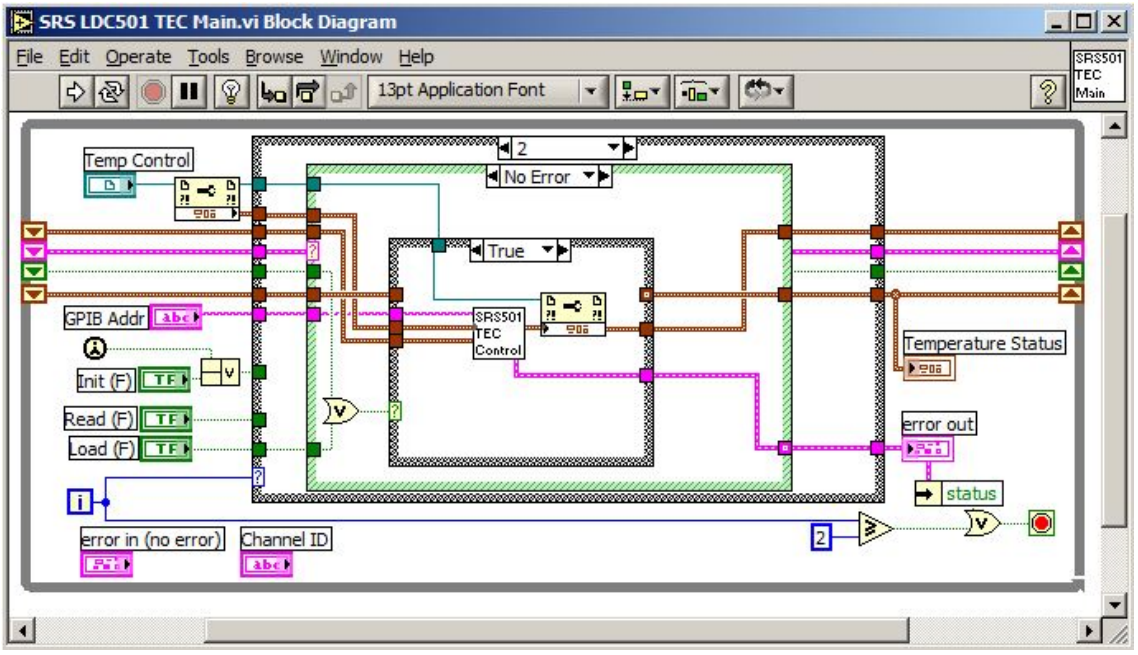
SRS LDC501 TEC Main.vi Block Diagram
File Edit Operate Tools Browse Window Help
13pt Application Font
SRS501 TEC Main
Temp Control
2
No Error
True
GPIB Addr
SRS501 TEC Control
Temperature Status
Init (F)
Read (F)
Load (F)
error out
status
error in (no error)
Channel ID
2

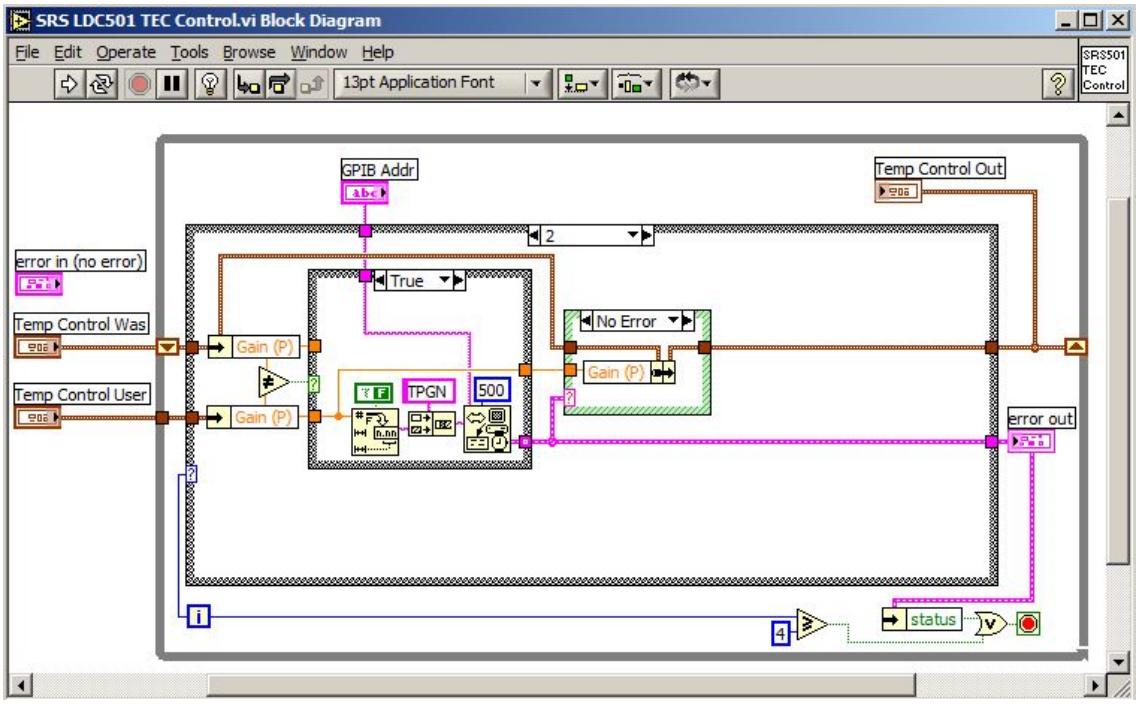
SRS LDC501 TEC Control.vi Block Diagram
File Edit Operate Tools Browse Window Help
13pt Application Font
SRS501 TEC Control
GPIB Addr
Temp Control Out
2
error in (no error)
True
No Error
Temp Control Was
Gain (P)
Temp Control User
TPGN
500
error out
status
4

LabVIEW Function: Oriel MIR8000 FTIR Main

Description:
This control software uses Direct Memory Access available in Windows 98 software and removed from all later operating systems. The software code shown is a combination of proprietary software purchased from Oriel, Inc. in 1998 for LabVIEW Version 6.1 that uses pre-compiled dynamically linked libraries (.dll). All software was upgraded to LabVIEW Version 7.0 that required significant modification and removal of legacy code segments except for use of global variables that remain in the current version of code.

1. Initialize Routine
    a. Open and parse text file from hard disk
    b. Set Motor Control Board (MCB)
        i. Wavenumber Resolution
        ii. Laser Frequency
        iii. Oversampling
    c. Set Gain/Filter
        i. Low Wavenumber
        ii. High Wavenumber
        iii. Gain
        iv. MCB Delay
2. Read Routine
    a. Acquire semaphore "Oriel MIR80000"
    b. Wait for buffer ready
    c. Read interferogram buffer (n points)
    d. Release buffer
    e. Perform FFT
    f. Release semaphore
3. Control/Load Routine
    a. Coadds
    b. Wavenumber Resolution
    c. Laser Frequency
    d. Oversampling
    e. Low wavenumber
    f. High wavenumber
    g. Gain
4. FFT Routine for interferogram
    a. Find centerburst (max index)
    b. Adjust for phase (zero padding)
    c. Perform window apodization
    d. Calculate real FFT

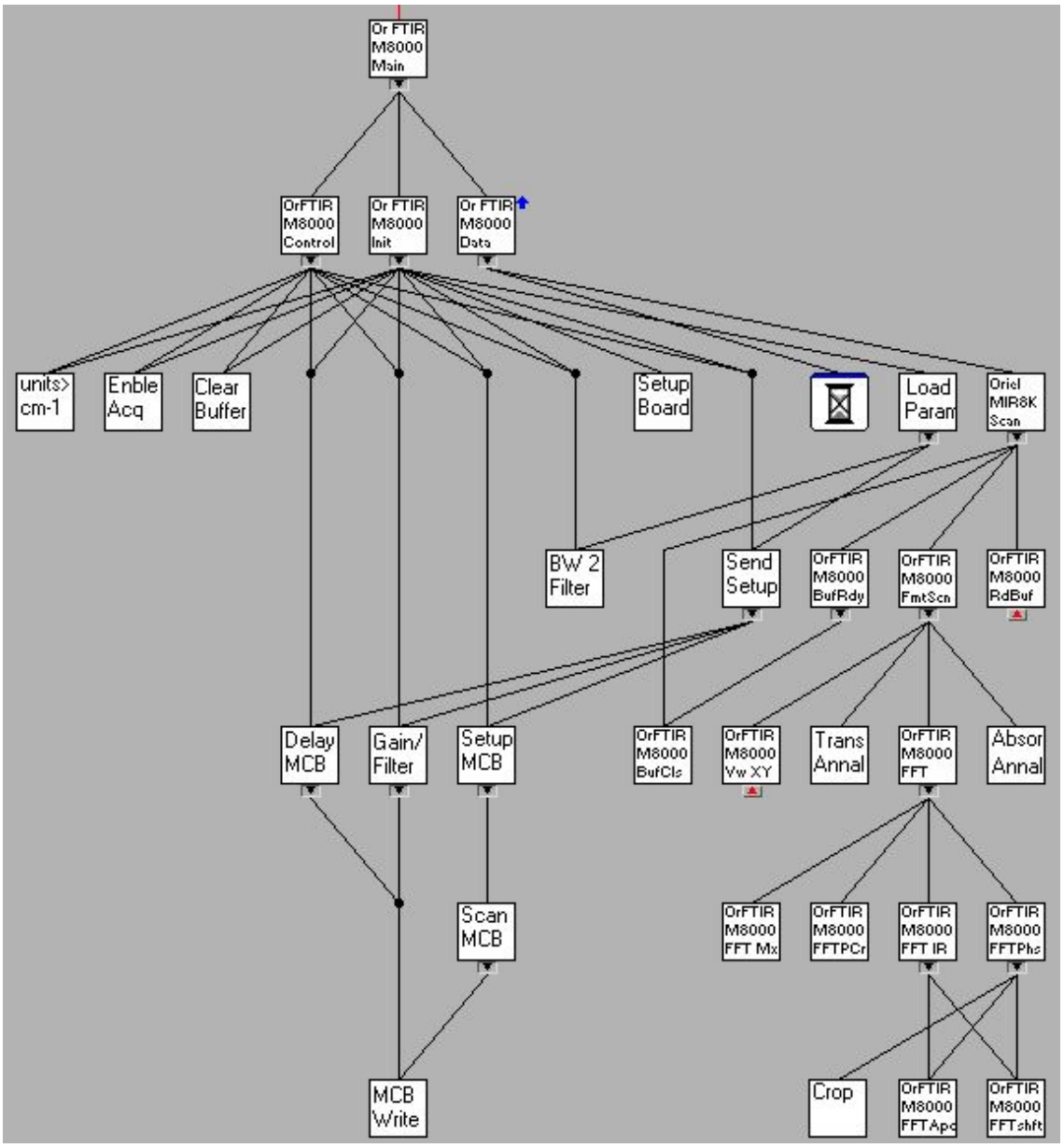
Or FTIR M8000 Main
OrFTIR M8000 Control
Or FTIR M8000 Init
Or FTIR M8000 Data
units> cm-1
Enble Acq
Clear Buffer
Setup Board
Load Param
Oriel MIR8K Scan
BW 2 Filter
Send Setup
OrFTIR M8000 BufRdy
OrFTIR M8000 FmtScn
OrFTIR M8000 RdBuf
Delay MCB
Gain/ Filter
Setup MCB
OrFTIR M8000 BufCls
OrFTIR M8000 Vw XY
Trans Annal
OrFTIR M8000 FFT
Absor Annal
Scan MCB
OrFTIR M8000 FFT Mx
OrFTIR M8000 FFTPCr
OrFTIR M8000 FFT IR
OrFTIR M8000 FFTPhs
MCB Write
Crop
OrFTIR M8000 FFTApo
OrFTIR M8000 FFTshft

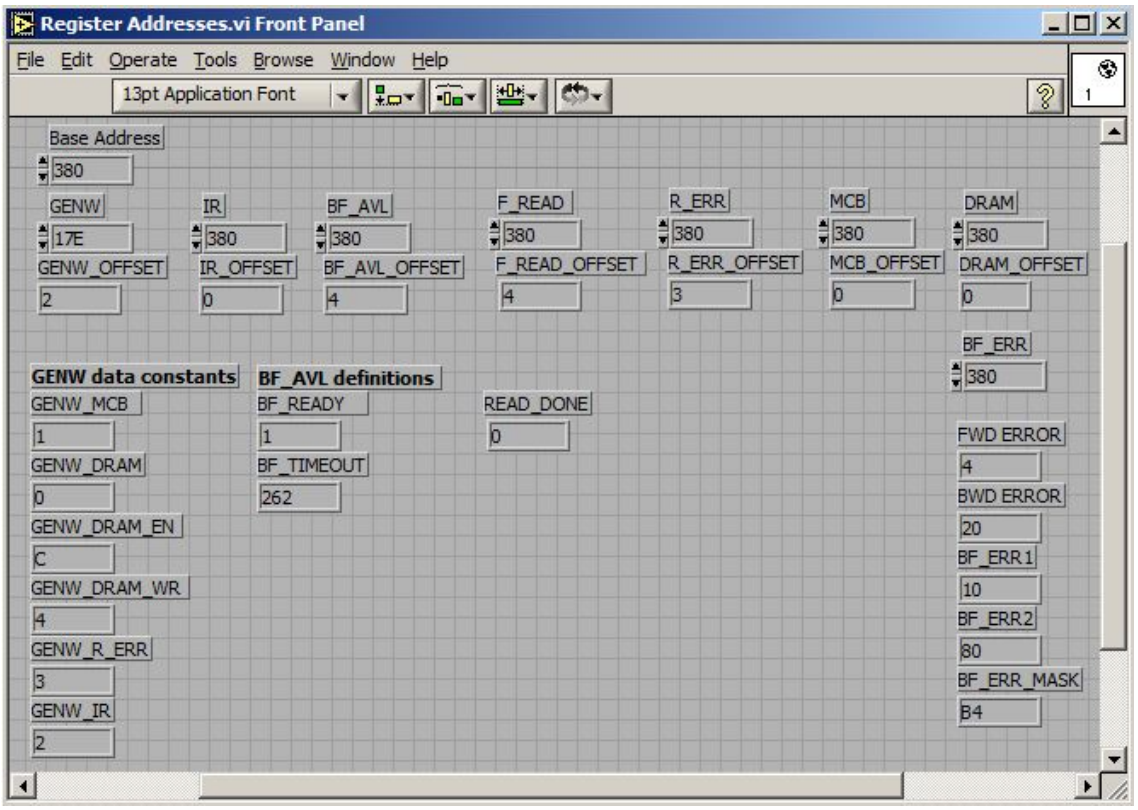
Register Addresses.vi Front Panel
File Edit Operate Tools Browse Window Help
13pt Application Font
Base Address
380
GENW
17E
IR
380
BF_AVL
380
F_READ
380
R_ERR
380
MCB
380
DRAM
380
GENW_OFFSET
2
IR_OFFSET
0
BF_AVL_OFFSET
4
F_READ_OFFSET
4
R_ERR_OFFSET
3
MCB_OFFSET
0
DRAM_OFFSET
0
BF_ERR
380
GENW data constants
GENW_MCB
1
GENW_DRAM
0
GENW_DRAM_EN
C
GENW_DRAM_WR
4
GENW_R_ERR
3
GENW_IR
2
BF_AVL definitions
BF_READY
1
BF_TIMEOUT
262
READ_DONE
0
FWD ERROR
4
BWD ERROR
20
BF_ERR1
10
BF_ERR2
80
BF_ERR_MASK
B4

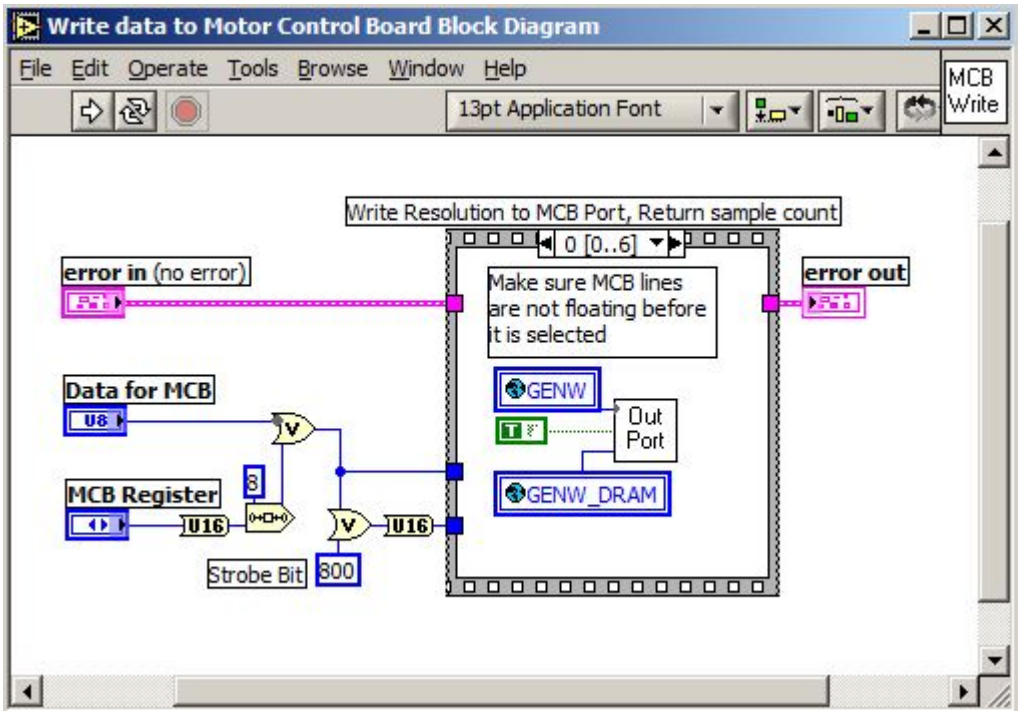
Write data to Motor Control Board Block Diagram
File Edit Operate Tools Browse Window Help
13pt Application Font
MCB Write
Write Resolution to MCB Port, Return sample count
0 [0..6]
error in (no error)
error out
Make sure MCB lines are not floating before it is selected
Data for MCB
U8
MCB Register
U16
8
U16
GENW
Out Port
GENW_DRAM
Strobe Bit
800

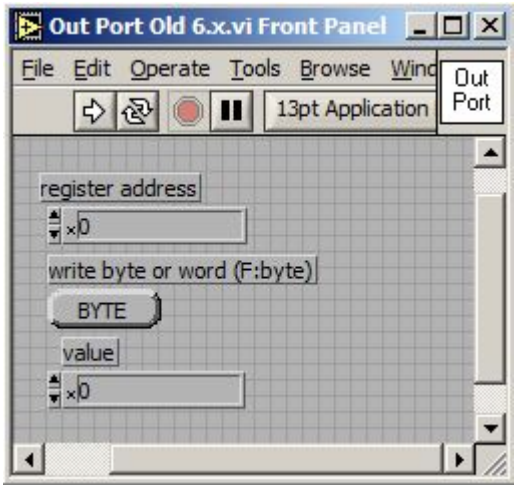
Out Port Old 6.x.vi Front Panel
File Edit Operate Tools Browse Wind
13pt Application
Out Port
register address
0
write byte or word (F:byte)
BYTE
value
0

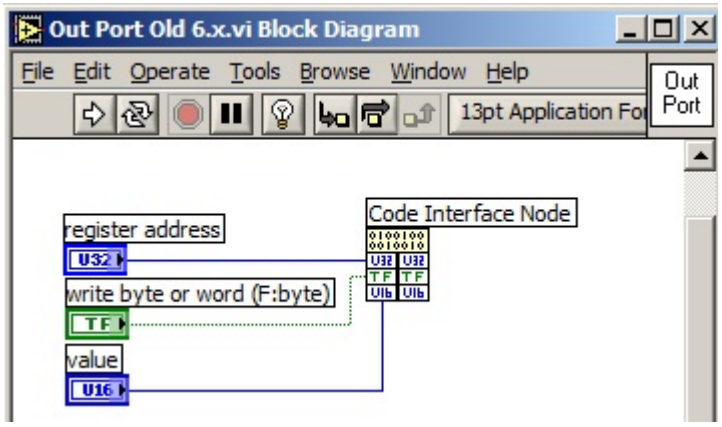
Out Port Old 6.x.vi Block Diagram
File Edit Operate Tools Browse Window Help
13pt Application Fo
Out Port
register address
U32
write byte or word (F:byte)
TF
value
U16
Code Interface Node

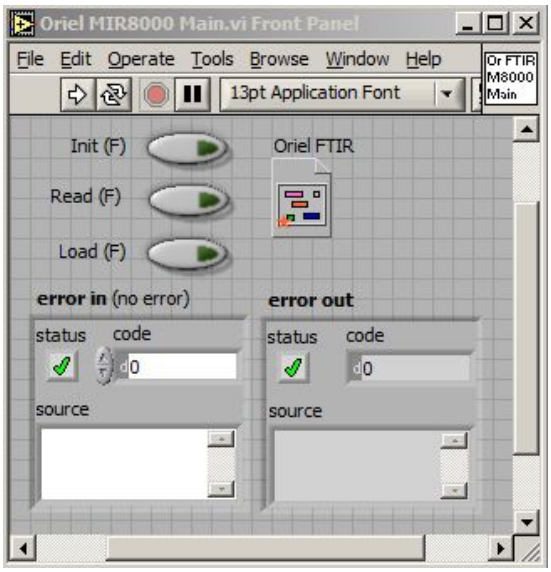
Oriel MIR8000 Main.vi Front Panel
File Edit Operate Tools Browse Window Help
13pt Application Font
Or FTIR M8000 Main
Init (F)
Read (F)
Load (F)
Oriel FTIR
error in (no error)
status
code
0
source
error out
status
code
0
source

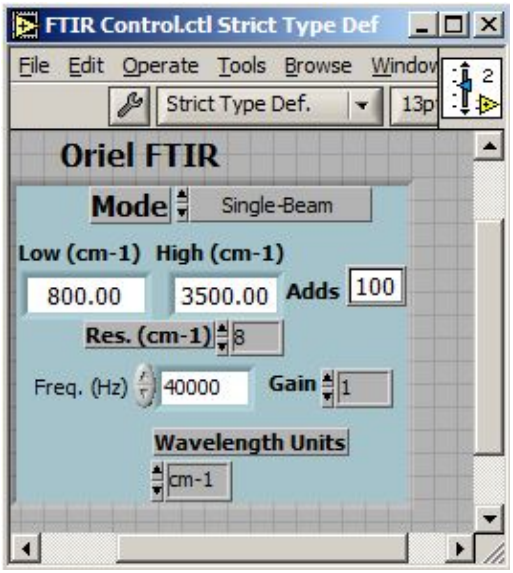
FTIR Control.ctl Strict Type Def
File Edit Operate Tools Browse Windo
Strict Type Def.
13p
Oriel FTIR
Mode
Single-Beam
Low (cm-1)
High (cm-1)
800.00
3500.00
Adds
100
Res. (cm-1)
8
Freq. (Hz)
40000
Gain
1
Wavelength Units
cm-1

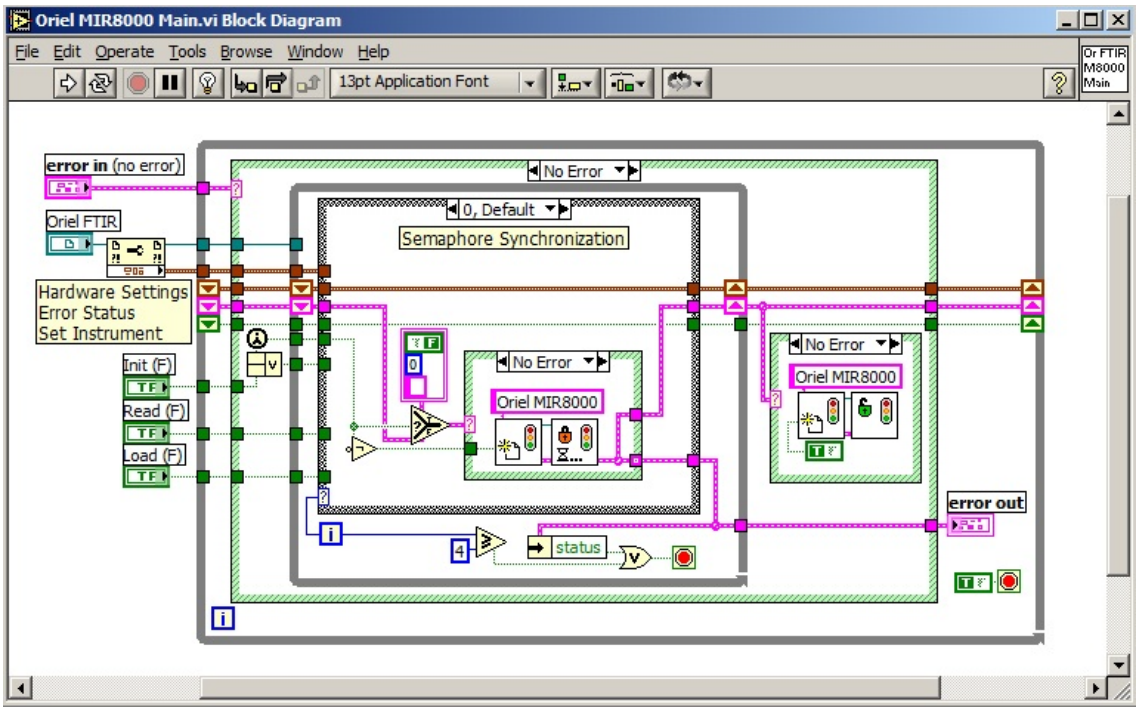
Oriel MIR8000 Main.vi Block Diagram
File Edit Operate Tools Browse Window Help
13pt Application Font
Or FTIR M8000 Main
error in (no error)
Oriel FTIR
Hardware Settings
Error Status
Set Instrument
Init (F)
Read (F)
Load (F)
No Error
0, Default
Semaphore Synchronization
Oriel MIR8000
status
error out

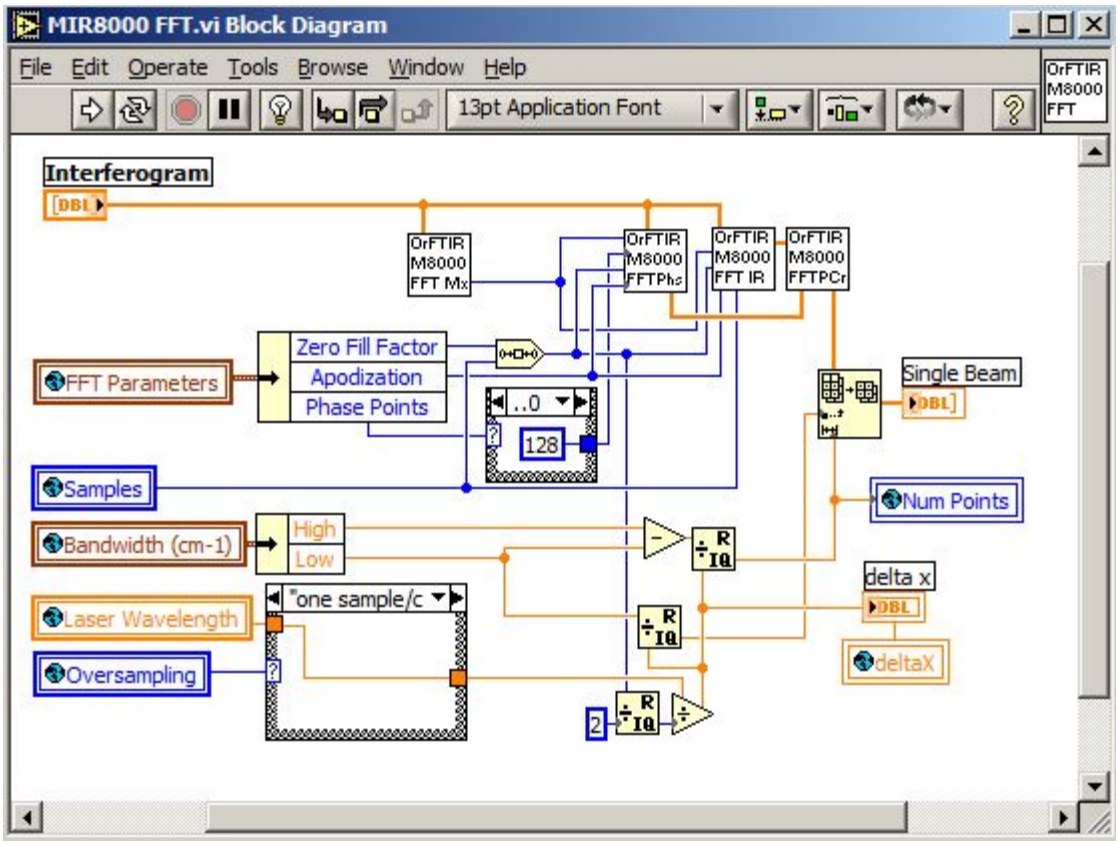
MIR8000 FFT.vi Block Diagram
File Edit Operate Tools Browse Window Help
13pt Application Font
OrFTIR M8000 FFT
Interferogram
DBL
OrFTIR M8000 FFT Mx
OrFTIR M8000 FFTPhs
OrFTIR M8000 FFT IR
OrFTIR M8000 FFTPCr
FFT Parameters
Zero Fill Factor
Apodization
Phase Points
..0
128
Single Beam
Samples
Num Points
Bandwidth (cm-1)
High
Low
delta x
Laser Wavelength
"one sample/c
deltaX
Oversampling
2

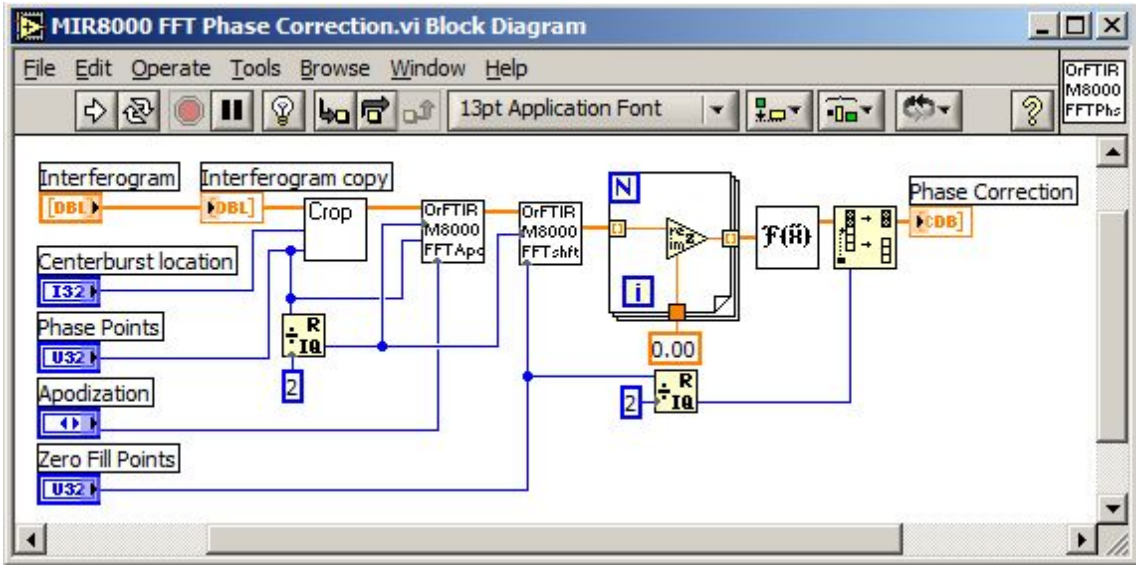
MIR8000 FFT Phase Correction.vi Block Diagram
File Edit Operate Tools Browse Window Help
13pt Application Font
OrFTIR M8000 FFTPhs
Interferogram
Interferogram copy
Crop
OrFTIR M8000 FFTApo
OrFTIR M8000 FFTshift
N
i
0.00
Phase Correction
Centerburst location
I32
Phase Points
U32
Apodization
Zero Fill Points
U32
2
2

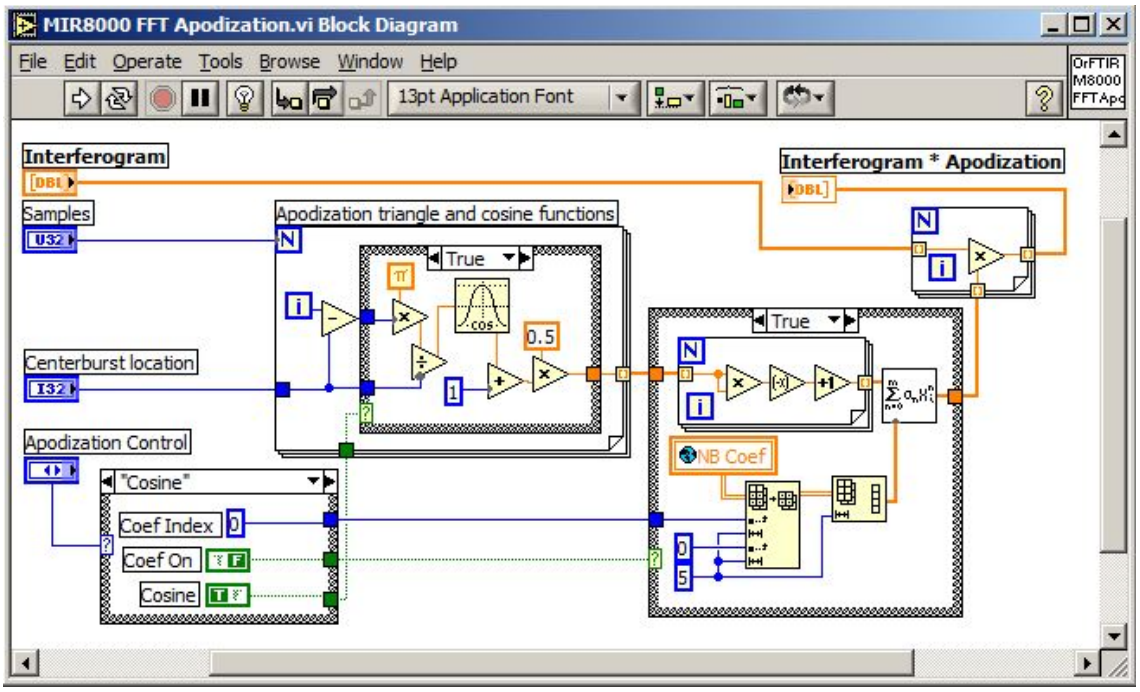
MIR8000 FFT Apodization.vi Block Diagram
File Edit Operate Tools Browse Window Help
13pt Application Font
OrFTIR M8000 FFTApo
Interferogram
Samples
U32
Centerburst location
I32
Apodization Control
Apodization triangle and cosine functions
True
0.5
1
"Cosine"
Coef Index
Coef On
Cosine
Interferogram * Apodization
NB Coef

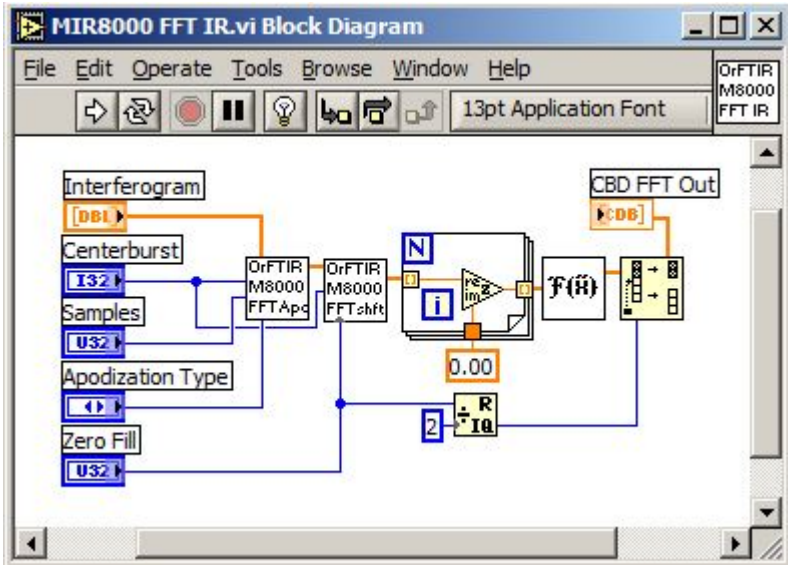
MIR8000 FFT IR.vi Block Diagram
File Edit Operate Tools Browse Window Help
13pt Application Font
OrFTIR M8000 FFT IR
Interferogram
Centerburst
Samples
Apodization Type
Zero Fill
OrFTIR M8000 FFTApo
OrFTIR M8000 FFTshft
0.00
2
CBD FFT Out

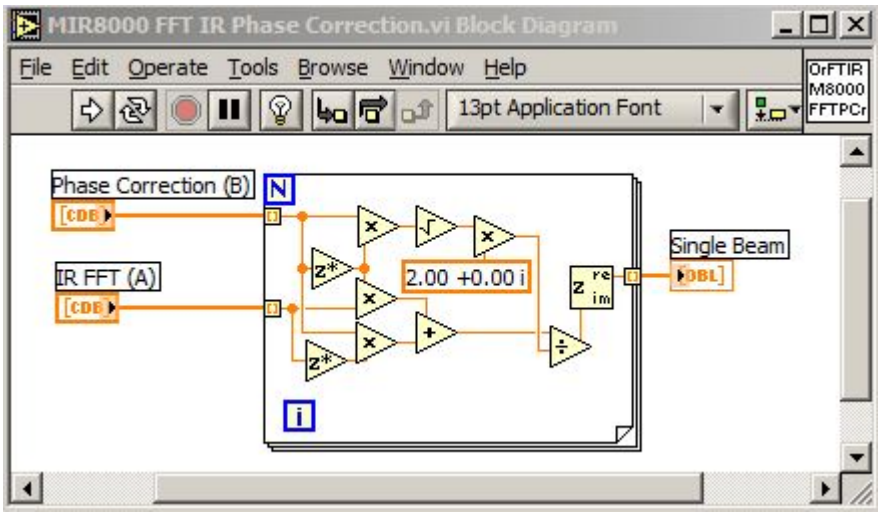
MIR8000 FFT IR Phase Correction.vi Block Diagram
File Edit Operate Tools Browse Window Help
13pt Application Font
OrFTIR
M8000
FFTPCr
Phase Correction (B)
IR FFT (A)
2.00 +0.00 i
Single Beam
DBL

Photoluminescence Data Analysis Software

LabVIEW Function: PL Data Processing.vi

Description: This VI is the main function and user interface for post-test analysis of PL emission spectra from the "Automated FTIR Test" software. This software allows the user to edit and calculate various properties of the XY text file output described in this dissertation. There are 93 declared variables that includes data structures containing multiple primitive type variables. The software implements a run-time menu with traditional "File", "View", and "Help" menus.

VI Block Diagram

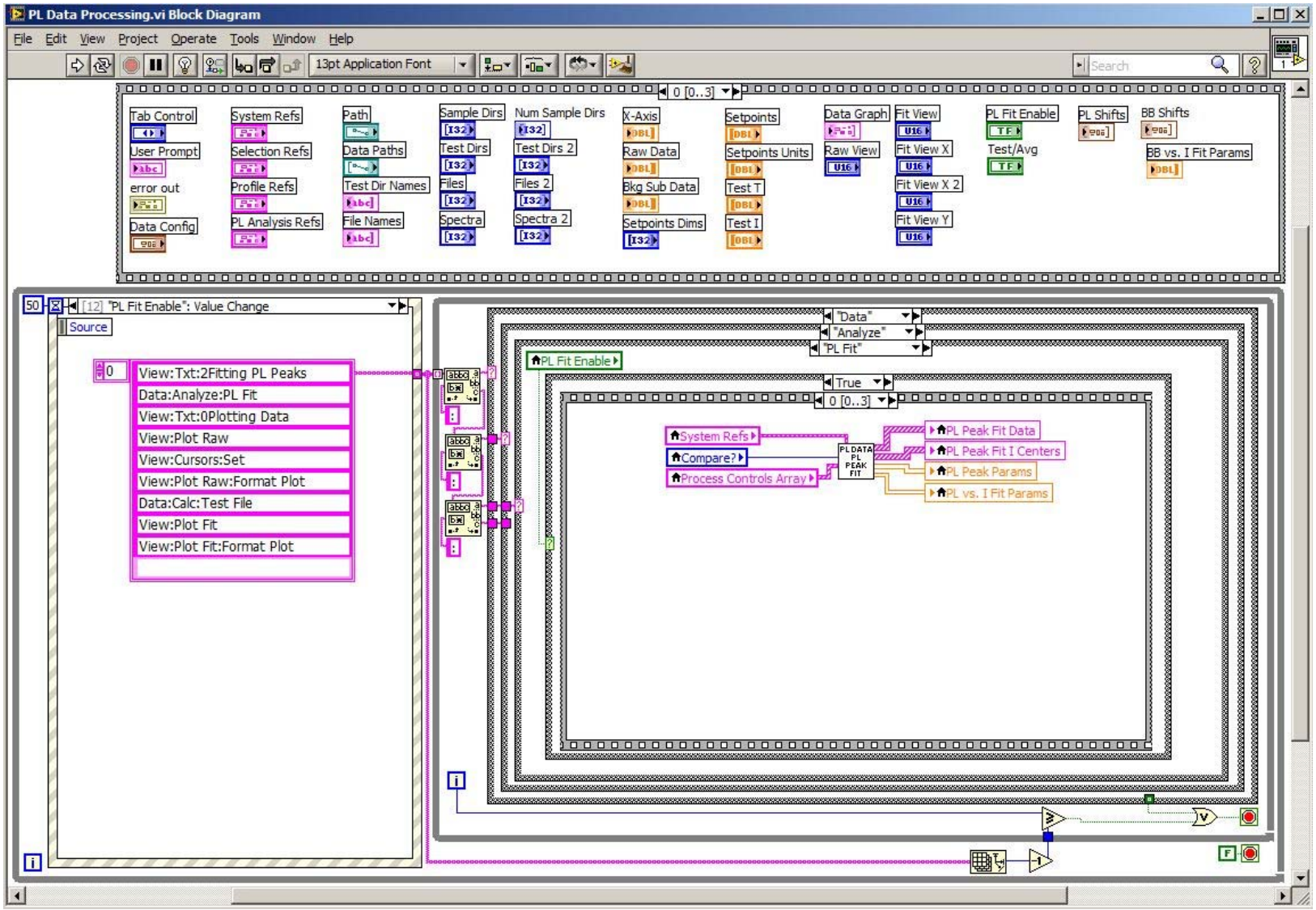
PL Data Processing.vi Block Diagram
File Edit View Project Operate Tools Window Help
13pt Application Font
Search
Tab Control
User Prompt
error out
Data Config
System Refs
Selection Refs
Profile Refs
PL Analysis Refs
Path
Data Paths
Test Dir Names
File Names
Sample Dirs
Test Dirs
Files
Spectra
Num Sample Dirs
Test Dirs 2
Files 2
Spectra 2
X-Axis
Raw Data
Bkg Sub Data
Setpoints Dims
Setpoints
Setpoints Units
Test T
Test I
Data Graph
Raw View
Fit View
Fit View X
Fit View X 2
Fit View Y
PL Fit Enable
Test/Avg
PL Shifts
BB Shifts
BB vs. I Fit Params
[12] "PL Fit Enable": Value Change
Source
0
View:Txt:2Fitting PL Peaks
Data:Analyze:PL Fit
View:Txt:0Plotting Data
View:Plot Raw
View:Cursors:Set
View:Plot Raw:Format Plot
Data:Calc:Test File
View:Plot Fit
View:Plot Fit:Format Plot
"Data"
"Analyze"
"PL Fit"
PL Fit Enable
True
System Refs
Compare?
Process Controls Array
PL DATA PL PEAK FIT
PL Peak Fit Data
PL Peak Fit I Centers
PL Peak Params
PL vs. I Fit Params

LabVIEW Function: PL Data Peak Fit.vi

Description:
This VI manipulates the XY spectral data to calculate the PL peak energy maximum. The first step is to separate the energy range of interest, filter the data, and remove optical artifacts including blackbody radiation and molecular absorption. The data equation is guessed. This then uses the Non-linear Levenberg-Marquardt Fit (NLLM) Function.

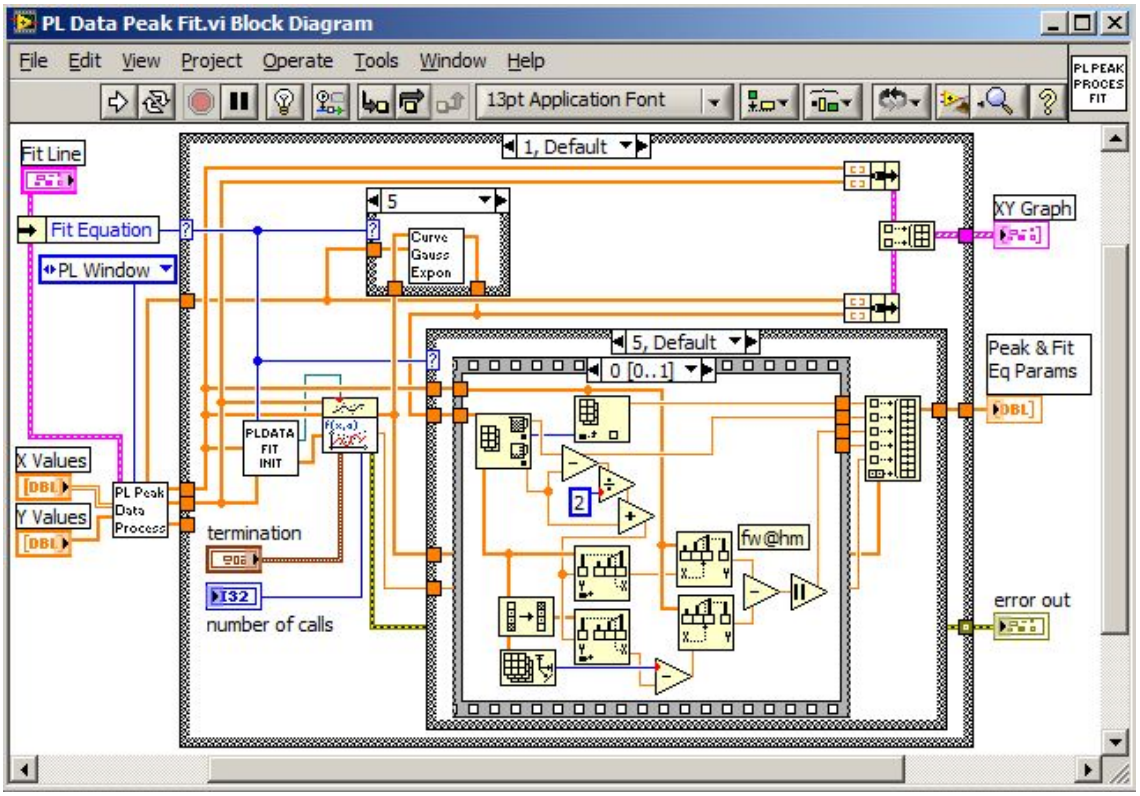

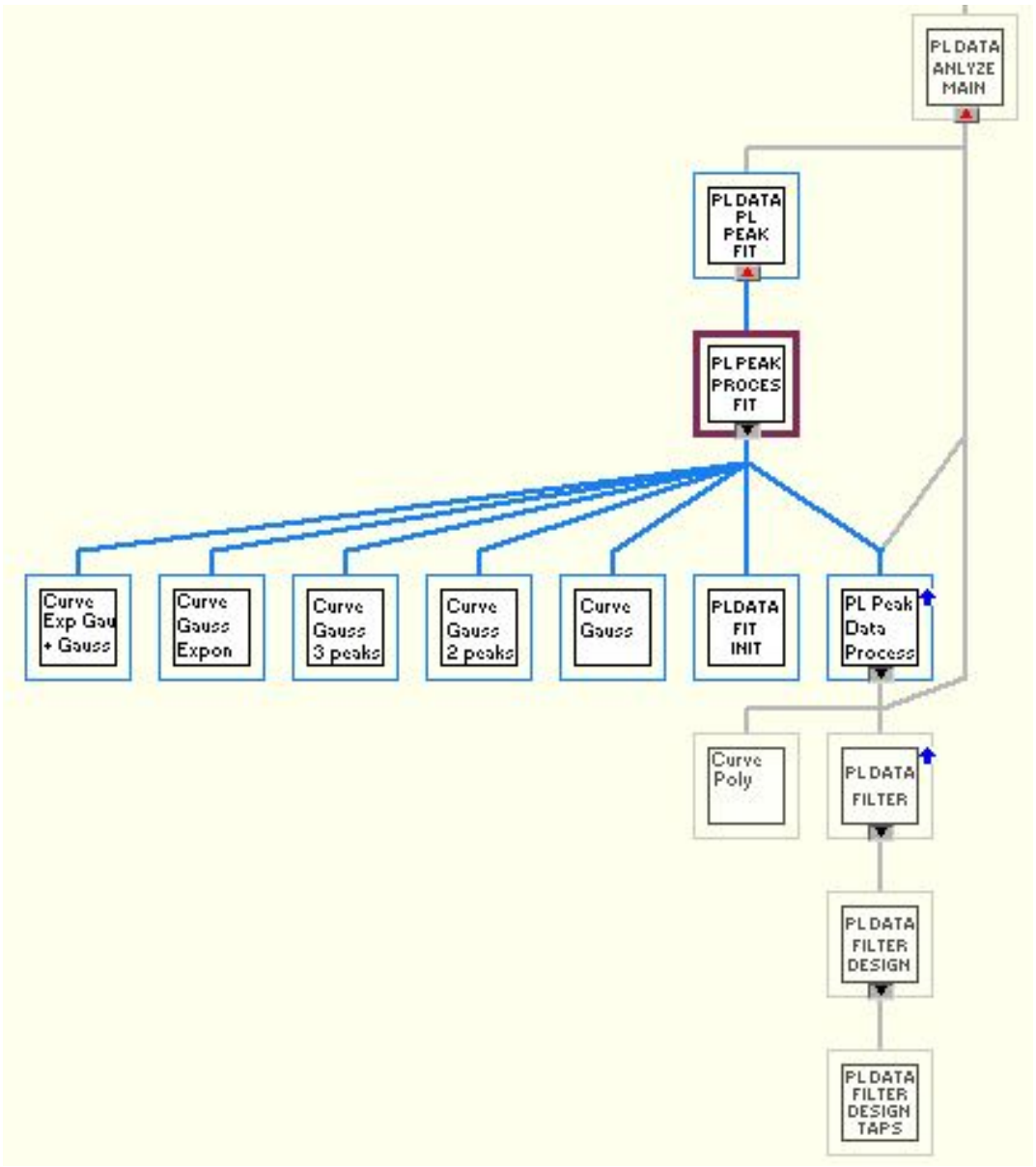
PL DATA ANLYZE MAIN
PL DATA PL PEAK FIT
PL PEAK PROCES FIT
Curve Exp Gau + Gauss
Curve Gauss Expon
Curve Gauss 3 peaks
Curve Gauss 2 peaks
Curve Gauss
PLDATA FIT INIT
PL Peak Data Process
Curve Poly
PL DATA FILTER
PL DATA FILTER DESIGN
PL DATA FILTER DESIGN TAPS

LabVIEW Function: PL Data Peak Data Processing.vi

Description:
This VI applies DSP algorithms to the FTIR intensity spectral data. The first step is to separate the energy range of interest, filter the data, and remove optical artifacts including blackbody radiation and molecular absorption.

The image below shows the fourth step of this function that applies a digital filter to the FTIR intensity spectral data

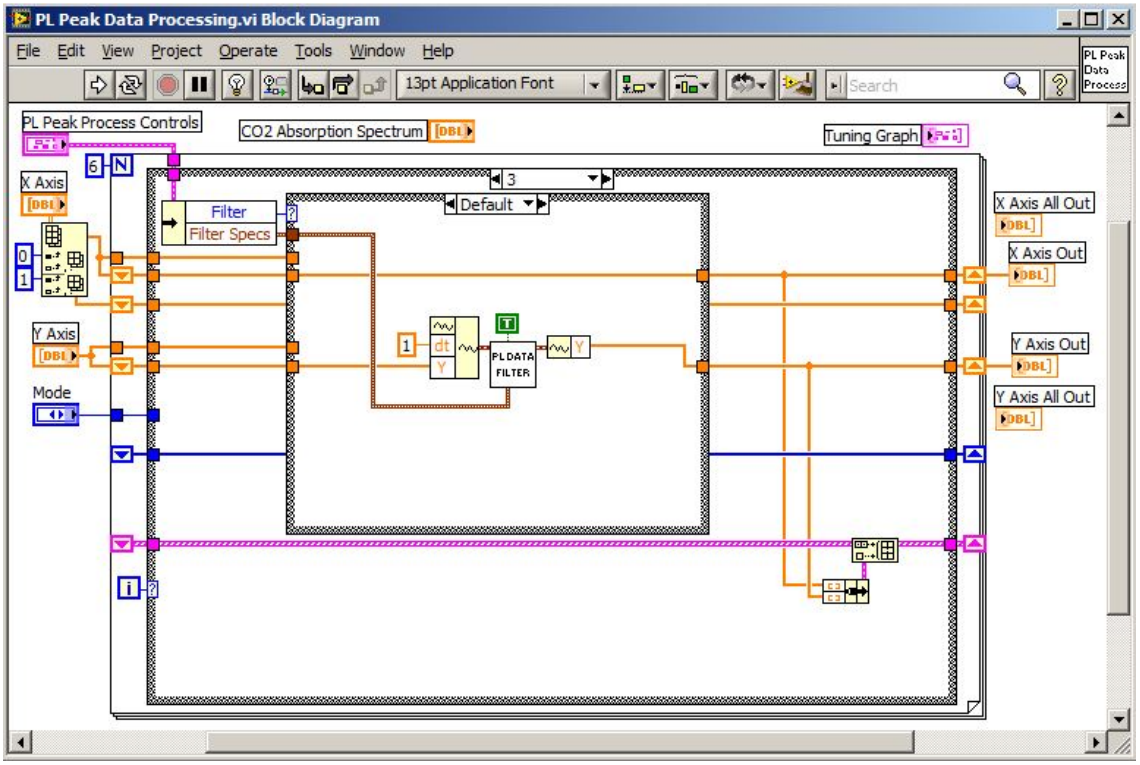

LabVIEW Functions: PL Data Filter.vi and PL Data Filter Design Coefficients.vi

Description: This VI performs both infinite impulse response (IIR) and frequency based filtering. The block diagram shown below was developed from the LabVIEW 7.0 real-time filter example. The code segment shown is for an IIR filter with the "Butterworth" design method being the default coefficient calculation.

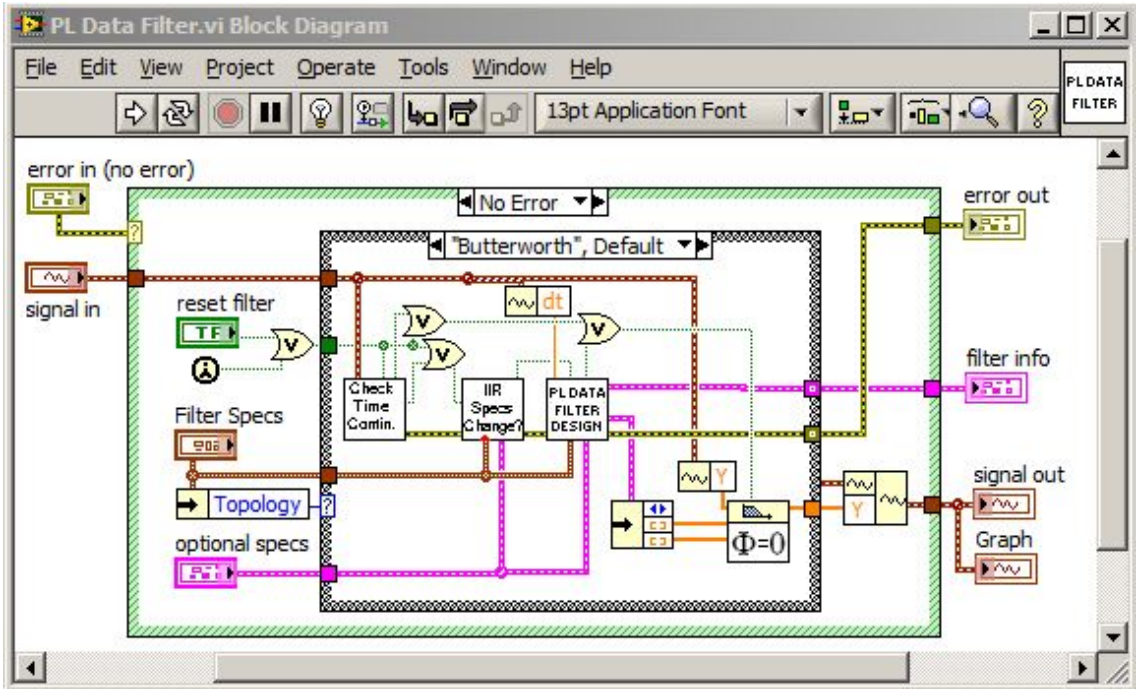

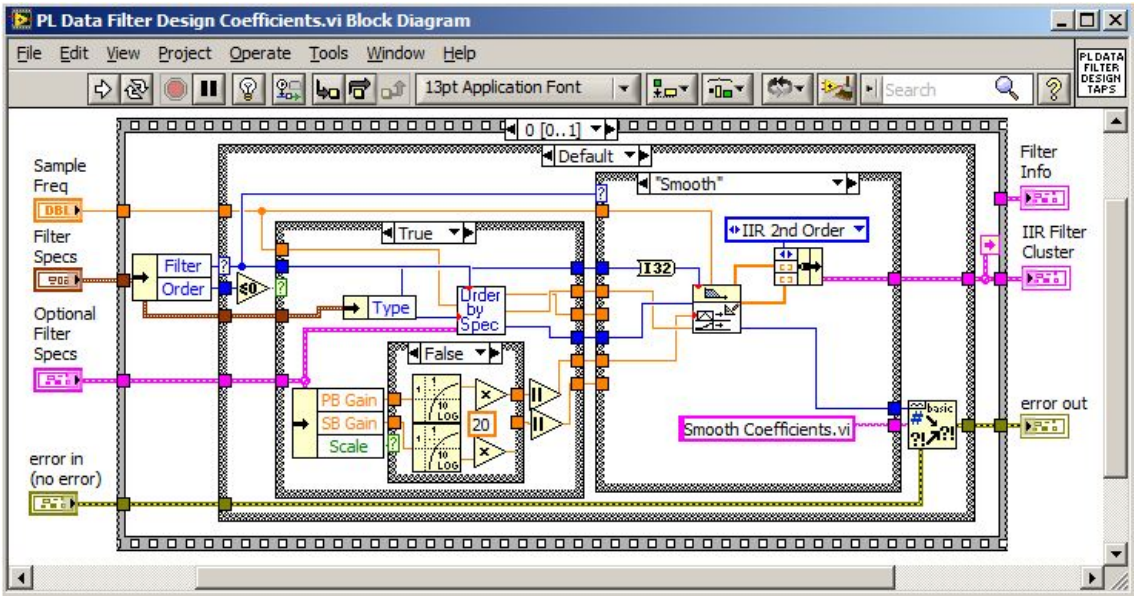

LabVIEW Function: PL Data Fit Initialize.vi

Description:
This VI is used to select and initialize the mathematical function y = F(x, a0, a1 …) for the NLLM fit in the parent caller. The default is the Gaussian function with three parameters: amplitude, width (sigma), and an x-axis offset.

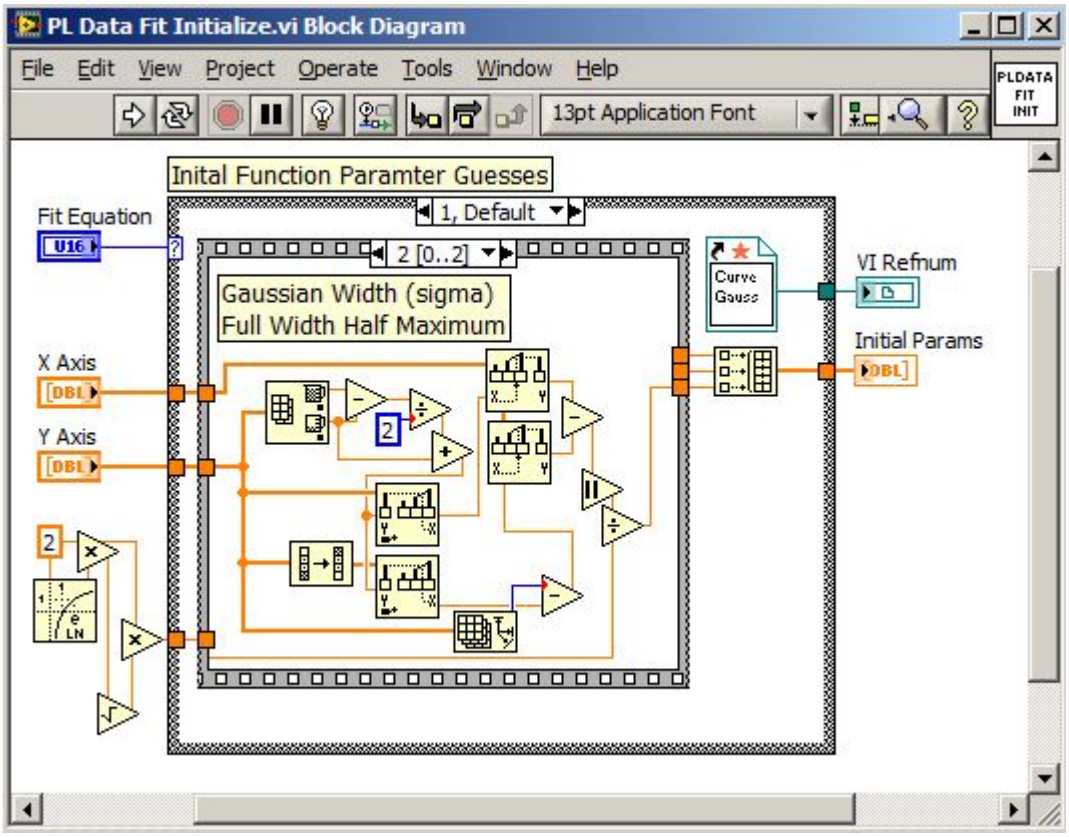

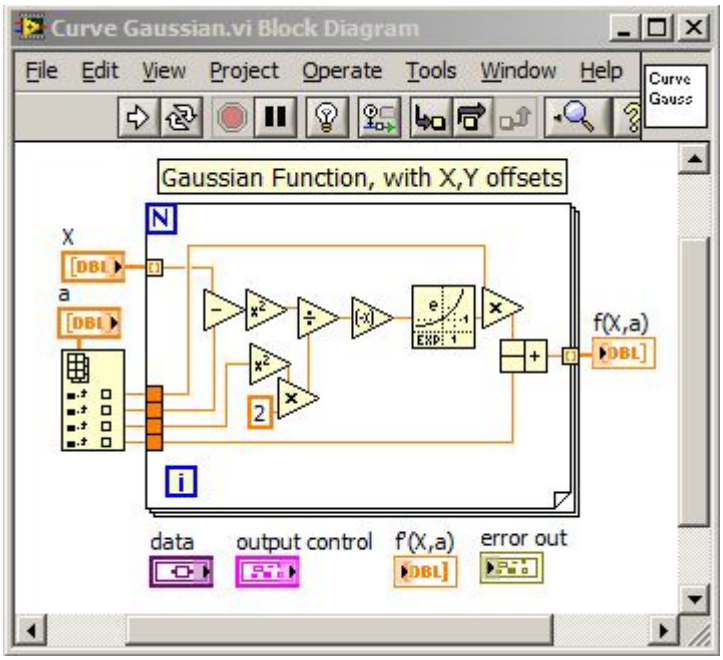
Curve Gaussian.vi Block Diagram
File Edit View Project Operate Tools Window Help
Curve Gauss
Gaussian Function, with X,Y offsets
X
a
f(X,a)
2
data
output control
f'(X,a)
error out

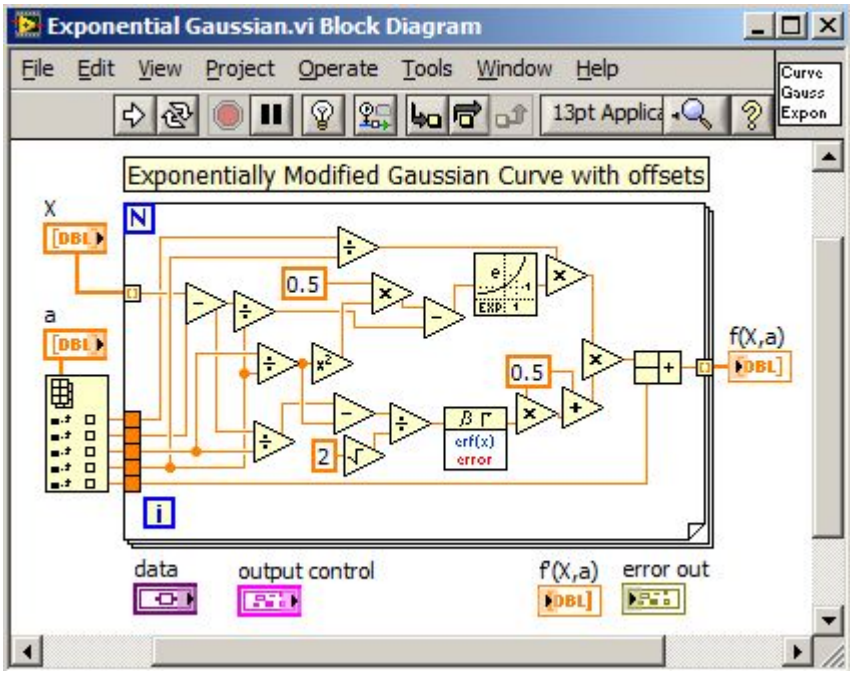
Exponential Gaussian.vi Block Diagram
File Edit View Project Operate Tools Window Help
Curve Gauss Expon
13pt Applica
Exponentially Modified Gaussian Curve with offsets
X
a
f(X,a)
0.5
0.5
2
erf(x)
error
data
output control
f'(X,a)
error out

Acoustic Bragg Reflector Calculation Software

Created: August 2010
Modified: January 2013

Original Language: LabVIEW Version 8.2
Current Language: LabVIEW 2010

Description:
This software performs all theoretical calculations shown in this dissertation. The three primary functions: general math functions, optical Distributed Bragg Reflector (oDBR), and acoustic Distributed Bragg Reflector (aDBR).

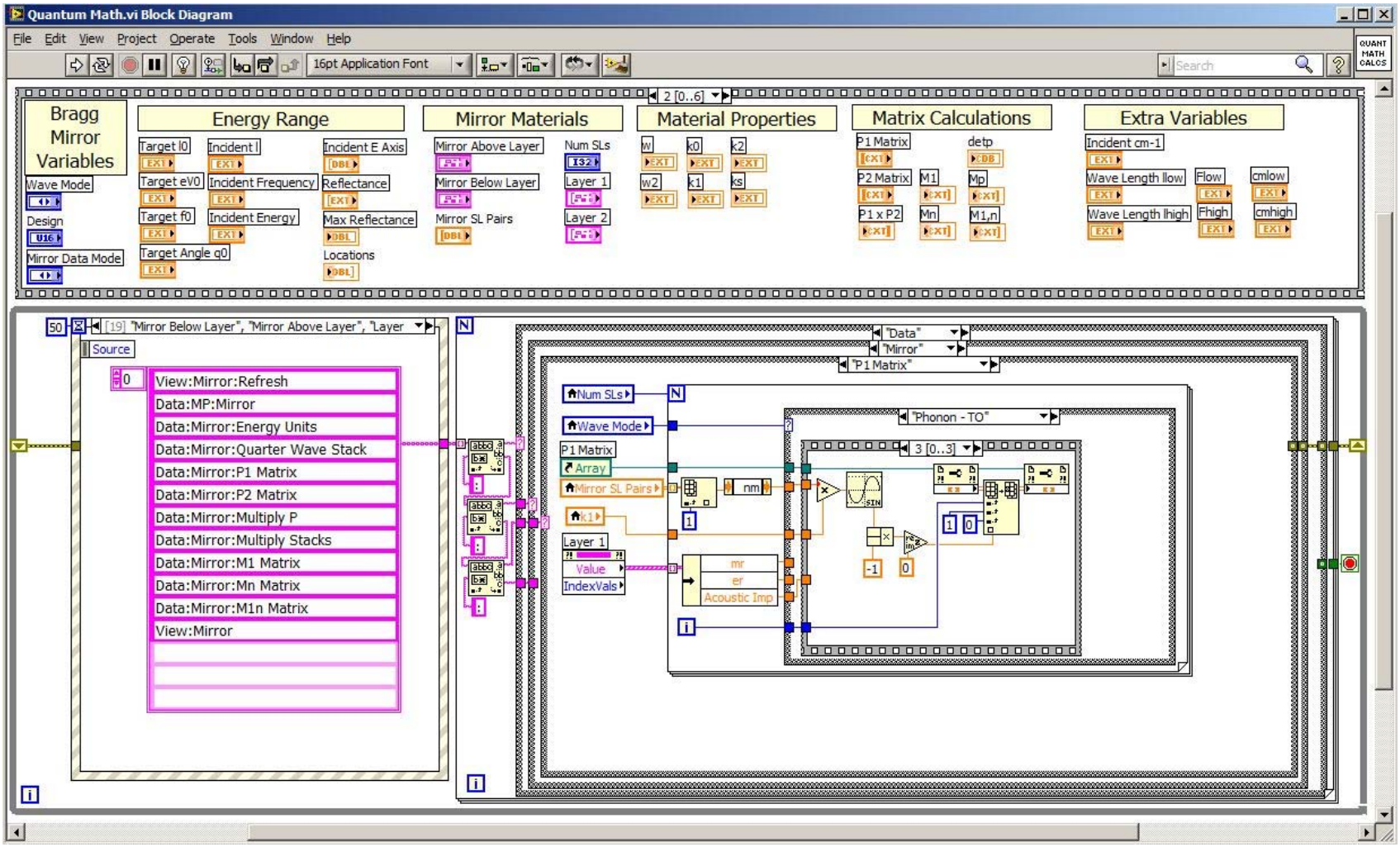
Quantum Math.vi Block Diagram
File Edit View Project Operate Tools Window Help
16pt Application Font
Search
Bragg Mirror Variables
Wave Mode
Design
Mirror Data Mode
Energy Range
Target l0
Incident l
Incident E Axis
Target eV0
Incident Frequency
Reflectance
Target f0
Incident Energy
Max Reflectance
Target Angle q0
Locations
Mirror Materials
Mirror Above Layer
Mirror Below Layer
Mirror SL Pairs
Num SLs
Layer 1
Layer 2
Material Properties
Matrix Calculations
P1 Matrix
P2 Matrix
P1 x P2
M1
Mn
detp
Mp
M1,n
Extra Variables
Incident cm-1
Wave Length llow
Wave Length lhigh
Flow
Fhigh
cmlow
cmhigh
[19] "Mirror Below Layer", "Mirror Above Layer", "Layer
Source
View:Mirror:Refresh
Data:MP:Mirror
Data:Mirror:Energy Units
Data:Mirror:Quarter Wave Stack
Data:Mirror:P1 Matrix
Data:Mirror:P2 Matrix
Data:Mirror:Multiply P
Data:Mirror:Multiply Stacks
Data:Mirror:M1 Matrix
Data:Mirror:Mn Matrix
Data:Mirror:M1n Matrix
View:Mirror
"Data"
"Mirror"
"P1 Matrix"
"Phonon - TO"
Wave Mode
Array
nm
Value
IndexVals
Acoustic Imp

The next two code segments shows the calculation of the angular frequency “w” of the incident energy wave incident on the DBR structures and the wave vector “k” of each material layer: “Above” is typically air for oDBRs and “Below” is also referred to as the substrate.

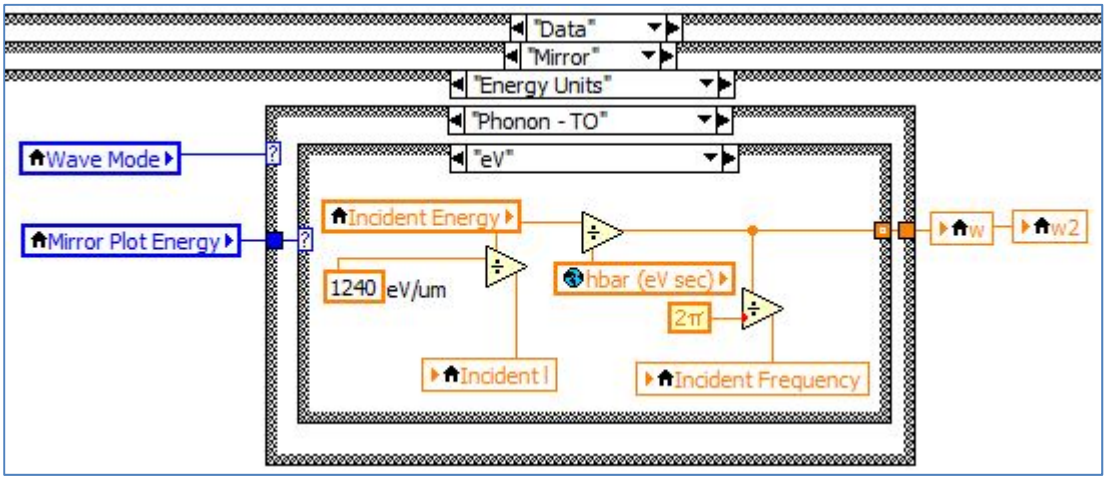

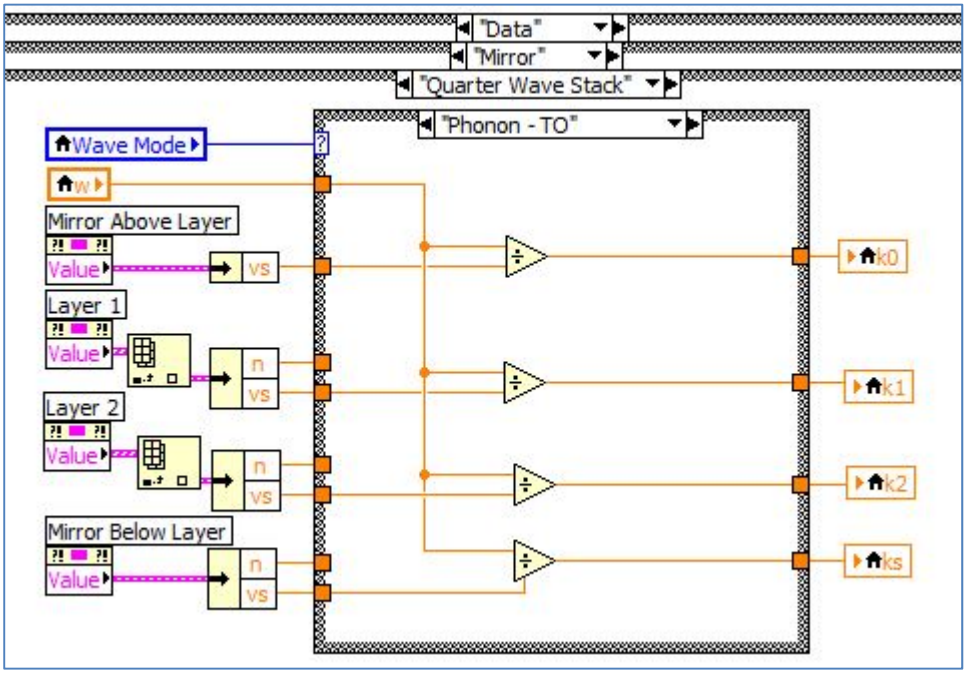

The next two code segments show the calculation of the “Propagator Matrix” for the two different materials (“Layer 1” and “Layer 2”) used for the aDBRs. Each matrix is a 2x2 with complex numbers.

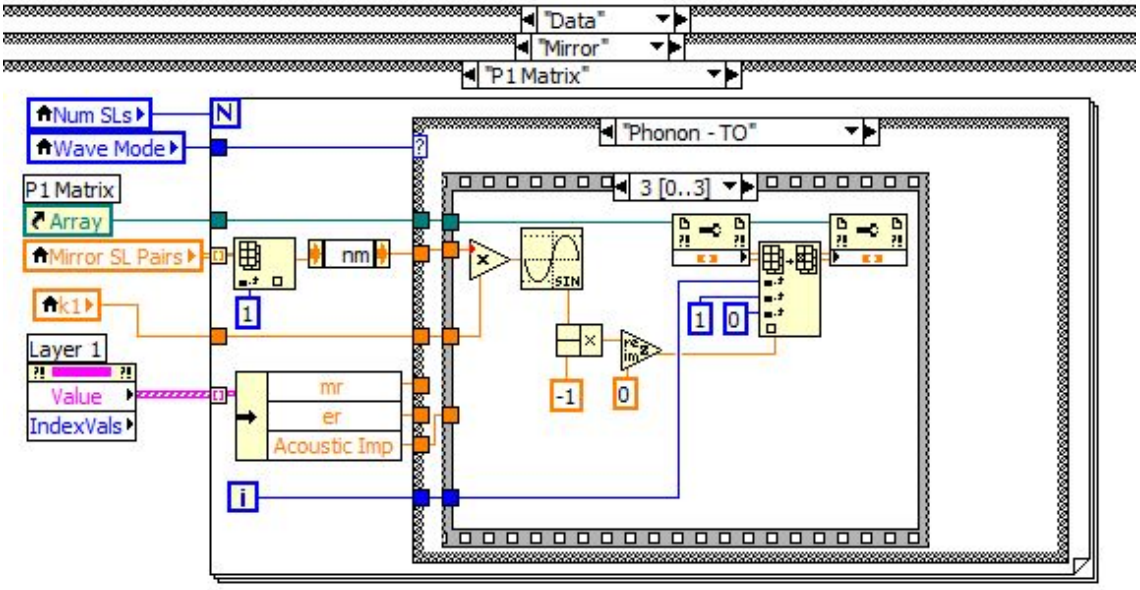

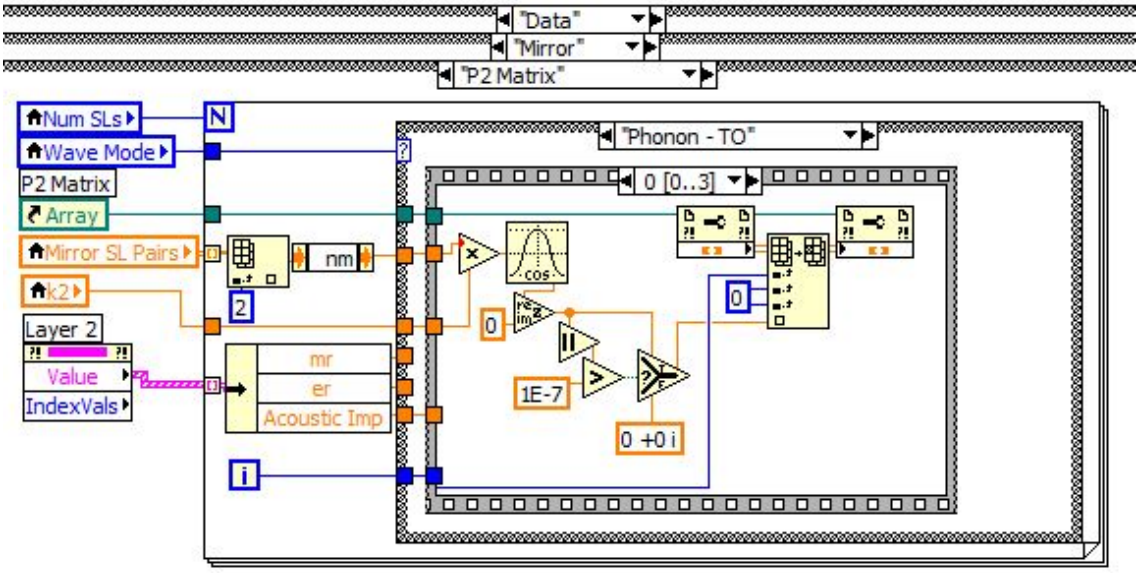

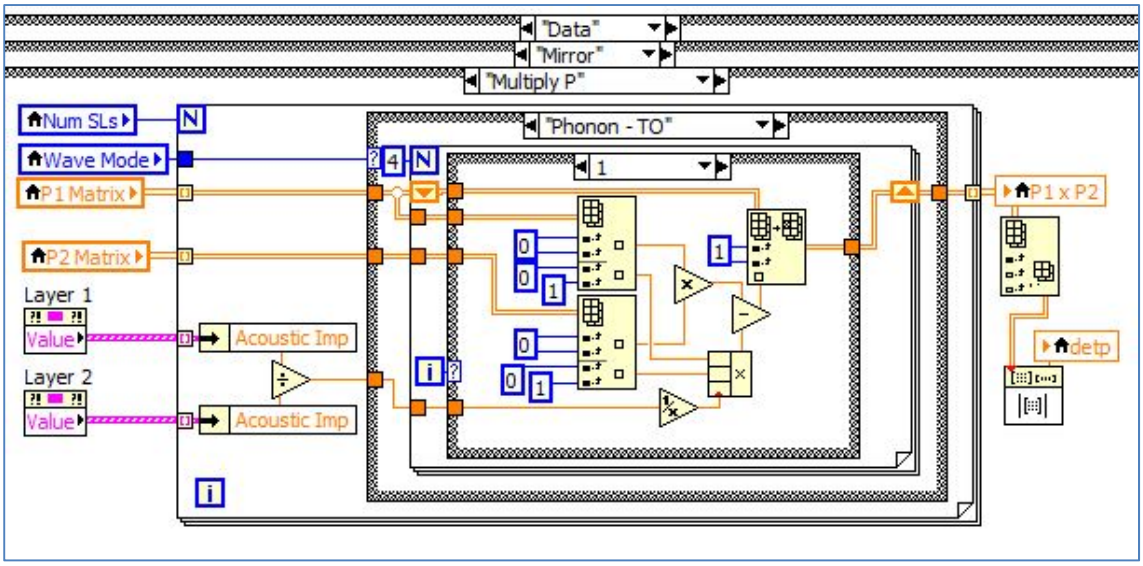
"Data"
"Mirror"
"Multiply P"
Num SLs
Wave Mode
P1 Matrix
P2 Matrix
Layer 1
Value
Acoustic Imp
Layer 2
Value
Acoustic Imp
"Phonon - TO"
1
P1 x P2
detp

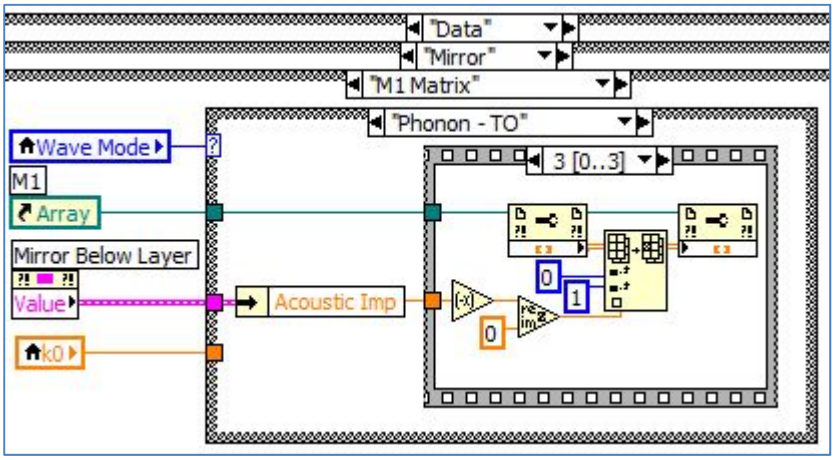
"Data"
"Mirror"
"M1 Matrix"
"Phonon - TO"
3 [0..3]
Wave Mode
M1
Array
Mirror Below Layer
Value
Acoustic Imp
k0

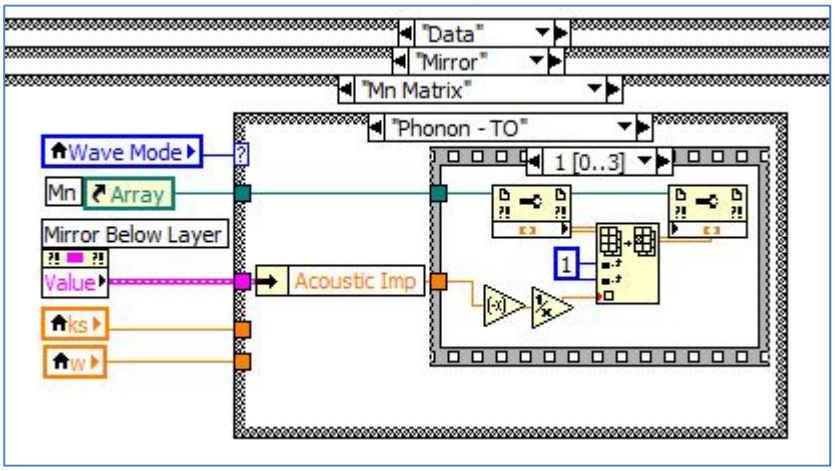
"Data"
"Mirror"
"Mn Matrix"
"Phonon - TO"
1 [0..3]
Wave Mode
Mn
Array
Mirror Below Layer
Value
Acoustic Imp
ks
w

This code segment calculates the reflectance of the aDBR “Reflectance” from the propagation matrix at the the given angular frequency “ω”.

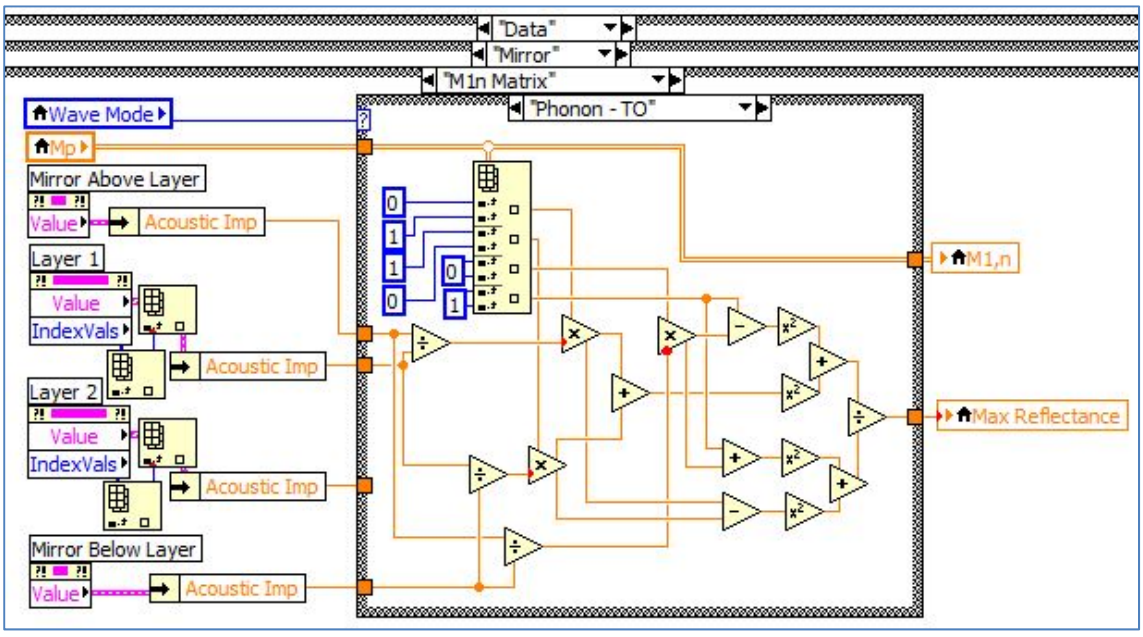

The next code segments show the custom “Dynamic Variable Signal Loop” technique developed using LabVIEW programming to calculate the aDBR reflectance over a given “Incident Energy” range with a given number of steps between the low and high values.

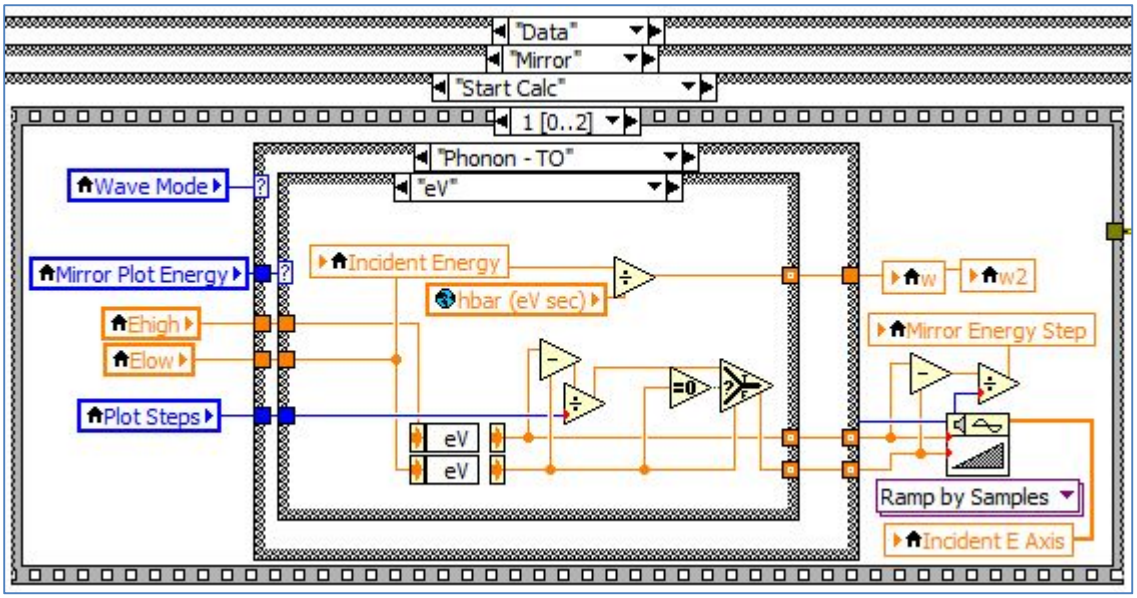

Appendix B

Detailed MBE Sample Growth Summary

Growth M046: Bulk PbSe

Date, Grown By	Target Thickness	Measured Thickness	
6/24/2009, L. Olona	> 3.0 μm	4.65 μm	
Target Alloy	**XRD FWHM**	**Carrier Doping**	**Substrate Batch**
PbSe	94.8"	None	PCA #8685

Hall Effect Summary

n (100K), cm^{-3}	μ, cm^2/Vs	σ, S/cm	n (300K), cm^{-3}	μ, cm^2/Vs	σ, S/cm
$+9.25 \times 10^{16}$	10,600	180	$+4.30 \times 10^{17}$	236	18.0
n(150K), cm^{-3}	**μ, cm^2/Vs**	**σ, S/cm**	**n (200K), cm^{-3}**	**μ, cm^2/Vs**	**σ, S/cm**
$+1.07 \times 10^{17}$	3801	64.8	$+1.51 \times 10^{17}$	1497	36.1

Epitaxial Layer Design

	Name	Material	Targ. Thick. μm	Time	T_{sub}	PbSe T_{Cell}	Se_2 T_{Cell}	Act. Thick. μm
0	Buffer	CaF_2	0.002	1m	800			0.002
1	Bulk	PbSe	> 3.00	2h30m	350	740	1000/285	4.65

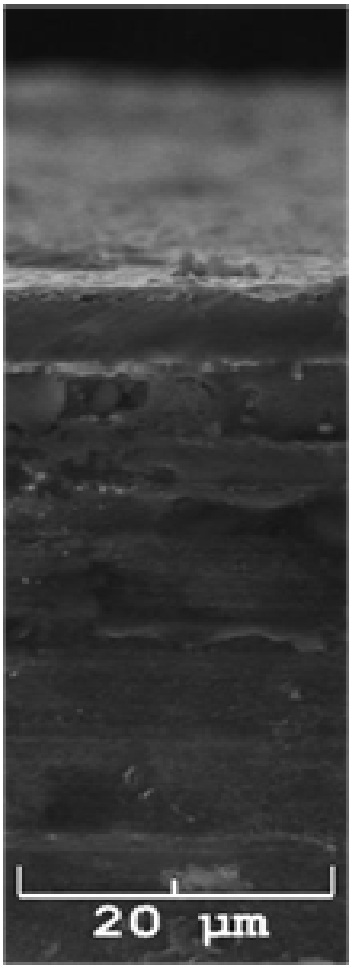

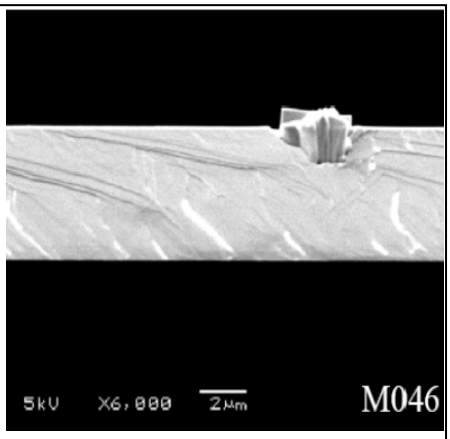

Sample
M046-B

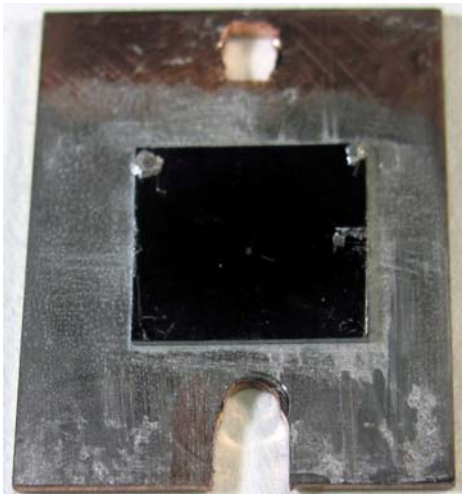

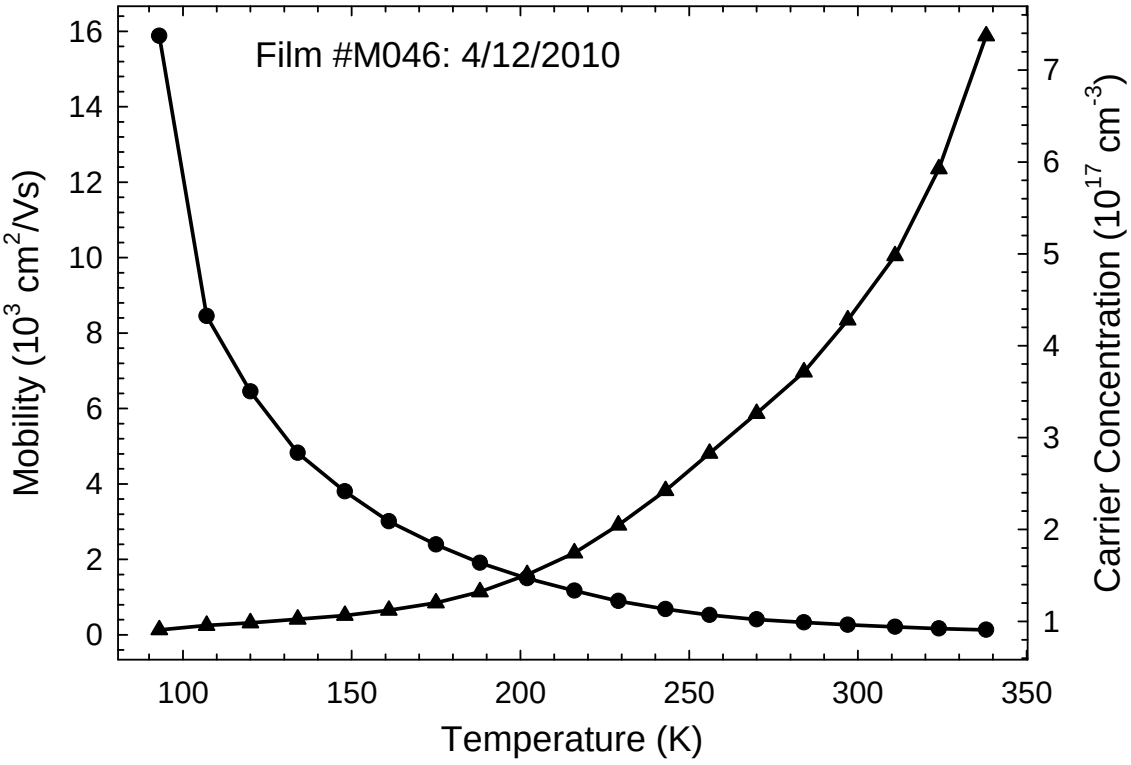
Film #M046: 4/12/2010
Mobility (10^3 cm^2/Vs)
Carrier Concentration (10^{17} cm^{-3})
Temperature (K)
0
2
4
6
8
10
12
14
16
1
2
3
4
5
6
7
100
150
200
250
300
350

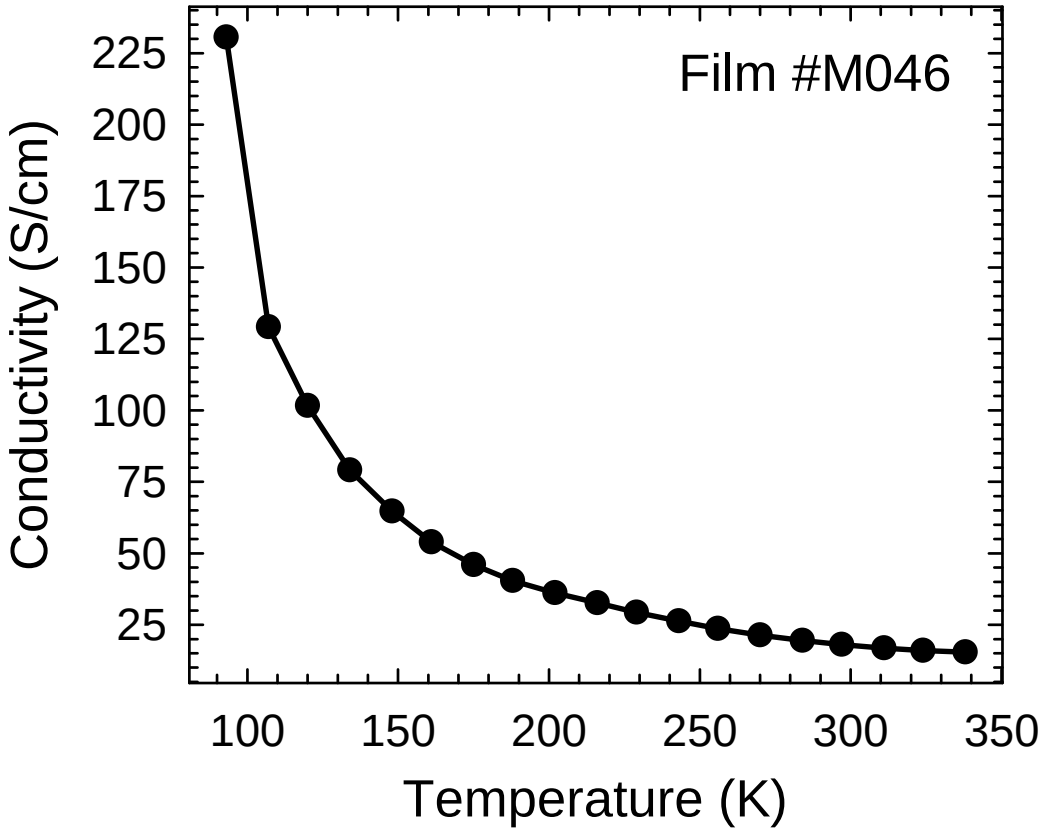
Film #M046
Conductivity (S/cm)
Temperature (K)
25
50
75
100
125
150
175
200
225
100
150
200
250
300
350

Growth M047: Bulk PbSe

Date, Grown By			Target Thickness		Measured Thickness			
6/25/2009, L. Olona			> 3.00 µm		4.37 µm			
Target Alloy			**XRD FWHM**		**Carrier Doping**		**Substrate Batch**	
PbSe			112.6"		None		PCA #8685	
Hall Effect Summary								
n (100K), cm^{-3}		**µ, cm^2/Vs**	**σ, S/cm**		**n (300K), cm^{-3}**		**µ, cm^2/Vs**	**σ, S/cm**
+ x 10^{17}					+ x 10^{17}			
n(150K), cm^{-3}		**µ, cm^2/Vs**	**σ, S/cm**		**n (200K), cm^{-3}**		**µ, cm^2/Vs**	**σ, S/cm**
Epitaxial Layer Design								
	Name	**Material**	**Targ. Thick. µm**	**Time**	**T_{sub}**	**PbSe T_{Cell}**	**Se_2 T_{Cell}**	**Act. Thick. µm**
0	Buffer	CaF_2	0.002	1m	800			0.002
1	Bulk	PbSe	> 3.00	2h30m	350	740	1000/285	4.37

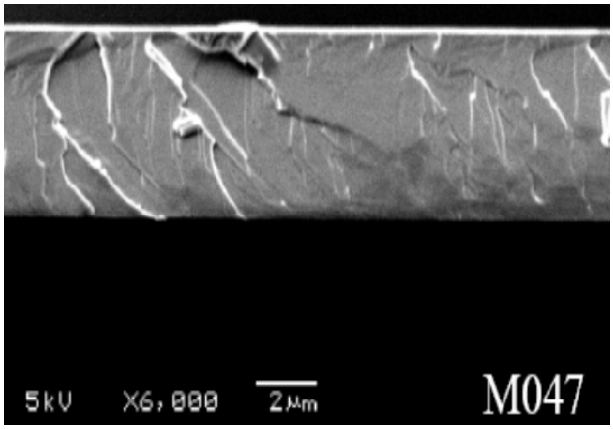

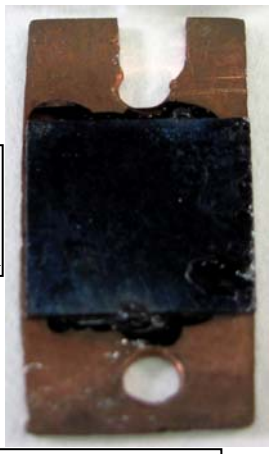

Sample
M047-A
Black Wax

M047-A1 EGaIn | M047-PL2 Indium | M047-PL3 GaIn

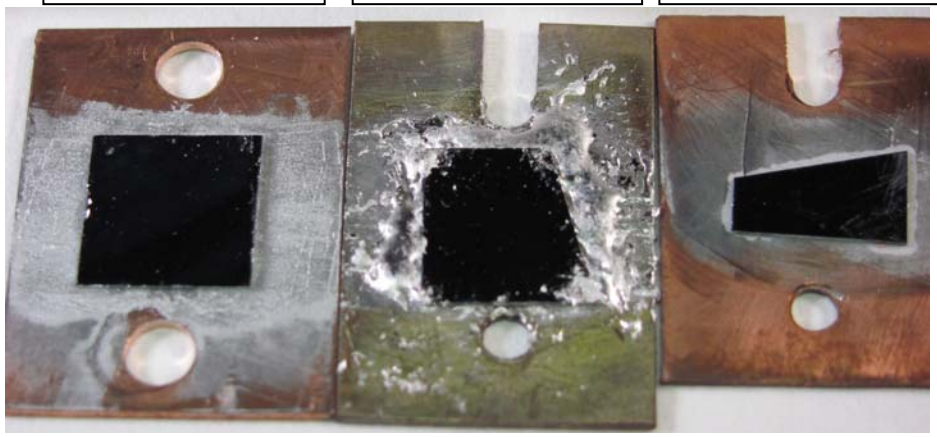

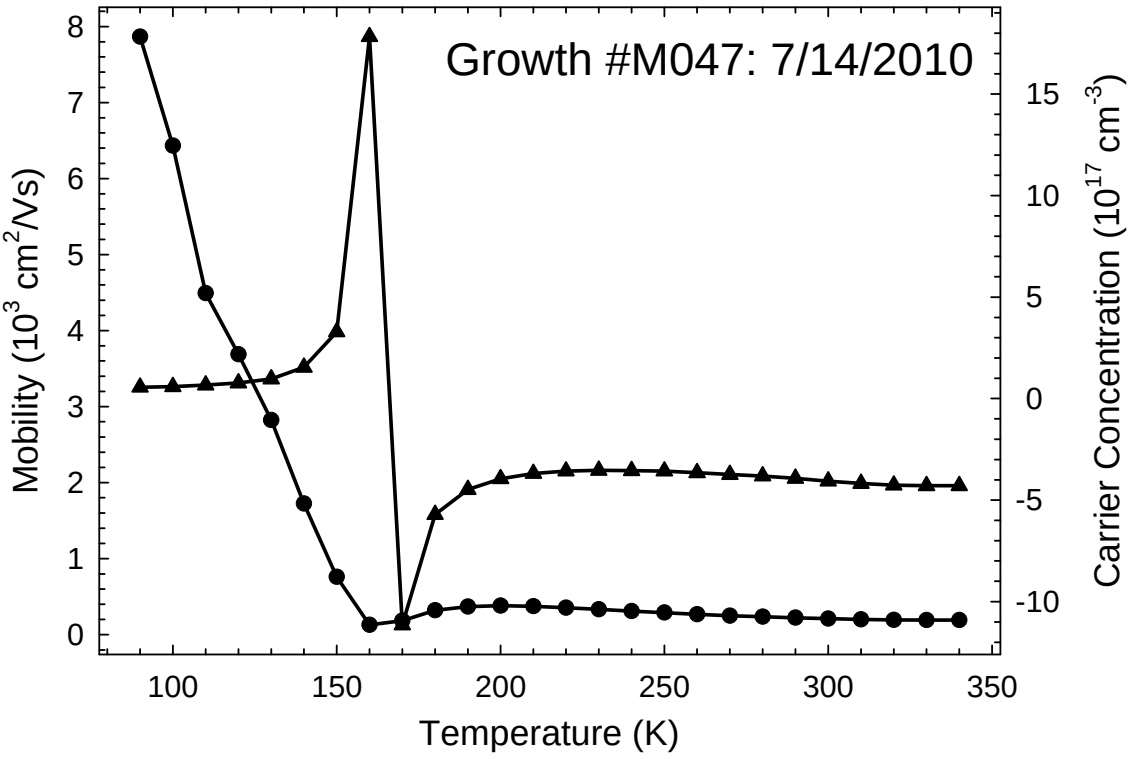
Growth #M047: 7/14/2010
Mobility (10^3 cm^2/Vs)
Carrier Concentration (10^{17} cm^{-3})
Temperature (K)
0
1
2
3
4
5
6
7
8
15
10
5
0
-5
-10
100
150
200
250
300
350

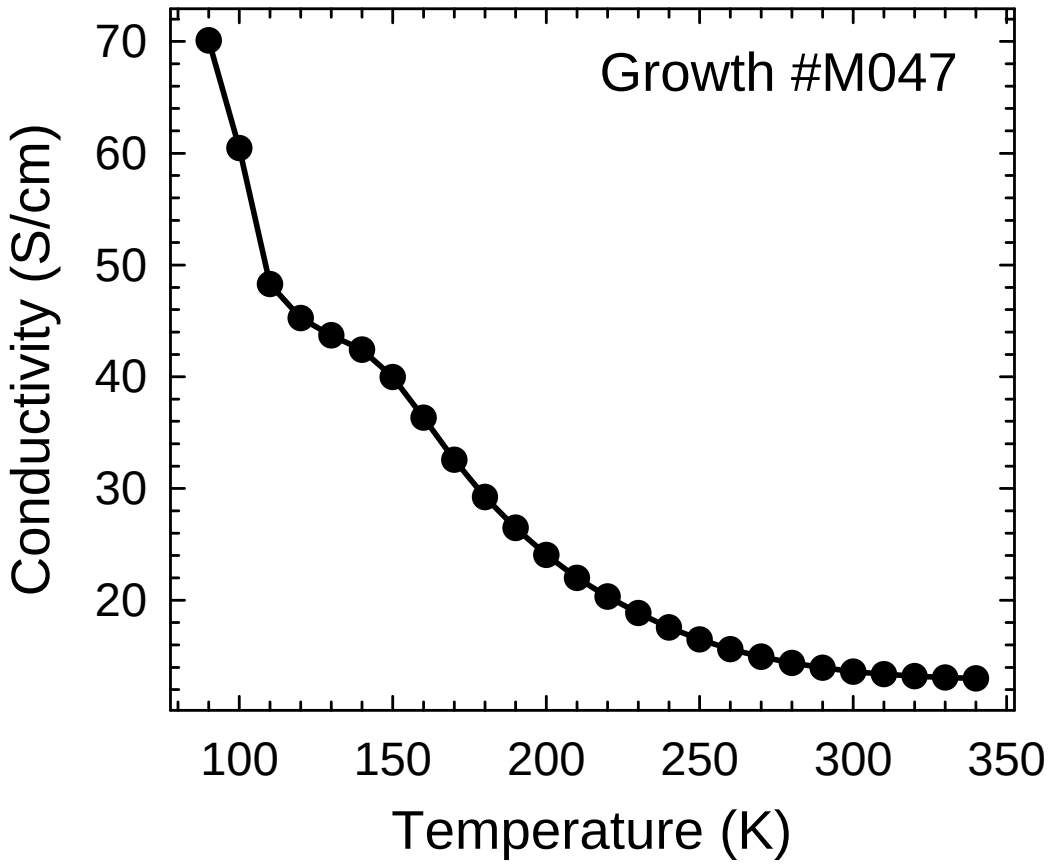
Growth #M047
Conductivity (S/cm)
Temperature (K)
20
30
40
50
60
70
100
150
200
250
300
350

Growth M048: Bulk PbSe

Date, Grown By	Target Thickness	Measured Thick.	
6/26/2009, F. Zhao	> 3.0 µm	3.94 µm	
Target Alloy	**XRD FWHM**	**Carrier Doping**	**Substrate Batch**
PbSe	84.0"	None	PCA #8685

Hall Effect Summary

n (100K), cm^{-3}	µ, cm^2/Vs	σ, S/cm	n (300K), cm^{-3}	µ, cm^2/Vs	σ, S/cm
$+6.24 \times 10^{16}$	14,330	143.1	$+2.85 \times 10^{17}$	302.3	13.77
n(150K), cm^{-3}	**µ, cm^2/Vs**	**σ, S/cm**	**n (200K), cm^{-3}**	**µ, cm^2/Vs**	**σ, S/cm**
$+8.86 \times 10^{16}$	3,845	54.51	$+1.37 \times 10^{17}$	1381	30.34

Epitaxial Layer Design

	Name	Material	Targ. Thick. µm	Time	T_{sub}	PbSe T_{Cell}	Se_2 T_{Cell}	Act. Thick. µm
0	Buffer	CaF_2	0.002	1m	800			0.002
1	Bulk	PbSe	> 3.00	2h30m	350	740	1000/285	3.94

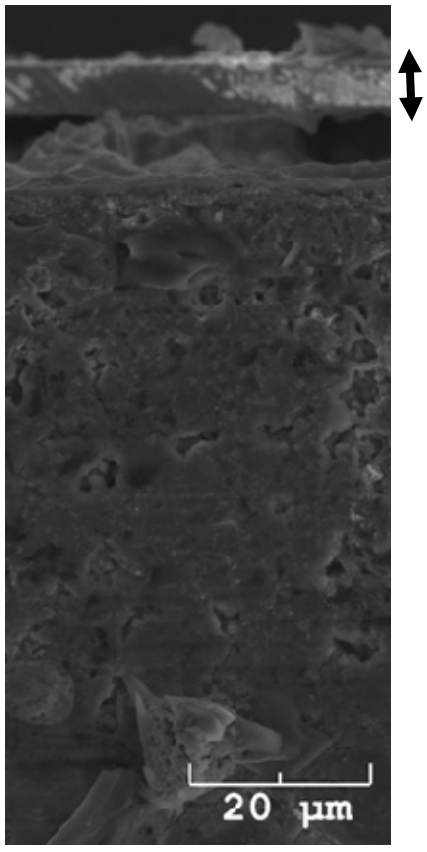

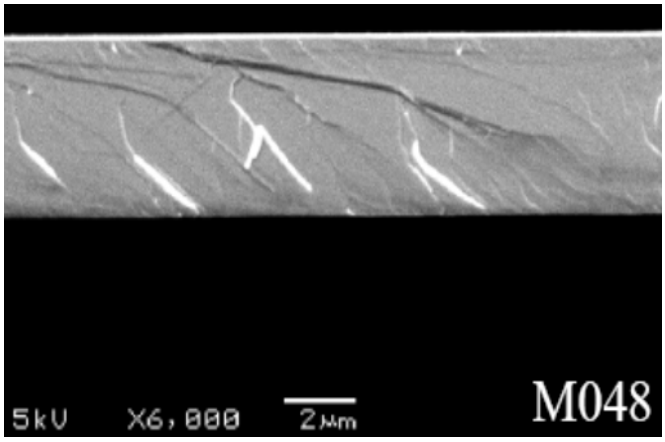

Sample
M048-A

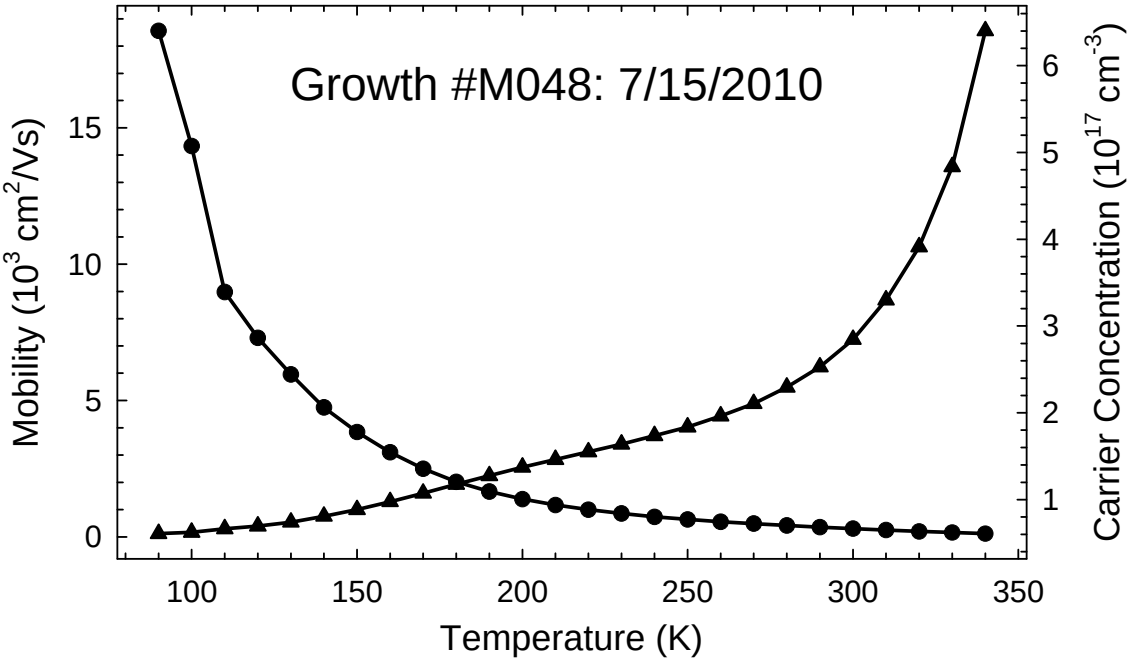
Growth #M048: 7/15/2010
Mobility (10^3 cm^2/Vs)
Carrier Concentration (10^{17} cm^{-3})
Temperature (K)
0
5
10
15
1
2
3
4
5
6
100
150
200
250
300
350

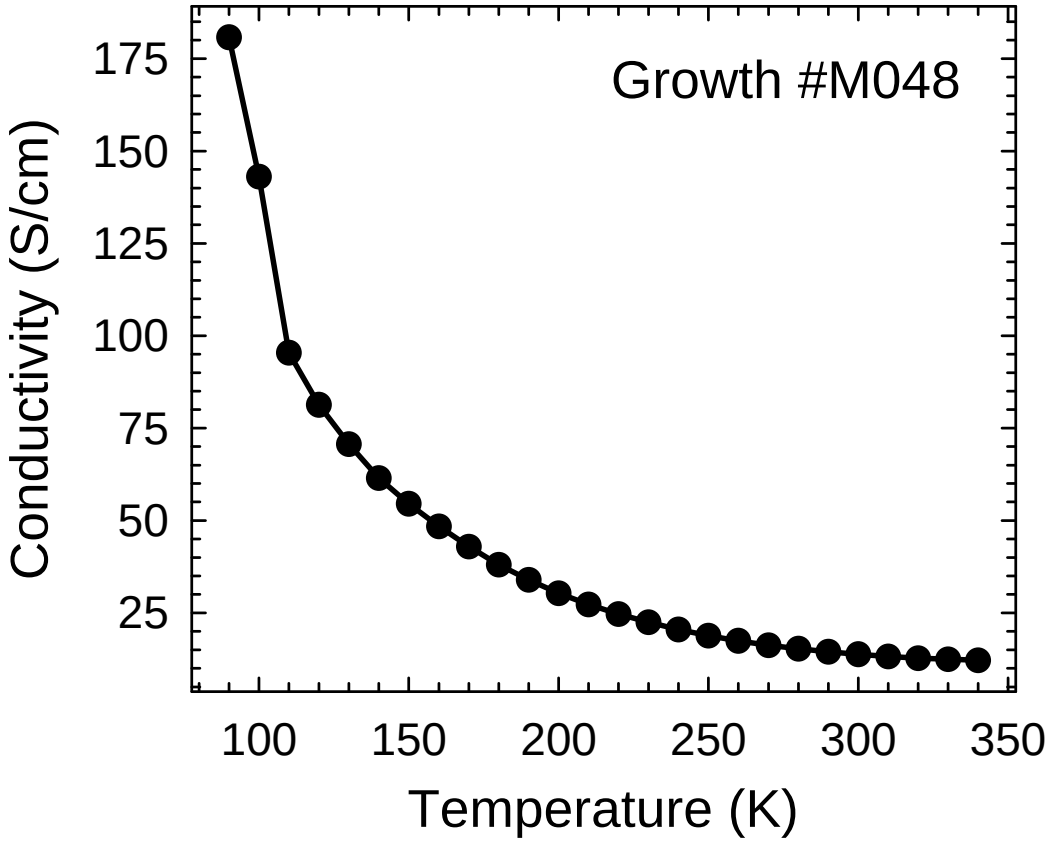
Growth #M048
Conductivity (S/cm)
Temperature (K)
25
50
75
100
125
150
175
100
150
200
250
300
350

Growth M049: Bulk PbSe

Date, Grown By			Target Thickness		Measured Thick.			
6/29/2009, F. Zhao			> 3.0 μm		3.78 μm			
Target Alloy			XRD FWHM		Carrier Doping		Substrate Batch	
PbSe			143.1"		None		PCA #8685	
Hall Effect								
100 K					**300 K**			
n(100K), cm^{-3}		**μ, cm^2/Vs**	**σ, S/cm**		**n (300K), cm^{-3}**		**μ, cm^2/Vs**	**σ, S/cm**
$+1.09 \times 10^{17}$		14,850	259.0		$+2.08 \times 10^{17}$		652	21.67
150 K					**200 K**			
n(150K), cm^{-3}		**μ, cm^2/Vs**	**σ, S/cm**		**n (200K), cm^{-3}**		**μ, cm^2/Vs**	**σ, S/cm**
$+1.16 \times 10^{17}$		4,882	90.53		$+1.19 \times 10^{17}$		2,436	46.34
Epitaxial Layer Design								
	Name	**Material**	**Targ. Thick. μm**	**Time**	**T_{sub}**	**PbSe T_{Cell}**	**Se_2 T_{Cell}**	**Act. Thick. μm**
0	Buffer	CaF_2	0.002	1m	800			0.002
1	Bulk	PbSe	> 3.00	30m	325	737	1000/285	3.78
2	Bulk	PbSe		2h00m	275	737	1000/285	

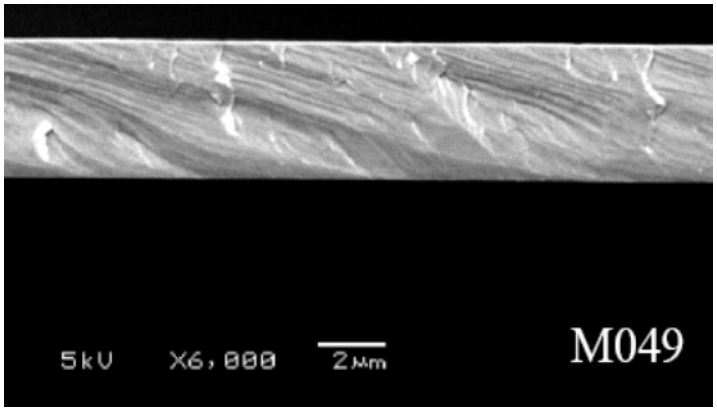

M049-PL3
Gallium
Indium

M049-PL3
Indium

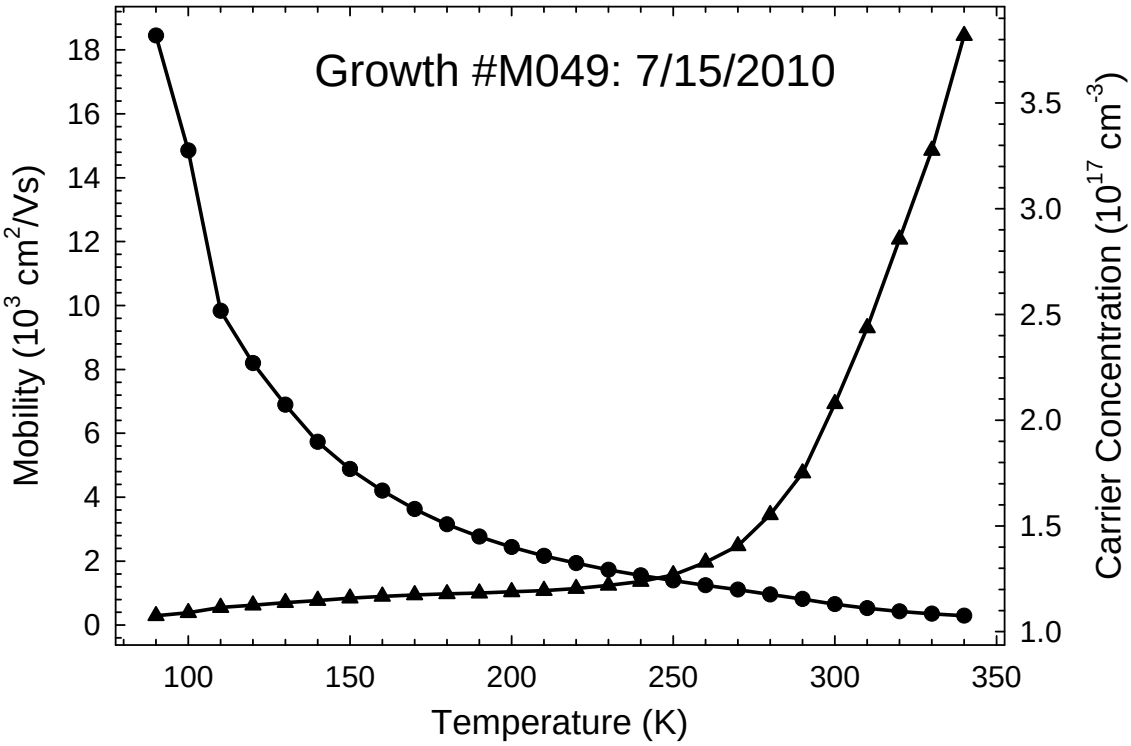
Growth #M049: 7/15/2010
Mobility (10^3 cm^2/Vs)
Carrier Concentration (10^{17} cm^{-3})
Temperature (K)
0
2
4
6
8
10
12
14
16
18
1.0
1.5
2.0
2.5
3.0
3.5
100
150
200
250
300
350

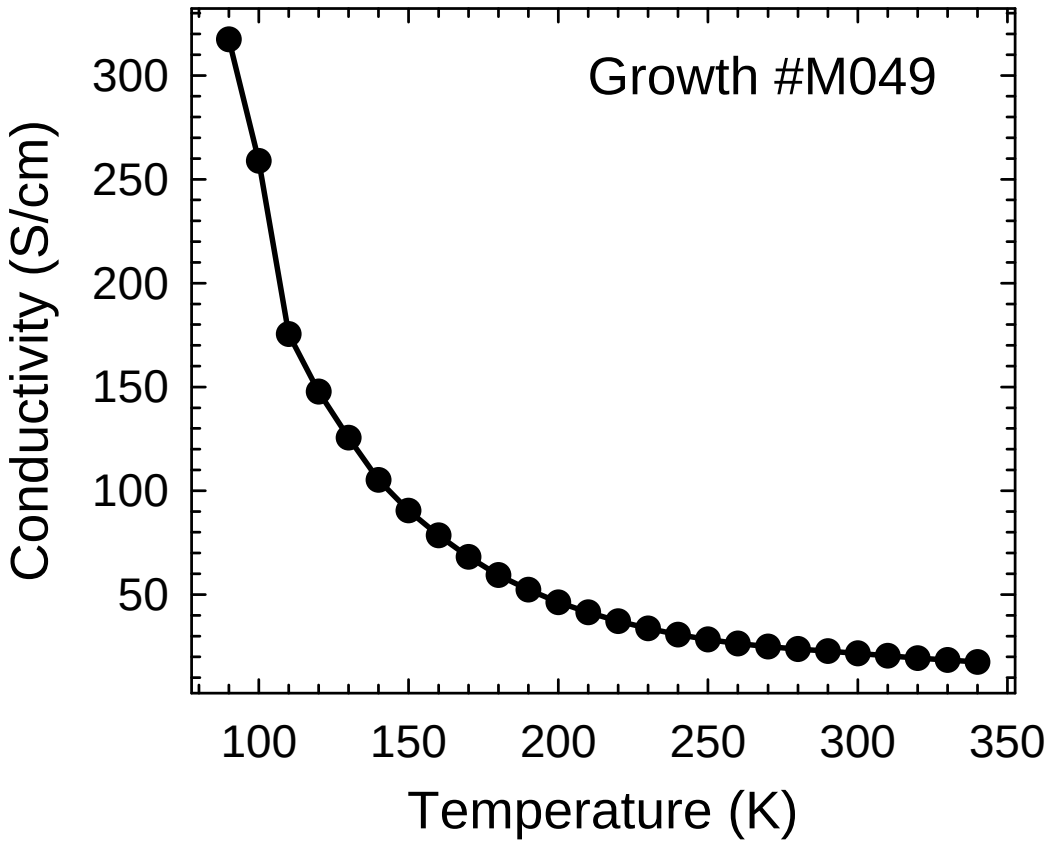
Growth #M049
Conductivity (S/cm)
Temperature (K)
50
100
150
200
250
300
100
150
200
250
300
350

Growth M141: Multiple Quantum Wells on PbSe

Date, Grown By	Target Thickness	Measured Thickness	%
10/1/2010, L. Olona	3.33 μm	2.47	-25.8
Target Alloy	**Target Alloy**	**Carrier Doping**	**Substrate Batch**
$Pb_{0.85}Sn_{0.15}Se$	$Pb_{0.85}Sn_{0.15}Se$	None/Bismuth	Virginia Semi. SS

Hall Effect Summary (pn junction formed by MQW and PbSe:Bi)					
n (100K), cm^{-3}	**μ, cm^2/Vs**	**σ, S/cm**	**n (300K), cm^{-3}**	**μ, cm^2/Vs**	**σ, S/cm**
$+1.01 \times 10^{18}$	5228	846.44	-5.59×10^{18}	1192	1066
n (150K), cm^{-3}	**μ, cm^2/Vs**	**σ, S/cm**	**n (200K), cm^{-3}**	**μ, cm^2/Vs**	**σ, S/cm**
-1.16×10^{19}	1352	2505	-5.64×10^{18}	1702	1535

Epitaxial Layer Design

	Name	Material	Thick nm	Material	Thick nm	Repeat	Total nm	Adjusted nm
0	Nuc.	PbSe	30					22
1	Bulk	PbSe	2000					1484
2	Barrier	PbSrSe	200					148
3	MQW	PbSrSe	30	PbSe	15	20	0.900	22 x 11 / 0.667
4	Barrier	PbSrSe	170					126
5	PL Cap	PbSe	30					22

Sample M141-H1

Sample M141-PL1

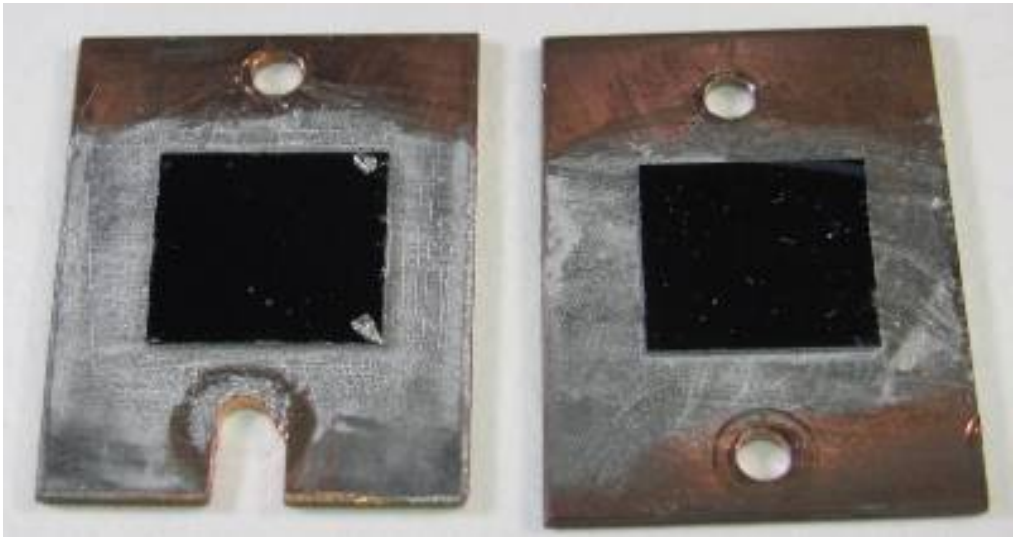

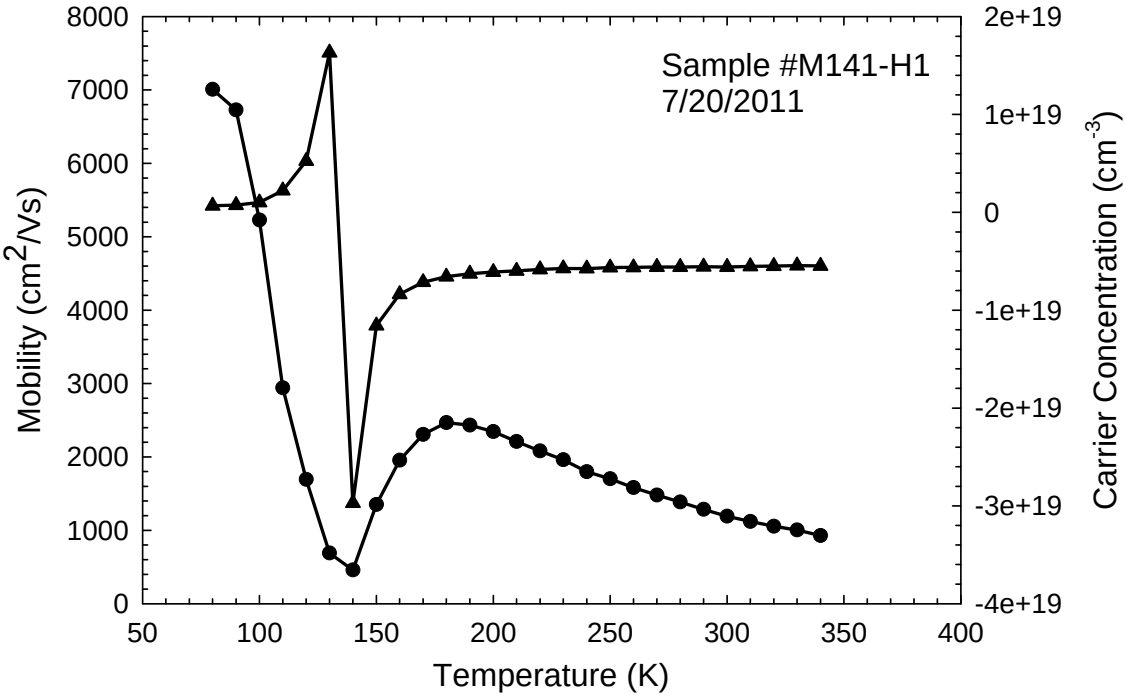
Sample #M141-H1
7/20/2011
Mobility (cm2/Vs)
Carrier Concentration (cm-3)
Temperature (K)
8000
7000
6000
5000
4000
3000
2000
1000
0
2e+19
1e+19
0
-1e+19
-2e+19
-3e+19
-4e+19
50
100
150
200
250
300
350
400

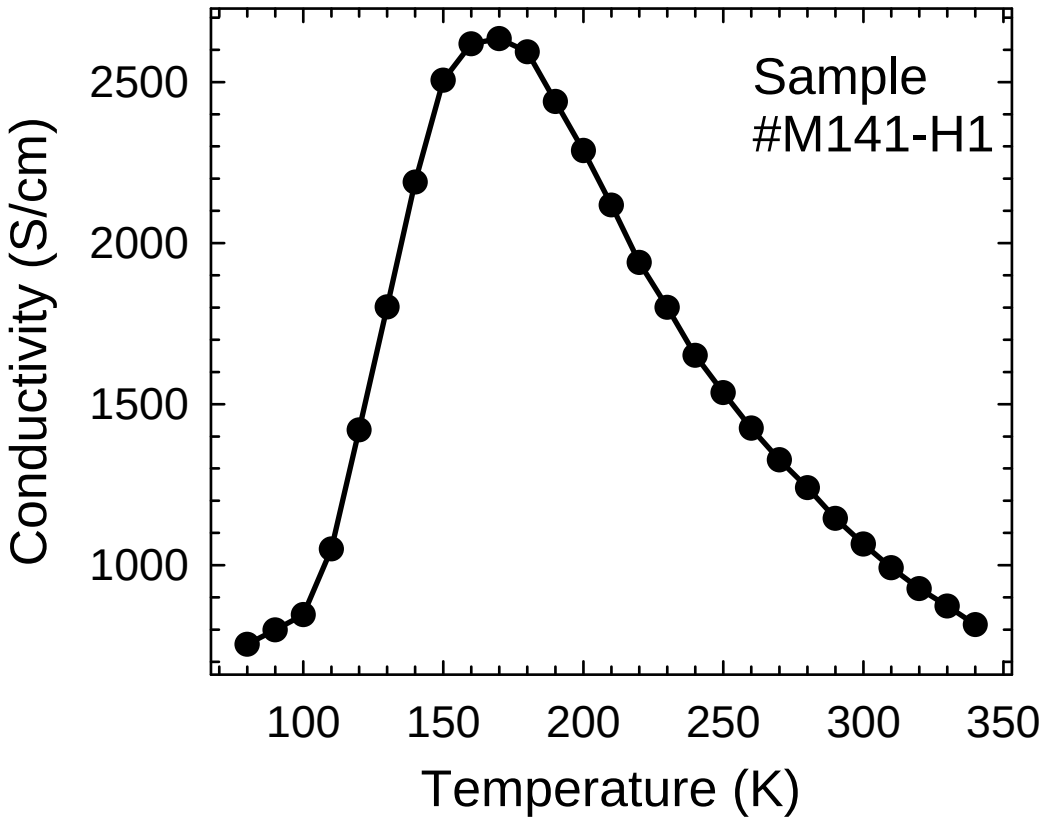
Sample
#M141-H1
Conductivity (S/cm)
Temperature (K)
2500
2000
1500
1000
100
150
200
250
300
350

Growth M168: Multiple Quantum Wells on 3-Period Superlattice

Date, Grown By	Target Thickness	Measured Thickness	Variation %
11/3/2010, L. Olona	2.591 µm	3.075 µm	+18.7
MQW Alloy %	**SL Alloy %**	**Carrier Doping**	**Substrate Batch**
$Pb_{0.93}Sr_{0.07}Se$	$Pb_{0.85}Sn_{0.15}Se$	Bismuth	Virginia Semi. SS

Hall Effect Summary *** (Data for Sample #M103)					
n (100K), cm^{-3}	**µ, cm^2/Vs**	**σ, S/cm**	**n (300K), cm^{-3}**	**µ, cm^2/Vs**	**σ, S/cm**
-5.926×10^{18}	6697	6350	-5.592×10^{18}	1170	1047
n(150K), cm^{-3}	**µ, cm^2/Vs**	**σ, S/cm**	**n (200K), cm^{-3}**	**µ, cm^2/Vs**	**σ, S/cm**
-5.666×10^{18}	3792	3438	-5.648×10^{18}	2530	2286

Qualitative Visual Assessment

	Type	Material	Thick nm	Material	Thick nm	Repeat	Total nm	Adjusted nm
0	Nuc	-	200					236
1	SL1	PbSnSe	1.00	PbSe	1.00	250	0.500	1.190 / 0.595
2	SL2	PbSnSe	1.50	PbSe	1.50	167	0.500	1.780 / 0.595
3	SL3	PbSnSe	2.00	PbSe	2.00	125	0.500	2.380 / 0.595
Averages & Totals			1.38		1.38	542	1.500	1.647 / 1.785
4	Barrier	PbSrSe	133					134
5	MQW	PbSrSe	20.0	PbSe	10	20	0.600	24 x 12 / 0.712
6	Barrier	PbSrSe	113					140
7	Cap	PbSe	5					6

Growth Wafer

Sample M168-C Gallium Indium

Sample M168-CCR Indium

Sample M168-F Gallium Indium

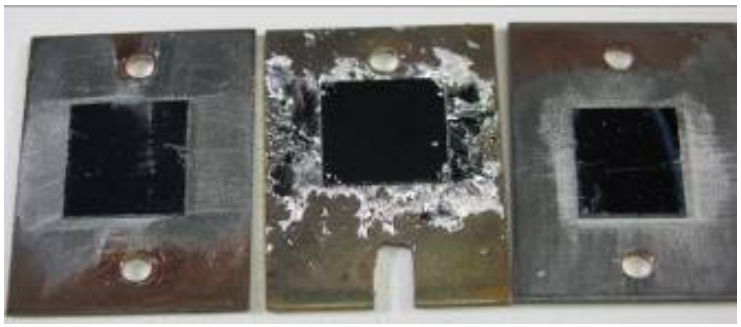

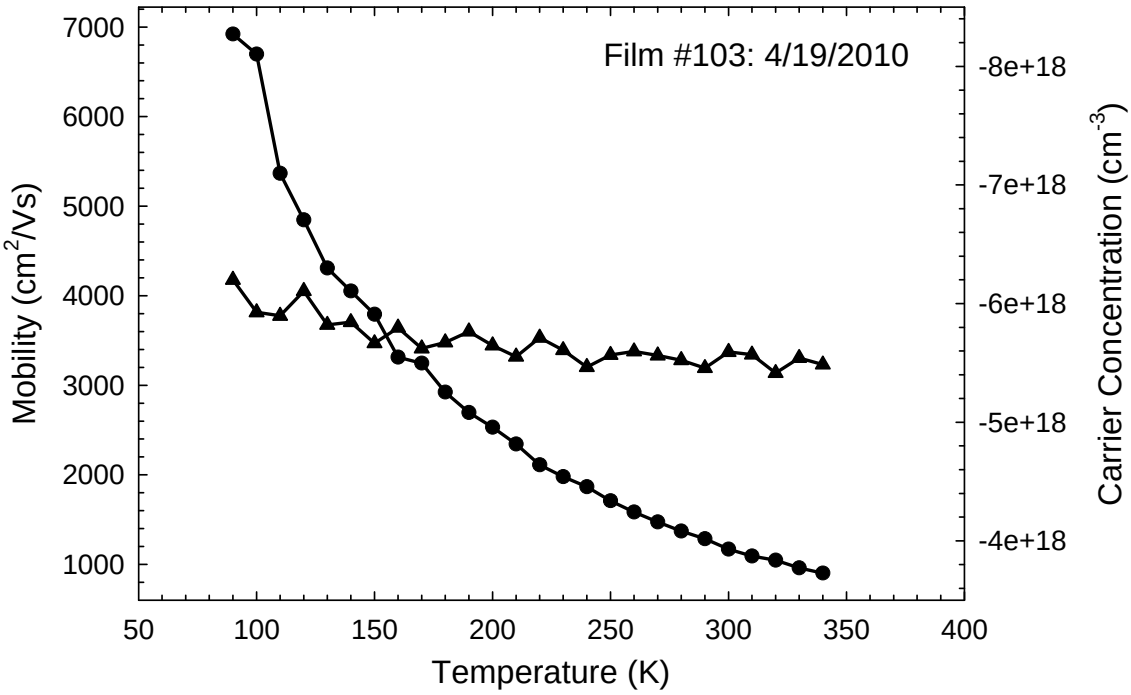
Film #103: 4/19/2010
Mobility (cm²/Vs)
Carrier Concentration (cm⁻³)
Temperature (K)
7000
6000
5000
4000
3000
2000
1000
-8e+18
-7e+18
-6e+18
-5e+18
-4e+18
50
100
150
200
250
300
350
400

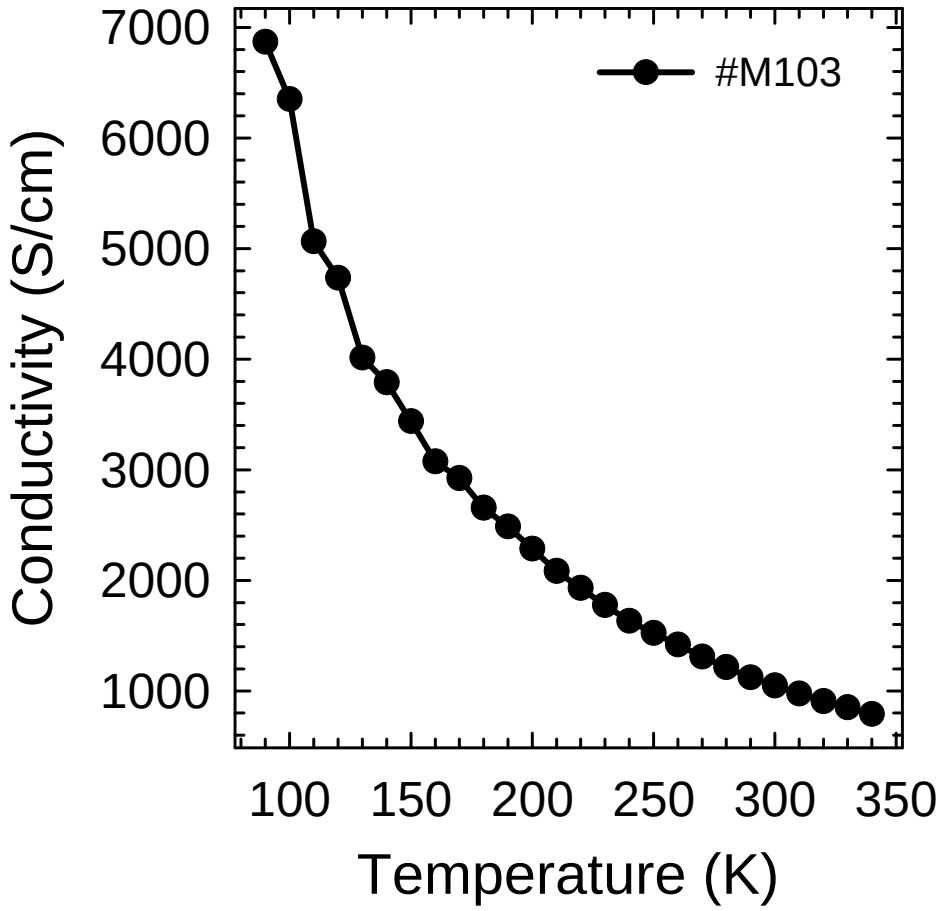
#M103
Conductivity (S/cm)
Temperature (K)
7000
6000
5000
4000
3000
2000
1000
100
150
200
250
300
350

Growth M207: Multiple Quantum Wells on 5-period Superlattice

Date, Grown By			Target Thickness		Measured Thick.			Variation %
5/9/2011, Z. Cai			2.551 μm		2.200 μm			-13.8
MQW Alloy %			**SL Alloy %**		**Carrier Doping**			**Substrate Batch**
$Pb_{0.93}Sr_{0.07}Se$			$Pb_{0.85}Sn_{0.15}Se$		Bismuth: -3.0 x 10^{18}			Virginia Semi. SS
Epitaxial Layer Design								
	Name	**Material**	**Thick nm**	**Material**	**Thick nm**	**Repeat**	**Total nm**	**Adjusted nm**
0	Nuc.	PbSe	200					
1	SL1	PbSnSe	5.00	PbSe	5.00	30	300	4.3 / 259
2	SL2	PbSnSe	4.00	PbSe	4.00	38	304	3.4 / 262
3	SL3	PbSnSe	3.00	PbSe	3.00	50	300	2.6 / 259
4	SL4	PbSnSe	2.00	PbSe	2.00	75	300	1.7 / 259
5	SL5	PbSnSe	1.00	PbSe	1.00	150	300	0.9 / 259
Averages & Totals			2.19		2.19	343	1504	1.88 / 1293
6	Barrier	PbSrSe	133					115
7	MQW	PbSe	20.00	PbSe	10.00	20		17 x 8.6 / 517
8	Barrier	PbSrSe	113					97
9	Cap	PbSe	5					4.3

Growth Wafer

Sample M207-A

Sample M207-CF

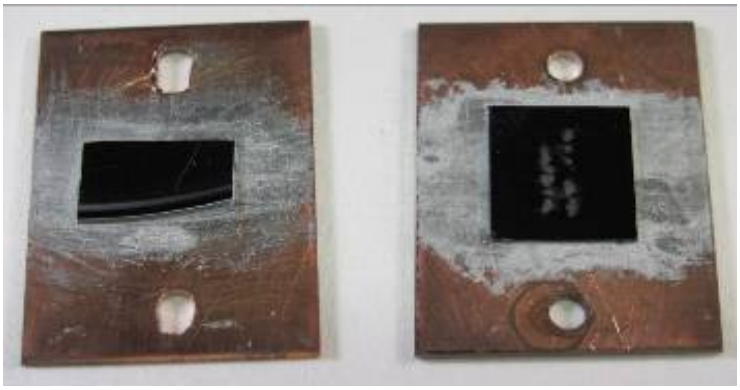

Growth M211: Multiple Quantum Wells on 5-Period Superlattice

Date, Grown By	Target Thickness	Measured Thick.	%
6/22/2011, Z. Cai	2.551 μm	2.85 μm	+11.7%
MQW Alloy %	**SL Alloy %**	**Carrier Doping**	**Substrate Batch**
$Pb_{0.93}Sr_{0.07}Se$	$Pb_{0.85}Sn_{0.15}Se$	None	CVD #051606-B

Hall Effect Summary

n (100K), cm^{-3}	μ, cm^2/Vs	σ, S/cm	n (300K), cm^{-3}	μ, cm^2/Vs	σ, S/cm
$+1.455 \times 10^{17}$	11540	268.7	$+ 4.193 \times 10^{17}$	445.4	29.88
n(150K), cm^{-3}	**μ, cm^2/Vs**	**σ, S/cm**	**n (200K), cm^{-3}**	**μ, cm^2/Vs**	**σ, S/cm**
$+1.587 \times 10^{17}$	4514	114.6	$+ 1.868 \times 10^{17}$	2135	63.81

Epitaxial Layer Design

	Name	Material	Thick nm	Material	Thick nm	Repeat	Total nm	Adjusted nm
0	Nuc.	PbSe	200					223
1	SL1	PbSnSe	1.00	PbSe	1.00	150	300	1.1 / 335
2	SL2	PbSnSe	2.00	PbSe	2.00	75	300	2.2 / 335
3	SL3	PbSnSe	3.00	PbSe	3.00	50	300	3.4 / 335
4	SL4	PbSnSe	4.00	PbSe	4.00	38	304	4.5 / 335
5	SL5	PbSnSe	5.00	PbSe	5.00	30	300	5.6 / 335
Averages & Totals			2.19		2.19	343	1504	2.45 / 1680
6	Barrier	PbSrSe	133					149
7	MQW	PbSrSe	20.0	PbSe	10.0	20	600	22 x 11 / 670
8	Barrier	PbSrSe	113					126
9	Cap	PbSe	5.00					5.6

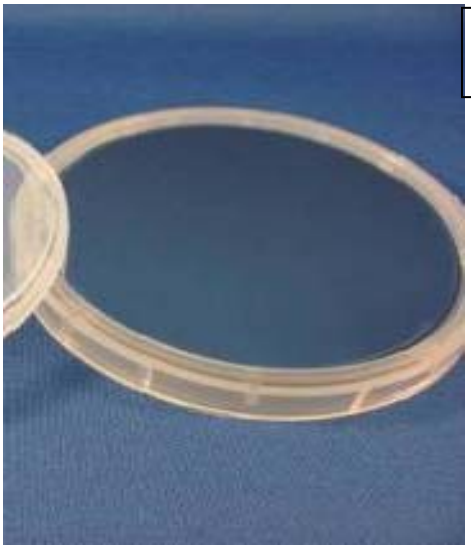

Growth Wafer

Sample M211-R

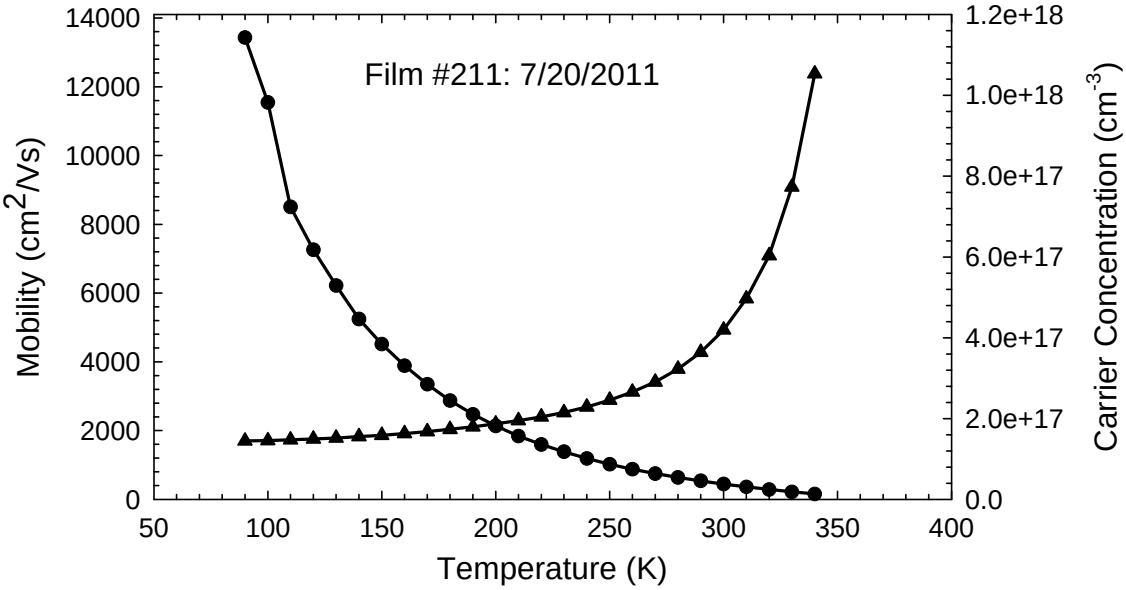
Film #211: 7/20/2011
Mobility (cm2/Vs)
Carrier Concentration (cm-3)
Temperature (K)
14000
12000
10000
8000
6000
4000
2000
0
1.2e+18
1.0e+18
8.0e+17
6.0e+17
4.0e+17
2.0e+17
0.0
50
100
150
200
250
300
350
400

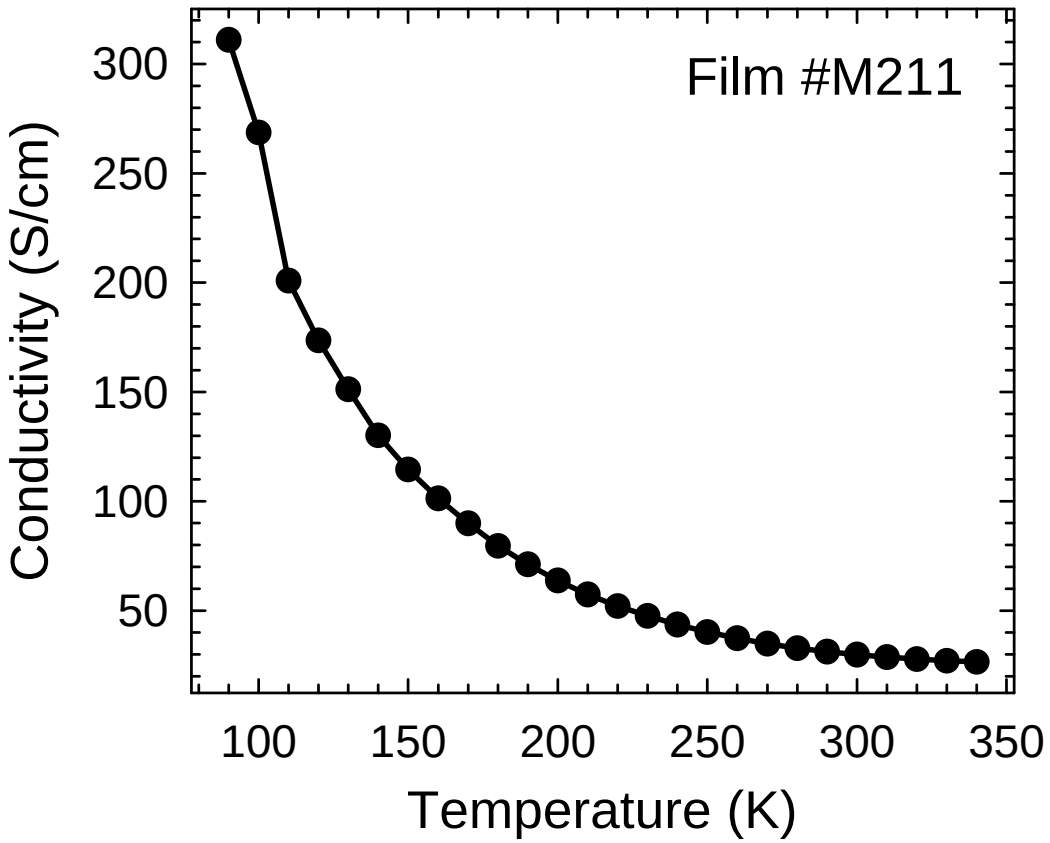
Film #M211
Conductivity (S/cm)
Temperature (K)
300
250
200
150
100
50
100
150
200
250
300
350

Growth M212: Multiple Quantum Wells on 5-Period Superlattice

Date, Grown By	Target Thickness	Measured	%
6/24/2011, Z. Cai	2.551 µm	2.88 µm	+12.9
MQW Alloy %	**SL Alloy %**	**Carrier Doping**	**Substrate Batch**
$Pb_{0.93}Sr_{0.07}Se$	$Pb_{0.85}Sn_{0.15}Se$	None	CVD #051606-B

Hall Effect Summary

n (100K), cm^{-3}	µ, cm^2/Vs	σ, S/cm	n (300K), cm^{-3}	µ, cm^2/Vs	σ, S/cm
+ 1.895 x 10^{17}	15070	456.8	+ 4.313 x 10^{17}	564	38.91
n(150K), cm^{-3}	**µ, cm^2/Vs**	**σ, S/cm**	**n (200K), cm^{-3}**	**µ, cm^2/Vs**	**σ, S/cm**
+ 1.980 x 10^{17}	5860	185.6	+ 2.222 x 10^{17}	2711	96.36

Epitaxial Layer Design

	Name	Material	Thick nm	Material	Thick nm	Repeat	Total nm	Adjusted nm
0	Nuc.	PbSe	200					226
1	SL1	PbSnSe	0.50	PbSe	0.50	300	300	0.6 / 339
2	SL2	PbSnSe	1.00	PbSe	1.00	150	300	1.1 / 339
3	SL3	PbSnSe	1.50	PbSe	1.50	100	300	1.7 / 339
4	SL4	PbSnSe	2.00	PbSe	2.00	75	300	2.3 / 339
5	SL5	PbSnSe	2.50	PbSe	2.50	60	300	2.8 / 339
Averages & Totals			1.09		1.09	685	1500	1.24 / 1694
6	Barrier	PbSrSe	133					150
7	MQW	PbSe	20.0	PbSrSe	10.0	20	600	23 x 11 / 677
8	Barrier	PbSrSe	113					128
9	Cap	PbSe	5.00					5.6

Sample
M212-R

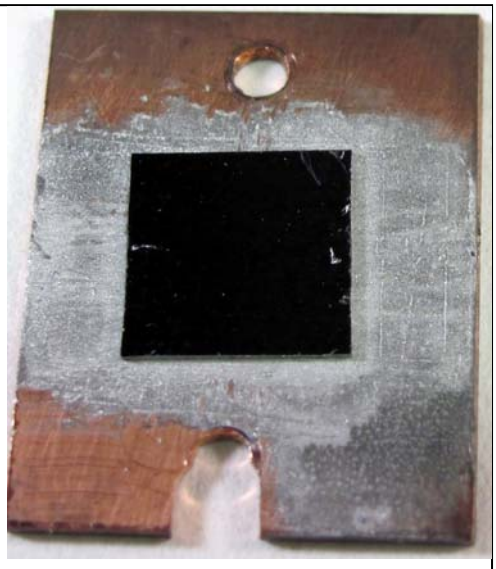

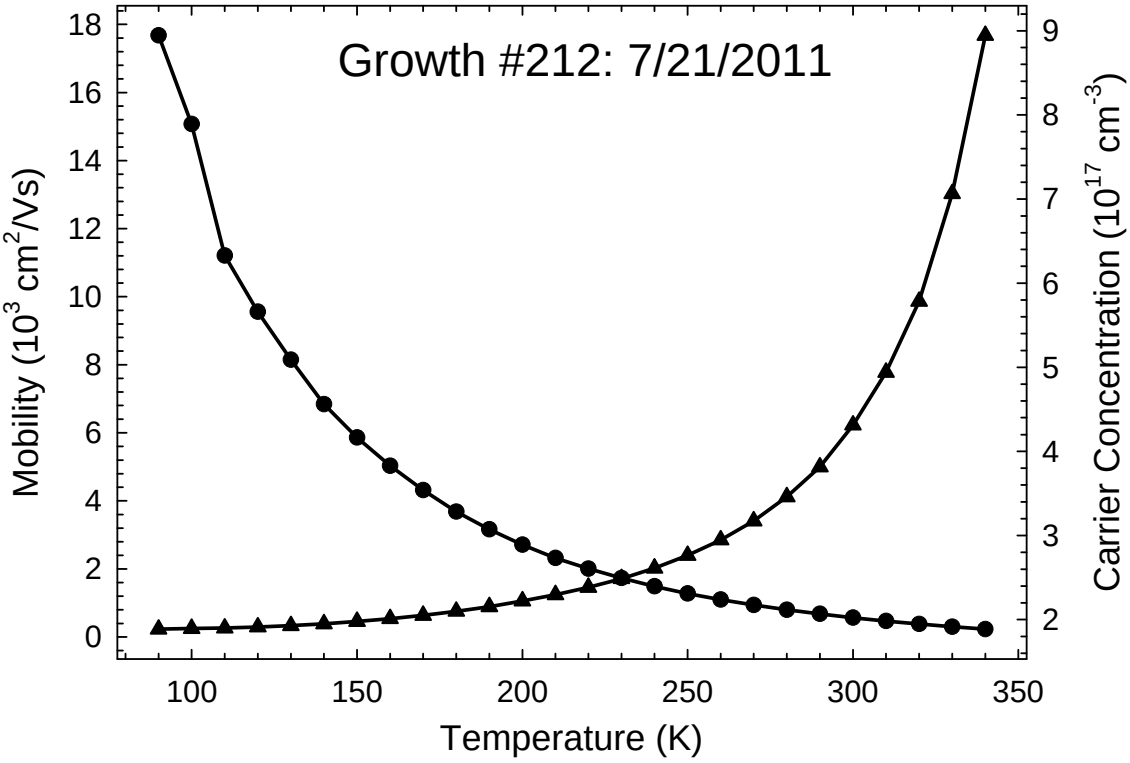
Growth #212: 7/21/2011
Mobility (10^3 cm^2/Vs)
Carrier Concentration (10^{17} cm^{-3})
Temperature (K)
0
2
4
6
8
10
12
14
16
18
2
3
4
5
6
7
8
9
100
150
200
250
300
350

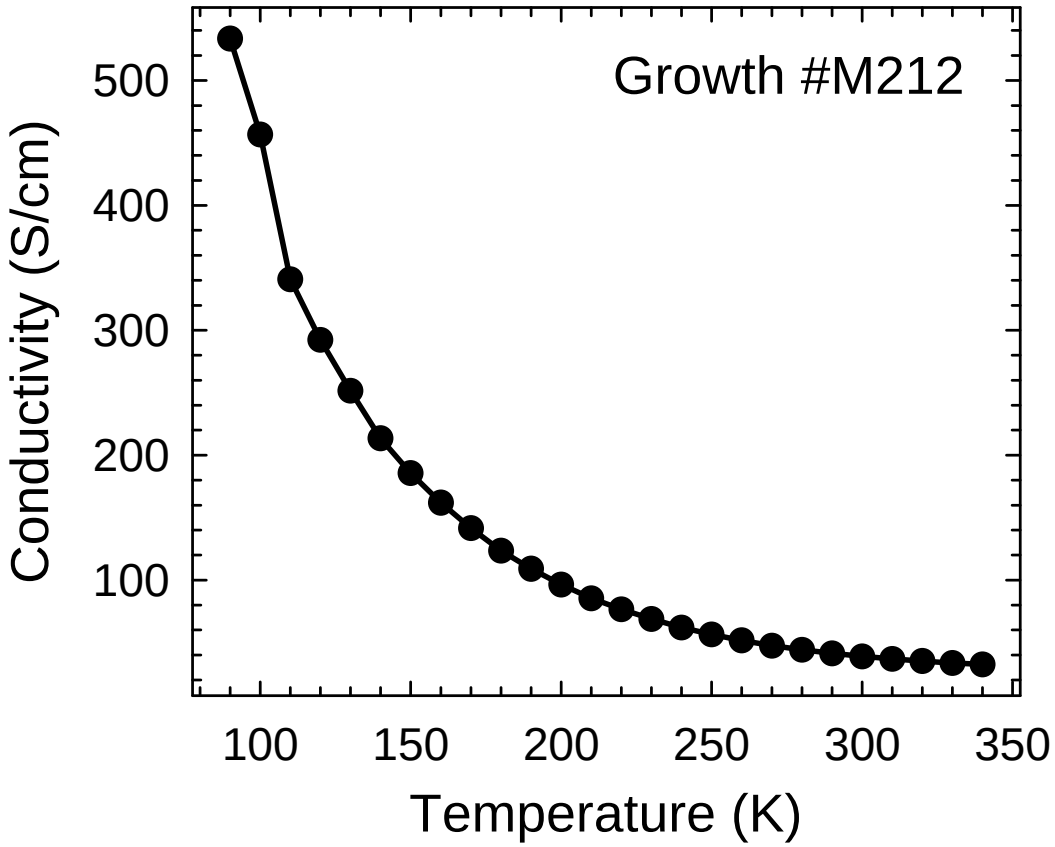
Growth #M212
Conductivity (S/cm)
Temperature (K)
100
200
300
400
500
100
150
200
250
300
350

Growth M213: Multiple Quantum Wells on 7-Period Superlattice

Date, Grown By	Target Thickness	Measured Thickness	Variation %
6/29/2011, Z. Cai	2.451 μm	2.72 μm	+11.0
MQW Alloy %	**SL Alloy %**	**Carrier Doping**	**Substrate Batch**
$Pb_{0.93}Sr_{0.07}Se$	$Pb_{0.85}Sn_{0.15}Se$	None	CVD #051606-B

Hall Effect Summary

n (100K), cm^{-3}	μ, cm^2/Vs	σ, S/cm	n (300K), cm^{-3}	μ, cm^2/Vs	σ, S/cm
$+ 1.60 \times 10^{17}$	14110	361.5	$+ 4.49 \times 10^{17}$	492.7	35.40
n(150K), cm^{-3}	**μ, cm^2/Vs**	**σ, S/cm**	**n (200K), cm^{-3}**	**μ, cm^2/Vs**	**σ, S/cm**
$+ 1.75 \times 10^{17}$	5225	146.7	$+ 2.05 \times 10^{17}$	2405	78.92

Epitaxial Layer Design

	Name	Material	Thick nm	Material	Thick nm	Repeat	Total nm	Adjusted nm
0	Nuc.	PbSe	200					222
1	SL1	PbSnSe	0.50	PbSe	0.50	200	200	0.6 / 222
2	SL2	PbSnSe	0.75	PbSe	0.75	133	200	0.8 / 222
3	SL3	PbSnSe	1.00	PbSe	1.00	100	200	1.1 / 222
4	SL4	PbSnSe	1.25	PbSe	1.25	80	200	1.4 / 222
5	SL5	PbSnSe	1.50	PbSe	1.50	67	201	1.7 / 223
6	SL6	PbSnSe	1.75	PbSe	1.75	57	200	1.9 / 222
7	SL7	PbSnSe	2.00	PbSe	2.00	50	200	2.2 / 222
Averages & Totals			1.02		1.02	687	1401	1.13 / 1555
8	Barrier	PbSrSe	133					148
9	MQW	PbSe	20.0	PbSrSe	10.0	20	600	22 x 11 / 666
10	Barrier	PbSrSe	113					125
11	Cap	PbSe	5.00					5.6

Growth Wafer

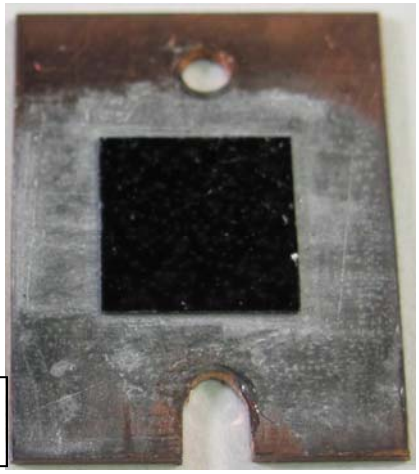

Sample M213-R

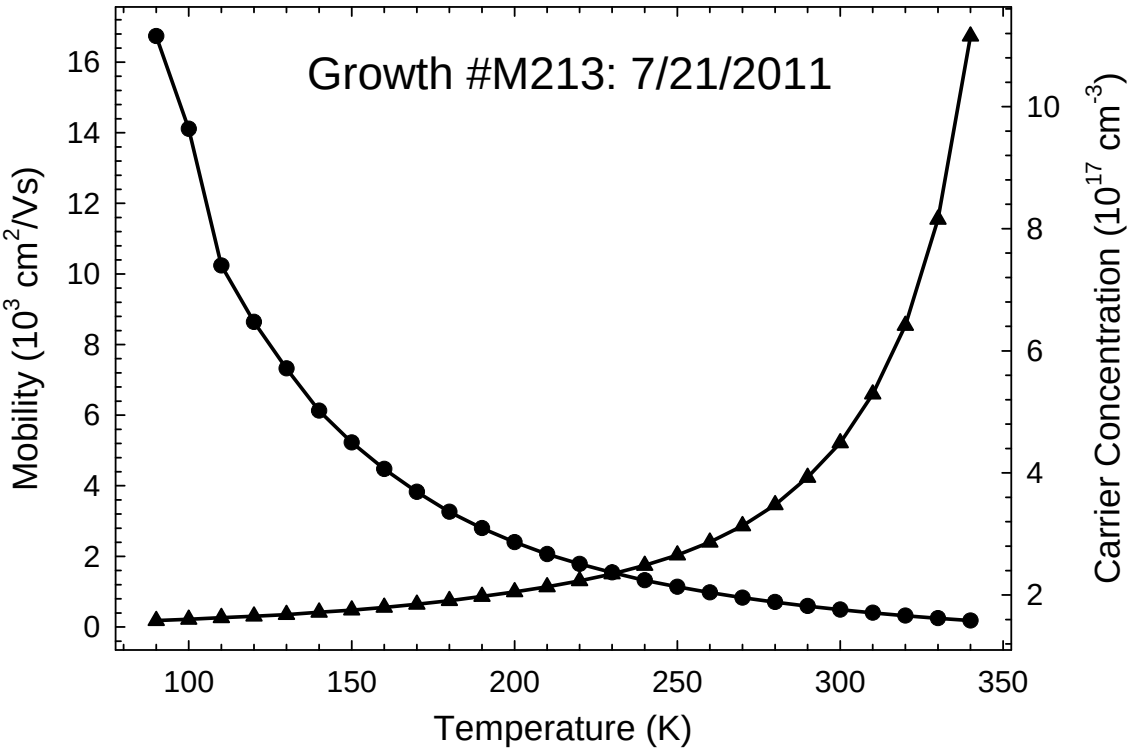
Growth #M213: 7/21/2011
Mobility (10^3 cm^2/Vs)
Carrier Concentration (10^{17} cm^{-3})
Temperature (K)
0
2
4
6
8
10
12
14
16
100
150
200
250
300
350

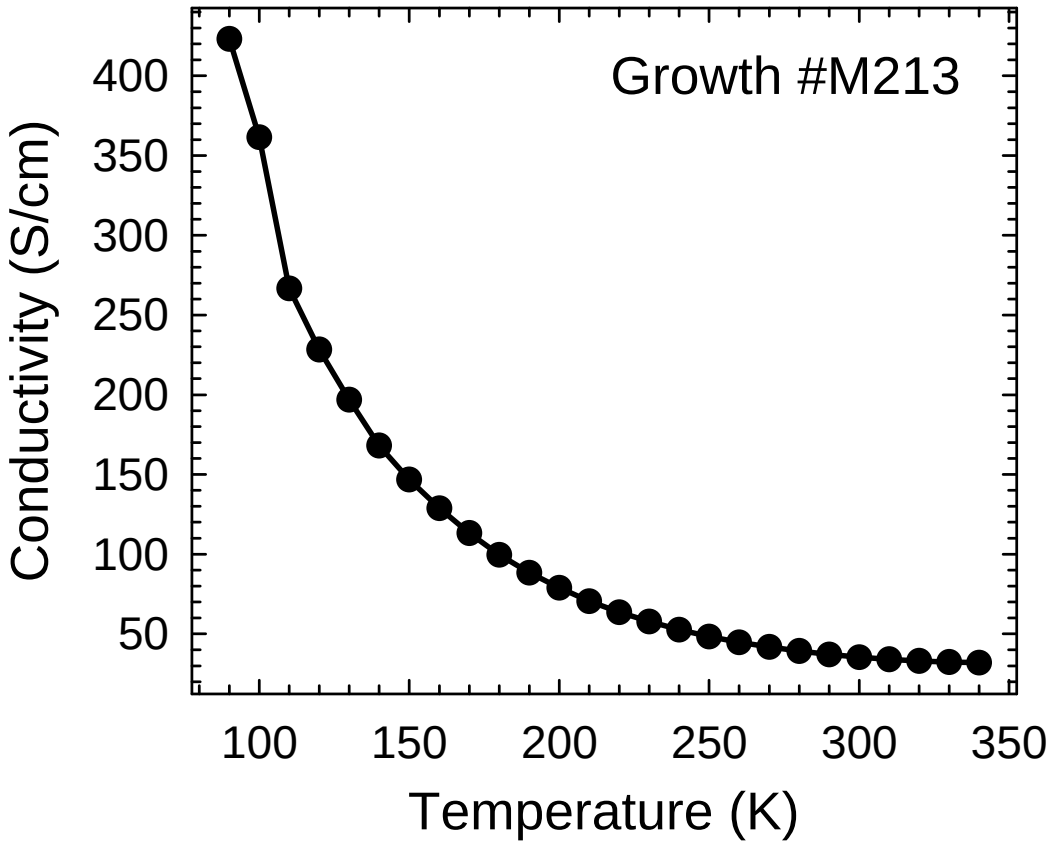
Growth #M213
Conductivity (S/cm)
Temperature (K)
50
100
150
200
250
300
350
400
100
150
200
250
300
350

Growth M214: Multiple Quantum Wells on 7-Period Superlattice

Date, Grown By	Target Thickness	Measured Thickness	Variation %
6/30/2011, Z. Cai	2.451 μm	3.03 μm	+23.6
MQW Alloy %	**SL Alloy %**	**Carrier Doping**	**Substrate Batch**
$Pb_{0.93}Sr_{0.07}Se$	$Pb_{0.85}Sn_{0.15}Se$	None	CVD #051606-B

Hall Effect Summary

n (100 K), cm^{-3}	μ, cm^2/Vs	σ, S/cm	n (300 K), cm^{-3}	μ, cm^2/Vs	σ, S/cm
+ 1.01 x 10^{17}	8839	150.3	+ 5.03 x 10^{17}	313	25.17
n (150 K), cm^{-3}	**μ, cm^2/Vs**	**σ, S/cm**	**n (200 K), cm^{-3}**	**μ, cm^2/Vs**	**σ, S/cm**
+ 1.34 x 10^{17}	3291	70.71	+ 1.76 x 10^{17}	1535	43.31

Epitaxial Layer Design

	Name	Material	Thick nm	Material	Thick nm	Repeat	Total nm	Adjusted nm
0	Nuc.	PbSe	200					247
1	SL1	PbSnSe	1.50	PbSe	1.50	67	201	1.9 / 248
2	SL2	PbSnSe	1.75	PbSe	1.75	57	200	2.2 / 247
3	SL3	PbSnSe	2.00	PbSe	2.00	50	200	2.5 / 247
4	SL4	PbSnSe	2.25	PbSe	2.25	44	198	2.8 / 245
5	SL5	PbSnSe	2.50	PbSe	2.50	40	200	3.1 / 247
6	SL6		2.75		2.75	36	198	3.4 / 245
7	SL7		3.00		3.00	33	198	3.7 / 245
Averages & Totals			2.13		2.13	327	1395	2.64 / 1724
8	Barrier	PbSrSe	133					164
9	MQW	PbSrSe	20.0	PbSe	10.0	20	600	25 x 12 / 742
10	Barrier	PbSrSe	113					140
11	Cap	PbSe	5.00					6.2

Growth Wafer

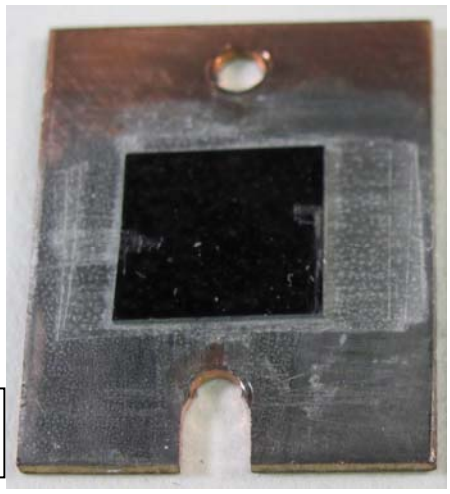

Sample M214-R

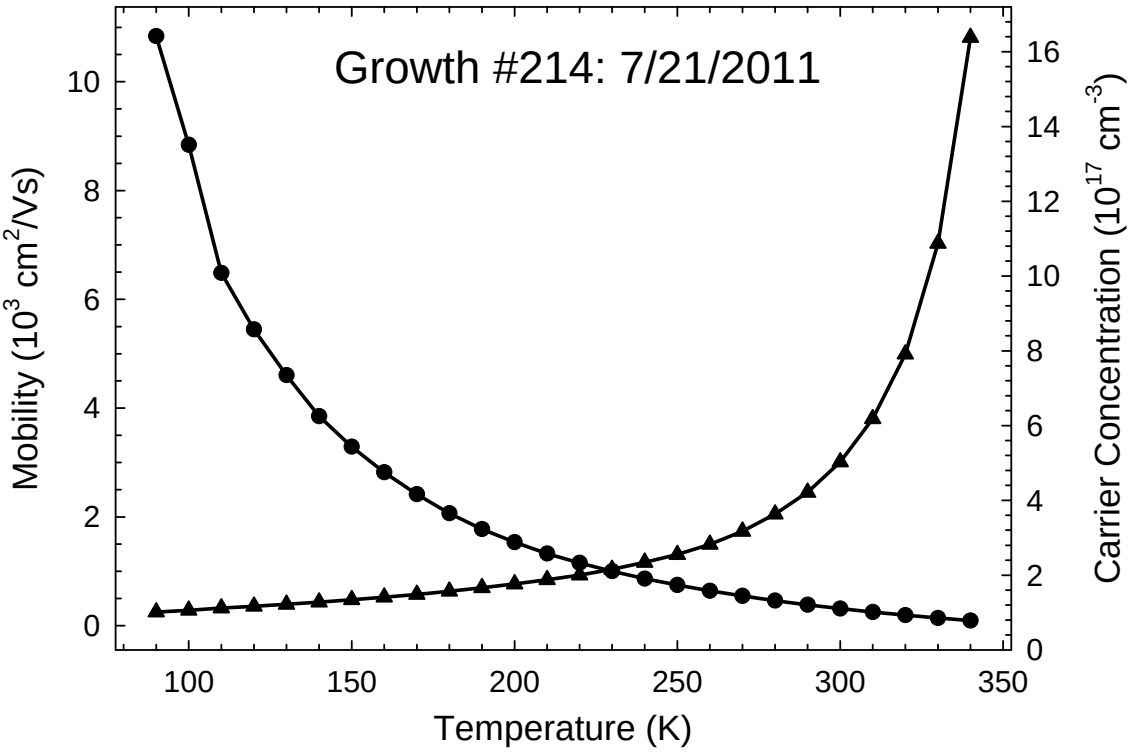
Growth #214: 7/21/2011
Mobility (10^3 cm^2/Vs)
Carrier Concentration (10^{17} cm^{-3})
Temperature (K)
0
2
4
6
8
10
0
2
4
6
8
10
12
14
16
100
150
200
250
300
350

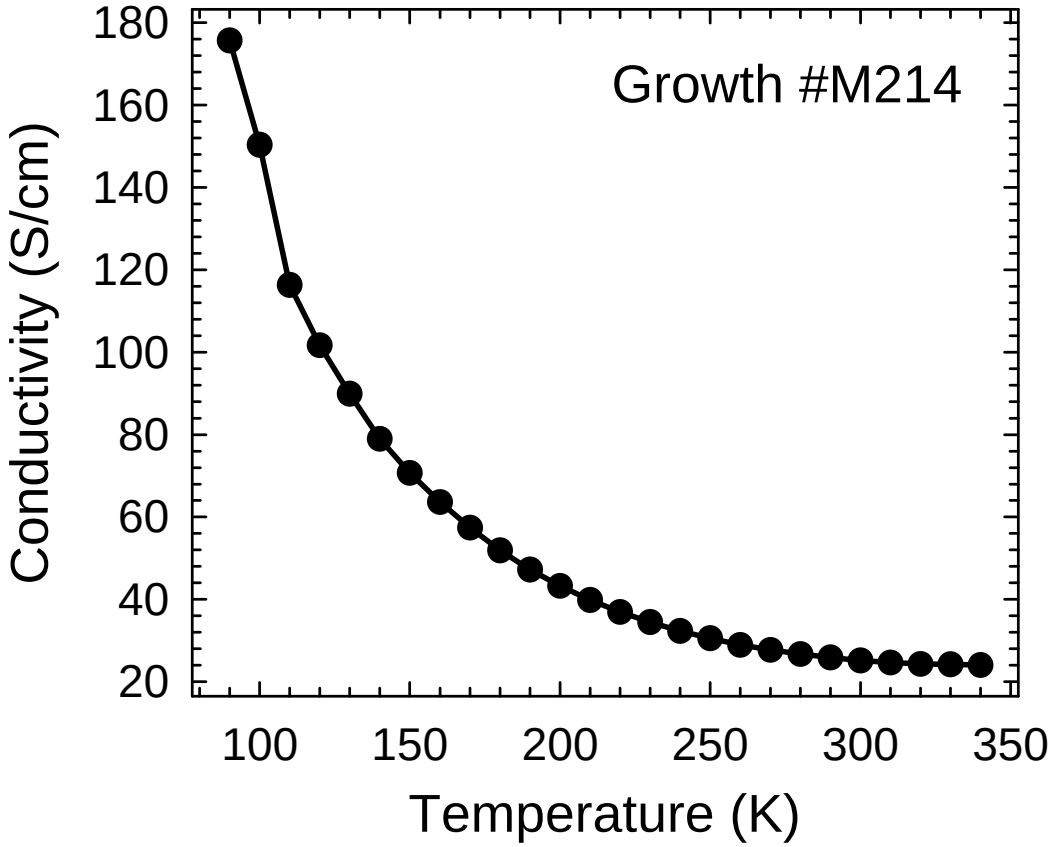
Growth #M214
Conductivity (S/cm)
Temperature (K)
20
40
60
80
100
120
140
160
180
100
150
200
250
300
350

Appendix C

Detailed MBE Sample Test Summary

PL Laser Power Calibration:

Laser #06JUN16	Date: 7/2011	Date 5/2010
0.40	12	15
0.45	65	69
1.00	424	430
2.00	1123	1136
3.00	1814	1829
4.00	2480	2513
5.00	3110	3208
6.00	3700	3903
7.00	4220	4598

Sample #M046-PL2

Test Date	7/31/11	Laser	#06JUN16		Results
FTIR System	#2	$I_{reflect}$	3.0 A		PL Peak
Range (cm-1)	500-3500 cm^{-1}	$P_{reflect}$	565 mW		17.0 ± 0.93 K/Watt
Co-adds/Gain/Res.	100 / 8 / 8 cm^{-1}	P_{Inc}	1814 mW		
Detector Type	PC	Absorb	68.8 %		
Detector Current	35 mA	Test (A)	P_{Inc}	P_{abs}	
Preamp Gain/Filter	10/300 kHz/AC	3.0	1814	1370	BB Power
Power Meter	New. 1916-C	4.0	2480	1718	1.05 ± 0.06 K/Watt
Sample TEC	Lakeshore 330	5.0	3110	2044	
Sample Mount	InGa/Cu/InGa	6.0	3700	2331	
Repeat	3	BB Range	800 – 1609 cm^{-1}		
PL Analysis	Exp. Gauss	PL Range	1800 – 3500 cm^{-1}		

T_{HS} (K)	P_{abs} (mW)	E_{max} (meV)	Std. Dev.	ΔE_{max} (meV/W)	BB_{Pow} (a.u.)	Std. Dev.	ΔP_{BB} a.u./W
293	0	276.14	0.705	9.30 ± 0.612	72.97	0.85	1.42 ± 0.56
	1370	288.22	0.830		73.99	1.04	
	1718	291.25	0.277		74.79	0.83	
	2044	294.29	0.277		75.65	0.48	
	2331	297.17	0.553		76.45	0.36	
303	0	280.82	1.091	8.48 ± 1.14	89.39	0.34	2.21 ± 0.08
	1370	293.33	0.732		92.19	0.38	
	1718	296.53	0.277		92.96	0.20	
	2044	299.56	0.553		93.85	0.19	
	2331	301.64	0.959		94.60	0.21	
313	0	286.26	0.045	8.67 ± 0.657	110.42	0.21	2.70 ± 0.06
	1370	298.28	0.000		113.79	0.16	
	1718	301.00	0.732		114.77	0.12	
	2044	304.04	0.959		115.78	0.21	
	2331	306.11	0.998		116.85	0.12	
323	0	295.73	0.059	6.32 ± 0.443	135.70	0.22	3.29 ± 0.04
	1370	304.04	0.479		139.87	0.16	
	1718	306.43	0.479		141.10	0.15	
	2044	308.19	0.732		142.29	0.24	
	2331	310.27	0.830		143.47	0.06	

P_{abs} (mW)	ΔE_{max} (μeV/K)	St. Dv. (μeV/K)	$\Delta E_{max,avg}$ (μeV/K)	Stef-Boltz	St. Dv. (au)	T_0 (K)	T_{HS} (K)	ΔP_{BB} (au/K)
0				0.315	0.004	242	293	1.92
1370	522.64	24.0	481 ± 22.1	0.330	0.004	242	303	2.12
1718	498.27	20.9		0.332	0.003	242	313	2.34
2044	466.51	30.8		0.334	0.001	242	323	2.57
2331	441.29	17.3		0.336	0.002	242		

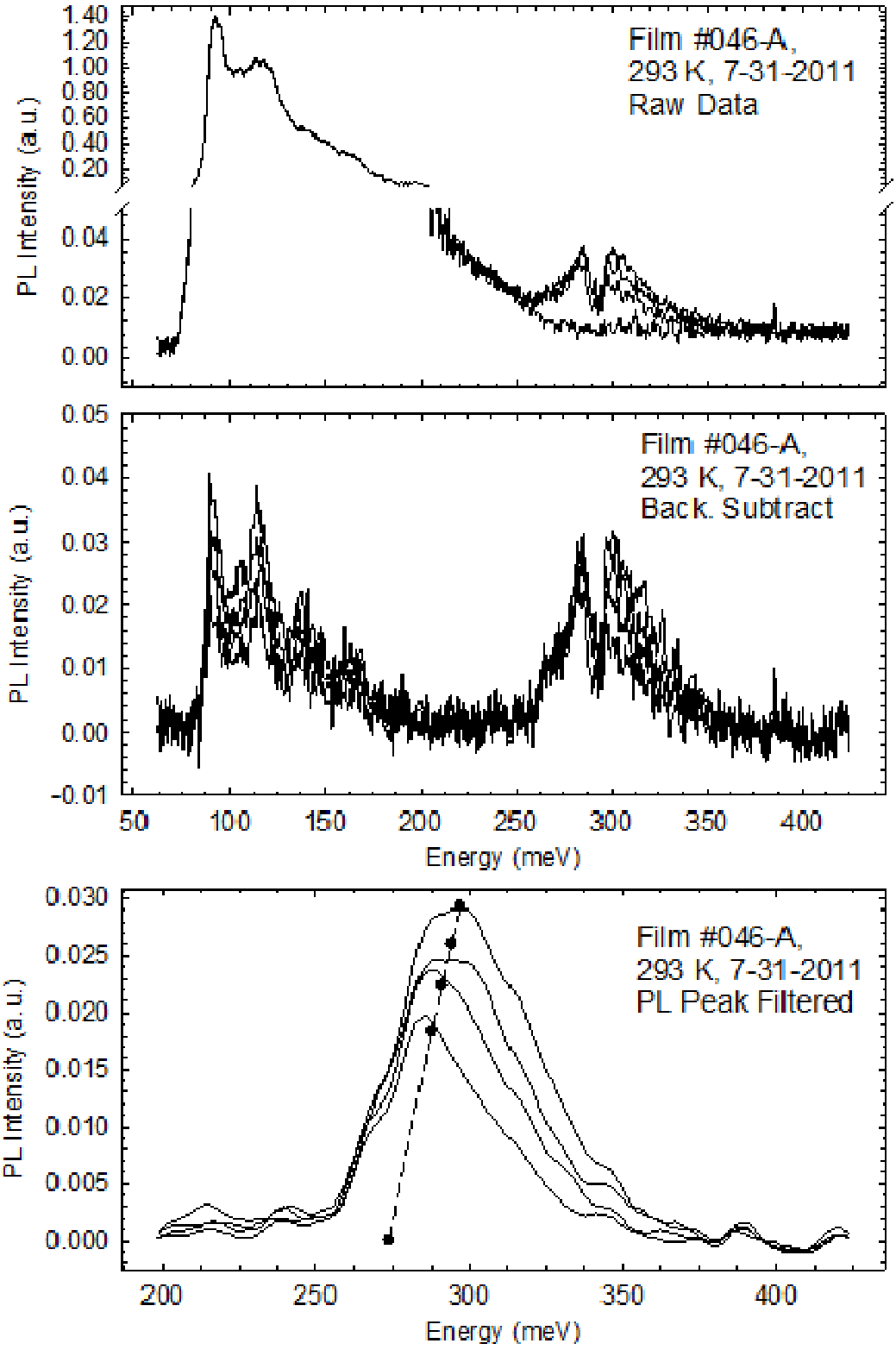
Film #046-A,
293 K, 7-31-2011
Raw Data
PL Intensity (a.u.)
1.40
1.20
1.00
0.80
0.60
0.40
0.20
0.04
0.02
0.00
Film #046-A,
293 K, 7-31-2011
Back. Subtract
PL Intensity (a.u.)
0.05
0.04
0.03
0.02
0.01
0.00
-0.01
50
100
150
200
250
300
350
400
Energy (meV)
Film #046-A,
293 K, 7-31-2011
PL Peak Filtered
PL Intensity (a.u.)
0.030
0.025
0.020
0.015
0.010
0.005
0.000
200
250
300
350
400
Energy (meV)

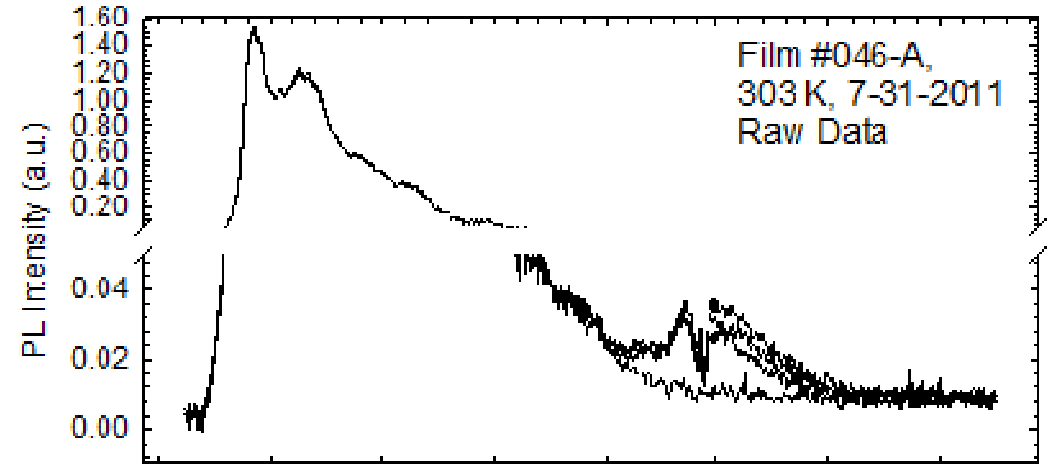
Film #046-A,
303 K, 7-31-2011
Raw Data
PL Intensity (a.u.)
1.60
1.40
1.20
1.00
0.80
0.60
0.40
0.20
0.04
0.02
0.00

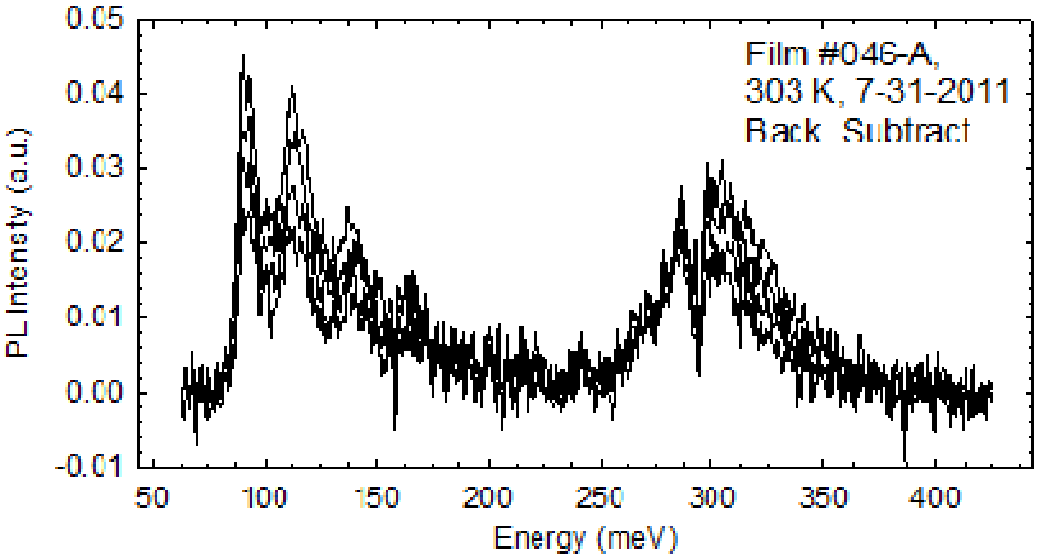
Film #046-A,
303 K, 7-31-2011
Back Subtract
PL Intensity (a.u.)
0.05
0.04
0.03
0.02
0.01
0.00
-0.01
50
100
150
200
250
300
350
400
Energy (meV)

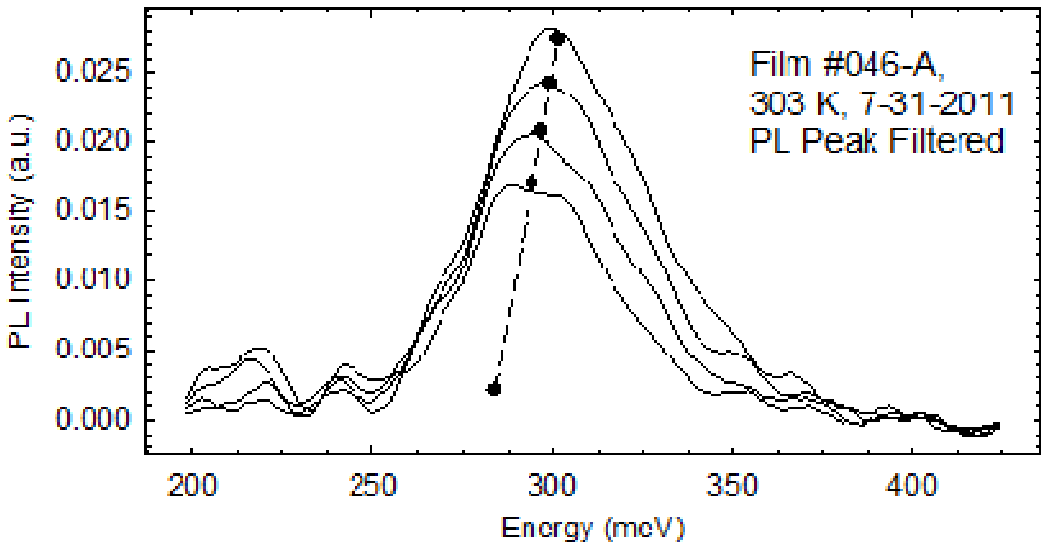
Film #046-A,
303 K, 7-31-2011
PL Peak Filtered
PL Intensity (a.u.)
0.025
0.020
0.015
0.010
0.005
0.000
200
250
300
350
400
Energy (meV)

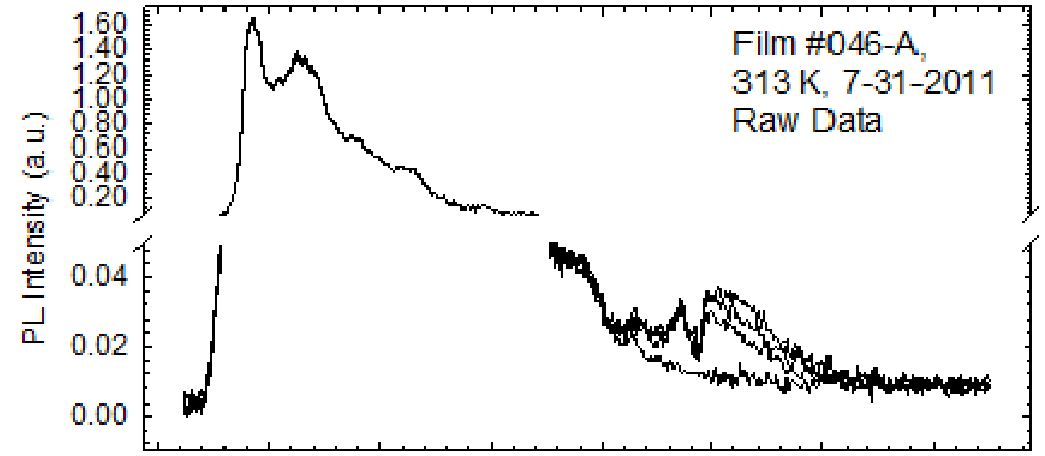
Film #046-A,
313 K, 7-31-2011
Raw Data
PL Intensity (a.u.)
1.60
1.40
1.20
1.00
0.80
0.60
0.40
0.20
0.04
0.02
0.00

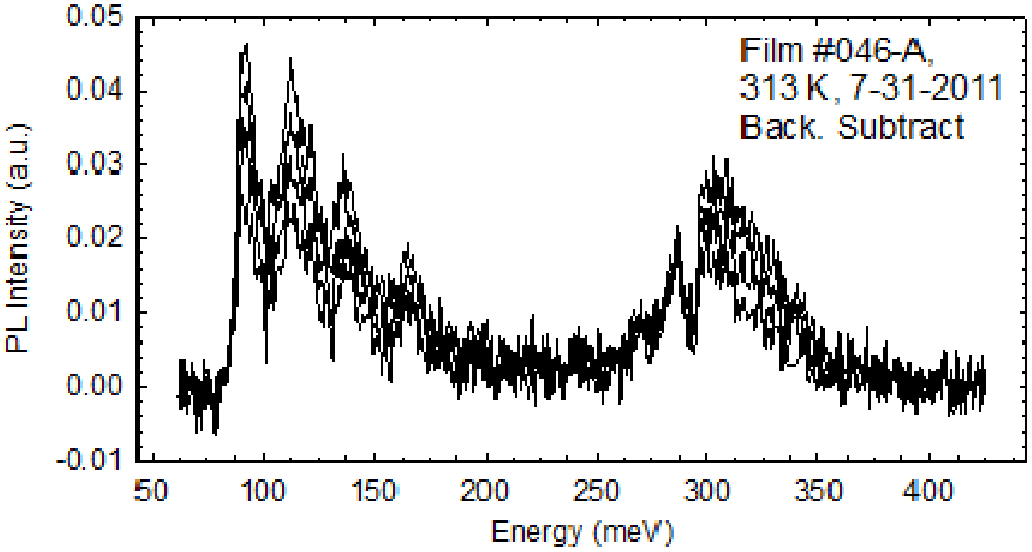
Film #046-A,
313 K, 7-31-2011
Back. Subtract
PL Intensity (a.u.)
0.05
0.04
0.03
0.02
0.01
0.00
-0.01
50
100
150
200
250
300
350
400
Energy (meV)

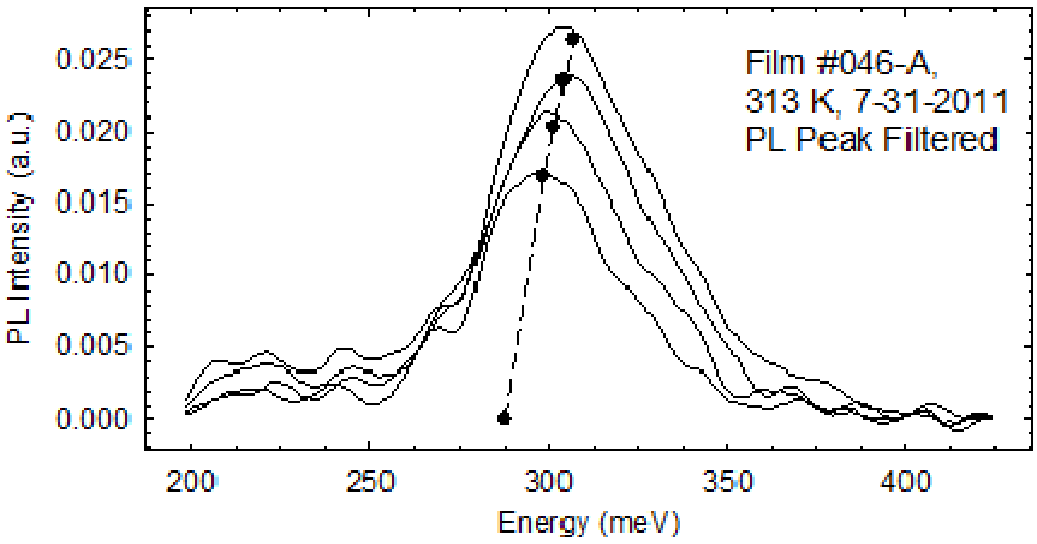
Film #046-A,
313 K, 7-31-2011
PL Peak Filtered
PL Intensity (a.u.)
0.025
0.020
0.015
0.010
0.005
0.000
200
250
300
350
400
Energy (meV)

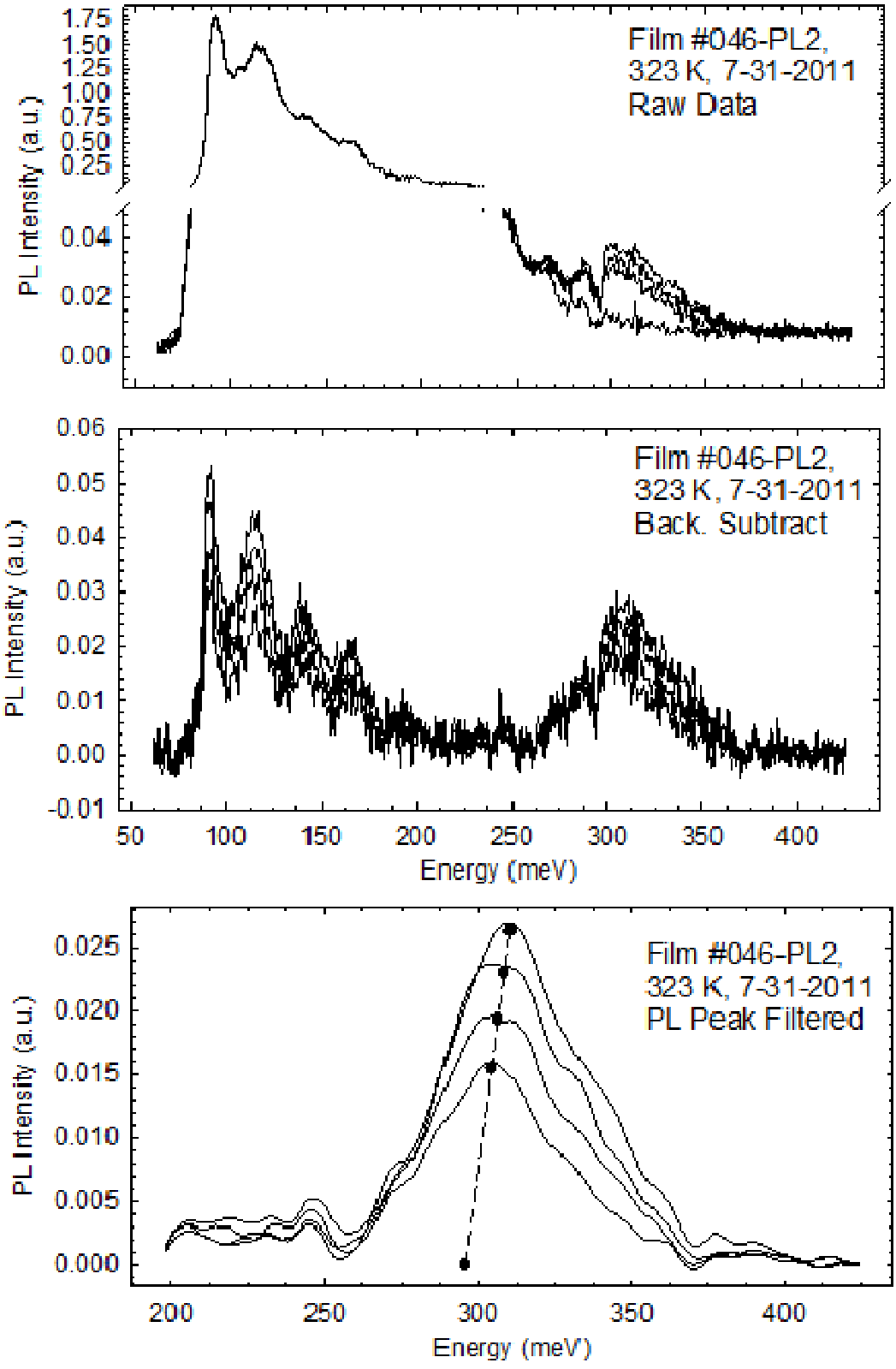
Film #046-PL2,
323 K, 7-31-2011
Raw Data
PL Intensity (a.u.)
1.75
1.50
1.25
1.00
0.75
0.50
0.25
0.04
0.02
0.00
Film #046-PL2,
323 K, 7-31-2011
Back. Subtract
PL Intensity (a.u.)
0.06
0.05
0.04
0.03
0.02
0.01
0.00
-0.01
50
100
150
200
250
300
350
400
Energy (meV)
Film #046-PL2,
323 K, 7-31-2011
PL Peak Filtered
PL Intensity (a.u.)
0.025
0.020
0.015
0.010
0.005
0.000
200
250
300
350
400
Energy (meV)

Sample #M047 – A1: Bulk PbSe

Test Date	2/24/11	Laser	#06JUN16		Results
FTIR System	#2	$I_{reflect}$	2.0 A		PL Peak
Range	500-3500 cm^{-1}	$P_{reflect}$	465 mW		16.5 ± 0.60 K/Watt
Co-adds/Gain/Res.	100 / 8 / 8 cm^{-1}	P_{Inc}	1123 mW		
Detector Type	PC	Absorb	58.6 %		
Detector Current	35 mA	Test (A)	P_{Inc}	P_{abs}	
Preamp Gain/Filter	10/300 kHz/AC	2.0	1123	658	BB Power
Power Meter	New. 1916-C	3.0	1814	1063	0.264 ± 0.02 K/Watt
Sample TEC	Lakeshore 330	4.0	2480	1453	
Sample Mount	InGa/Cu/InGa	5.0	3110	1822	
Repeat	3	BB Range	800 – 1609 cm-1		
PL Analysis	Exp. Gauss	PL Range	1800 – 3333 cm-1		

T_{HS} (K)	P_{abs} (mW)	E_{max} (meV)	Std. Dev.	ΔE_{max} meV/W	BB_{Pow}	Std. Dev.	ΔP_{BB} a.u./W
293	0	277.20	0.563	6.54 ± 0.252	285.30	5.33	1.44 ± 0.225
	658	281.58	0.471		285.94	5.37	
	1063	283.98	0.473		286.51	5.51	
	1453	286.85	0.009		287.14	5.73	
	1822	289.09	0.268		287.98	5.64	
303	0	280.95	1.34	6.81 ± 0.569	341.96	7.00	1.55 ± 0.423
	658	285.09	1.10		342.79	6.66	
	1063	288.61	0.551		343.26	6.38	
	1453	291.01	0.551		344.00	6.46	
	1822	293.09	0.472		344.86	6.20	
313	0	285.17	0.799	6.63 ± 0.437	409.61	7.57	2.09 ± 0.338
	658	289.57	0.548		410.81	7.80	
	1063	292.13	0.478		411.67	7.65	
	1453	294.84	0.280		412.50	7.59	
	1822	297.24	0.280		413.44	7.36	

P_{abs} (mW)	ΔE_{max} (μeV/K)	$\Delta E_{max,avg}$ (μeV/K)	Stef-Boltz Emissivity (au)	T_0 (K)	T_{HS} (K)	ΔP_{BB} (au/K)
0			0.983 ± 0.018	218	293	5.77
658	399.54 ± 13.85	404 ± 22.7	0.988 ± 0.019	219	303	6.37
1063	407.53 ± 41.53		0.990 ± 0.017	219	313	7.02
1453	399.54 ± 13.85		0.992 ± 0.015	218		
1822	407.53 ± 23.99		0.993 ± 0.014	218		

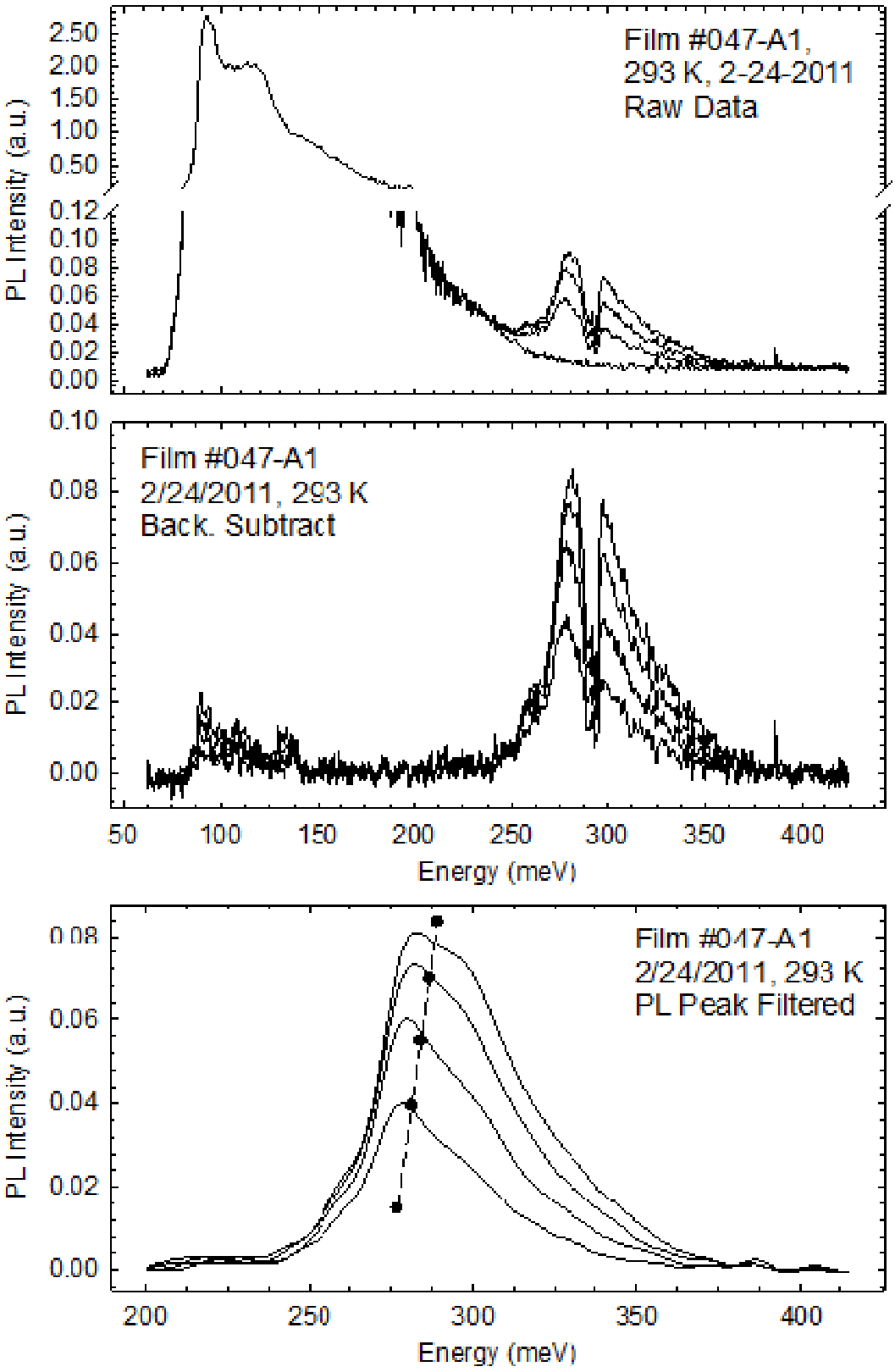
Film #047-A1,
293 K, 2-24-2011
Raw Data
PL Intensity (a.u.)
2.50
2.00
1.50
1.00
0.50
0.12
0.10
0.08
0.06
0.04
0.02
0.00
Film #047-A1
2/24/2011, 293 K
Back. Subtract
PL Intensity (a.u.)
0.10
0.08
0.06
0.04
0.02
0.00
50
100
150
200
250
300
350
400
Energy (meV)
Film #047-A1
2/24/2011, 293 K
PL Peak Filtered
PL Intensity (a.u.)
0.08
0.06
0.04
0.02
0.00
200
250
300
350
400
Energy (meV)

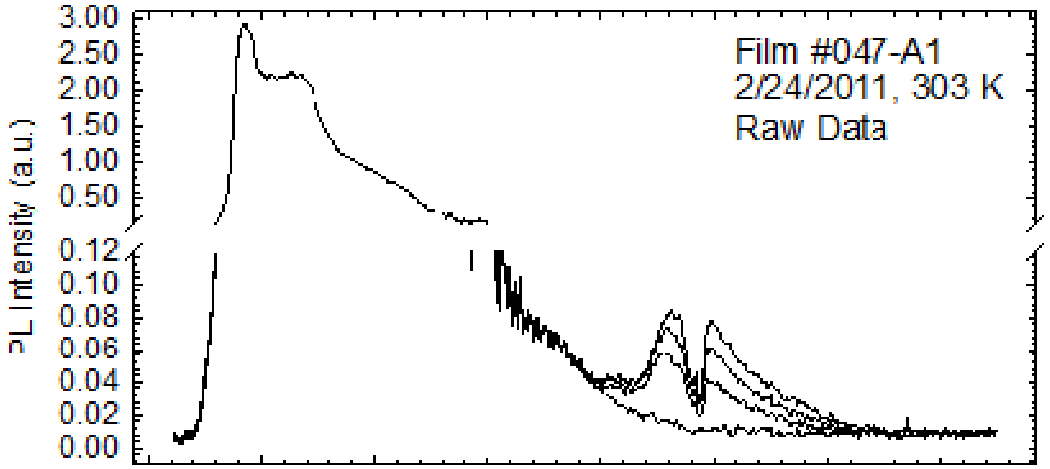
Film #047-A1
2/24/2011, 303 K
Raw Data
PL Intensity (a.u.)
3.00
2.50
2.00
1.50
1.00
0.50
0.12
0.10
0.08
0.06
0.04
0.02
0.00

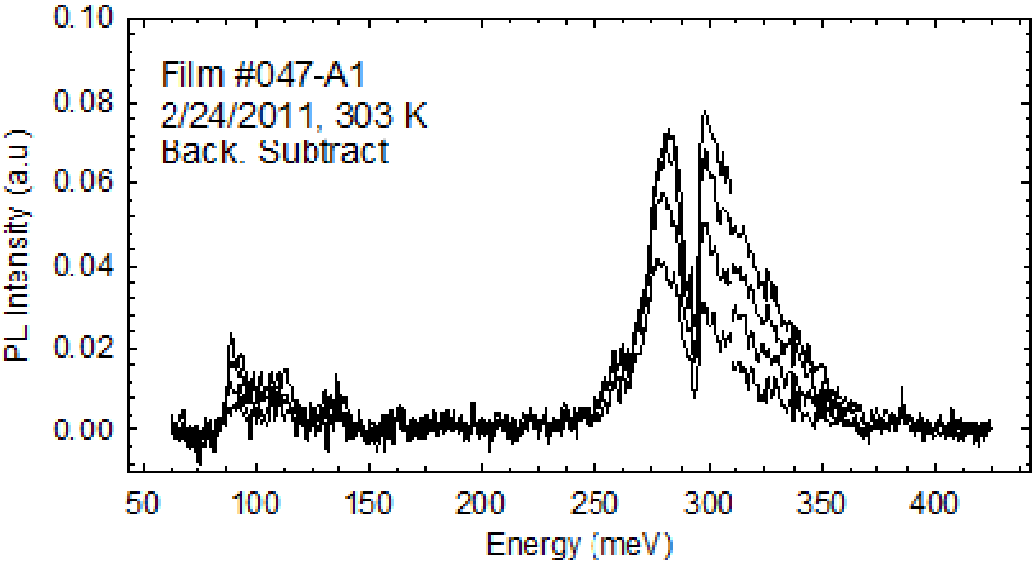
Film #047-A1
2/24/2011, 303 K
Back. Subtract
PL Intensity (a.u.)
0.10
0.08
0.06
0.04
0.02
0.00
50
100
150
200
250
300
350
400
Energy (meV)

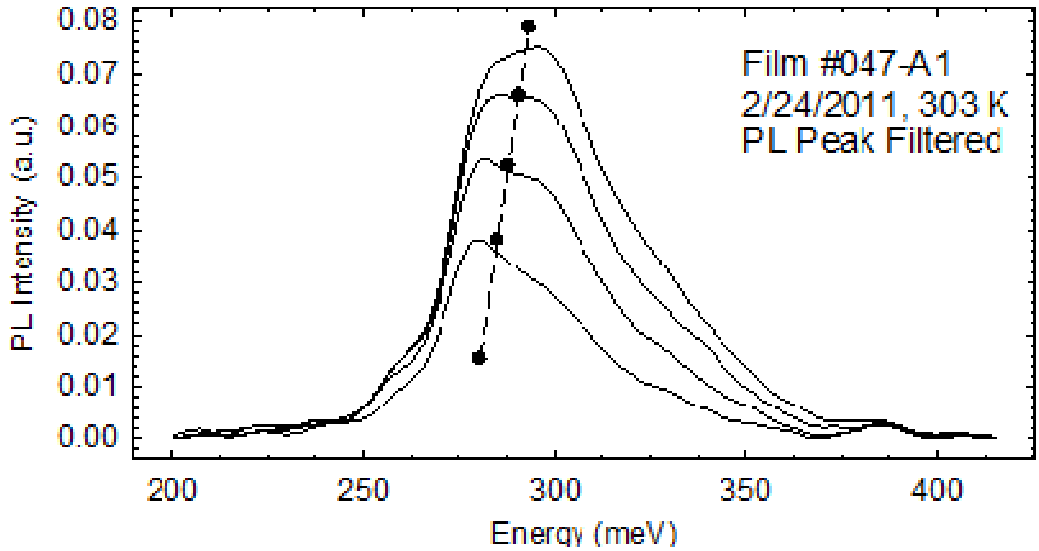
Film #047-A1
2/24/2011, 303 K
PL Peak Filtered
PL Intensity (a.u.)
0.08
0.07
0.06
0.05
0.04
0.03
0.02
0.01
0.00
200
250
300
350
400
Energy (meV)

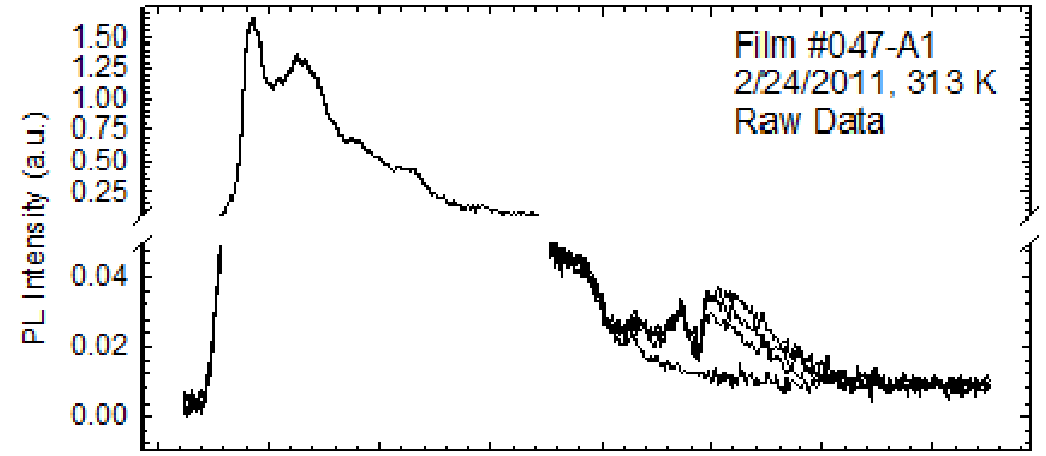
Film #047-A1
2/24/2011, 313 K
Raw Data
PL Intensity (a.u.)
1.50
1.25
1.00
0.75
0.50
0.25
0.04
0.02
0.00

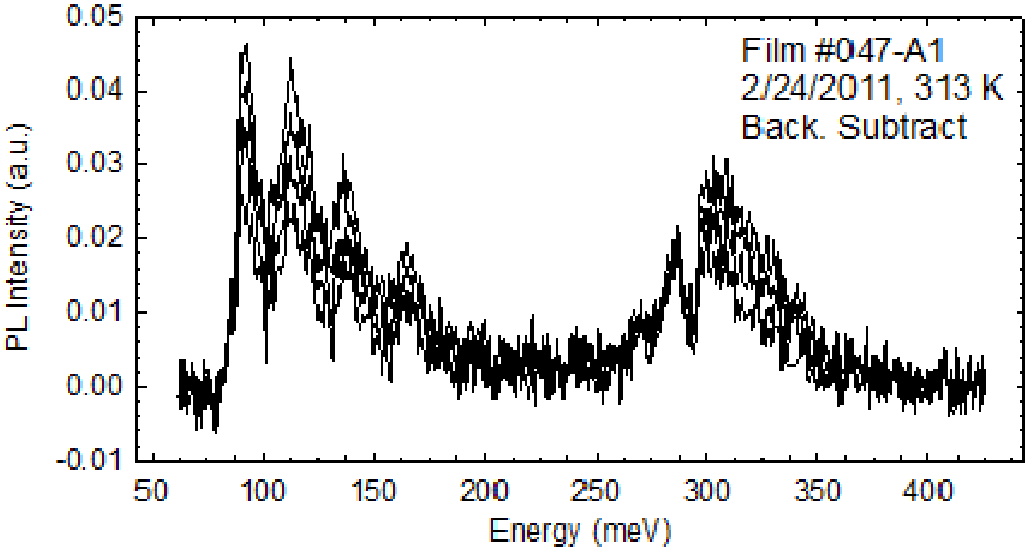
Film #047-A1
2/24/2011, 313 K
Back. Subtract
PL Intensity (a.u.)
0.05
0.04
0.03
0.02
0.01
0.00
-0.01
50
100
150
200
250
300
350
400
Energy (meV)

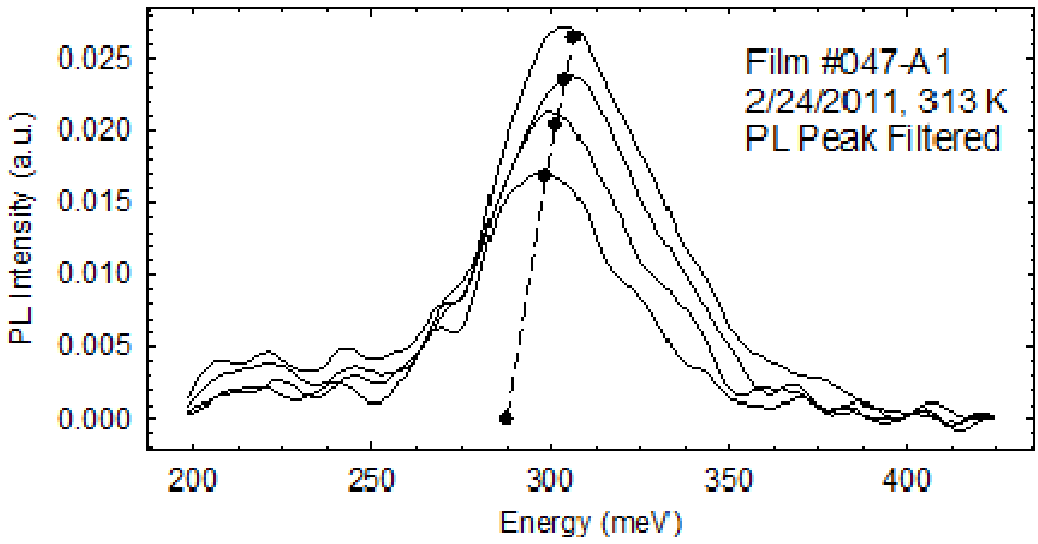
Film #047-A1
2/24/2011, 313 K
PL Peak Filtered
PL Intensity (a.u.)
0.025
0.020
0.015
0.010
0.005
0.000
200
250
300
350
400
Energy (meV)

Sample #M048 – A1: Bulk PbSe

Test Date	2/28/11	Laser	#06JUN16		Results
FTIR System	#2	$I_{reflect}$	2.0 A		PL Peak
Range	500-3500 cm^{-1}	$P_{reflect}$	462 mW		14.7 ± 1.20 K/Watt
Co-adds/Gain/Res.	100 / 8 / 8 cm^{-1}	P_{Inc}	1123 mW		
Detector Type	PC	Absorb	58.8 %		
Detector Current	35 mA	Test (A)	P_{Inc}	P_{abs}	
Preamp Gain/Filter	10/300 kHz/AC	2.0	1123	661	BB Power
Power Meter	New. 1916-C	3.0	1814	1068	0.312 ± 0.08 K/Watt
Sample TEC	Lakeshore 330	4.0	2480	1460	
Sample Mount	InGa/Cu/InGa	5.0	3110	1831	
Repeat	3	BB Range	800 – 1609 cm-1		
PL Analysis	Exp. Gauss	PL Range	1800 – 3500 cm-1		

T_{HS} (K)	P_{abs} (mW)	E_{max} (meV)	Std. Dev.	ΔE_{max} meV/W	BB_{Pow}	Std. Dev.	ΔP_{BB} a.u./W
293	0	278.67	0.458	6.47 ± 0.388	262.02	5.37	1.35 ± 0.665
	661	283.11	0.277		262.87	4.98	
	1068	285.34	0.479		263.39	4.69	
	1460	288.06	0.277		263.93	4.53	
	1831	290.62	0.479		264.53	4.16	
303	0	281.56	0.892	7.79 ± 0.612	316.66	4.62	2.17 ± 0.489
	661	286.46	0.553		317.85	4.59	
	1068	290.30	0.732		318.57	4.42	
	1460	292.85	0.277		319.40	4.23	
	1831	295.73	0.277		320.79	3.98	
313	0	287.34	1.15	7.38 ± 0.688	383.69	4.55	2.41 ± 0.341
	661	291.89	0.732		385.10	4.70	
	1068	295.73	0.553		386.06	4.61	
	1460	298.12	0.277		387.03	4.22	
	1831	300.68	0.000		388.15	4.07	

P_{abs} (mW)	ΔE_{max} (μeV/K)	$\Delta E_{max,avg}$ (μeV/K)	Stef-Boltz Emissivity (au)	T_0 (K)	T_{HS} (K)	ΔP_{BB} (au/K)
0			0.962 ± 0.007	226	293	5.66
661	439.40 ± 49.9	491 ± 22.7	0.967 ± 0.005	226	303	6.25
1068	519.24 ± 49.9		0.970 ± 0.004	226	313	6.89
1460	503.26 ± 0.00		0.974 ± 0.004	226		
1831	503.26 ± 24.0		0.978 ± 0.005	226		

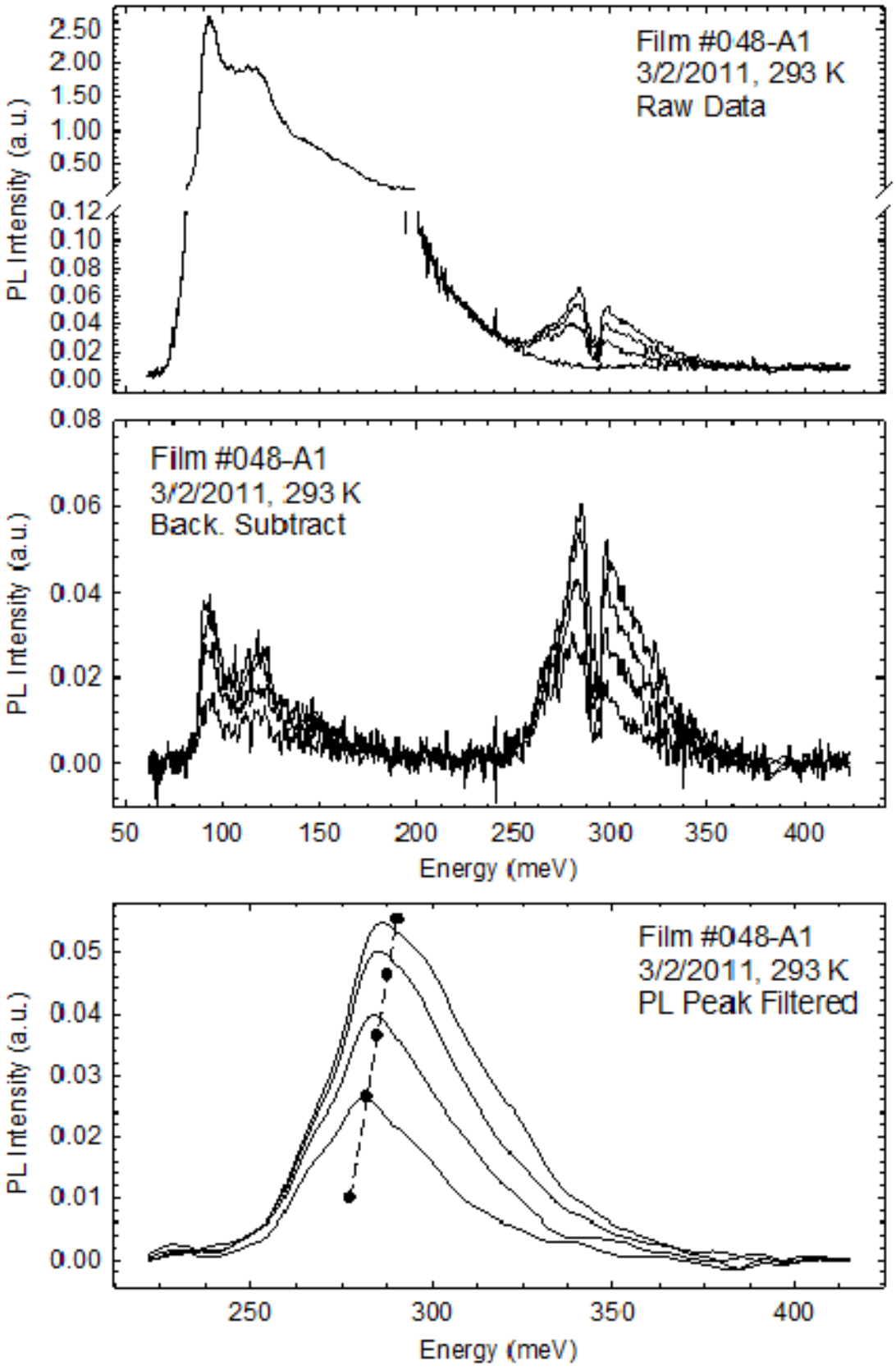
Film #048-A1
3/2/2011, 293 K
Raw Data
PL Intensity (a.u.)
2.50
2.00
1.50
1.00
0.50
0.12
0.10
0.08
0.06
0.04
0.02
0.00
Film #048-A1
3/2/2011, 293 K
Back. Subtract
PL Intensity (a.u.)
0.08
0.06
0.04
0.02
0.00
50
100
150
200
250
300
350
400
Energy (meV)
Film #048-A1
3/2/2011, 293 K
PL Peak Filtered
PL Intensity (a.u.)
0.05
0.04
0.03
0.02
0.01
0.00
250
300
350
400
Energy (meV)

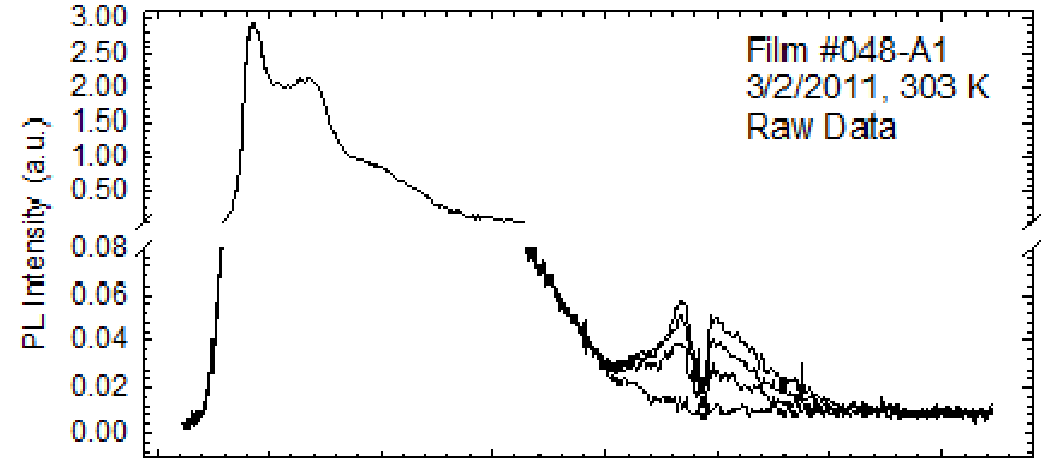
Film #048-A1
3/2/2011, 303 K
Raw Data
PL Intensity (a.u.)
3.00
2.50
2.00
1.50
1.00
0.50
0.08
0.06
0.04
0.02
0.00

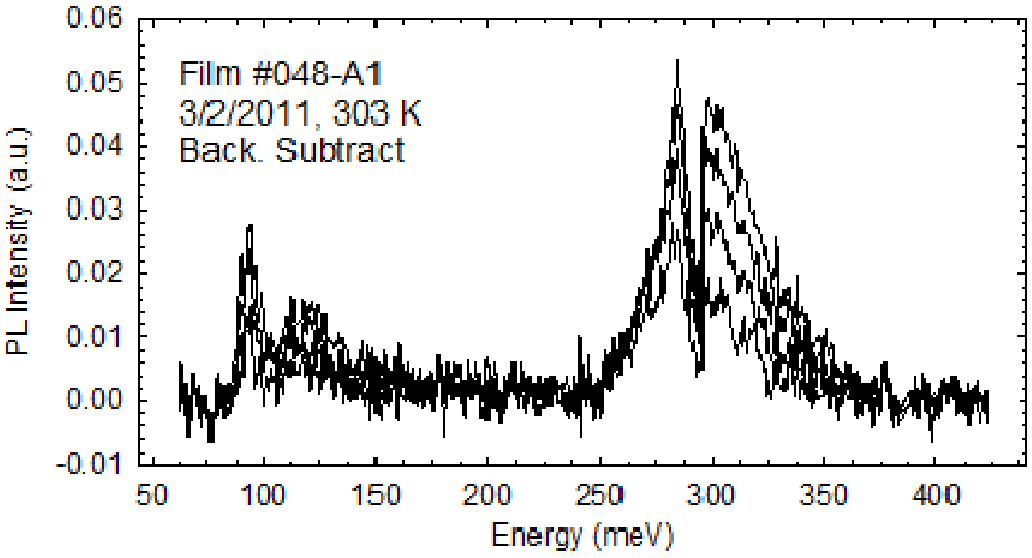
Film #048-A1
3/2/2011, 303 K
Back. Subtract
PL Intensity (a.u.)
0.06
0.05
0.04
0.03
0.02
0.01
0.00
-0.01
50
100
150
200
250
300
350
400
Energy (meV)

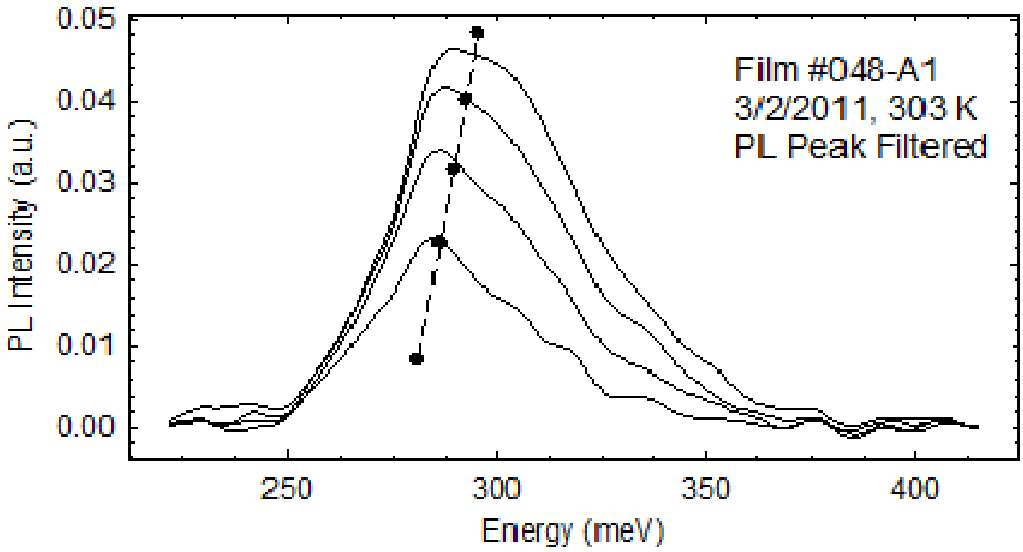
Film #048-A1
3/2/2011, 303 K
PL Peak Filtered
PL Intensity (a.u.)
0.05
0.04
0.03
0.02
0.01
0.00
250
300
350
400
Energy (meV)

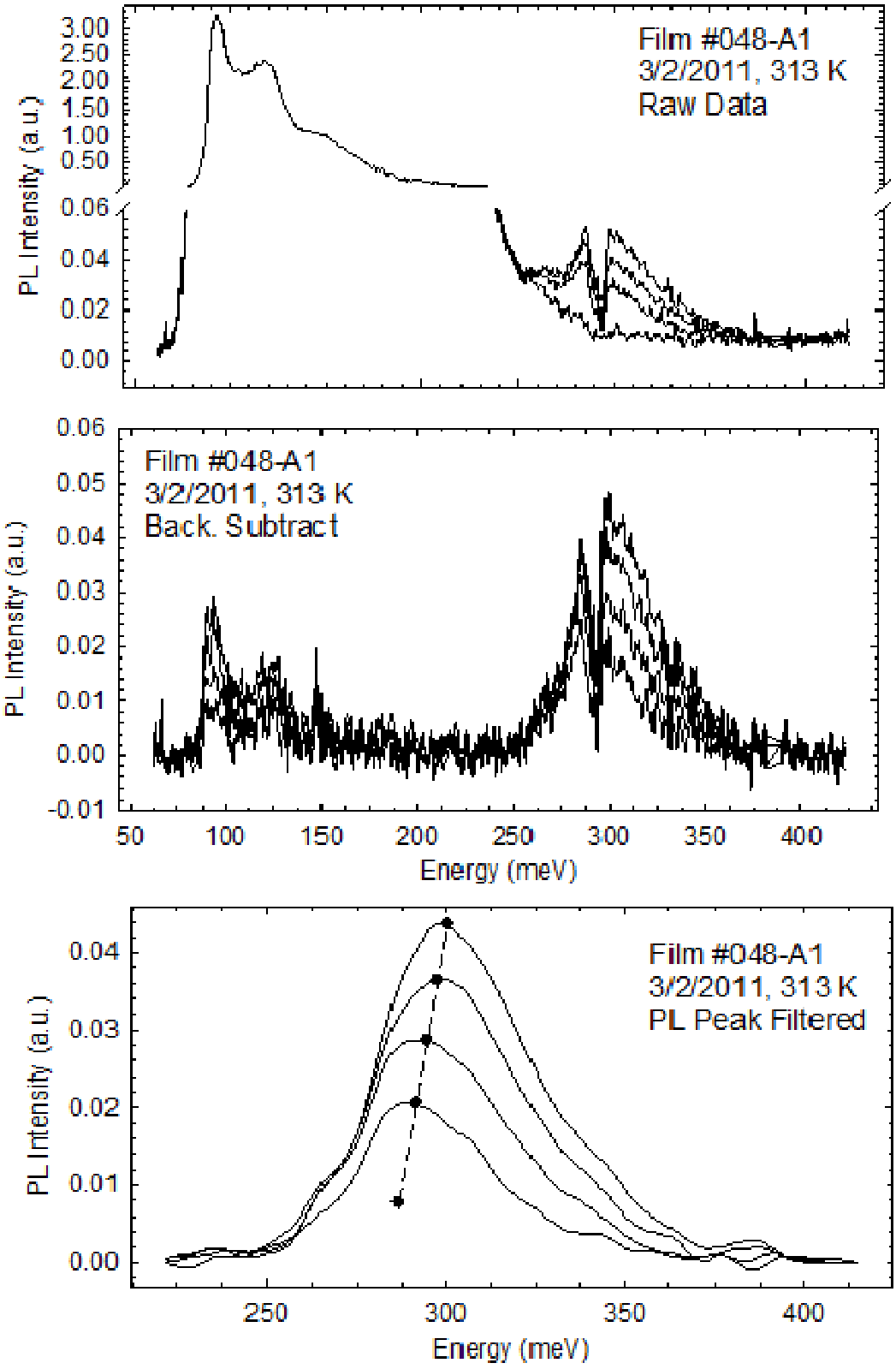
Film #048-A1
3/2/2011, 313 K
Raw Data
PL Intensity (a.u.)
3.00
2.50
2.00
1.50
1.00
0.50
0.06
0.04
0.02
0.00
Film #048-A1
3/2/2011, 313 K
Back. Subtract
PL Intensity (a.u.)
0.06
0.05
0.04
0.03
0.02
0.01
0.00
-0.01
50
100
150
200
250
300
350
400
Energy (meV)
Film #048-A1
3/2/2011, 313 K
PL Peak Filtered
PL Intensity (a.u.)
0.04
0.03
0.02
0.01
0.00
250
300
350
400
Energy (meV)

Sample #M049-PL1: Bulk PbSe

Test Date	2/24/11	Laser	#06JUN16		Results
FTIR System	#2	$I_{reflect}$	2.0 A		PL Peak
Range	500-3500 cm^{-1}	$P_{reflect}$	465 mW		13.7 ± 0.42 K/Watt
Co-adds/Gain/Res.	100 / 8 / 8 cm^{-1}	P_{Inc}	1123 mW		
Detector Type	PC	Absorb	58.8 %		
Detector Current	35 mA	Test (A)	P_{Inc}	P_{abs}	
Preamp Gain/Filter	10/300 kHz/AC	2.0	1123	661	BB Power
Power Meter	New. 1916-C	3.0	1814	1068	0.513 ± 0.02 K/Watt
Sample TEC	SRS LDC 501	4.0	2480	1460	
Sample Mount	InGa/Cu/InGa	5.0	3110	1831	
Repeat	3	BB Range	800 – 1609 cm-1		
PL Analysis	Exp. Gauss	PL Range	1800 – 3333 cm-1		

T_{HS} (K)	P_{abs} (mW)	E_{max} (meV)	Std. Dev. (meV)	ΔE_{max} (meV/W)	BB_{Pow} (a.u.)	Std. Dev. (a.u.)	ΔP_{BB} (a.u./W)
293	0	279.95	1.07	5.25 ± 0.582	268.85	4.01	2.56 ± 0.488
	661	283.34	0.730		270.38	3.89	
	1068	285.58	0.729		271.56	3.71	
	1460	287.82	0.003		272.46	3.47	
	1831	289.42	0.277		273.55	3.13	
303	0	283.78	0.958	5.57 ± 0.807	326.44	3.39	3.23 ± 0.248
	661	287.50	0.730		328.39	3.48	
	1068	289.58	0.554		329.80	3.21	
	1460	292.13	0.003		330.94	3.18	
	1831	293.89	0.554		332.39	2.97	
313	0	286.01	0.368	7.02 ± 0.327	396.77	3.40	4.18 ± 0.227
	661	290.37	0.277		399.49	3.44	
	1068	293.89	0.277		400.98	3.17	
	1460	296.29	0.280		402.62	3.02	
	1831	298.69	0.277		404.56	3.09	

P_{abs} (mW)	ΔE_{max} (μeV/K)	$\Delta E_{max,avg}$ (μeV/K)	Stef-Boltz Emissivity (au)	T_0 (K)	T_{HS} (K)	ΔP_{BB} (au/K)
0	--	--	0.972 ± 0.003	222.9	293	5.16
658	362.79 ± 12.06	409 ± 9.00	0.979 ± 0.002	222.9	303	5.72
1063	399.55 ± 15.42		0.981 ± 0.003	222.7	313	6.33
1453	421.93 ± 16.61		0.984 ± 0.004	222.6	--	--
1822	452.29 ± 19.97		0.990 ± 0.003	222.8	--	--

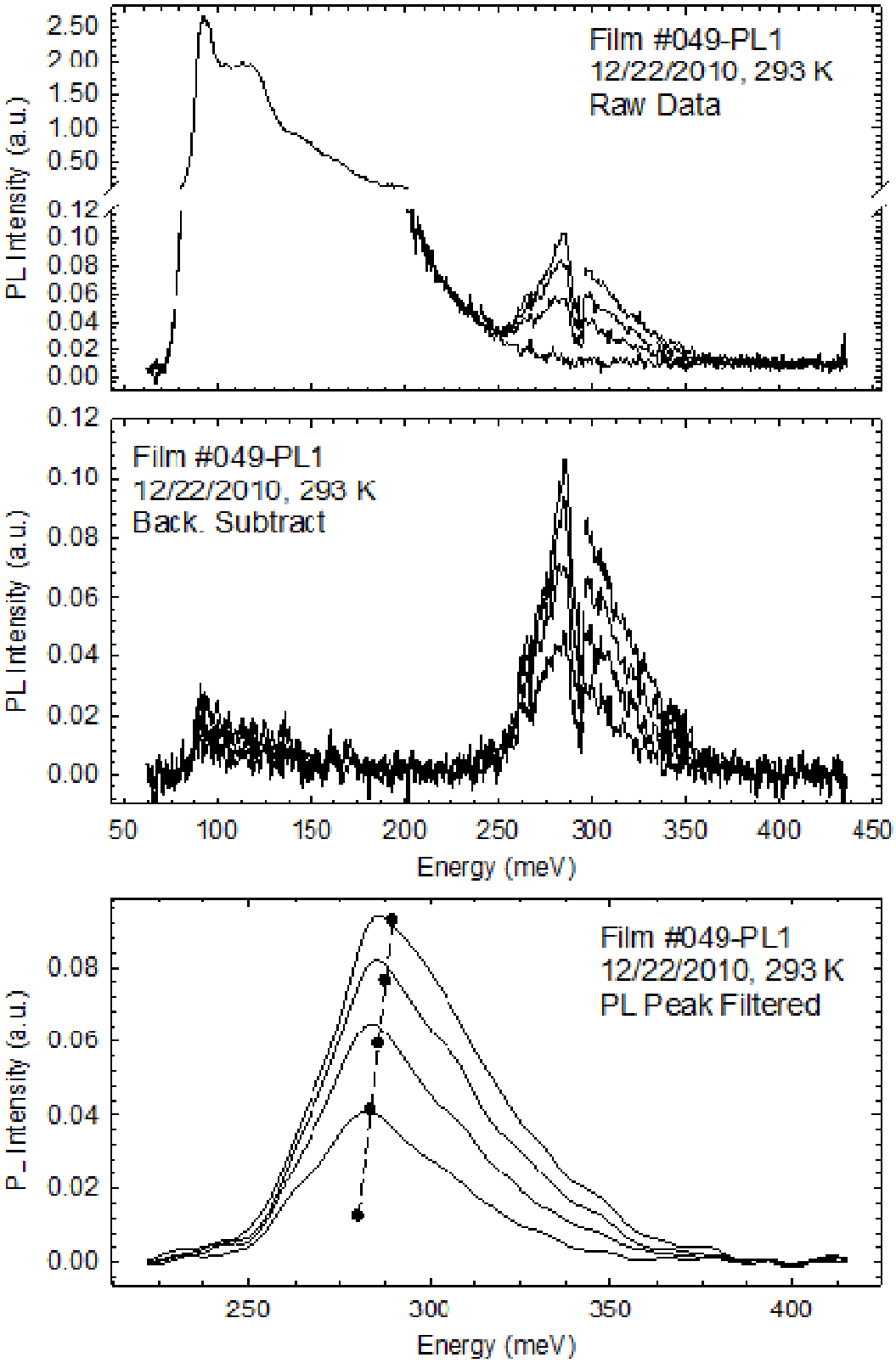
Film #049-PL1
12/22/2010, 293 K
Raw Data
PL Intensity (a.u.)
2.50
2.00
1.50
1.00
0.50
0.12
0.10
0.08
0.06
0.04
0.02
0.00
Film #049-PL1
12/22/2010, 293 K
Back. Subtract
PL Intensity (a.u.)
0.12
0.10
0.08
0.06
0.04
0.02
0.00
50
100
150
200
250
300
350
400
450
Energy (meV)
Film #049-PL1
12/22/2010, 293 K
PL Peak Filtered
P_ Intensity (a.u.)
0.08
0.06
0.04
0.02
0.00
250
300
350
400
Energy (meV)

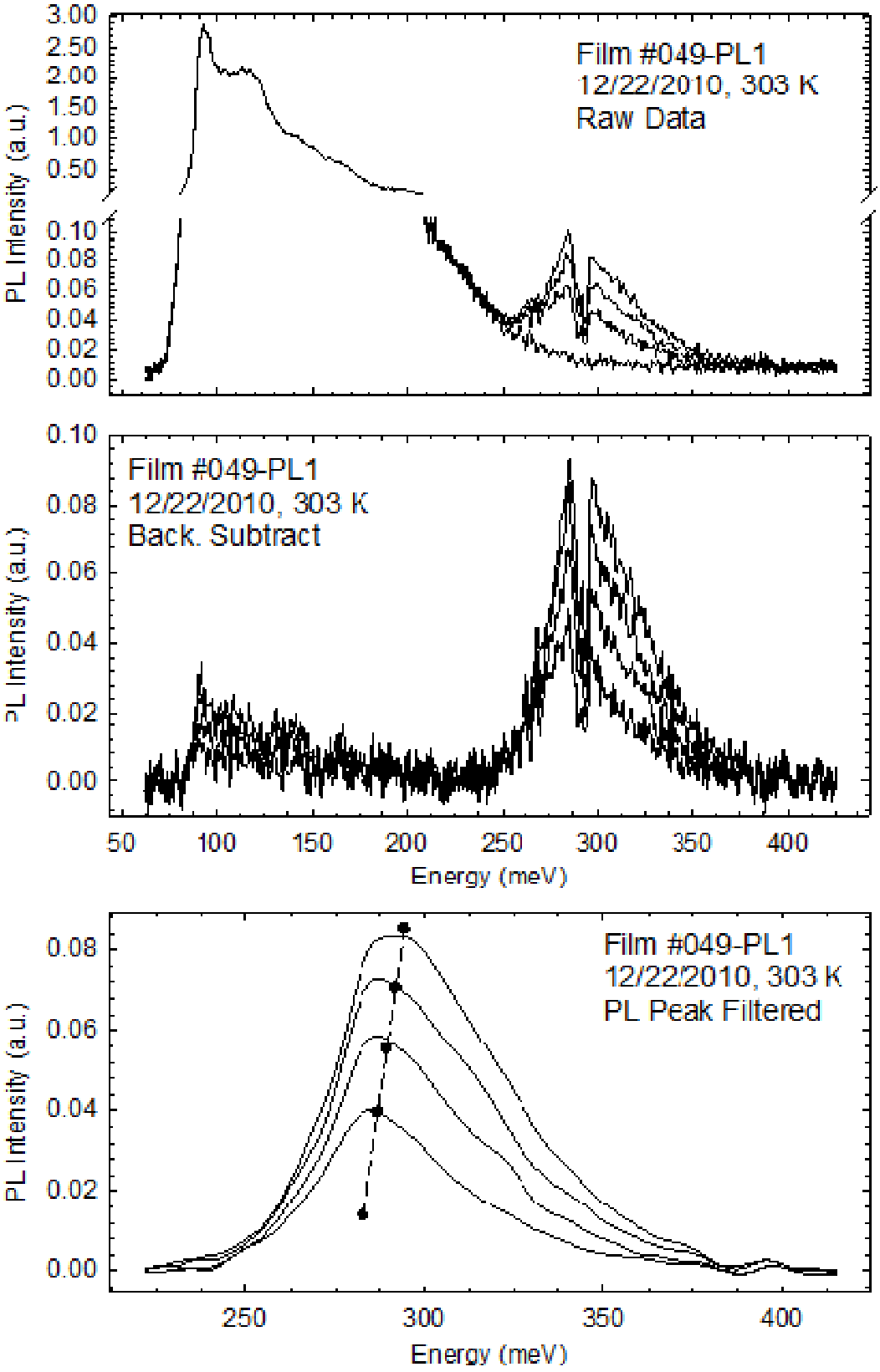
Film #049-PL1
12/22/2010, 303 K
Raw Data
PL Intensity (a.u.)
3.00
2.50
2.00
1.50
1.00
0.50
0.10
0.08
0.06
0.04
0.02
0.00
Film #049-PL1
12/22/2010, 303 K
Back. Subtract
PL Intensity (a.u.)
0.10
0.08
0.06
0.04
0.02
0.00
50
100
150
200
250
300
350
400
Energy (meV)
Film #049-PL1
12/22/2010, 303 K
PL Peak Filtered
PL Intensity (a.u.)
0.08
0.06
0.04
0.02
0.00
250
300
350
400
Energy (meV)

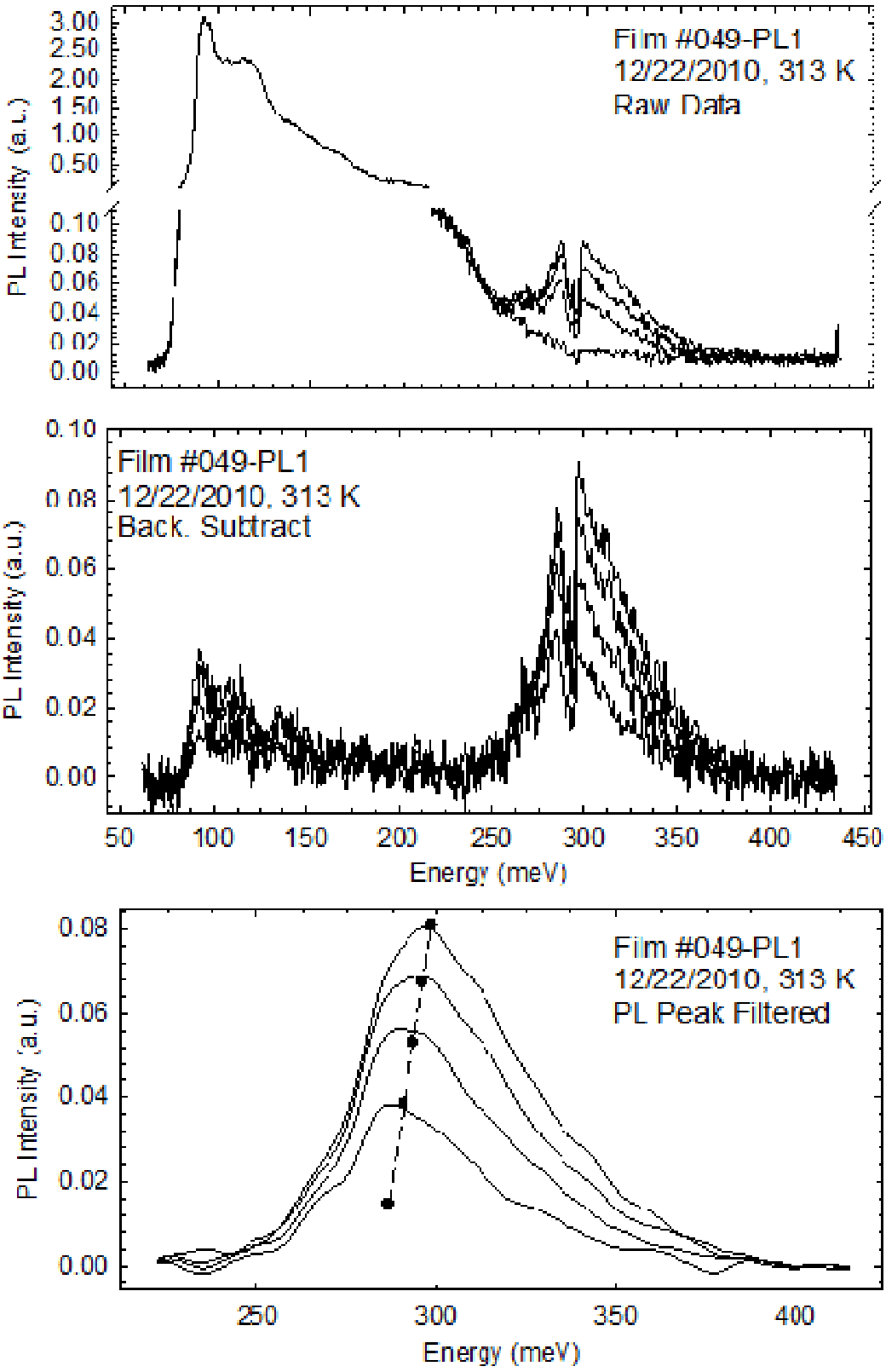
Film #049-PL1
12/22/2010, 313 K
Raw Data
PL Intensity (a.u.)
3.00
2.50
2.00
1.50
1.00
0.50
0.10
0.08
0.06
0.04
0.02
0.00
Film #049-PL1
12/22/2010, 313 K
Back. Subtract
PL Intensity (a.u.)
0.10
0.08
0.06
0.04
0.02
0.00
50
100
150
200
250
300
350
400
450
Energy (meV)
Film #049-PL1
12/22/2010, 313 K
PL Peak Filtered
PL Intensity (a.u.)
0.08
0.06
0.04
0.02
0.00
250
300
350
400
Energy (meV)

Sample #M141-PL1

Test Date	1/4/2011	**Laser**	#06JUN16		**Results**
FTIR System	#2-TE	**$I_{reflect}$**	2.0 A		**PL Peak**
Range	500-3500 cm^{-1}	**$P_{reflect}$**	477 mW		**6.58 ± 0.54 K/Watt**
Co-adds/Gain/Res.	100 / 8 / 8 cm^{-1}	**P_{Inc}**	1123 mW		
Detector Type	PC	**Absorb**	57.5 %		
Detector Current	35 mA	**Test (A)**	**P_{Inc}**	**P_{abs}**	
Preamp Gain/Filter	10/300 kHz/AC	2.0	1123	646	**BB Power**
Power Meter	New. 1916-C	3.0	1817	1043	**0.643 ± 0.04 K/Watt**
Sample TEC	SRS LDC 501	4.0	2480	1427	
Sample Mount	InGa/Cu/InGa	5.0	3110	1789	
Repeat	3	**BB Range**	800 – 1609 cm-1		
PL Analysis	Exp. Gauss	**PL Range**	1800 – 3500 cm-1		

T_{HS} (K)	**P_{abs} (mW)**	**E_{max} (meV)**	**Std. Dev. (meV)**	**ΔE_{max} (meV/W)**	**BB_{Pow} (a.u.)**	**Std. Dev. (a.u.)**	**ΔP_{BB} (a.u./W)**
293	0*	332.02	0.49	2.85 ± 0.29	192.56	0.54	1.71 ± 0.04
	646	333.91	0.28		193.56	0.63	
	1043	334.87	0.28		194.23	0.61	
	1427	336.15	0.00		194.90	0.61	
	1789	337.11	0.00		195.63	0.56	
303	0*	334.34	0.34	2.81 ± 0.25	215.76	0.57	2.04 ± 0.06
	646	336.15	0.00		217.00	0.66	
	1043	337.27	0.28		217.92	0.53	
	1427	338.39	0.28		218.62	0.60	
	1789	339.34	0.28		219.40	0.60	
313	0*	336.47	1.18	2.90 ± 0.66	242.06	0.78	2.23 ± 0.02
	646	338.23	1.00		243.50	0.72	
	1043	339.66	0.28		244.32	0.68	
	1427	340.62	0.28		245.17	0.83	
	1789	341.58	0.28		246.09	0.80	

P_{abs} (mW)	**ΔE_{max} (μeV/K)**	**$\Delta E_{max,avg}$ (μeV/K)**	**Stef-Boltz Emissivity (au)**	**T_0 (K)**	**T_{HS} (K)**	**ΔP_{BB} (au/K)**
0	266.9 ± 28.7	*238 ± 11.4	0.950 ± 0.031	165.3	293	2.668
646	252.5 ± 23.6		0.961 ± 0.029	166.2	303	2.949
1043	244.5 ± 8.31		0.953 ± 0.025	166.8	313	3.248
1427	228.5 ± 9.96		0.971 ± 0.031	167.4		
1789	228.5 ± 9.98		0.958 ± 0.020	168.0		

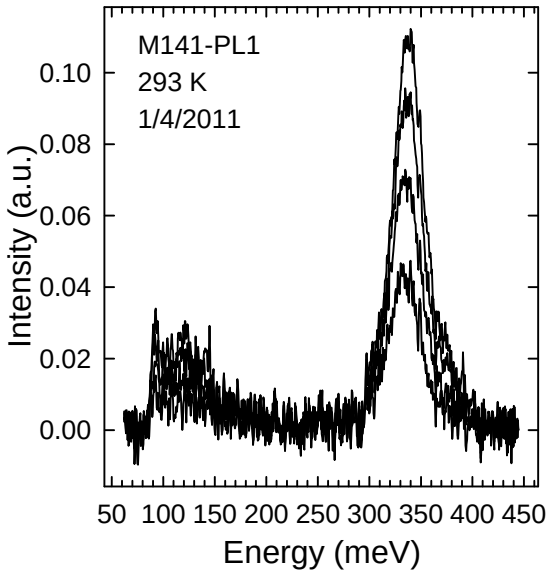
M141-PL1
293 K
1/4/2011
Intensity (a.u.)
0.10
0.08
0.06
0.04
0.02
0.00
50 100 150 200 250 300 350 400 450
Energy (meV)

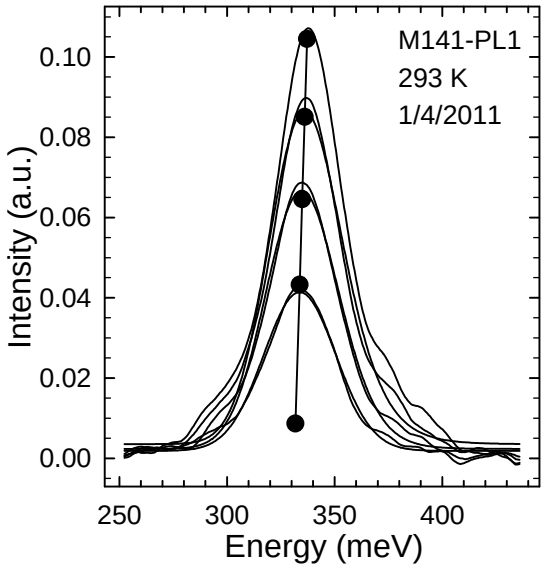
M141-PL1
293 K
1/4/2011
Intensity (a.u.)
0.10
0.08
0.06
0.04
0.02
0.00
250 300 350 400
Energy (meV)

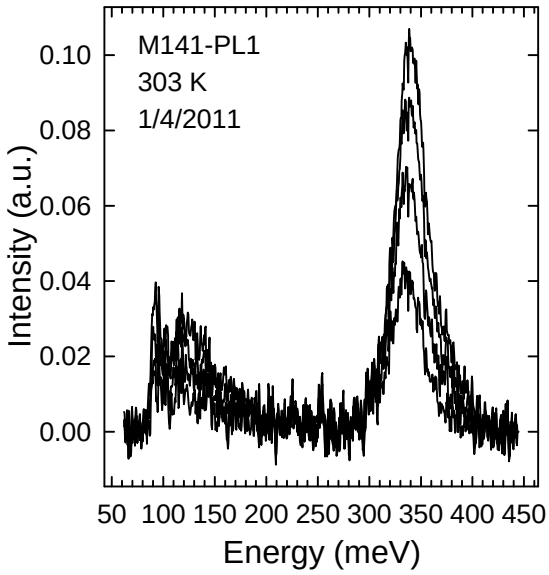
M141-PL1
303 K
1/4/2011
Intensity (a.u.)
0.10
0.08
0.06
0.04
0.02
0.00
50 100 150 200 250 300 350 400 450
Energy (meV)

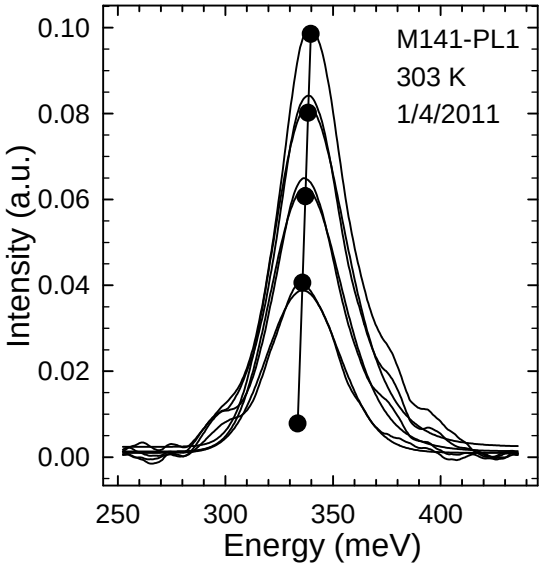
M141-PL1
303 K
1/4/2011
Intensity (a.u.)
0.10
0.08
0.06
0.04
0.02
0.00
250 300 350 400
Energy (meV)

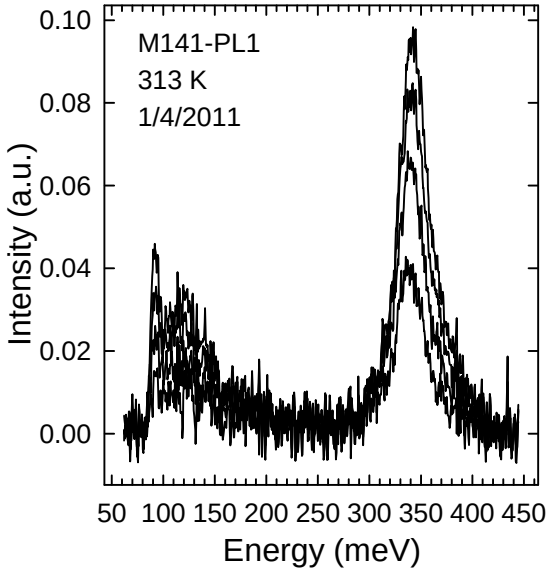
M141-PL1
313 K
1/4/2011
Intensity (a.u.)
0.10
0.08
0.06
0.04
0.02
0.00
50 100 150 200 250 300 350 400 450
Energy (meV)

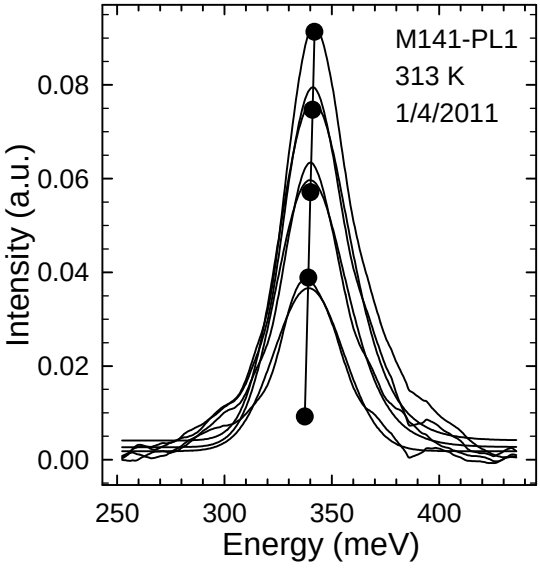
M141-PL1
313 K
1/4/2011
Intensity (a.u.)
0.08
0.06
0.04
0.02
0.00
250 300 350 400
Energy (meV)

Sample #M141-PL1

Test Date	2/11/2012	**Laser**	#06JUN16 @ ≈ 20 °C		
FTIR System	#2-LN2	**$I_{reflect}$**	3.0 A		**Windows**
Range	500-3500 cm^{-1}	**$P_{reflect}$**	613 mW		93 %
Co-adds/Gain/Res.	100 / 8 / 8 cm^{-1}	**P_{Inc}**	1814 mW		93 %
Detector Type	PC	**Absorb**	60.9 %		
Detector Current	35 mA	**Test (A)**	**P_{Inc}**	**P_{abs}**	**Results**
Preamp Gain/Filter	10/300kHz/AC	3.0	1814	1105	**PL Peak**
Power Meter	New. 1916-C	4.0	2480	1511	**5.44 ± 2.30 K/Watt**
Sample TEC	Lakeshore 330	5.0	3110	1895	
Sample Mount	InGa/Cu/InGa	6.0	3700	2254	
Repeat	3	7.0	4220	2571	
PL Analysis	Exp. Gauss	**BB Range**	N/A		
		PL Range	1400 – 3255 cm-1		

T_{HS} (K)	**P_{abs} (mW)**	**E_{max} (meV)**	**Std. Dev.**	**ΔE_{max} (meV/W)**	**HE_{PL} (K/Watt)**
260	0*	312.55	0.43	2.72 ± 0.43	6.28 ± 0.99
	1105	315.54	0.00		
	1511	316.74	0.34		
	1895	317.70	0.34		
250	0*	306.88	0.24	3.62 ± 0.01	8.36 ± 0.02
	1105	310.99	0.34		
	1511	312.18	0.00		
	1895	313.86	0.34		
240	0*	300.93	0.34	4.22 ± 0.00	9.75 ± 0.00
	1105	305.71	0.34		
	1511	307.15	0.34		
	1895	309.07	0.34		
210	0*	280.89	0.53	1.82 ± 0.86	4.20 ± 1.99
	1105	282.47	0.00		
	1511	283.43	0.00		
	1895	283.67	0.34		
200	0*	279.52	2.44	2.41 ± 0.01	5.57 ± 0.02
	1105	280.79	1.69		
	1511	281.51	0.68		
	1895	281.75	1.02		
190	0*	277.13	0.43	3.32 ± 0.42	7.67 ± 0.97
	1105	278.63	0.00		
	1511	279.83	0.34		
	1895	279.83	0.34		

T_{HS} (K)	P_{abs} (mW)	E_{max} meV	Std. Dev.	ΔE_{max} (meV/W)	HE_{PL} (K/Watt)
160	0*	270.50	0.19	1.93 ± 0.15	4.46 ± 0.35
	1511	273.36	0.00		
	1895	274.32	0.68		
	2254	274.80	0.00		
150	0*	267.23	2.70	2.26 ± 0.25	5.22 ± 0.58
	1511	270.49	0.68		
	1895	271.92	0.00		
	2254	272.16	0.34		
140	0*	265.85	1.14	0.63 ± 0.05	1.45 ± 0.12
	1511	266.89	0.34		
	1895	266.89	0.34		
	2254	267.37	1.02		
110	0*	233.79	1.19	1.76 ± 0.53	4.06 ± 1.22
	1895	237.17	0.34		
	2254	237.65	0.34		
	2571	238.37	0.00		
100	0*	230.93	0.07	1.43 ± 0.02	3.30 ± 0.05
	1895	233.58	0.00		
	2254	234.30	0.34		
	2571	234.54	0.00		
90	0*	226.23	0.00	2.14 ± 0.00	4.94 ± 0.00
	1895	230.22	0.00		
	2254	231.18	0.00		
	2571	231.66	0.00		

P_{abs} (Watts)	ΔE_{max} (μeV/K)	Std. Dev. (μeV/K)	Mean (μeV/K)	Offset (meV)	Std. Dev. (meV)
1895	433	5.15	433 ± 5.15	201.99	0.88

Sample #168-C

Test Date	1/5/2011	**Laser**	#06JUN16		**Results**
FTIR System	#2-TE	$\mathbf{I_{reflect}}$	2.0 A		**PL Peak**
Range	500-3500 cm^{-1}	$\mathbf{P_{reflect}}$	437 mW		**11.60 ± 1.20 K/Watt**
Co-adds/Gain/Res.	100 / 8 / 8 cm^{-1}	$\mathbf{P_{Inc}}$	1123 mW		
Detector Type	PC	**Absorb**	61.1 %		
Detector Current	35 mA	**Test (A)**	$\mathbf{P_{Inc}}$	$\mathbf{P_{abs}}$	
Preamp Gain/Filter	10/300kHz/AC	3.0	1814	1108	**BB Power**
Power Meter	New. 1916-C	4.0	2480	1515	**0.438 ± 0.002 K/Watt**
Sample Temp.	SRS LDC 501	5.0	3110	1900	
Sample Mount	InGa/Cu/InGa				
Repeat	3	**BB Range**	800 – 1609 cm-1		
PL Analysis	Exp. Gauss	**PL Range**	1800 – 3500 cm-1		

$\mathbf{T_{HS}}$ (K)	$\mathbf{P_{abs}}$ (mW)	$\mathbf{E_{max}}$ (meV)	Std. Dev. (meV)	$\mathbf{\Delta E_{max}}$ meV/W	$\mathbf{BB_{Pow}}$ (a.u.)	Std. Dev. (a.u.)	$\mathbf{\Delta P_{BB}}$ (a.u./W)
293	0*	328.44	0.73	5.65 ± 0.35	167.88	0.48	1.20 ± 0.12
	1108	334.73	0.48		169.12	0.77	
	1515	336.96	0.25		169.56	0.70	
	1900	339.20	0.27		169.96	0.60	
303	0*	332.39	1.41	4.44 ± 0.94	186.03	0.46	1.42 ± 0.05
	1108	337.28	0.57		187.27	0.40	
	1515	339.20	0.53		187.80	0.33	
	1900	340.80	0.25		188.34	0.21	
313	0*	334.79	1.33	4.83 ± 1.05	206.36	0.20	1.66 ± 0.01
	1108	340.32	0.29		207.88	0.14	
	1515	341.76	0.54		208.46	0.17	
	1900	344.15	0.71		209.07	0.14	

$\mathbf{P_{abs}}$ (mW)	$\mathbf{\Delta E_{max}}$ (μeV/K)	$\mathbf{\Delta E_{max,avg}}$ (μeV/K)	Stef-Boltz Emissivity (au)	$\mathbf{T_0}$ (K)	$\mathbf{T_{HS}}$ (K)	$\mathbf{\Delta P_{BB}}$ (au/K)
0	285.68 ± 41.6	*258 ± 12	2.29 ± 0.01	167.9	293	2.30
1108	270.02 ± 14.6		2.30 ± 0.01	169.1	303	2.31
1515	247.65 ± 7.32		2.31 ± 0.01	169.6	313	2.32
1900	255.64 ± 32.6		2.32 ± 0.01	170.0		

Sample #168-C

Test Date	2/12/2012	**Laser**	#06JUN16 @ ≈ 20 °C		
FTIR System	#2-LN2	$I_{reflect}$	3.0 A		**Windows**
Range	500-3500 cm^{-1}	$P_{reflect}$	555 mW		93 %
Co-adds/Gain/Res.	100 / 8 / 8 cm^{-1}	P_{Inc}	1814 mW		93 %
Detector Type	PC	**Absorb**	69.4 %		
Detector Current	35 mA	**Test (A)**	P_{Inc}	P_{abs}	**Results**
Preamp Gain/Filter	10/300kHz/AC	3.0	1814	1259	**PL Peak**
Power Meter	New. 1916-C	4.0	2480	1721	**6.57 ± 1.31 K/Watt**
Sample TEC	Lakeshore 330	5.0	3110	2158	
Sample Mount	InGa/Cu/InGa	6.0	3700	2568	
Repeat	3	**BB Range**	N/A		
PL Analysis	Exp. Gauss	**PL Range**	1400 cm^{-1} to 3255 cm^{-1}		

T_{HS} (K)	P_{abs} (mW)	E_{max} (meV)	Std. Dev.	ΔE_{max} (meV/W)	HE_{PL} (K/Watt)
260	0*	312.48	1.58	3.41 ± 0.81	7.93 ± 1.88
	1721	318.21	0.29		
	2158	320.13	0.39		
	2568	321.09	0.39		
250	0*	309.56	0.78	2.84 ± 0.02	6.60 ± 0.05
	1721	314.38	0.97		
	2158	315.81	0.29		
	2568	316.77	0.97		
240	0*	303.23	1.67	3.96 ± 0.80	9.21 ± 1.86
	1721	310.06	0.29		
	2158	311.74	0.05		
	2568	313.42	0.39		
210	0*	294.07	0.63	2.67 ± 0.01	6.21 ± 0.02
	1259	297.36	0.63		
	1721	298.80	0.63		
	2158	299.76	0.63		
200	0*	290.17	0.81	2.94 ± 0.38	6.84 ± 0.79
	1259	293.76	0.39		
	1721	295.44	0.05		
	2158	296.40	0.05		

T_{HS} (K)	P_{abs} (mW)	E_{max} meV	Std. Dev.	ΔE_{max} (meV/W)	HE_{PL} (K/Watt)
160	0*	271.46	0.06	2.66 ± 0.01	6.19 ± 0.02
	1259	274.83	0.04		
	1721	276.03	0.30		
	2158	277.23	0.04		
150	0*	267.39	0.06	2.89 ± 0.31	6.72 ± 0.72
	1259	270.99	0.04		
	1721	272.43	0.04		
	2158	273.36	0.00		
140	0*	262.88	0.30	3.20 ± 0.00	7.44 ± 0.00
	1259	266.92	0.30		
	1721	268.36	0.30		
	2158	269.80	0.30		
110	0*	250.83	0.70	1.98 ± 0.40	4.60 ± 0.93
	1721	254.22	0.04		
	2158	255.17	0.04		
	2568	255.89	0.38		
100	0*	246.78	0.21	2.26 ± 0.01	5.26 ± 0.02
	1721	250.62	0.30		
	2158	251.82	0.04		
	2568	252.54	0.30		
90	0*	243.60	0.04	2.26 ± 0.00	5.26 ± 0.00
	1721	247.51	0.04		
	2158	248.46	0.04		
	2568	249.42	0.04		

P_{abs} (Watts)	ΔE_{max} (μeV/K)	Std. Dev. (μeV/K)	Mean (μeV)	Offset (meV)	Std. Dev. (meV)
1259	443.0	1.60	430 ± 8.60	204.46	0.22
1721	423.5	2.88		208.70	0.25
2158	427.1	0.20		209.33	3.04
2568	428.3	0.57		209.79	0.09

Sample #211-R

Test Date	2/13/2012	**Laser**	#06JUN16		
FTIR System	#2-LN2	**$I_{reflect}$**	3.0 A		Window
Range	500-3500 cm^{-1}	**$P_{reflect}$**	533 mW		93 %
Co-adds/Gain/Res.	100 / 8 / 8 cm^{-1}	**P_{Inc}**	1814 mW		93 %
Detector Type	PC	**Absorb**	66.0 %		
Detector Current	35 mA	**Test (A)**	**P_{Inc}**	**P_{abs}**	**Results**
Preamp Gain/Filter	10/300kHz/AC	3.0	1814	1175	**PL Peak**
Power Meter	New. 1916-C	4.0	2480	1606	**15.20 ± 3.16 K/Watt**
Sample TEC	Lakeshore 330	5.0	3110	2014	
Sample Mount	InGa/Cu/InGa	6.0	3700	2396	
Repeat	1 and 2	7.0	4220	2733	
		BB Range	N/A		
PL Analysis	Exp. Gauss	**PL Range**			

T_{HS} (K)	**P_{abs} (mW)**	**E_{max} (meV)**	**Std. Dev. (meV)**	**ΔE_{max} (meV/W)**	**HE_{PL} (K/Watt)**
260	0*	319.97	1.90	3.33 ± 0.02	8.22 ± 0.05
	2014	328.00	0.00		
	2396	329.68	0.34		
	2733	330.88	0.68		
250	0*	318.68	0.37	3.34 ± 0.00	8.25 ± 0.00
	2014	325.36	0.34		
	2396	326.80	0.34		
	2733	327.76	0.34		
240	0*	315.04	0.07	4.00 ± 0.94	9.88 ± 2.32
	2014	321.77	0.00		
	2396	322.97	0.34		
	2733	324.17	0.00		
210	0*	300.97	--	4.00	9.88
	1175	305.51	0.05		
	1606	307.53	--		
	2014	308.97	--		
200	0*	299.44	1.24	2.85 ± 0.81	7.04 ± 2.00
	1175	302.87	0.39		
	1606	303.83	0.29		
	2014	305.27	0.29		
190	0*	296.28	--	2.84	7.01
	1175	299.86	--		
	1606	300.34	--		
	2014	302.25	--		

T_{HS} (K)	P_{abs} (mW)	E_{max} (meV)	Std. Dev.	ΔE_{max} (meV/W)	HE_{PL} (K/Watt)
160	0*	275.54	--	3.08	7.60
	1175	283.43	--		
	1606	285.34	--		
	2014	286.78	--		
150	0*	277.59	--	2.85	7.04
	1175	281.03	--		
	1606	281.99	--		
	2014	283.43	--		
140	0*	275.54	--	2.22	5.48
	1175	278.15	--		
	1606	279.11	--		
	2014	--	--		
110	0*	261.80	--	3.93	9.70
	1198	265.69	--		
	1637	267.61	--		
	2053	268.57	--		
100	0*	255.66	--	4.49	11.09
	1198	260.90	--		
	1637	263.30	--		
	2053	264.73	--		
90	0*	252.91	--	3.37	8.32
	1198	257.54	--		
	1637	259.46	--		
	2053	260.90	--		

P_{abs} (Watts)	ΔE_{max} (μeV/K)	Std. Dev. (μeV/K)	Mean (μeV/K)	Offset (meV)	Std. Dev. (meV)
0			404.9 ± 3.0		
1175	408.3	4.17		220.34	0.58
1606	403.6	2.48		222.82	0.03
2014	402.7	0.91		224.28	0.33

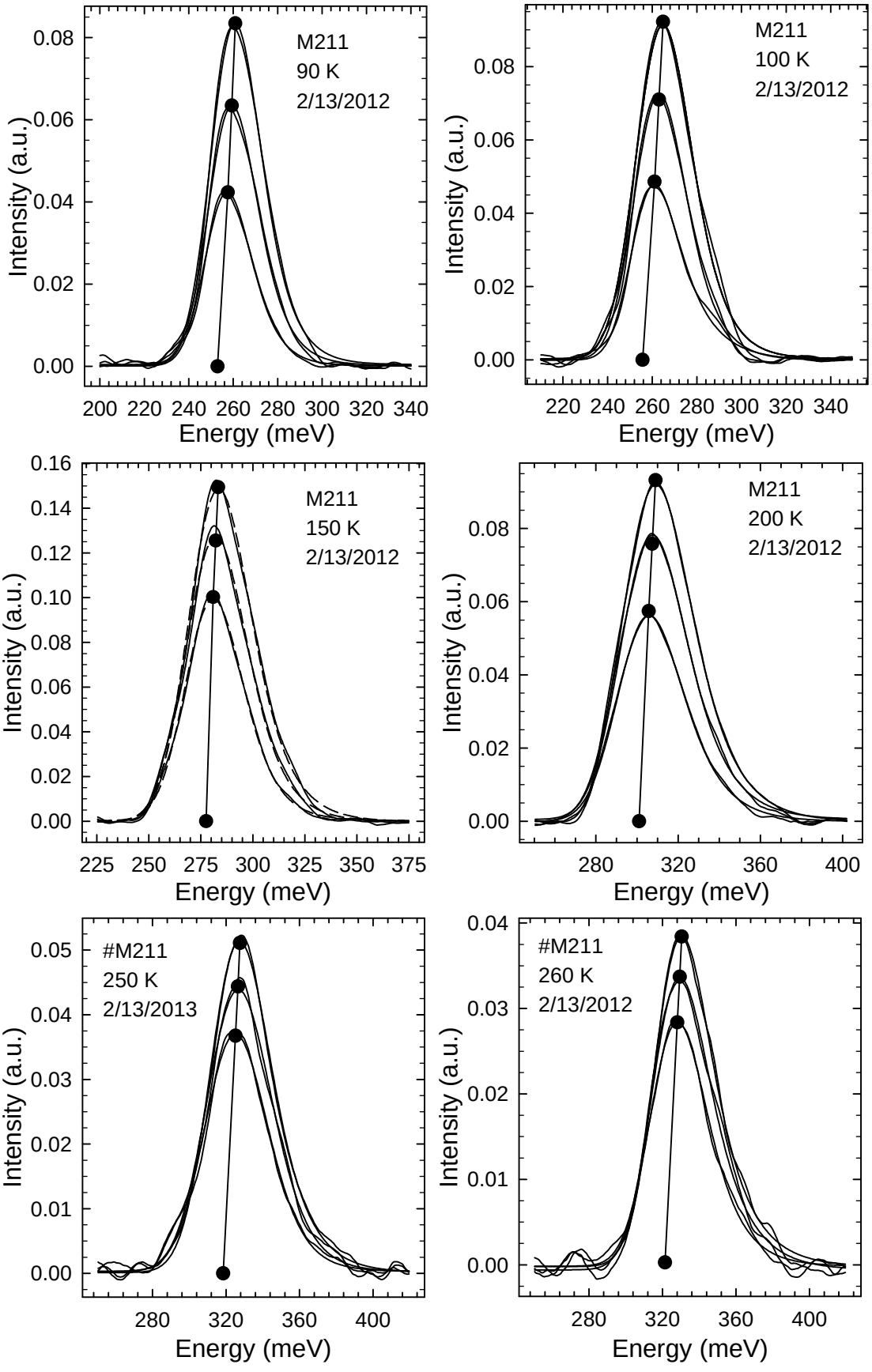
M211
90 K
2/13/2012
Intensity (a.u.)
Energy (meV)
M211
100 K
2/13/2012
M211
150 K
2/13/2012
M211
200 K
2/13/2012
#M211
250 K
2/13/2013
#M211
260 K
2/13/2012

Sample #212-R

Test Date	2/16/2012	**Laser**	#06JUN16 @ ≈ 20 °C		
FTIR System	#1-LN2	**$I_{reflect}$**	3.0 A		**Window**
Range	500-3500 cm^{-1}	**$P_{reflect}$**	533 mW		93 %
Co-adds/Gain/Res.	100 / 8 / 8 cm^{-1}	**P_{Inc}**	1814 mW		93 %
Detector Type	PC	**Absorb**	68.8 %		
Detector Current	35 mA	**Test (A)**	**P_{Inc}**	**P_{abs}**	**Results**
Preamp Gain/Filter	10/300 kHz/AC	4.0	2480	1606	**PL Peak**
Power Meter	New. 1916-C	5.0	3110	2014	**13.53 ± 1.20 K/Watt**
Sample Temp.	Lakeshore 330	6.0	3700	2396	
Sample Mount	InGa/Cu/InGa				
Repeat	2X	**BB Range**	N/A		
PL Analysis	Exp. Gauss	**PL Range**	1400 cm^{-1} to 3255 cm^{-1}		

T_{HS} (K)	**P_{abs} (mW)**	**E_{max} (meV)**	**Std. Dev. (meV)**	**ΔE_{max} (meV/W)**	**HE_{PL} (K/Watt)**
260	0	315.69	2.56	4.87 ± 2.6	11.12 ± 5.94
	1606	323.5	1.61		
	2014	328.6	--		
	2396	327.9	1.6		
250	0	309.70	0.119	7.00 ± 0.45	15.98 ± 1.03
	1606	320.94	0.607		
	2014	323.80	0.792		
	2396	326.47	0.965		
240	0	307.53	0.402	6.37 ± 0.42	14.54 ± 0.96
	1606	317.76	0.279		
	2014	320.35	0.452		
	2396	322.79	0.615		
210	0	296.20	1.63	6.08 ± 0.87	13.88 ± 1.98
	1606	305.96	0.237		
	2014	308.44	0.117		
	2396	310.77	0.449		
200	0	292.05	2.06	6.08 ± 0.00	13.88 ± 0.00
	1606	301.81	0.685		
	2014	304.29	0.335		
	2396	306.61	0.007		
190	0	287.95	1.08	5.47 ± 0.00	12.49 ± 0.00
	1606	297.22	0.399		
	2014	299.57	0.225		
	2396	301.77	0.063		

T_{HS} (K)	P_{abs} (mW)	E_{max} (meV)	Std. Dev.	ΔE_{max} (meV/W)	HE_{PL} (K/Watt)
160	0*	272.15	0.24	5.47 ± 0.00	12.49 ± 0.00
	1606	281.91	0.22		
	2014	284.39	0.22		
	2396	286.71	0.22		
150	0*	268.08	0.09	5.77 ± 0.43	13.17 ± 0.98
	1606	277.83	0.1		
	2014	280.31	0.11		
	2396	282.63	0.11		
140	0*	264.52	0.99	6.07 ± 0.01	13.86 ± 0.02
	1606	273.80	0.29		
	2014	276.15	0.11		
	2396	278.36	0.05		
110	0*	251.31	0.01	6.07 ± 0.01	13.86 ± 0.02
	1606	260.09	0.01		
	2014	262.32	0.01		
	2396	264.41	0.01		
100	0*	247.72	0.34	5.77 ± 0.42	13.17 ± 0.96
	1606	256.50	0.34		
	2014	258.73	0.34		
	2396	260.82	0.34		
90	0	242.73	0.01	6.07 ± 0.86	13.86 ± 1.96
	1606	252.49	0.01		
	2014	254.98	0.01		
	2396	257.30	0.01		

P_{abs} (Watts)	ΔE_{max} (μeV/K)	Std. Dev. (μeV/K)	Mean (μeV/K)	Offset (meV)	Std. Dev. (meV)
0	429.31	8.95	438 ± 1.8	203.42	0.81
1606	432.23	3.68		212.97	0.64
2014	440.40	1.38		214.34	0.01
2396	441.30	0.32		216.61	0.01

Sample #213-R

Test Date	2/17/2012	**Laser**	#06JUN16 @ ≈ 20°C		
FTIR System	#1-LN2	**$I_{reflect}$**	3.0 A		**Window**
Range	500-3500 cm^{-1}	**$P_{reflect}$**	565 mW		93 %
Co-adds/Gain/Res.	100 / 8 / 8 cm^{-1}	**P_{Inc}**	1814 mW		93 %
Detector Type	PC	**Absorb**	63.7 %		
Detector Current	35 mA	**Test (A)**	**P_{Inc}**	**P_{abs}**	**Results**
Preamp Gain/Filter	10/300 kHz/AC	4.0	2480	1579	**PL Peak**
Power Meter	New. 1916-C	5.0	3110	1980	**15.20 ± 3.16 K/Watt**
Sample TEC	Lakeshore 330	6.0	3700	2356	
Sample Mount	InGa/Cu/InGa				
Repeat	3	**BB Range**	N/A		
PL Analysis	Exp. Gauss	**PL Range**	1400 cm^{-1} to 3255 cm^{-1}		

T_{HS} (K)	**P_{abs} (mW)**	**E_{max} (meV)**	**Std. Dev.**	**ΔE_{max} (meV/W)**	**HE_{PL} (K/Watt)**
260	0*	297.22	4.55	7.69 ± 1.73	18.18 ± 4.09
	1579	309.51	1.69		
	1980	312.15	1.35		
	2356	315.50	0.34		
250	0*	290.16	5.58	9.25 ± 2.20	21.87 ± 5.20
	1579	304.73	2.37		
	1980	308.56	0.68		
	2356	311.91	0.38		
240	0*	291.49	5.46	6.61 ± 2.40	15.63 ± 5.67
	1579	302.09	1.69		
	1980	304.25	0.68		
	2356	307.24	0.17		
210	0*	276.95	1.75	8.02 ± 0.89	18.96 ± 2.10
	1579	289.53	0.51		
	1980	293.00	0.34		
	2356	295.75	0.17		
200	0*	273.35	0.61	7.23 ± 0.22	17.09 ± 0.52
	1579	284.86	0.34		
	1980	287.49	0.00		
	2356	290.48	0.17		
190	0*	272.09	0.08	5.85 ± 0.01	13.83 ± 0.02
	1579	281.39	0.17		
	1980	283.54	0.17		
	2356	285.93	0.17		

T_{HS} (K)	P_{abs} (mW)	E_{max} meV	Std. Dev.	ΔE_{max} (meV/W)	HE_{PL} (K/Watt)
160	0*	259.62	0.66	5.40 ± 0.22	12.77 ± 0.52
	1579	268.10	0.34		
	1980	270.37	0.17		
	2356	272.29	0.17		
150	0*	255.68	0.17	5.55 ± 0.00	13.12 ± 0.00
	1579	264.39	0.17		
	1980	266.78	0.17		
	2356	268.70	0.17		
140	0*	251.05	0.22	5.85 ± 0.01	13.83 ± 0.02
	1579	260.32	0.17		
	1980	262.59	0.34		
	2356	264.87	0.17		
110	0*	238.06	0.00	5.24 ± 0.00	12.39 ± 0.00
	1579	246.32	0.00		
	1980	248.47	0.00		
	2356	250.39	0.00		
100	0*	235.31	0.12	4.93 ± 0.01	11.65 ± 0.02
	1579	243.08	0.17		
	1980	245.12	0.00		
	2356	246.92	0.17		
90	0*	230.66	0.00	5.55 ± 0.00	13.12 ± 0.00
	1579	239.37	0.00		
	1980	241.77	0.00		
	2356	243.68	0.00		

P_{abs} (Watts)	ΔE_{max} (μeV/K)	Std. Dev. (μeV/K)	Mean (μeV/K)	Offset (meV)	Std. Dev. (meV)
0	385.63	13.0	423 ± 1.9	196.67	1.62
1579	416.04	5.28		201.51	0.71
1980	421.41	0.38		203.14	0.03
2356	430.88	0.82		203.98	0.18

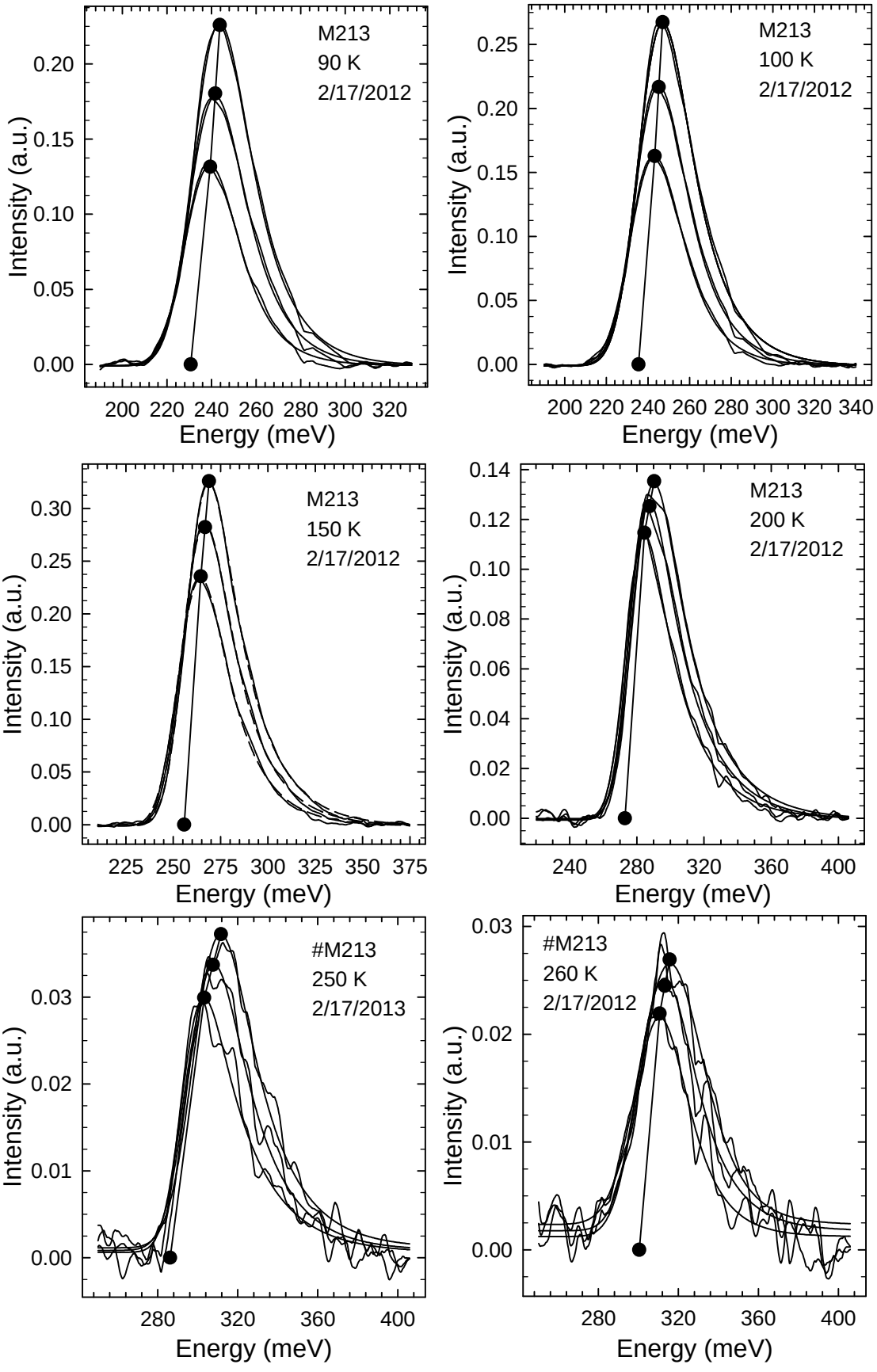
M213
90 K
2/17/2012
Intensity (a.u.)
Energy (meV)
M213
100 K
2/17/2012
Intensity (a.u.)
Energy (meV)
M213
150 K
2/17/2012
Intensity (a.u.)
Energy (meV)
M213
200 K
2/17/2012
Intensity (a.u.)
Energy (meV)
#M213
250 K
2/17/2013
Intensity (a.u.)
Energy (meV)
#M213
260 K
2/17/2012
Intensity (a.u.)
Energy (meV)

Sample #M214 - R

Test Date	2/14/12	**Laser**	#06JUN16 @ ≈ 20 °C		
FTIR System	#1-LN2	$\mathbf{I_{reflect}}$	3.0 A		**Window**
Range	500-3500 cm^{-1}	$\mathbf{P_{reflect}}$	565 mW		93 %
Co-adds/Gain/Res.	100 / 8 / 8 cm^{-1}	$\mathbf{P_{Inc}}$	1814 mW		93 %
Detector Type	PC	**Absorb**	64.0 %		
Detector Current	35 mA	**Test (A)**	$\mathbf{P_{Inc}}$	$\mathbf{P_{abs}}$	**Results**
Preamp Gain/Filter	10/300 kHz/AC	4.0	2480	1587	**PL Peak**
Power Meter	New. 1916-C	5.0	3110	1990	**8.24 ± 1.03 K/Watt**
Sample TEC	Lakeshore 330	6.0	3700	2368	
Sample Mount	InGa/Cu/InGa				
Repeat	2	**BB Range**	N/A		
PL Analysis	Exp. Gauss	**PL Range**	1400 cm^{-1} to 3300 cm^{-1}		

$\mathbf{T_{HS}}$ **(K)**	$\mathbf{P_{abs}}$ **(mW)**	$\mathbf{E_{max}}$ **(meV)**	**Std. Dev. (meV)**	$\mathbf{\Delta E_{max}}$ **(meV/W)**	$\mathbf{HE_{PL}}$ **(K/Watt)**
260	0*	305.10	0.98	3.37 ± 0.44	8.28 ± 1.08
	1587	310.51	0.34		
	1990	311.70	0.00	R^2 =	
	2368	313.14	0.00		
250	0*	302.05	0.74	3.07 ± 0.87	7.54 ± 2.14
	1587	307.39	0.00		
	1990	308.83	0.00	R^2 = 0.	
	2368	310.03	0.34		
240	0*	299.44	1.17	2.77 ± 0.42	6.81 ± 1.03
	1587	303.80	0.34		
	1990	305.47	0.68	R^2 = 0.	
	2368	305.95	0.00		
210	0*	288.87	1.08	3.38 ± 0.43	8.30 ± 1.06
	1587	294.21	0.34		
	1990	295.89	0.34	R^2 = 0.	
	2368	296.85	0.00		
200	0*	282.58	0.24	4.29 ± 0.01	10.54 ± 0.02
	1587	289.42	0.34		
	1990	291.10	0.00	R^2 = 0.	
	2368	292.77	0.34		
190	0*	279.01	0.00	3.68 ± 0.00	9.04 ± 0.00
	1587	284.86	0.00		
	1990	286.30	0.00	R^2 = 0.	
	2368	287.74	0.00		

T_{HS} (K)	P_{abs} (mW)	E_{max} meV	Std. Dev. (meV)	ΔE_{max} (meV/W)	HE_{PL} (K/Watt)
160	0*	266.15	0.00	3.08 ± 0.00 $R^2 = 0.9907$	7.57 ± 0.00
	1587	270.96	0.00		
	1990	272.40	0.00		
	2368	273.36	0.00		
150	0*	262.31	0.00	3.08 ± 0.00 $R^2 = 0.9907$	7.57 ± 0.00
	1587	267.13	0.00		
	1990	268.57	0.00		
	2368	269.53	0.00		
140	0*	258.48	0.00	3.08 ± 0.00 $R^2 = 0.9911$	7.57 ± 0.00
	1587	263.30	0.00		
	1990	264.73	0.00		
	2368	265.69	0.00		
110	0*	245.54	0.00	3.08 ± 0.00 $R^2 = 0.9907$	7.57 ± 0.00
	1587	250.35	0.00		
	1990	251.79	0.00		
	2368	252.75	0.00		
100	0*	240.73	0.09	3.69 ± 0.01 $R^2 = 0.9940$	9.07 ± 0.02
	1587	246.52	0.00		
	1990	248.20	0.34		
	2368	249.40	0.00		
90	0*	237.31	0.00	3.68 ± 0.00 $R^2 = 0.9996$	9.04 ± 0.00
	1587	243.17	0.00		
	1990	244.60	0.00		
	2368	246.04	0.00		

P_{abs} Watts	ΔE_{max} (μeV/K)	Std. Dev. (μeV/K)	Mean (μeV/K)	Offset (meV)	Std. Dev. (meV)
0	408.1	0.56	407 ± 0.72	200.88	0.24
1587	407.6	0.48		206.16	0.12
1990	406.4	0.84		207.80	0.65
2368	407.2	1.08		208.82	1.33